universität wien

DISSERTATION / DOCTORAL THESIS

Titel der Dissertation / Title of the Doctoral Thesis

"Cavity cooling by coherent scattering of a levitated nanosphere in vacuum"

verfasst von / submitted by

Uroš Delić, MSc

angestrebter akademischer Grad / in partial fulfilment of the requirements for the degree of

Doktor der Naturwissenschaften (Dr. rer. nat.)

Wien, 2019 / Vienna, 2019

Studienkennzahl lt. Studienblatt / degree programme code as it appears on the student record sheet:	A 796 605 411
Dissertationsgebiet lt. Studienblatt / field of study as it appears on the student record sheet:	Physik
Betreut von / Supervisor :	Univ.-Prof. Dr. Markus Aspelmeyer
Mitbetreut von / Co-Supervisor	Dr. Nikolai Kiesel

To my parents

To Ana

ACKNOWLEDGMENTS

I met Markus at a fun workshop in Kragujevac in 2007, just after starting my bachelor studies. Shortly afterwards, he invited me to get the first experimental experience at the IQOQI. I didn't need long to decide to move to Vienna for good after one of his epic motivational speeches about an "incredibly awesome optical levitation experiment"[1]. Ten years later, I am finishing what you might call a *group treble*[2]. Thank you, Markus, for the opportunity to work on such an interesting experiment with you. I grew as a scientist thanks to you, but I learned much more. Progress meetings, conversations over beers and blackboard discussions about crazy ideas taught me how to balance responsibilities, become passionate about a project and convey my ideas. I know there is still a lot to learn and I am looking forward to it!

The (cavity) trappers deserve special thanks as we spent days and nights together in the lab and office.

To Nikolai, the second boss: I am glad we started levitating particles together, as I can't think of a better person to share lab problems. I really appreciate the much needed push and guidance you provided (and all the coffees at Cafe Milano). Thank you immensely for everything you did for me over the years.

To David: the reason the group history is divided into BG (before Grass) and AG (after Grass). It took us only a couple of beers in ppp to become such great friends. Thanks for being my best man at the wedding and learning how to say "Da" (although a much tougher "Ne" was required). Thanks for an incredible (although that doesn't even start to describe it) bachelor party. Thanks for letting me sleep on your couch after nights of "discussion" and for all the adventures. I miss all that fun.

To Florian: the original cavity lab buddy (see Figure 0.1). Thank you for teaching me everything about the lab stuff (especially cavities!) and for enough lab fun for an eternity (for example, trying to pump down to vacuum without cooling while watching Djokovic vs. Federer matches). And to both Florian and Nouchki, thank you for sharing the love for fondue.

To Lorenzo: finally a fellow Italian chef! Thanks for sharing interesting lab problems (didn't say solve, some of them will probably re-

[1] Disclaimer: I cannot claim those were his exact words but it was along those lines.

[2] A treble in association football is achieved when a club team wins three trophies in a single season. A group treble is finishing bachelor, master and PhD degree in a single group.

main unresolved forever) and guanciale. It's always fun to complain together, either about the stupid spectrum analyzer or about people overcooking pasta. I'm looking forward to seeing you graduate soon, in five years or so!

To Manuel: I'm extremely happy you joined the experiment! I know you suffered in the first months while I was away (thanks for labeling all 1000 BNC cables!), but isn't it amazing what we managed to achieve afterwards? Here's that manual that you always wanted to read. Go do more amazing stuff now, lock the lab forever.

A good part of my research came as a result of my visit to the Vuletic group at the MIT. Thank you, Vladan, for generously inviting me to conduct my secondment in your group and for teaching me the new cavity cooling tricks. The discussions we had are always incredibly interesting and there's never enough time to go over everything. I sincerely hope to meet more often in the future.

As being a part of this group for so long, I had an opportunity to work with so many special humans that it's hard to remember. Thanks go to Ramon (for the "Best" times), Jonas (for our Badeschiff conversations into the night), (Le) Maxime (for discussing teaching), Claus (for showing me the Mannheim Wasserturm - over and over again), Philipp (for the most awesome spontaneous birthday party ever), Ralf (We'll always have Paris), Josh the Canook (for awkward dancing at my wedding), Jason (for git), Witti (for hardcore basketball games and drinks afterwards), Stefan (for hardcore basketball games and Bauernbrot afterwards), Garrett (for showing me some videos I didn't want to see), Julian (for crepes), Sebi (for clarifying some "easy" problems), Rainer (for our fun with the SAW devices), Mario, Corentin, Clemens, Hans, Joachim, Sungkun, Jeremias, Alex, TOBIAS, tobias, Mathias...

I have to thank my extraordinary physics' teachers Đorđe Ćiparizović and Nataša Čaluković for inspiring a true affection toward science through some tough problems. I am happy to have obtained my education in the Mathematical Grammar School and the Petnica Science Center. I was lucky to gain true friends from that period: Nenad, Veličko, Marina, Andrija, Srećko, Branko, Bojan... Thank you, Bori, for being a good friend over the years in Vienna (this also goes to Boka and "Bata i Seka").

The biggest thanks are for family. My parents gave me everything they could in order to be here where I am today. My brother, Igor, taught me how to add and subtract numbers when I was a really small kid, probably just to get rid of me as he understood early on how busy scientists are. Thanks for that! Ana, my partner for life, was there for me since I started my PhD studies. You were there to listen to all of my problems (although, physics - boring, right?). You taught me how to relax, enjoy, communicate, learn, work, succeed.

This thesis is finished only because of you. Thank you for love and patience during all of the nights and weekends I spent working on it.

Figure 0.1: Photograph of the experimental setup done in the style of small world photography. Using quantum mechanics, Florian Blaser and me are able to execute several tasks at once. Copyright by Jonas Schmöle.

ABSTRACT

The motion of an optically levitated dielectric nanosphere is well isolated from the environment in ultra-high vacuum. For that reason, it is a promising system to demonstrate quantum behavior at room temperature. One route to achieve this is to couple the nanosphere motion to an optical cavity field, i.e. levitated cavity optomechanics. This thesis considers two very different cavity cooling schemes on the path to demonstrate motional ground state cooling of a levitated nanosphere, which is a first step towards full quantum control at room temperature.

In the first part of this thesis we present our experimental setup for levitated cavity optomechanics. The nanosphere is trapped in an optical tweezer and positioned inside the optical cavity, with the tweezer frequency far away from all cavity resonances. The cavity is driven externally with a red-detuned laser, which controls (e.g. cools) the nanosphere motion along the cavity axis. In order to fully stabilize the nanosphere motion in vacuum, the non-axial directions are cooled with parametric feedback cooling. We characterize the optomechanical coupling rates as well as mechanical and optical loss rates in order to determine the optomechanical cooperativity. We demonstrate for the first time stable cavity cooling in high vacuum ($p \sim 10^{-6}$ mbar).

The second part introduces a significantly improved cooling scheme based on cavity-enhanced coherent scattering off the optical tweezer, i.e. the initially empty optical cavity is driven only by the light scattered off the nanosphere. Subsequently, for a tweezer red-detuned with respect to a cavity resonance the motion along all directions is strongly cooled. We demonstrate genuine three-dimensional cavity cooling, which also allows for stable levitation in high vacuum without active feedback control. In contrast to the dispersive regime in conventional cavity optomechanics, coupling of the axial motion is largest at the cavity node (intensity minimum of the cavity standing wave), which results in a strong suppression of the phase noise heating (> 40 dB for our parameters). Our observed performance implies that cavity cooling by coherent scattering should enable quantum ground state cooling of levitated nanoparticles for background pressures below 10^7 mbar and without additional laser noise filtering.

ZUSAMMENFASSUNG

Die Bewegung eines optisch levitierten, dielektrischen Nanoteilchens im Ultrahochvakuum ist gut von der Umgebung isoliert. Aus diesem Grund ist es ein vielversprechendes System um Quantenverhalten bei Raumtemperatur nachzuweisen. Ein Weg um dies zu erreichenist die Bewegung des Nanoteilchens an ein optisches Resonator zu koppeln (levitated cavity optomechanics). In dieser Arbeit werden zwei sehr unterschiedliche Methoden des Resonatorkühlens betrachtet die einerseits notwendig sind um den Bewegungsgrundzustand eines levitierten Nanoteilchens zu demonstrieren und andererseits den ersten Schritten zur totalen Quantenkontrolle bei Raumtemperatur darstellen.

Im ersten Teil dieser Arbeit wird unser experimenteller Aufbau für Optomechanik mit levitierten Nanoteilchen vorgestellt. Das Nanoteilchen ist in einer optischen Pinzette gefangen und in dem optischen Resonator positioniert, wobei die Oszillationsfrequenzen in der Pinzette weit von allen Resonanzen des optischen Resonators entfernt sind. Der Resonator wird extern mit einem rotverstimmtem Laser gepumpt, der die Bewegung des Nanoteilchens entlang der Resonatorachse steuert (z.B. kühlen). Um die Nanoteilchenbewegung im Vakuum vollständig zu stabilisieren werden die nicht axialen Richtungen mit parametrischer Rückkühlung gekühlt. Wir charakterisieren die optomechanischen Kopplungsraten sowie die mechanischen und optischen Verlustraten um die optomechanische Kooperativität zu bestimmen. Wir demonstrieren erstmals stabiles Resonatorkühlen im Hochvakuum ($p \sim 10^{-6}$ mbar).

Der zweite Teil beschäftigt sich mit einem deutlich verbessertem Kühlschema, das auf einer resonatorverstärkten, kohärenten Streuung der optischen Pinzette basiert, d.h. der zunächst leere optische Resonator wird nur durch das von dem Nanoteilchen gestreuten Licht gepumpt. Folglich wird mit einer Pinzette, die bezüglich der Resonanz des optischen Resonators rotverstimmt ist, die Bewegung in alle Richtungen stark gekühlt. Wir zeigen echtes, dreidimensionales Resonatorkühlen, das stabiles levitieren im Hochvakuum ohne aktive Rückkühlung ermöglicht. Im Gegensatz zum dispersiven Regime der konventionellen Cavityoptomechanik ist die Kopplung der axialen Bewegung am Wellenknoten (Intensitätsminimum der Stehwelle) am größten, was zu einer starken Unterdrückung des Heizens durch Phasenrauschen führt (> 40 dB) für unsere Parameter). Unsere beobachtete Leistungsfähigkeit impliziert, dass Resonatorkühlen durch kohärente Streuung die Kühlung von levitierten Nanoteilchen

in den Grundzustand bei Hintergrunddrücken von unter 10^{-7} mbar und ohne zusätzliche Laserrauschfilterung ermöglichen sollte.

CONTENTS

1

INTRODUCTION

The field of quantum cavity optomechanics, which focuses on the mutual interaction between an optical cavity field and the motion of a mechanical object via radiation pressure, has grown tremendously in the past ten years [Aspelmeyer et al., 2013]. The cooling of the motion of a mechanical object to its ground state [Teufel et al., 2011a, Chan et al., 2011], strong coupling [Aoki et al., 2006, Teufel et al., 2011b, Gröblacher et al., 2009], mechanical squeezing [Safavi-Naeini et al., 2013b, Purdy et al., 2013] and (opto-)mechanical entanglement [Palomaki et al., 2013, Riedinger et al., 2018] are important milestones in this field. Objects under investigation cover many orders of magnitude in mass, from atom clouds [Murch et al., 2008, Schleier-Smith et al., 2011], over microtoroids [Schliesser et al., 2006] and membranes [Thompson et al., 2008], to microscopic mirrors [Gigan et al., 2006, Arcizet et al., 2006].

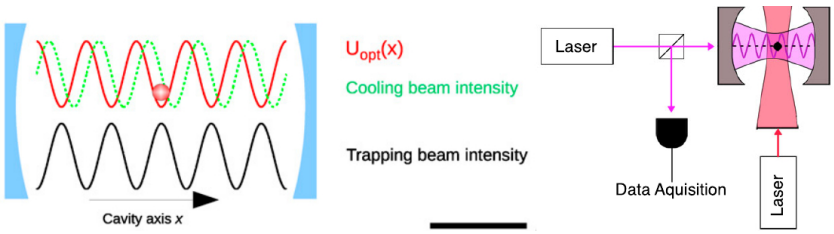

Figure 1.1: Schemes of the experiment with levitated nanoparticles from [Chang et al., 2010] (left panel) and [Romero-Isart et al., 2010] (right panel). While in the first case the particle was trapped by a cavity mode, the latter setup proposes trapping with a focused external laser. However, both proposals include an optical cavity to reach significant cooling and to realize quantum protocols.

More recently, a system consisting of an optically levitated subwavelength dielectric particle in an optical cavity was proposed (Figure 1.1) [Romero-Isart et al., 2010, Chang et al., 2010, Barker and Shneider, 2010]. Due to no internal material losses the nanosphere motion should reach high quality factors, which will mostly be limited by gas damping (quality factor $Q \approx 2 \times 10^8$ at a pressure of $p = 10^{-6}$ mbar). Partial decoupling from thermal environment should lead to an experimental regime of room-temperature quantum optomechanics. Realizing a quantum superposition of a nanosphere [Romero-Isart et al., 2011] or teleportation of quantum state of light

to a nanosphere [Hofer et al., 2013] is an achievable goal with this system, given large enough cooperativity $C = 4g^2/\kappa\Gamma$, a ratio of light-particle coupling g to all decoherence mechanisms (κ: cavity decay loss, Γ: motional heating). In contrast to majority of optomechanical systems, by creating arbitrary potential shapes (for example, with a spatial light modulator: SLM) we could obtain access to nonlinear potentials and achieve unprecedented control over the mechanical motion.

Both levitated nanoparticles and atoms interact with light through dipole interaction. Atoms driven with far detuned laser beams (such that no internal transitions are excited) have been shown to couple to an externally driven cavity mode [Horak et al., 1997, Vuletić and Chu, 2000, Schleier-Smith et al., 2011, Purdy et al., 2010], as well as by coherent scattering into an initially empty cavity mode [Vuletić et al., 2001, Murr et al., 2006, Leibrandt et al., 2009, Hosseini et al., 2017]. Conventional optomechanical interaction with nanoparticles is readily explained by a position-dependent change of the cavity length due to the presence of a nanoparticle with higher refractive index in the cavity mode. On the other hand, coherent scattering off the nanosphere into the cavity mode was not investigated in the past.

Early levitation experiments were conducted with microparticles. Optical levitation of glass microspheres in air (diameter of $15-25\ \mu$m) was first realized by trapping in a single laser beam against gravity [Ashkin and Dziedzic, 1971]. Follow-up experiments included a feedback stabilization of the levitated microsphere [Ashkin and Dziedzic, 1977] and achieved trapping in high vacuum down to 10^{-6} mbar [Ashkin and Dziedzic, 1976]. Since the initial pioneering experiments by Ashkin, optical levitation was used primarily for trapping molecular and biological samples in liquids and has become an important tool in atomic physics [Ashkin, 2006].

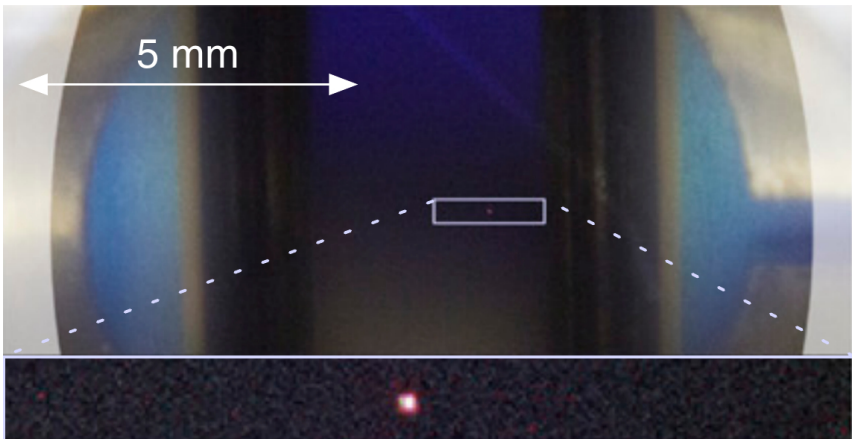

Figure 1.2: Levitated sub-micron particle (diameter of 254 nm) trapped in an optical cavity (length $L = 1.1$ cm) [Kiesel et al., 2013]. The trapping was realized with a resonant cavity mode, while a different, detuned cavity mode was responsible for cavity cooling. ©Jonas Schmöle

One of the main requirements for quantum control of a levitated particle is to achieve stable levitation in high vacuum. Since the revival of interest in optical levitation, this has been one of the main challenges in the past years all around the world, where the actual loss mechanism is not fully resolved yet. Series of results has gradually removed the major experimental obstacles: Feedback cooling of the nanosphere motion was developed to levitate a particle in high vacuum [Gieseler et al., 2012, Jain et al., 2016, Monteiro et al., 2018]. In order to place a single particle in the optical cavity, successful transport of trapped nanoparticles over long distances was demonstrated with a movable optical trap (MOBOT) [Mestres et al., 2015] and a hollowcore fiber [Grass et al., 2016]. Cavity cooling of the particle motion was first demonstrated at $p \approx 8$ mbar by us in an experimental setup preceding this thesis (Figure 1.2) [Kiesel et al., 2013], as well as with freely propagating particles in high vacuum (10^{-8} mbar) [Asenbaum et al., 2013]. In the case of our previous experiment, the axial particle motion was cooled from room temperature to $\sim$ 60 K, which was limited only by the background pressure. However, to this day no successful experimental combination of a stable trapping potential with an optical cavity was realized, although overhanding of a particle to the cavity in vacuum (resulting in an almost instantaneous loss) has been accomplished [Mestres et al., 2015].

The goal of this doctoral work was to develop a new experimental setup which would allow us to achieve high optomechanical cooperativity ($C > 1$) of the nanosphere motion, as this is a necessary precondition to achieve quantum control of a nanosphere. In addition to building a current state-of-the-art setup, we explain and demonstrate genuine three-dimensional cavity cooling by coherent scattering.

1.1 OVERVIEW OF THIS THESIS

This thesis investigates two paradigms of cavity cooling of a levitated nanosphere. In Chapters 2, 3 and 4 we achieve optomechanical coupling to a cavity driven by an external laser field. In Chapters 5 and 6 we focus on cavity cooling by coherently scattered light into an initially empty cavity. Note that conventional optomechanical interaction can be explained also by coherent scattering of the externally driven cavity mode, which we point out in Section 5.1.3 [Tanji-Suzuki et al., 2011].

1.1.1 *Levitated cavity optomechanics in high vacuum*

Chapter 2: Starting from the dipole interaction of the nanosphere with the tweezer and the externally driven cavity mode we introduce the optomechanical interaction between the one-dimensional motion of the nanosphere and the externally driven cavity mode. By assum-

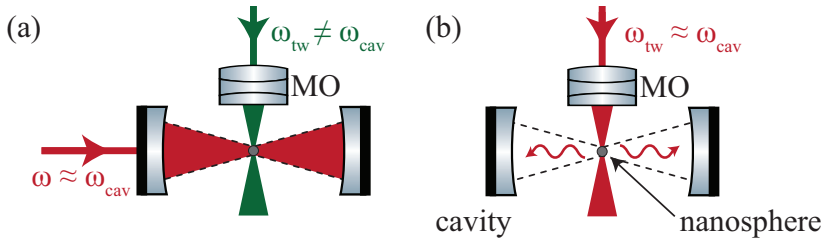

Figure 1.3: **Two different paradigms of cavity cooling of the nanosphere motion.** (a) The nanosphere is initially trapped in an optical tweezer and placed within an externally driven, far-detuned cavity mode. The nanosphere motion along the cavity axis is cooled when the external cavity drive is red detuned with respect to the cavity resonance. (b) The tweezer optical frequency is now in the vicinity of an initially empty cavity mode. The scattered light off the nanosphere is driving the cavity mode. Subsequently, the nanosphere motion along both optical axes is cooled strongly, with a possibility to add the cooling of the third dimension.

ing an arbitrary trapping position along the cavity axis, we consider both linear and quadratic coupling. We then cover possible heating mechanisms of the nanosphere motion and calculate the optomechanical cooperativity including all relevant decoherence terms.

Chapter 3: We focus on the experimental setup, with an emphasis on the tweezer and the optomechanical cavity. We describe the detection schemes, particularly the homodyne detection and the detection of optomechanically induced transparency (OMIT). We present a novel method to determine the nanosphere radius, which is based solely on the linear and quadratic interaction with a cavity mode. We subsequently discuss the observed optical trapping of both droplets and nanospheres with a liquid shell.

Chapter 4: We use the three-dimensional feedback cooling to stabilize the nanosphere motion in high vacuum ($p = 4 \times 10^{-7}$ mbar). We measure the heating rate with relaxation measurements as a function of pressure. The optomechanical coupling is obtained from the OMIT measurements both at high and low pressures. From these we calculate the optomechanical cooperativity $C \approx 0.01$, a five orders of magnitude improvement over previous experiments. We estimate the limit imposed on the cooperativity by joint trapping. We further explore strategies to achieve the strong cooperativity regime $C > 1$ and calculate the minimum achievable phonon number for sideband cooling.

1.1.2 *Cavity cooling of a levitated nanosphere by coherent scattering*

Chapter 5: We show in theory how the tweezer light scattered off the nanosphere can be used for three-dimensional cavity cooling of the nanosphere motion. Based on previously achieved experimen-

tal parameters we compare coupling rates and cooperativity of these schemes.

Chapter 6: We demonstrate all of the predicted effects from Chapter 5, including the unprecedented high coupling rates. The achieved three-dimensional cavity cooling will be enough to stabilize the nanosphere motion even in high vacuum, removing the need for an active feedback cooling scheme. Moreover, we show that the coupling of the laser phase noise to the cavity is suppressed at the position of optimal axial cooling. Due to much higher coupling and no noise limiting the performance of cavity cooling, we conclude that the ground state cooling is within reach. We provide an outlook for future experiments operating deep in the quantum regime.

Part I

LEVITATED CAVITY OPTOMECHANICS IN HIGH VACUUM

2

OPTOMECHANICS WITH LEVITATED NANOSPHERES

In this chapter we cover the theory of cavity optomechanics with a levitated nanosphere. In contrast to previous work [Kiesel et al., 2013, Millen et al., 2015, Fonseca et al., 2016] the nanosphere is held in a tweezer generated with an external laser, which allows independent positioning with respect to the optical cavity. The cavity mode is used only to control the nanosphere motion. We focus on the dipole interaction of the nanosphere with a cavity mode and investigate linear and quadratic coupling terms as a function of position. We generate and solve the Langevin equations of nanosphere motion and light quadratures from the system Hamiltonian. All relevant heating mechanisms are included in the system dynamics. We assume a red-detuned cavity mode and calculate the resulting minimum phonon occupation and the optomechanical cooperativity. Finally, we discuss the detection of the nanosphere motion from the light quadratures, which is an essential part in this experiment.

Contents

2.1 DISSECTING THE HAMILTONIAN

Our optomechanical system comprises of three distinct driven optical modes: tweezer, cavity probe and cavity control modes. The tweezer mode creates a three-dimensional harmonic potential in which the nanosphere is optically trapped. The weak probe mode is frequency-locked to a cavity resonance and is used for detection of the nanosphere motion. The control mode is typically red-detuned and additionally shifted in frequency space by a cavity free spectral range ($\Delta\nu_{FSR}$). The system Hamiltonian is split into the free (marked with f) and the interaction terms (marked with i), which exist only in the presence of a nanosphere. We focus here on providing a detailed insight into the relevant interactions and the effects which arise from it. An important part of this study also comprises the loss channels of both the nanosphere motion and the cavity mode.

$\hat{H}^f$: Free Hamiltonian

$\hat{H}^i$: Interaction Hamiltonian

2.1.1 *Free Hamiltonian of the cavity mode*

Here we follow a well known procedure to quantize a cavity mode [Loudon, 1973]. The total electric field operator of a single cavity mode $\vec{E}_{cav}(t) = \vec{E}^+(t) + \vec{E}^-(t)$ can be decomposed into:

$$\begin{aligned} \vec{E}^+(t) &= \sqrt{\frac{\hbar\omega_{cav}}{2\epsilon_0 V_{cav}}}\hat{a} f(\vec{r})\vec{e}_p e^{-i\omega_{cav}t} \\ \vec{E}^-(t) &= \sqrt{\frac{\hbar\omega_{cav}}{2\epsilon_0 V_{cav}}}\hat{a}^\dagger f^*(\vec{r})\vec{e}_p e^{i\omega_{cav}t}, \end{aligned} \tag{2.1}$$

where ω_{cav} is the frequency of an arbitrary cavity resonance, $f(\vec{r})$ is the cavity mode function and V_{cav} is the cavity mode volume (See Appendix A for more details on V_{cav}). Operators $\hat{a}$ and $\hat{a}^\dagger$ are the annihilation and creation ladder operators, respectively. The magnetic field component is easy to attain from $\vec{B}_{cav}(t) = \frac{1}{\omega_{cav}}\vec{k} \times \vec{E}_{cav}(t)$. The Hamiltonian of the total electromagnetic energy of a single cavity mode is given by:

$$\hat{H}^f_{cav} = \frac{1}{2}\int_{V_{cav}} \left(\epsilon_0 \vec{E}^2_{cav}(t) + \mu_0^{-1}\vec{B}^2_{cav}(t)\right) d\vec{r} = \hbar\omega_{cav}\left(\hat{a}^\dagger\hat{a} + \frac{1}{2}\right). \tag{2.2}$$

For the sake of brevity, we omit the factor $\frac{1}{2}\hbar\omega_{cav}$ from future considerations.

Input-output formalism

We drive a cavity mode by an external free mode through a partially transmissive cavity mirror. In the case of a double-sided cavity, both mirrors have certain transmission[1] losses, such that the cavity mode

[1] *In general: transmission, absorption and scattering losses*

can be driven from each side. Coupling between the external free mode and a single cavity mode is given by:

$$\hat{H}^d_{free-cav} = i\hbar \int_{-\infty}^{\infty} d\omega \sqrt{\kappa(\omega)} \left(\hat{b}(\omega)\hat{a}^\dagger - \hat{b}^\dagger(\omega)\hat{a} \right), \tag{2.3}$$

where $\hat{b}$ ($\hat{b}^\dagger$) is the external field's annihilation (creation) operator, which satisfies the commutation relation $[\hat{b}(\omega), \hat{b}^\dagger(\omega')] = \delta(\omega - \omega')$, and $\kappa(\omega)$ is the broadband coupling rate. Using the Markov approximation, $\kappa(\omega)$ is considered to be constant over all frequencies ω and equal to the cavity linewidth $\frac{\kappa}{2\pi}$ (full width at half maximum, FWHM). The external mode includes a strong coherent drive E_d: $\hat{b} \to E_d + \hat{b}$, which acts as the cavity drive at the laser frequency ω_d. The coupling Hamiltonian hence becomes:

$$\hat{H}^d_{free-cav} = i\hbar E_d (\hat{a}^\dagger e^{-i\omega_d t} - \hat{a} e^{i\omega_d t}), \tag{2.4}$$

where $E_d = \sqrt{\frac{P_{in}\kappa_{in}}{\hbar\omega_d}}$ is the cavity drive in units of $\sqrt{\text{photons}}/\text{s}$ and κ_{in} is the input mirror coupling rate. The remaining fluctuation is an input field operator on the input cavity side:

$$\hat{a}_{\text{IN}} = -\frac{1}{\sqrt{2\pi}} \int_{-\infty}^{\infty} d\omega e^{-i\omega(t-t_0)} \hat{b}_0(\omega), \tag{2.5}$$

with its commutation relation $[\hat{a}_{\text{IN}}(t), \hat{a}^\dagger_{\text{IN}}(t')] = \delta(t - t')$. The input-output relation at the input mirror is:

$$\hat{a}_{\text{OUT}}(t) = \sqrt{\kappa_{in}}\hat{a}(t) - \hat{a}_{\text{IN}}(t). \tag{2.6}$$

Assuming a coherent drive applied only through a single cavity mirror, the Hamiltonian describing the driven cavity mode is:

$$\hat{H}_{cav} = \hbar\omega_{cav}\hat{a}^\dagger\hat{a} + i\hbar E_d(\hat{a}^\dagger \mathrm{e}^{-i\omega_d t} - \hat{a}\mathrm{e}^{i\omega_d t}). \tag{2.7}$$

We are able to eliminate the time dependence by applying a unitary operator $\mathrm{e}^{i\omega_d \hat{a}^\dagger \hat{a} t}$, which puts the Hamiltonian in the frame rotating at the drive laser frequency ω_d. The annihilation operator is redefined as $\hat{a} \to \hat{a}\mathrm{e}^{-i\omega_d t}$ and $-\hbar\omega_d\hat{a}^\dagger\hat{a}$ is added to the Hamiltonian, which results in the Hamiltonian in the rotating frame picture:

$$\hat{H}_{cav} = \hbar\Delta\hat{a}^\dagger\hat{a} + i\hbar E_d(\hat{a}^\dagger - \hat{a}), \tag{2.8}$$

where $\Delta = \omega_{cav} - \omega_d$ is the laser detuning with respect to the cavity mode. The Hamiltonian containing the incoherent part of the external free modes is not explicitly written, but the input and output operators will be taken into account when we explore the system dynamics. In the following, we will also use a common helpful technique, where the cavity operators are displaced by the coherent drive

$\hat{a} \rightarrow \alpha_0 + \hat{a}$. The cavity amplitude α_0 is related to the cavity drive via $\alpha_0 = E_d/(\kappa/2 + i\Delta)$ and provides the intracavity photon number $n_{phot} = |\alpha_0|^2$. Neglecting the constant energy terms, the Hamiltonian of the cavity mode is:

$$\hat{H}_{cav} = \hbar\Delta\left(\alpha_0(\hat{a}^\dagger + \hat{a}) + \hat{a}^\dagger\hat{a}\right) + i\hbar E_d(\hat{a}^\dagger - \hat{a}) \tag{2.9}$$

More detail on the formalism presented above can be found in [Walls and Milburn, 2008, Gardiner and Zoller, 2000].

2.1.2 *Dipole interaction*

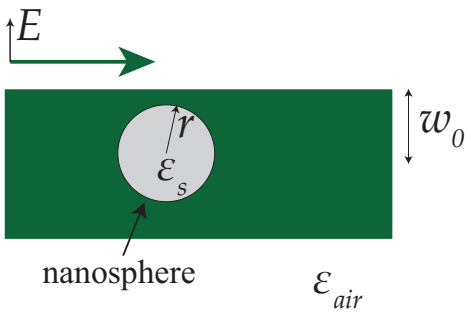

Figure 2.1: A silica nanosphere with radius r and dielectric constant ε_s is placed within the laser beam with waist $w_0 \gg r$ (in this drawing the nanosphere is disproportionate with respect to the waist).

Consider a silica dielectric nanosphere with dielectric constant $\varepsilon_s = n_s^2 \approx 2.1$ placed in an arbitrary optical mode under normal air environment $\varepsilon_{air} \approx 1$ (Figure 2.1). The mode energy is perturbed due to the presence of a nanosphere, specifically through an induced polarization density. In the Rayleigh regime, where the nanosphere radius is much smaller than the optical wavelength $r \ll \lambda$ (in practice, this is considered valid for $r < \lambda/10$), the polarization density is assumed to have a linear dependence on the electric field: $\vec{P} = \varepsilon_0\chi\vec{E}$, where $\chi = 3\,\mathrm{Re}\left(\frac{\varepsilon_s - 1}{\varepsilon_s + 2}\right)$ is the electric susceptibility of the nanosphere. The perturbation energy integrated over the volume of the induced dipole is [Jackson, 1998]:

$$\hat{H}^i_{light-nano} = -\frac{1}{2}\int_V \vec{P}(\vec{x})\vec{E}(\vec{x})d\vec{x} = -\frac{1}{2}\varepsilon_0\chi\int_V |\vec{E}(\vec{x})|^2 d\vec{x}. \tag{2.10}$$

In our system we work with optical fields that extend over ranges much larger than the nanosphere radius (waist $w_0, \lambda \gg r$). Thus we assume that the electric field is uniform over the extent of the nanosphere:

$$\hat{H}^i_{light-nano} = -\frac{1}{2}\alpha|\vec{E}|^2, \tag{2.11}$$

where $\alpha = 3\varepsilon_0 V \,\mathrm{Re}\left(\frac{\varepsilon_s - 1}{\varepsilon_s + 2}\right)$ is the nanosphere polarizability [Stratton, 1941]. To obtain the interaction energy with larger nanospheres ($\lambda/10 < r \lesssim \lambda$) it is required to use Mie calculus [Pflanzer et al., 2012] (Appendix B). The optical forces on microspheres ($r \gg \lambda$) are fully explained with ray optics.

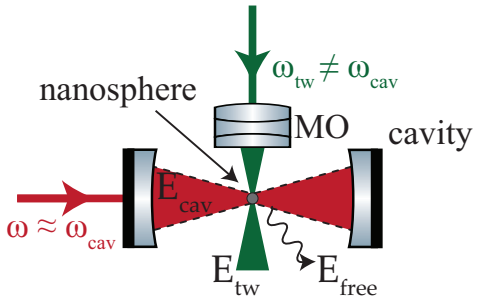

Figure 2.2: **Three different optical modes in our system.** A silica nanosphere is trapped in a tweezer mode E_{tw} formed with a microscope objective (MO). The nanosphere is placed in a cavity mode E_{cav} with resonant frequency ω_{cav}. Additionally, the nanosphere couples the tweezer and cavity modes to the continuum of free modes E_{free}.

In our experiment, the total electric field $\vec{E} = \vec{E}_{cav} + \vec{E}_{tw} + \vec{E}_{free}$ consists of three components: the cavity field(s) $\vec{E}_{cav}$, the single-beam trapping field (tweezer) $\vec{E}_{tw}$ and the free optical modes $\vec{E}_{free}$ of the mode continuum (Figure 2.2). Terms of the type $H^i_{field-nano} \propto |\vec{E}_{field}|^2$ contain the relevant light-nanosphere interaction, although we expect that $H^i_{free-nano}$ will have negligible interaction strength. The cross-terms $|\vec{E}_i \vec{E}_{j\neq i}|$ are a source of coupling between the different optical modes. For example, the terms $|\vec{E}_{cav}\vec{E}_{free}|$ and $|\vec{E}_{tw}\vec{E}_{free}|$ describe scattering of photons from the cavity and tweezer modes into free space, respectively. These processes provide an additional cavity decay rate and the recoil heating of the nanosphere motion. The interaction $|\vec{E}_{cav}\vec{E}_{tw}|$ can be suppressed both by orienting the tweezer polarization along the cavity axis to minimize the mode overlap and by tuning the two lasers far apart in frequency space. This is fulfilled for experiment in the first part of this thesis. In the following, we investigate the common contributions to the system Hamiltonian.

Interaction with the tweezer field

We first explore the dipole interaction of the nanosphere in the tweezer mode. We focus solely on the strong coherent drive of the tweezer electric field E_{tw} with intensity $I_{tw}(\vec{r}) = \varepsilon_0 c |\vec{E}_{tw}(\vec{r})|^2/2$. The dipole interaction Hamiltonian is:

$$\hat{H}^i_{tw-nano} = -\frac{\alpha}{\varepsilon_0 c} I_{tw}(\vec{r}). \tag{2.12}$$

The tweezer intensity can be expanded in Taylor series around the focal point[2]. To a first approximation, the dipole interaction with a Gaussian-shaped tweezer mode resembles a three-dimensional harmonic potential for the nanosphere center-of-mass (COM) motion, i.e. an optical trap. For more details on the complex electric field in the tweezer focus, refer to Appendix C.

[2] $I_{tw}(\vec{r}) \approx I_0 - \sum_{i=x,y,z} \frac{1}{2}\frac{\partial^2 I_{tw}}{\partial i^2} i^2$

In the most general case, the trap is characterized by the three mechanical frequencies Ω_x, Ω_y and Ω_z. As we are interested mostly in the system Hamiltonian along the x-axis, from now on we neglect the role of other directions of motion and simplify the Hamiltonian to the potential energy of a harmonic oscillator:

$$H^i_{tw-nano} = \frac{m\Omega_x^2 \hat{x}^2}{2}. \tag{2.13}$$

Beyond the harmonic approximation to Equation (2.12), the higher-order terms $\propto \mathcal{O}(\hat{x}^4)$ effectively limit the depth of the potential well. The nanosphere is able to experience these nonlinearities [Gieseler et al., 2013], which is typically prevented by reducing the motional amplitude, e.g. via feedback cooling schemes [Gieseler et al., 2012, Mestres et al., 2015, Jain et al., 2016].

Interaction with the cavity mode

The interaction of the nanosphere with the quantized cavity mode from Section 2.1.1 is described by:

$$\hat{H}^i_{cav-nano} = -\frac{1}{2}\alpha |\vec{E}_{cav}|^2 = -\hbar U(\vec{x})\hat{a}^\dagger \hat{a}, \tag{2.14}$$

where we make use of the rotating wave approximation (RWA) as terms $\hat{a}^\dagger\hat{a}^\dagger$ and $\hat{a}\hat{a}$ oscillate too fast. The total cavity Hamiltonian $\hbar(\omega_{cav} - U(\vec{x}))\hat{a}^\dagger\hat{a}$ is modified to include the position-dependent cavity frequency shift $U(\vec{x})$ (Figure 2.3):

$$U(\vec{x}) = \underbrace{\frac{3\omega_{cav}V}{2V_{cav}} \mathrm{Re}\left(\frac{\varepsilon_s - 1}{\varepsilon_s + 2}\right)}_{U_0} |f(\vec{r})|^2, \tag{2.15}$$

with the cavity mode profile:

$$|f(x,y,z)|^2 = \frac{w_0^2}{w^2(x)} \cos^2(kx) \mathrm{e}^{-\frac{2y^2}{w_0^2}} \mathrm{e}^{-\frac{2z^2}{w_0^2}},$$

where with $x_0 = 0$ we mark the cavity waist. The interaction strength depends on the nanosphere's relative position in the cavity standing wave and reaches its maximal value $\hbar U_0$ in the cavity waist, with a nanosphere-induced frequency shift to the cavity resonance U_0 [Nimmrichter et al., 2010, Monteiro et al., 2013]. $|f(\vec{r})|^2$ is the cavity mode profile:

U_0: *frequency shift*

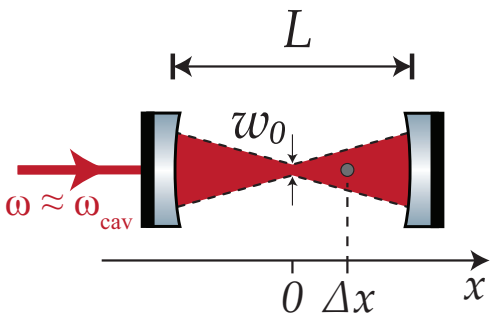

Figure 2.3: **A silica nanosphere in the optical cavity with cavity waist w_0 and length L.** The nanosphere is placed on the optical axis of the externally driven cavity mode at a distance Δx from the cavity center, resulting in a frequency shift $U(\Delta x)$ of the cavity resonance.

We focus on a special case where the nanosphere is positioned on the cavity axis, rendering $y_0 = z_0 = 0$ while allowing for an arbitrary x. Consequently, the cavity mode function is restricted to $|f(\vec{r})|^2 = \frac{1}{2}(1 - \cos(kL)\cos(2k\Delta x))$, where Δx is the distance from the cavity center and L is the cavity length (Figure 2.3). The final expression for the mode function depends on the boundary condition $f_b(k) = \cos(kL) = \pm 1$, i.e. if the cavity standing wave has an odd or even number of half-wavelengths between the cavity mirrors. Here we have neglected the change of the mode waist as a function of x, as the Rayleigh range of the cavity mode $x_R \approx 5$ mm is comparable to $L/2$. Therefore, the waist changes insignificantly along the cavity axis. Without a loss of generality, we choose $\cos(kL) = -1$, which is equivalent to having an intensity maximum at the cavity center. Keep in mind that all Hamiltonians containing the interaction with a cavity field are susceptible to a sign reversal in the opposite case of $\cos(kL) = 1$, as this corresponds to having an intensity minimum at the cavity waist. Through trivial trigonometric identities and a Taylor expansion of the nanosphere motion $\hat{x}$ around the trap position x_0, we obtain:

$$\cos^2(k\Delta x) \approx \cos^2(kx_0) - \sin(2kx_0)k\hat{x} - \cos(2kx_0)k^2\hat{x}^2 + \mathcal{O}(\hat{x}^3). \tag{2.16}$$

g_0: linear coupling

The linear optomechanical interaction Hamiltonian with single-photon coupling rate $g_0 = U_0 k x_{zpf}$ and the zero point fluctuation $x_{zpf} = \sqrt{\frac{\hbar}{2m\Omega_x}}$ is:

$$\hat{H}^i_{cav-nano} = \hbar U_0 k \sin(2kx_0)\hat{a}^\dagger\hat{a}\hat{x} \approx \hbar g_0 |\alpha_0| \sin(2kx_0)(\hat{a}^\dagger + \hat{a})(\hat{b}^\dagger + \hat{b}), \tag{2.17}$$

where the nanosphere motion is expressed as a quantum harmonic oscillator $\hat{x} = x_{zpf}\left(\hat{b} + \hat{b}^\dagger\right)$. The cavity field operators are displaced as $\hat{a} \to \alpha_0 + \hat{a}$, where α_0 is the amplitude of the light field. We subsequently constrain the Hamiltonian only to the strongest interaction

between the motional and cavity operators $\hat{b}$ and $\hat{a}$, respectively. This results in the well-known interaction Hamiltonian for levitated cavity optomechanics [Chang et al., 2010, Romero-Isart et al., 2010, Monteiro et al., 2013]. The single-photon coupling g_0 is often combined with the strength of the coherent drive to give a total coupling rate $g = g_0|\alpha_0|$.

g: total coupling

NONLINEAR CONTRIBUTIONS. There are several terms we have not included in the considerations so far:

- Non-interaction term $-\hbar U_0 \cos^2(kx_0)\hat{a}^\dagger\hat{a}$ is combined with Equation (2.2) to give the total relative detuning between the cavity resonance and the drive laser $\overline{\Delta} = \Delta - U_0\cos^2(kx_0)$.
- A constant force on the nanosphere $\hbar\frac{g_0}{x_{zpf}}\sin(2kx_0)|\alpha_0|^2\hat{x}$ is responsible for a displacement of the nanosphere position and is typically neglected for weakly populated cavity modes (small $|\alpha_0|^2$).
- Terms quadratic in $\hat{x}$ from Equation (2.16) provide higher-order contributions to the Hamiltonian:

$$\text{Harmonic potential:} \quad \hat{H}^{hp} = \hbar U_0 k^2 \cos(2kx_0)|\alpha_0|^2\hat{x}^2 \tag{2.18}$$

$$\text{Quadratic coupling:} \quad \hat{H}^{qc} = \hbar\frac{g_q\alpha_0}{x_{zpf}^2}\cos(2kx_0)(\hat{a}^\dagger + \hat{a})\hat{x}^2, \tag{2.19}$$

$$\text{Tertiary coupling:} \quad \hat{H}^{cc} = -\hbar\frac{g_t\alpha_0}{x_{zpf}^3}\sin(2kx_0)(\hat{a}^\dagger + \hat{a})\hat{x}^3, \tag{2.20}$$

with $g_q = U_0k^2x_{zpf}^2$ and $g_t = \frac{2}{3}U_0k^3x_{zpf}^3$.

quadratic and tertiary coupling

The Hamiltonian $\hat{H}^{hp}$ adds to the tweezer harmonic potential and induces a shift of the mechanical frequency:

mechanical frequency shift

$$(\Omega_x')^2 = \Omega_x^2 + \frac{2\hbar U_0k^2|\alpha_0|^2}{m}\cos(2kx_0). \tag{2.21}$$

The effect can be both constructive and destructive depending on the trap position x_0 (see Section 3.3.2 for the experimental confirmation): the nanosphere experiences an additional restoring force $F = -k_{cav}x$ at the intensity maximum, where $k_{cav} = 2\hbar U_0k^2|\alpha_0|^2$ is the spring constant due to the cavity potential. At the intensity minimum of the cavity standing wave, the nanosphere is exactly halfway between the two intensity maxima, thus experiencing a pulling force $F = k_{cav}x$ in each direction. This leads to a decrease in the trapping frequency. For small perturbations of the frequency we can use a first-order approximation, which is a direct function of the quadratic coupling g_q:

$$\Omega_x' \approx \Omega_x + 2g_q|\alpha_0|^2\cos(2kx_0). \tag{2.22}$$

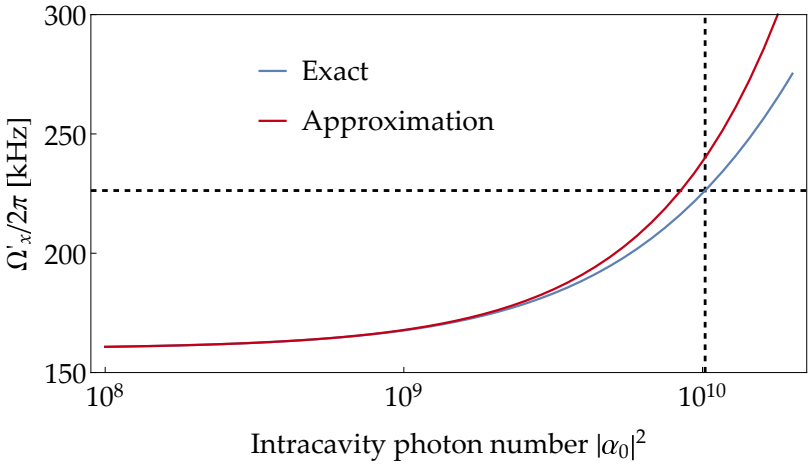

Figure 2.4: **Modified mechanical frequency due to co-trapping by the cavity mode.** We assume the nanosphere is positioned at the intensity maximum, where the largest frequency shift is observed. The exact solution from Equation (2.21) (blue) is compared to the approximation from Equation (2.22) (red), where in both cases we assume an equal initial mechanical frequency $\Omega_x = 2\pi \times 160$ kHz. The dashed lines mark the case of equal tweezer and cavity intensities.

This approximation is an overestimate to the full mechanical frequency, which we see in Figure 2.4.

The second contribution ($\hat{H}^{qc}$) describes the quadratic optomechanical interaction, which can be used in quantum nondemolition measurements of $\hat{x}^2$, quadratic cavity cooling as well as optomechanical squeezing [Nunnenkamp et al., 2010]. The cubic interaction ($\hat{H}^{cc}$) leads to the detection of $\hat{x}^3$, at the same position along the cavity axis where we directly detect the motion $\hat{x}$.

Finally, at the cavity antinodes and nodes (maximum and minimum intensity of the cavity standing wave) the nanosphere will experience exclusively the quadratic effects. Maximum linear coupling, on the contrary, is featured at the largest intensity gradient of the standing wave, halfway between the intensity minimum and maximum. We will investigate this behavior in Section 3.3.2.

COUPLING TO THE y- AND z-MOTION. Under the constraints $y_0 = z_0 = 0$, the Taylor expansion of the cavity mode function $|f(\vec{r})|^2$ reveals quadratic coupling of the y- and z-motion to the cavity mode:

$$|f(\vec{r})|^2 \overset{y_0=z_0=0}{\approx} \cos^2(kx_0)\left(1 - 2\frac{\hat{y}^2}{w^2(x_0)} - 2\frac{\hat{z}^2}{w^2(x_0)}\right). \tag{2.23}$$

However, due to the large cavity waist the coupling rates are negligible compared to the optimal quadratic coupling g_q to the x-motion:

$$\frac{g_q^{y,z}}{g_q} = \frac{2}{k^2 w^2(x_0)} \approx \frac{2}{kL} \sim 10^{-4}. \tag{2.24}$$

Here we used that the cavity waist of confocal cavities is approximately $w_0 = \sqrt{L/k}$.

We now relax the condition on the nanosphere trap position and let y_0, z_0 take arbitrary values (Figure 2.5):

$$|f(\vec{r})|^2 \approx \cos^2(kx_0) e^{-\frac{2(y_0^2+z_0^2)}{w^2(x_0)}} \left(1 - 4\frac{y_0}{w^2(x_0)}\hat{y}\right)\left(1 - 4\frac{z_0}{w^2(x_0)}\hat{z}\right). \tag{2.25}$$

The maximum linear coupling of the y- and z-motion is reached at the maximum gradient of the Gaussian mode envelope, which is approximately at $y_0 = z_0 \approx w(x_0)$:

$$\frac{g_0^{y,z}}{g_0} = \frac{4}{kw(x_0)} \approx \frac{4}{\sqrt{kL}} \approx 10^{-2}. \tag{2.26}$$

However, due to the displacement off-axis in both the z and y direction, the linear coupling of the x-motion decreases significantly by a factor of $e^{-4} \approx 10^{-2}$, rendering this approach unsuitable for genuine three-dimensional linear coupling. On the other hand, by rotating the tweezer polarization we could achieve the coupling of both x- and y-motion to the cavity mode due to a rotated trap potential (see Appendix C). This comes with only a factor of $\sqrt{2}$ smaller coupling compared to g_0.

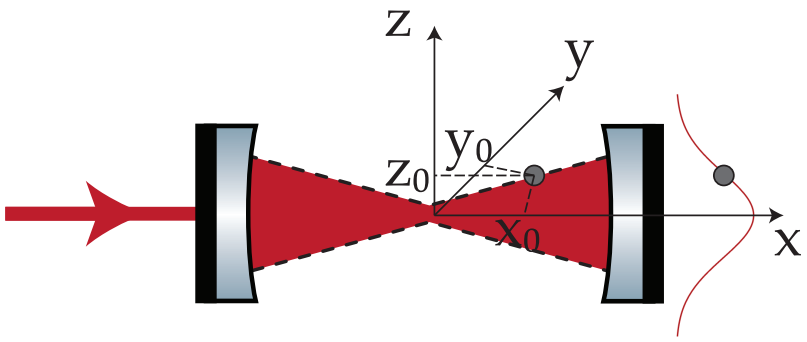

Figure 2.5: The nanosphere is placed at arbitrary coordinates (x_0, y_0, z_0). For example, the nanosphere displacement by $z_0 \neq 0$ from the cavity axis results in the linear coupling of the z-motion to the cavity mode, as the nanosphere is placed at the slope of the Gaussian mode envelope (shown to the right of the cavity).

SHIFT OF THE MECHANICAL FREQUENCIES Ω_y AND Ω_z. The Gaussian intensity profile of the cavity mode along the y- and z-axis provides an additional trapping potential for the nanosphere. For example, to first order along the y-axis the cavity mode induces (always) a positive frequency shift:

$$\Omega_y' = \Omega_y + \frac{4\hbar U_0 n_{phot}}{m w_0^2} \cos^2(kx_0). \tag{2.27}$$

Even for intracavity photon number as high as $n_{phot} = 10^{10}$ the frequency shift is only $\sim$ 1kHz.

Interaction with the free electromagnetic modes

We have neglected the free electromagnetic modes $\vec{E}_{free}$ so far. The interaction with the tweezer ($\propto \vec{E}_{tw}\vec{E}_{free}$) and the cavity modes ($\propto \vec{E}_{cav}\vec{E}_{free}$) introduces losses into our system. The scattering of the cavity mode into free space is a coupling mechanism of the cavity mode to the free electromagnetic modes, hence it contributes to both the cavity and mechanical losses. For example, each photon scattered elastically off the nanosphere will impact the nanosphere motion through a momentum kick. The shot noise-governed photon scattering rate will lead to recoil heating Γ_{rec} of the nanosphere motion. We investigate here the recoil heating in short. A more detailed description can be found in [Jain et al., 2016].

We assume that the tweezer is polarized along the x-axis (cavity optical axis). A photon scattered off the nanosphere under a polar angle θ and an azimuth angle ϕ will experience a momentum change, which can be projected along each motional axis as $\Delta\vec{p} = \hbar k\,(\cos\theta, \sin\theta\cos\phi, \sin\theta\sin\phi)$. The dipole scattering pattern $s(\theta) = \frac{3}{8\pi}\sin\theta$ provides the scattering rate in a particular direction. The resulting force on the nanosphere $\vec{F}_{rec}(\theta,\phi)$ at time t is:

$$\vec{F}_{rec}(\theta,\phi,t) = \sqrt{s(\theta)}\frac{P_{scatt}(t)}{c}\,(\cos\theta, \sin\theta\cos\phi, \sin\theta\sin\phi)\,. \tag{2.28}$$

This force has a white spectrum:

$$S_{F_{rec}F_{rec}} = \int_{-\infty}^{\infty}\langle F_{rec}(\omega)F_{rec}(\omega')\rangle d\omega' = \frac{\hbar\omega_l}{c^2}P_{scatt}\left(\frac{1}{5},\frac{2}{5},\frac{2}{5}\right), \tag{2.29}$$

where $P_{scatt} = \frac{k^4|\alpha|^2}{6\pi\varepsilon_0^2}I_0$ is the total scattered power by a nanosphere with polarizability α, I_0 is the laser intensity and ω_l is the laser frequency. The spectrum will add to the total spectrum of the nanosphere motion and set limits on the lowest achievable motional temperature. Note that the same result holds for the recoil heating by the cavity mode, where the laser intensity has to be taken at the nanosphere position: $I_0 = I_{cav}\cos^2 kx_0$.

As mentioned above, the coherent component of the electric field E_{cav} ($\propto \alpha_0$) yields the recoil heating by the cavity mode Γ_{rec}^{cav}. The coupling of the fluctuations ($\propto \hat{a}$) to the free modes leads to an additional cavity decay loss rate κ_{scatt} of the cavity operators [Chang et al., 2010, Pflanzer et al., 2012], as each interacting cavity photon scattered out of the cavity mode contributes to information loss. As in recoil heating, it is a position-dependent function:

$$\kappa_{scatt} = \frac{1}{6\pi}\omega\frac{k^3V^2}{V_c}\chi^2\cos^2 kx_0. \tag{2.30}$$

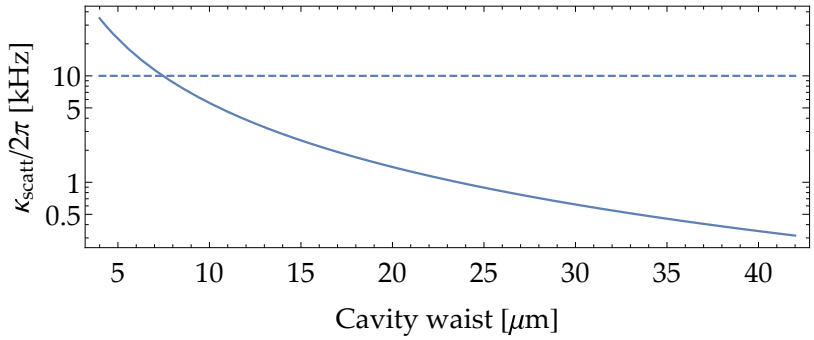

Figure 2.6: Nanosphere induced cavity decay rate κ_{scatt} as a function of the cavity waist w_0. We assume the constant cavity length $L = 1.07$ cm and a nanosphere with radius $r = 71.5$ nm. Even for a realistic cavity with a small waist $w_0 = 8$ μm we expect the loss to be less than a tenth of the total cavity decay rate $\kappa = 2\pi \times 200$ kHz.

Even for a nanosphere positioned at the intensity maximum and as small cavity waists as $w_0 = 8$ μm the scattering off the nanosphere contributes a small loss rate $\kappa_{scatt}/2\pi < 10$ kHz compared to the total cavity loss of our high-finesse cavity $\kappa = 200$ kHz (Figure 2.6).

2.1.3 *Thermal mechanical oscillator*

As seen in Section 2.1.2, a focused Gaussian laser beam provides a strong three-dimensional optical trap for the nanosphere. The total Hamiltonian associated with the nanosphere motion consists of the free part $\hat{H}^f_{nano}$, i.e. the kinetic energy, and the tweezer harmonic potential $\hat{H}^i_{tw-nano}$. In addition, the cavity mode adds to the trapping potential with $\hat{H}^{hp}$:

$$\hat{H}_{nano} = \hat{H}^f_{nano} + \hat{H}^i_{tw-nano} + \hat{H}^{hp} = \frac{\hat{p}^2}{2m} + \frac{m\Omega_x'^2\hat{x}^2}{2}. \tag{2.31}$$

Any extra cavity mode will lead to an additional trap potential adjustment. As we are currently interested only in the harmonic oscillator dynamics, we will neglect the co-trapping by the cavity modes and use the fundamental trapping frequency Ω_x at the moment.

Classical mechanics

Let us assume the dominant interaction of the nanosphere motion with the environment is through collisions with the surrounding gas. It is easy to obtain the differential equations for $\hat{x}$ and $\hat{p}$ from the Hamiltonian in Equation (2.31):

$$\begin{aligned} \dot{x} &= p/m \\ \dot{p} &= -m\Omega_x^2 x - \gamma_m p + F_{th}(t), \end{aligned} \tag{2.32}$$

where we added the gas-induced momentum dissipation rate γ_m and a random thermal force $F_{th}(t)$. Combining these two equations into a

well-known differential equation of the Brownian harmonic oscillator yields:

$$\ddot{x} + \gamma_m \dot{x} + \Omega_x^2 x = \frac{F_{th}(t)}{m}. \tag{2.33}$$

Gas damping is isotropic and follows the empirical formula [Beresnev et al., 1990]:

$$\gamma_m = \frac{6\pi\eta r}{m} \frac{0.619}{0.619 + \mathrm{Kn}} \left(1 + \frac{0.31\mathrm{Kn}}{0.785 + 1.152\mathrm{Kn} + \mathrm{Kn}^2}\right) \tag{2.34}$$

where $\mathrm{Kn} = \frac{\lambda_{\mathrm{mfp}}}{r}$ is the Knudsen number, η is the air viscosity, $\lambda_{\mathrm{mfp}} = \frac{\eta}{p}\sqrt{\frac{\pi RT}{2M_{gas}}}$ is the mean free path of air molecules with the molar mass M_{gas} at a certain pressure p, and R is the gas constant. In the case of a long mean free path (and high Knudsen number $\mathrm{Kn} \gg 1$, valid at low pressures $p < 10$ mbar), the gas damping is simplified to [Chang et al., 2010, Gieseler et al., 2013]:

$$\gamma_m = \frac{64}{3} \frac{r^2 p}{m \bar{v}_{gas}}, \tag{2.35}$$

where $\bar{v}_{gas} = \sqrt{\frac{8RT}{\pi M_{gas}}}$ is the average velocity of the air molecules. We take the textbook value for the molar mass of air $M_{gas} = 0.028964\,\mathrm{kg/mol}$. In the high pressure regime the gas damping from Equation (2.34) reduces to the constant damping from the Stokes drag (Figure 2.7). The relation between the damping rate γ_m and the thermal force $F_{th}(t)$ follows from the fluctuation-dissipation theorem [Kubo, 1966]:

$$F_{th}(t) = \sqrt{2\gamma_m m k_B T}\,\xi(t), \tag{2.36}$$

where ξ is a white noise process with delta-peaked correlation function $\langle \xi(t)\xi(t')\rangle = \delta(t - t')$.

In order to obtain the noise power spectrum (NPS) of the Brownian harmonic oscillator, a Fourier transform is usually applied to Equation (2.33):

$$\tilde{x}(\omega) = \frac{\tilde{F}_{th}(\omega)/m}{\Omega_x^2 - \omega^2 - i\omega\gamma_m} = \frac{\tilde{F}_{th}(\omega)}{m}\chi_m(\omega), \tag{2.37}$$

where the harmonic oscillator's response to the thermal force is defined as the mechanical susceptibility $\chi_m(\omega)$. The NPS follows from [Hauer et al., 2015]:

$$S_{xx}^{th}(\omega) = \int \langle \tilde{x}(\omega)\tilde{x}(\omega')\rangle d\omega' = \int \frac{\langle \tilde{F}_{th}(\omega)\tilde{F}_{th}(\omega')\rangle}{m^2}\chi_m(\omega)\chi_m^*(\omega')d\omega', \tag{2.38}$$

which has the units $\mathrm{m}^2/(\mathrm{rad\ s}^{-1})$. Using the thermal force given by Equation (2.36), the NPS is given by:

$$S_{xx}^{th}(\omega) = \frac{k_B T}{m\Omega_x^2} \frac{2\gamma_m \Omega_x^2}{(\Omega_x^2 - \omega^2)^2 + \omega^2\gamma_m^2}. \tag{2.39}$$

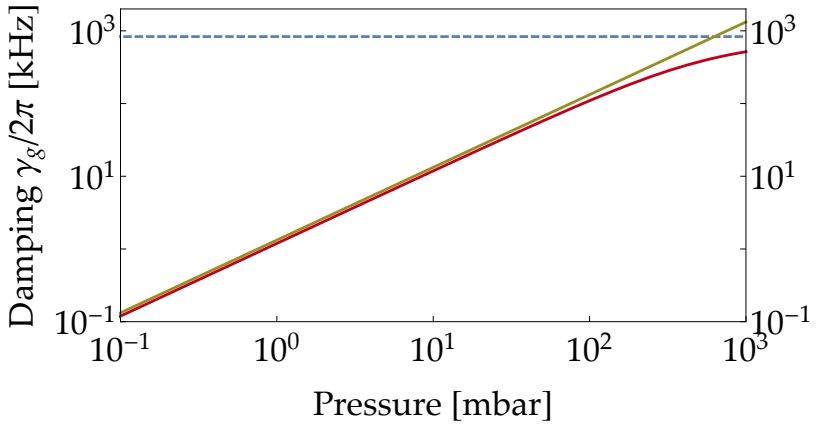

Figure 2.7: **Gas damping in different pressure regimes.** Gas damping γ_m from Equation (2.34) (green line) is compared to the low pressure approximation (red line) and the damping from the Stokes drag (blue, dashed line). We mostly keep in the regime below $p = 10$ mbar, well described by both the empirical formula and its approximation.

The spectral peak value is $S_{xx}^{th}(\omega = \Omega_x) = \frac{2}{\gamma_m}\frac{k_B T}{m\Omega_x^2}$, while the spectral area is the variance of the nanosphere motion:

$$\langle x^2(t)\rangle = \int_{-\infty}^{+\infty} S_{xx}^{th}(\omega)d\omega = \frac{k_B T}{m\Omega_x^2}. \tag{2.40}$$

The same result is obtained from the equipartition theorem, which divides the total energy of the harmonic oscillator equally between the potential and kinetic energy, thus leading to $\frac{1}{2}m\Omega_x^2\langle x^2\rangle = \frac{1}{2}k_B T$. Note that we consistently use the one-sided power spectral density in S_{xx}^{th} as a function of the angular frequency ω. However, the spectrum analyzer detects the NPS in the ordinary frequency ν, where the area of the spectrum is conveniently scaled as:

$$\int_0^{+\infty} S_{xx}(\nu)d\nu = \int_{-\infty}^{+\infty} S_{xx}(\omega)\omega. \tag{2.41}$$

Quantum mechanics

The Langevin equations obtained from the Hamiltonian in Equation (2.31) do not preserve the commutation relation $[\hat{x}, \hat{p}] = i\hbar$. Although the solution discussed in [Jacobs et al., 1999] solves this issue, it does so by introducing an additional noise term without a physical origin. However, in [Giovannetti and Vitali, 2001] authors propose a model of a thermal bath as an infinite series of independent harmonic oscillators. This approach leads to the non-Markovian dynamics of the quantum Brownian motion, which satisfies the commutation of $\hat{x}$ and

$\hat{p}$. The most important result is that the correlator of the thermal force $F_{th}(t)$ is not a Dirac delta function [Genes et al., 2008b]:

$$\langle F_{th}(t)F_{th}(t')\rangle = \hbar\gamma_m m \int \frac{d\omega}{2\pi} e^{-i\omega(t-t')}\omega \left[\coth\left(\frac{\hbar\omega}{2k_BT}\right)+1\right]. \quad (2.42)$$

The classical case is recovered in the limit of a high bath temperature T as $\coth\left(\frac{\hbar\omega}{2k_BT}\right)+1 \approx \frac{2k_BT}{\hbar\omega}$:

$$\langle F_{th}(t)F_{th}(t')\rangle = 2\gamma_m m k_B T\delta(t-t'). \quad (2.43)$$

The bath occupation is defined as $n_{th} = \frac{k_BT}{\hbar\Omega_x}$, which is equal to the occupation $\bar{n} = \frac{k_BT_{\text{eff}}}{\hbar\Omega_x}$ of the quantum harmonics oscillator (QHO) when in the thermal equilibrium with the environment at the temperature T. The noise power spectrum of the QHO position operator $\hat{x}$ has an analytic solution [Hauer et al., 2015]:

$$S_{xx}^{th}(\omega) = \gamma_m x_{zpf}^2 \left(\frac{\bar{n}}{(\omega+\Omega_x)^2+(\gamma_m/2)^2} + \frac{\bar{n}+1}{(\omega-\Omega_x)^2+(\gamma_m/2)^2}\right). \quad (2.44)$$

The contributions at $\pm\Omega_x$ are proportional to $\bar{n}+1$ and $\bar{n}$ as they correspond to the creation and annihilation operators of QHO, respectively. In the high temperature limit and assuming $\gamma_m \ll \Omega_x$, the contributions are approximately equal $\bar{n}+1 \approx \bar{n}$ and we obtain the spectrum from Equation (2.39). Integration of the power spectrum once again results in the variance of the position operator:

$$\langle \hat{x}^2\rangle = x_{zpf}^2(2\bar{n}+1) \overset{\bar{n}\gg 1}{\approx} \frac{k_BT}{m\Omega_x^2}, \quad (2.45)$$

demonstrating the correspondence to classical mechanics for large mechanical occupations $\bar{n} \gg 1$.

The contributions in Equation (2.44) are associated with the cooling processes (Anti-Stokes sideband at $\omega = -\Omega_x$) and the heating processes (Stokes sideband at $\omega = \Omega_x$). Note that in the low temperature limit ($\bar{n} \to 0$), the contribution at $\omega = -\Omega_x$ is noticeably suppressed with respect to the contribution at $\omega = \Omega_x$ (Figure 2.8(b)). In the most extreme case of a harmonic oscillator in its ground state only the heating sideband is visible, as the oscillator's energy can only increase. The ratio of the two sides of the spectrum is the basis of (Raman) sideband asymmetry thermometry, which provides an absolute measurement of the occupation. One way to observe the double-sided spectrum is with a heterodyne detection, which is described in detail in Chapter 6.

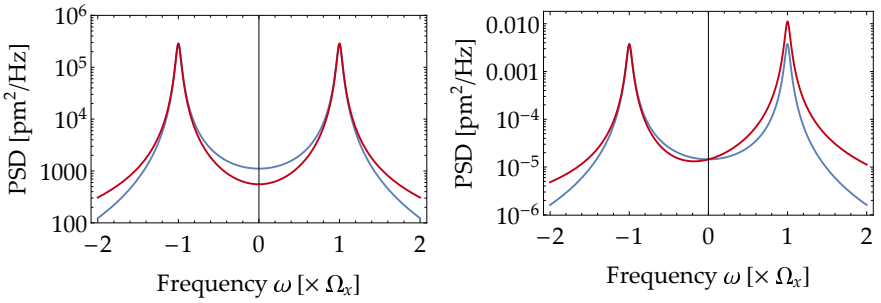

(a) High occupation $(\bar{n} = 3 \times 10^7)$ (b) Low occupation $(\bar{n} = 0.5)$

Figure 2.8: **Correspondence between the descriptions of the harmonic oscillator in the classical and quantum mechanics.** Noise power spectra of the nanosphere x-motion in the formalism of the classical (blue) and the quantum mechanics (red) are shown together. (a) The discrepancy between the harmonic oscillator spectrum predicted by the classical and quantum mechanics is non-existent in the vicinity of the mechanical frequency $\pm\Omega_x$. (b) The effect of the spectral asymmetry ($S_{xx}(\Omega_x) > S_{xx}(-\Omega_x)$) becomes visible for the low occupation of QHO, where the classical mechanics does not predict any asymmetry.

2.2 TOTAL SYSTEM HAMILTONIAN

We proceed by combining the Hamiltonians from the previous sections into the Hamiltonian of the total system. Let us assume that the nanosphere is trapped in the tweezer and placed in an optical cavity with the x-motion coupled to two cavity modes: the locking mode $\hat{a}_l$ and the control mode $\hat{a}_c$ driven with rates E_d^l and E_d^c and the laser frequencies $\omega_l = \omega_{cav,1} - \Delta_l$ and $\omega_c = \omega_{cav,2} - \Delta_c$, respectively (Figure 2.9). The two frequencies are separated roughly by the cavity free spectral range $|\omega_c - \omega_l| \approx 2\pi \times \Delta\nu_{FSR}$. The Hamiltonian is then:

$$\begin{aligned}
\hat{H}_{tot} &= \hbar\overline{\Delta}_l\hat{a}_l^\dagger\hat{a}_l + \hbar\overline{\Delta}_c\hat{a}_c^\dagger\hat{a}_c + i\hbar E_d^l(\hat{a}_l^\dagger - \hat{a}_l) + i\hbar E_d^c(\hat{a}_c^\dagger - \hat{a}_c) \\
&+ \frac{\hat{p}^2}{2m} + \frac{m\Omega_x^2\hat{x}^2}{2} \\
&\pm \hbar\frac{g_0}{x_{zpf}}\sin(2k_l x_0)\hat{a}_l^\dagger\hat{a}_l\hat{x} \pm \hbar\frac{g_q}{x_{zpf}^2}\cos(2k_l x_0)\hat{a}_l^\dagger\hat{a}_l\hat{x}^2 \\
&\mp \hbar\frac{g_0}{x_{zpf}}\sin(2k_c x_0)\hat{a}_c^\dagger\hat{a}_c\hat{x} \mp \hbar\frac{g_q}{x_{zpf}^2}\cos(2k_c x_0)\hat{a}_c^\dagger\hat{a}_c\hat{x}^2.
\end{aligned}$$

Note the following:

1. **Light operators are not displaced.** We don't use the displaced operators $\hat{a}$ and $\hat{a}^\dagger$ here for conciseness. Therefore, the mechanical frequency Ω_x is still defined solely by the tweezer harmonic potential.

2. **Opposite signs of the linear and quadratic coupling for the different cavity modes.** As discussed previously, the two cavity

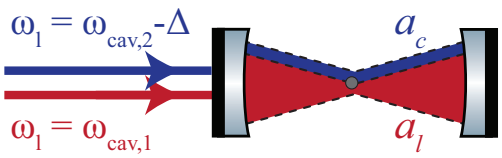

Figure 2.9: **Laser beams driving two cavity modes $\hat{a}_c$ and $\hat{a}_l$.** We assume the locking mode is resonant to the cavity resonance with frequency $\omega_{cav,1}$, while the control mode is detuned with respect to the adjacent cavity resonance at a frequency of $\omega_{cav,2} - \Delta$, where $\omega_{cav,2} - \omega_{cav,1} = 2\pi \times \Delta\nu_{FSR}$.

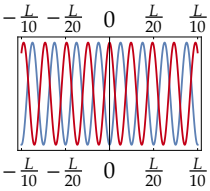

Figure 2.10: Intensity of the two successive cavity resonances around the cavity waist.

modes with a frequency difference $2\pi \times \Delta\nu_{FSR} = 2\pi \times \frac{c}{2L}$ experience the opposite boundary conditions at the cavity mirrors as $k_c L = k_l L + \pi$. This leads to a sign flip of the cavity mode function as $f_b(k) = \cos(kL) = \pm 1$ and the intensity profiles of the two modes are exactly out of phase (Figure 2.10).

3. **Single photon coupling rate** depends on the laser wavenumber k, which we can safely assume to be equal for the two modes $k_l = k_c$.

4. **Total detuning.** The laser driving the locking mode is always resonant to the cavity, thus $\bar{\Delta}_l = 0$. The control mode detuning is set manually to the desired detuning Δ_c by regularly measuring the cavity resonance $\omega_{cav,2}$ to account for any drifts. Hence we write $\bar{\Delta}_c \approx \Delta_c$ from now on.

5. **Modification to the mechanical frequency.** Both cavity modes add to the tweezer harmonic potential, resulting in the modified mechanical frequency Ω'_x:

$$\Omega_x'^2 = \Omega_x^2 \pm \frac{2\hbar U_0 k^2 (n^l_{phot})^2}{m} \cos(2kx_0) \mp \frac{2\hbar U_0 k^2 (n^c_{phot})^2}{m} \cos(2kx_0). \tag{2.46}$$

The locking mode is significantly weaker than the typical control mode $\left((n^c_{phot})^2 \gg (n^l_{phot})^2\right)$. However, in the absence of the control mode the locking mode still provides a small observable shift of the mechanical frequency and is not neglected.

6. **Optimal positions for linear optomechanics.** In the proximity of the cavity waist $x_0 \approx 0$ the coupling rates $|g^l_0|$ and $|g^c_0|$ are exactly in phase as $\sin 2k_l x_0 \approx \sin 2k_c x_0$. Therefore, by maximizing the coupling to the locking mode, we simultaneously optimize the interaction with the control mode.

7. **Additional contributions.** To keep things concise, we haven't included the mechanical and optical losses in H_{tot}. However, we will investigate them in the Langevin equations in the further text.

2.3 LANGEVIN EQUATIONS IN LINEAR OPTOMECHANICS

The system dynamics is contained in the Langevin equations of motion obtained from $\frac{d\hat{A}(t)}{dt} = \frac{i}{\hbar}[\hat{H}_{tot}, \hat{A}]$. Here we focus only on the linear interaction in $\hat{H}_{tot}$, now including all decay channels:

$$\begin{aligned}
\dot{\hat{a}}_l &= -\frac{\kappa}{2}\hat{a}_l + E_d^l + if_b(k_l)\frac{g_0}{x_{zpf}}\sin(2kx_0)\hat{a}_l\hat{x} + \sqrt{\kappa_{\mathrm{IN}}}(\hat{a}_{\mathrm{IN}}^{l,1} + \hat{a}_{\mathrm{IN}}^{l,2}) \\
\dot{\hat{a}}_c &= -\left(\frac{\kappa}{2} + i\Delta_c\right)\hat{a}_c + E_d^c + if_b(k_c)\frac{g_0}{x_{zpf}}\sin(2kx_0)\hat{a}_c\hat{x} + \sqrt{\kappa_{\mathrm{IN}}}(\hat{a}_{\mathrm{IN}}^{c,1} + \hat{a}_{\mathrm{IN}}^{c,2}) \\
\dot{\hat{x}} &= \frac{\hat{p}}{m} \\
\dot{\hat{p}} &= -m\Omega_x^2\hat{x} - \gamma_m\hat{p} + \sum_{i=l,c} f_b(k_i)\frac{\hbar g_0}{x_{zpf}}\sin(2kx_0)\hat{a}_i^\dagger\hat{a}_i + \sum_s F_s(t)
\end{aligned} \tag{2.47}$$

Here, $\sum_s F_s(t)$ is a sum of all random forces acting on the nanosphere motion, with s representing the source of the force (thermal force, recoil etc.). From the expectation value of the first two lines in Equation (2.47) we are able to determine the coherent amplitudes of operators $\hat{a}_i$:

$$\alpha_0^l = \frac{E_d^l}{\kappa/2}, \qquad \alpha_0^c = \frac{E_d^c}{\kappa/2 + i\Delta_c} \tag{2.48}$$

and the intracavity photon number $n_{phot}^i = |\alpha_0^i|^2$. We use the displaced cavity mode operators throughout the rest of this text:

$$\begin{aligned}
\dot{\hat{a}}_l &= -\frac{\kappa}{2}\hat{a}_l + if_b(k_l)\frac{g_0\alpha_0^l}{x_{zpf}}\sin(2kx_0)\hat{x} + \sqrt{\frac{\kappa}{2}}(\hat{a}_{\mathrm{IN}}^{l,1} + \hat{a}_{\mathrm{IN}}^{l,2}) \\
\dot{\hat{a}}_c &= -\left(\frac{\kappa}{2} + i\Delta_c\right)\hat{a}_c + if_b(k_c)\frac{g_0\alpha_0^c}{x_{zpf}}\sin(2kx_0)\hat{x} + \sqrt{\frac{\kappa}{2}}(\hat{a}_{\mathrm{IN}}^{c,1} + \hat{a}_{\mathrm{IN}}^{c,2}).
\end{aligned} \tag{2.49}$$

Note that we keep only the strongest interaction term $\propto g_0\alpha_0^i\hat{x}$ and neglect the significantly weaker contributions $\propto g_0\hat{a}_i\hat{x}$. The last two equations of Equation (2.47) describe the nanosphere motion. As described in Section 2.1.3, merging the results in a single differential equation of the nanosphere x-motion yields:

$$\ddot{\hat{x}} + \gamma_m\dot{\hat{x}} + \Omega_x'^2\hat{x} = \sum_{i=l,c} f_b(k_i)\frac{\hbar g_0\alpha_0^i}{x_{zpf}m}\sin(2kx_0)(\hat{a}_i^\dagger + \hat{a}_i) + \sum_s \frac{F_s(t)}{m}, \tag{2.50}$$

where we changed to the modified mechanical frequency Ω_x'.

2.3.1 *Solving the Langevin equations*

The usual method of solving a system of Langevin equations given by Equation (2.49) and Equation (2.50) is applying a Fourier transformation to eliminate the time dependence:

$$\begin{aligned}
\frac{\tilde{x}(\omega)}{\chi_m(\omega)} &= \sum_{i=l,c} f_b(k_i)\frac{\hbar g_0 \alpha_0^i}{x_{zpf} m}\sin(2kx_0)(\tilde{a}_i^\dagger(\omega)+\tilde{a}_i(\omega)) + \sum_s \frac{\tilde{F}_s}{m} \\
\tilde{a}_l(\omega) &= \chi_l(\omega)\left(i f_b(k_l)\frac{g_0\alpha_0^l}{x_{zpf}}\sin(2kx_0)\tilde{x} + \sqrt{\kappa_{\mathrm{IN}}}(\tilde{a}_{\mathrm{IN}}^{l,1}+\tilde{a}_{\mathrm{IN}}^{l,2})\right) \\
\tilde{a}_c(\omega) &= \chi_c(\omega)\left(i f_b(k_c)\frac{g_0\alpha_0^c}{x_{zpf}}\sin(2kx_0)\tilde{x} + \sqrt{\kappa_{\mathrm{IN}}}(\tilde{a}_{\mathrm{IN}}^{c,1}+\tilde{a}_{\mathrm{IN}}^{c,2})\right).
\end{aligned} \tag{2.51}$$

The optical susceptibilities $\chi_l(\omega) = \frac{1}{\frac{\kappa}{2}-i\omega}$ and $\chi_c(\omega) = \frac{1}{\frac{\kappa}{2}-i(\omega-\Delta_c)}$ are the cavity response functions for the two modes. It is straightforward to solve the system of equations given by Equation (2.51) and their complex conjugated counterparts. The Fourier transform of the $\hat{x}$-motion is:

$$\tilde{x}(\omega) = \left(\frac{\tilde{F}_{th}(\omega)}{m} + \frac{\tilde{F}_{rec}^{tw}(\omega)}{m} + \frac{\tilde{F}_{rec}^{cav}(\omega)}{m} + f_{rp}(\omega)\right)\chi_m'(\omega), \tag{2.52}$$

where $\chi_m'(\omega) = 1/\left((\Omega_x^{\mathrm{eff}})^2 - \omega^2 - i\gamma_m^{\mathrm{eff}}\omega\right)$ is the modified mechanical susceptibility:

$$\chi_m'(\omega) = \frac{1}{\Omega_x'^2 - \omega^2 - i\gamma_m\omega - \frac{4G^2\Omega_x'\Delta_c\left(\left(\frac{\kappa}{2}\right)^2-\omega^2+\Delta_c^2+i\kappa\omega\right)}{\left(\left(\frac{\kappa}{2}\right)^2+(\omega+\Delta_c)^2\right)\left(\left(\frac{\kappa}{2}\right)^2+(\omega-\Delta_c)^2\right)}}. \tag{2.53}$$

due to the interaction with the detuned cavity mode. This results in the effective mechanical frequency and damping, i.e. the optical spring and damping effects, respectively (Figure 2.11):

$$\begin{aligned}
\Omega_x^{\mathrm{eff}}(\omega) &= \sqrt{\Omega_x'^2 - \frac{4G^2\Omega_x'\Delta_c\left(\left(\frac{\kappa}{2}\right)^2-\omega^2+\Delta_c^2\right)}{\left(\left(\frac{\kappa}{2}\right)^2+(\omega+\Delta_c)^2\right)\left(\left(\frac{\kappa}{2}\right)^2+(\omega-\Delta_c)^2\right)}} \\
\gamma_m^{\mathrm{eff}}(\omega) &= \gamma_m + \frac{4G^2\Omega_x'\Delta_c\kappa}{\left(\left(\frac{\kappa}{2}\right)^2+(\omega+\Delta_c)^2\right)\left(\left(\frac{\kappa}{2}\right)^2+(\omega-\Delta_c)^2\right)}.
\end{aligned} \tag{2.54}$$

Note the following effects from the modified mechanical susceptibility:

1. **The resonant locking cavity mode does not induce any optical spring and damping effects.** As $\Delta_l = 0$, the optomechanical modifications to the mechanical frequency and damping are zero.

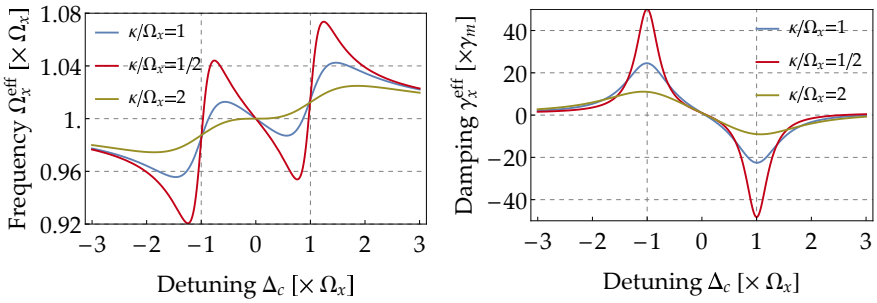

(a) Optical spring (b) Optical damping

Figure 2.11: **Optical spring effect (left panel) and optical damping effect (right panel) for different ratios of κ/Ω_x.** We assume a high quality factor $\Omega_x/\gamma_m = 2000$ and a reasonable coupling rate $g/\Omega_m = 1/4$, which still renders Ω_x^{eff} and γ_m^{eff} as valid approximations.

2. **Dependence on the Fourier frequency ω.** The effective mechanical frequency and damping depend on the frequency ω from the Fourier transform, which is not a physical parameter. However, for high mechanical quality factors $\gamma_m \ll \Omega_x'$ the largest contribution to the spectrum is in the vicinity of the spectral peak, i.e. $\omega \approx \Omega_x'$. If $\gamma_m \sim \Omega_x'$, the full expressions from Equation (2.54) have to be used.

3. **Negative damping.** The effective damping $\gamma_m^{\text{eff}}(\Omega_x')$ can become negative for $\Delta_c < 0$, which leads to heating of the nanosphere motion and subsequent loss of the nanosphere from the trap. Hence, the control laser has to be red detuned with respect to the cavity ($\Delta_c > 0$).

Spectrum of the cooled harmonic oscillator

In analogy to the NPS of the harmonic oscillator in Equation 2.39, the thermal noise spectrum of the cooled nanosphere motion is determined from the effective mechanical susceptibility:

$$S_{xx}^{th}(\omega) = \frac{k_B T}{m\Omega_x^2} \frac{2\gamma_m \Omega_x^2}{\left((\Omega_x^{\text{eff}})^2 - \omega^2\right)^2 + (\gamma_m^{\text{eff}}\omega)^2}. \tag{2.55}$$

The variance of the nanosphere motion from this contribution is:

$$\langle x^2 \rangle_{th} = \int_{-\infty}^{+\infty} S_{xx}^{th}(\omega) d\omega = \frac{k_B T}{m\Omega_x^2} \frac{\gamma_m}{\gamma_m^{\text{eff}}}, \tag{2.56}$$

where $T_{\text{eff}} = T \frac{\gamma_m}{\gamma_m^{\text{eff}}}$ is the effective temperature of the nanosphere motion. The variance can also be represented through the thermal occupation: $\langle x^2 \rangle_{th} = x_{zpf}^2 n_{th} \frac{\gamma_m}{\gamma_m^{\text{eff}}} = x_{zpf}^2 \bar{n}$. For positive detuning Δ_c (red-detuned control cavity mode) the x-motion is effectively cooled as

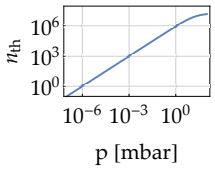

Figure 2.12: Thermal occupation of the quantum harmonic oscillator as a function of pressure.

$\gamma_m^{\text{eff}} > \gamma_m$. For a total coupling rate $g = 2\pi \times 40$ kHz we expect to reach $\bar{n} \approx 1$ at pressures below 10^{-7} mbar (Figure 2.12). However, this estimate provides a lower bound as it only includes the mechanical losses through the gas collisions and neglects effects of recoil or laser phase noise heating.

The intuition for cavity cooling is as follows: the nanosphere is coupled to two different reservoirs: the thermal bath and the control laser. The thermal bath at room temperature T results in the heating rate $\Gamma_m = \gamma_m n_{th}$. The reservoir created by the control cavity mode counteracts with a cooling rate $\Gamma_{opt} (\equiv \gamma_m^{\text{eff}} - \gamma_m)$. The interaction with the control mode is fully quantified by the Stokes (heating) and Anti-Stokes (cooling) scattering rates Γ_+ and Γ_-, respectively:

$$\Gamma_\pm = \frac{g^2 \kappa/2}{(\kappa/2)^2 + (\Omega_x \mp \Delta_c)^2}, \tag{2.57}$$

with a net cooling rate $\Gamma_{opt} = \Gamma_- - \Gamma_+$. The optimal cooling rate is reached for $\Delta_c^{\text{optimal}} = \sqrt{\Omega_x^2 + (\kappa/2)^2}$. In the case of a sideband-resolved regime ($\kappa \ll \Omega_x$), the final occupation of the harmonic oscillator is simplified to:

$$\bar{n} \approx \frac{\kappa \gamma_m n_{th}}{4g^2} \ (\text{at } \Delta_c^{\text{optimal}} \approx \Omega_x). \tag{2.58}$$

Spectrum of the recoil heating

The force of the photon recoil provides an additional component in the mechanical spectrum:

$$S_{xx}^{rec}(\omega) = \frac{1}{5mc^2} \frac{P_{scatt} \hbar \omega_l}{\left((\Omega_x^{\text{eff}})^2 - \omega^2 \right)^2 + (\gamma_m^{\text{eff}} \omega)^2}, \tag{2.59}$$

where $\hbar\omega_l$ is the energy of the incoming photons. The contribution to the occupation of the harmonic oscillator along the x axis is:

$$\bar{n}_{rec} = \langle x^2 \rangle_{rec} \frac{m\Omega_x^2}{\hbar \Omega_x} = \frac{\Gamma_{rec}}{\gamma_m^{\text{eff}}} = \frac{\kappa \Gamma_{rec}}{4g^2}, \tag{2.60}$$

where the recoil heating rate is:

$$\Gamma_{rec} = \frac{1}{5} \frac{P_{scatt}}{mc^2} \frac{\omega_l}{\Omega_0}. \tag{2.61}$$

The trap intensity is in general higher than the intensity of any cavity mode due to the discrepancy in the waists. Therefore, the recoil heating due to tweezer photons will be the dominant source of heating in the high vacuum.

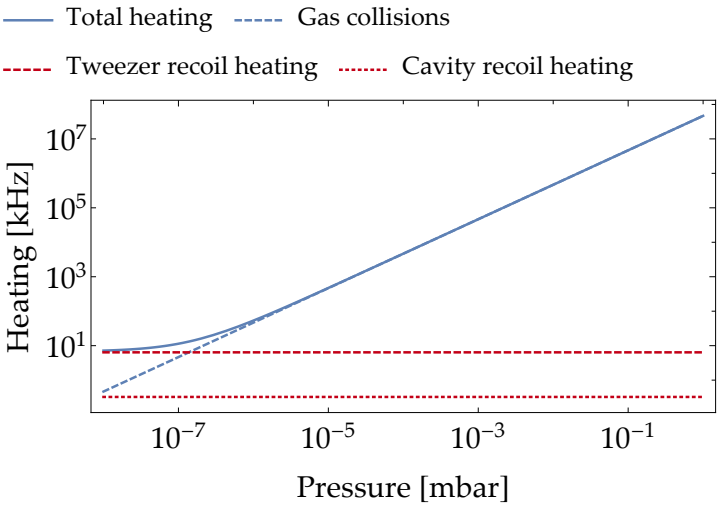

Figure 2.13: **Heating of mechanical motion divided by contributions.** Heating rate due to the gas collisions (blue, dashed) is significantly larger than tweezer recoil heating rate (red, dashed) at pressures $p > 10^{-6}$ mbar. Recoil heating from the cavity mode (red, dotted) is significantly lower than other heating rates (we assume an intracavity power $P_{cav} = 40$ W). All mentioned contributions are jointly shown as a solid blue line.

Spectrum of the radiation pressure

The radiation pressure noise spectrum depends on the cavity input noise $\tilde{a}^{i,j}_{\mathrm{IN}}$:

$$S^{rp}_{xx}(\omega) = |\chi'_m(\omega)|^2 x^2_{zpf} \frac{4\Omega'^2_x \kappa g^2 \left(\left(\frac{\kappa}{2}\right)^2 + \omega^2 + \Delta_c^2\right)}{\left(\left(\frac{\kappa}{2}\right)^2 + (\omega - \Delta_c)^2\right)\left(\left(\frac{\kappa}{2}\right)^2 + (\omega + \Delta_c)^2\right)}. \tag{2.62}$$

Assuming a small initial mechanical damping γ_m, such that the largest spectral contribution is around $\omega \approx \Omega_x$, and the optimal detuning $\Delta_c \sim \Omega_x$, we simplify Equation (2.62) to

$$S^{rp}_{xx}(\Omega_x) \approx |\chi'_m(\Omega_x)|^2 x^2_{zpf} 16\Omega_x^2 g^2/\kappa. \tag{2.63}$$

Spectrum of the phase noise

Every laser suffers from classical phase and intensity noise, which impact the performance of cavity cooling [Schliesser et al., 2008, Jayich et al., 2012, Safavi-Naeini et al., 2013a]. For example, due to non-zero detuning of the cooling laser, phase noise is converted into amplitude and intensity noise in the optomechanical cavity [Rabl et al., 2009, Phelps and Meystre, 2011].

Phase noise is included into the calculations as a phase variation of the driving field $E_d \to E_d e^{i\varphi(t)} \approx E_d(1 + i\varphi(t))$. Its impact on the mechanical oscillator is proportional to $|\chi_c(\omega) - \chi_c^*(-\omega)| \propto \Delta$, hence only the phase noise of the detuned control mode will influence

the nanosphere motion. The phase noise contribution to the position spectrum $S_{xx}^{phase}(\omega)$ is:

$$S_{xx}^{phase}(\omega) = |\chi_m'(\omega)|^2 x_{zpf}^2 \frac{16g^2\Omega_x'^2\omega\Delta|E_d|^2 S_{\varphi\varphi}(\omega)}{\left(\left(\frac{\kappa}{2}\right)^2 + (\omega-\Delta_c)^2\right)\left(\left(\frac{\kappa}{2}\right)^2 + (\omega+\Delta_c)^2\right)}. \tag{2.64}$$

We assume a red detuned laser $\Delta = \Omega_x$ and evaluate the spectrum around $\omega = \Omega_x$:

$$S_{xx}^{phase}(\Omega_x) = |\chi_m'(\Omega_x)|^2 x_{zpf}^2 \frac{16g^2\Omega_x^2 S_{\dot\varphi\dot\varphi}(\Omega_x) n_{phot}^2}{\kappa^2}, \tag{2.65}$$

where we used $|E_d|^2 = n_{phot}\left(\left(\frac{\kappa}{2}\right)^2 + \Delta^2\right) \approx n_{phot}\Omega_x^2$ and substituted the phase noise with the frequency noise:

$$S_{\dot\varphi\dot\varphi}(\omega) = \omega^2 S_{\varphi\varphi}(\omega). \tag{2.66}$$

The contribution to the phonon occupation is:

$$\bar{n}^{phase} = \frac{S_{xx}^{phase}(\Omega_x)}{S_{xx}^{rp}(\Omega_x)} = \frac{n_{phot}}{\kappa} S_{\dot\varphi\dot\varphi}(\Omega_x), \tag{2.67}$$

in perfect agreement with [Rabl et al., 2009]. In optomechanical setups with low mechanical frequencies $\Omega_x/2\pi < 1$ MHz, it is therefore typically required to filter the laser phase noise before driving the optical cavity.

Note that in [Safavi-Naeini et al., 2013a], the authors assume the phase noise as part of the noise input $\hat{a}_{\mathrm{IN}}^{c,1}$, which leads to $S_{xx}^{phase}(\omega) \propto |\chi_c(\omega) + \chi_c^*(-\omega)|$. Therefore, a phase noise contribution exists even at $\Delta = 0$, although it is expected to manifest only when the phase noise is able to be converted into intracavity intensity noise.

OPTOMECHANICAL COOPERATIVITY The optomechanical cooperativity $C = 4g^2/(\kappa\Gamma)$ compares the interaction strength between the nanosphere motion and the cavity mode (g^2) to all loss rates in the experiment (κ: optical loss rate, Γ: mechanical loss rate). In typical optomechanical setups only thermal noise and radiation pressure noise need to be considered (see Equation (2.52)). However, for a levitated nanosphere in ultra-high vacuum thermal coupling becomes negligible and other noise terms, particularly due to photon recoil, need to be taken into account.

The optomechanical cooperativity C is defined as a ratio of the radiation pressure noise spectrum and other noise spectra, evaluated at the mechanical frequency Ω_x':

$$C = \frac{S_{xx}^{rp}(\Omega_x')}{S_{xx}^{th}(\Omega_x') + S_{xx}^{rec}(\Omega_x')} = \frac{4g^2}{\kappa\left(\gamma_m n_{th} + \Gamma_{rec}\right)}. \tag{2.68}$$

If we compare Equation (2.68) with the phonon occupation in Equation (2.58) and Equation (2.60), we notice that the phonon occupation is a function of the cooperativity:

$$\bar{n} = \frac{\Gamma_+}{\Gamma_{opt}} + \frac{\gamma_m n_{th} + \Gamma_{rec}}{\Gamma_{opt}} + \bar{n}^{phase} = \left(\frac{\kappa}{4\Omega_x}\right)^2 + C^{-1} + \bar{n}^{phase}. \quad (2.69)$$

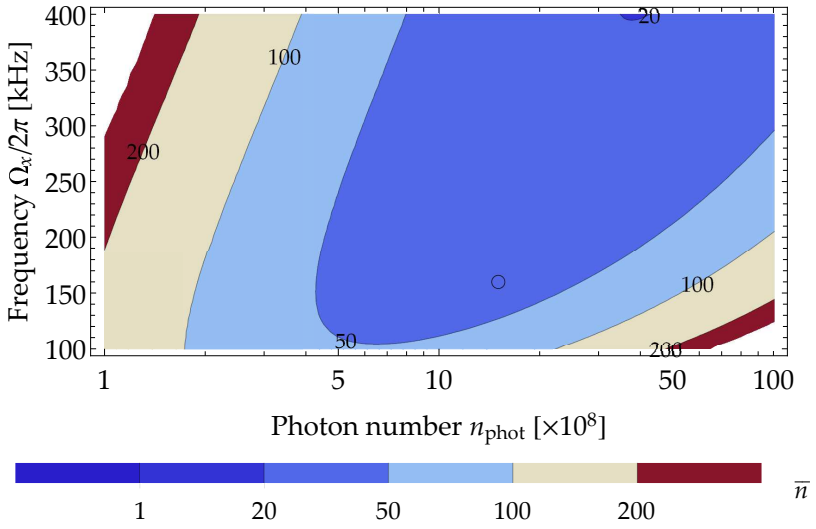

Figure 2.14: **Phonon occupation $\bar{n}$ of the nanosphere x-motion as a function of the intracavity photon number n_{phot} and the mechanical frequency Ω_x.** We assume a pressure of $p = 10^{-6}$ mbar, cavity linewidth $\kappa = 2\pi \times 193$ kHz and a silica nanosphere with a radius $r = 71.5$ nm. We include the sideband resolution, the gas and recoil heating mechanisms and the phase noise heating, where the phase noise has been extrapolated for the laser used in the experiment. The black circle marks the experimental parameters we reach in our setup ($n_{phot} = 1.5 \times 10^9$ photons and $\Omega_x = 2\pi \times 160$ kHz). We are limited by the tweezer and the cavity drive power, i.e. we can reach all points to the left and below of the circle. Ground state cooling is impossible to reach without a strong suppression of the phase noise.

We plot the phonon occupation as a function of the intracavity photon number n_{phot} and the mechanical frequency Ω_x in Figure 2.14. We assume that the tweezer power can be changed arbitrarily and include the respective optical power in the estimate of the tweezer recoil heating. We take a realistic pressure of $p = 10^{-6}$ mbar, cavity linewidth of $\kappa = 2\pi \times 193$ kHz and a nanosphere radius of $r = 71.5$ nm. Without phase noise, increasing the intracavity photon number in the control mode will always lead to a lower phonon occupation. However, the optimal photon number due to the balance between the cavity cooling and phase noise heating is $n_{phot} = \sqrt{\Gamma\kappa^2/(4g_0^2 S_{\dot{\phi}\dot{\phi}}(\Omega_x))}$, for which we obtain a minimal phonon occupation:

$$\bar{n}_x = \left(\frac{\kappa}{4\Omega_x}\right)^2 + 2\sqrt{\frac{\gamma_m n_{th} + \Gamma_{rec}}{4g_0^2} S_{\dot{\phi}\dot{\phi}}(\Omega_x)} \approx 40. \quad (2.70)$$

Filtering laser phase noise at the mechanical frequency $S_{\dot{\phi}\dot{\phi}}(\Omega_x)$ by at least 32 dB allows us to increase the control mode power and achieve ground state cooling of the x-motion in the current setup (Figure 2.15).

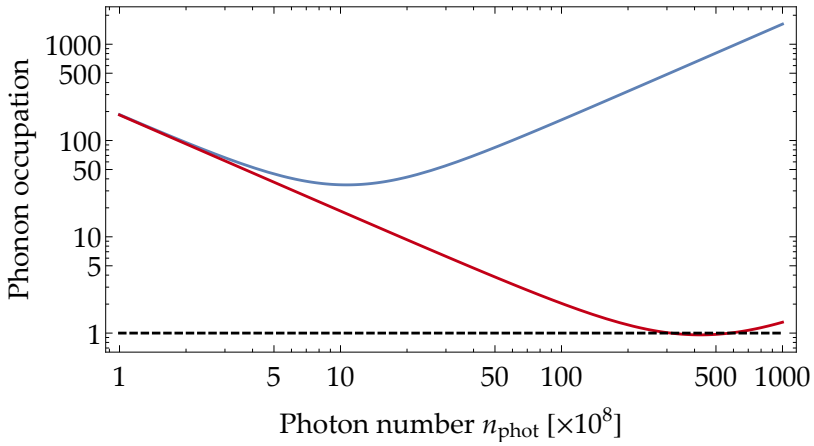

Figure 2.15: **Minimum phonon occupation with (red) and without (blue) filtering of phase noise.** For a harmonic motion with frequency $\Omega_x = 2\pi \times 160$ kHz and current cavity parameters, the optimal intracavity photon number depends on the balance between the cavity cooling and phase noise heating, limiting the minimum phonon occupation far from the ground state (black dashed line). However, by filtering the phase noise by at least 32 dB we are allowed to increase the intracavity power and further decrease the occupation below the ground state.

2.4 LIGHT QUADRATURES; DETECTION

Knowing the spectrum of the nanosphere motion from Equation (2.52), we are able to plug it back into the expression for the light operators $\tilde{a}_i(\omega)$. We subsequently calculate the spectra of the phase quadrature of the cavity mode $\tilde{Y}_i = (\tilde{a}^\dagger - \tilde{a})/i\sqrt{2}$ from Equation (2.51), which contains the nanosphere motion:

$$\begin{aligned} S^l_{YY} &= \frac{g_l^2}{x_{zpf}^2}|\chi_l(\omega) + \chi_l^*(-\omega)|^2 \left(S^{th}_{xx}(\omega) + S^{rp}_{xx}(\omega)\right) + S^{det,l}_{YY}(\omega) \\ S^c_{YY} &= \frac{g_c^2}{x_{zpf}^2}|\chi_c(\omega) + \chi_c^*(-\omega)|^2 \left(S^{th}_{xx}(\omega) + S^{rp}_{xx}(\omega)\right) + S^{det,c}_{YY}(\omega) \end{aligned}$$

where $S^{det}_{YY}(\omega)$ are the spectral contribution of the detection noise:

$$\begin{aligned} S^{det,l}_{YY}(\omega) &= 2\frac{\kappa_{\text{IN}}}{\left(\frac{\kappa}{2}\right)^2 + \omega^2} \\ S^{det,c}_{YY}(\omega) &= \frac{\kappa_{\text{IN}}}{\left(\frac{\kappa}{2}\right)^2 + (\omega + \Delta_c)^2} + \frac{\kappa_{\text{IN}}}{\left(\frac{\kappa}{2}\right)^2 + (\omega - \Delta_c)^2}. \end{aligned}$$

3

THE EXPERIMENTAL SETUP

Since the first demonstration of cavity cooling of a levitated submicron particle in our previous work [Kiesel et al., 2013], we focused on the open question of stable levitation below the typical loss pressure of ~ 1 mbar. Based on the successful levitation with an optical tweezer in high vacuum [Gieseler et al., 2012], we decided on combining a high NA microscope objective with an optical cavity and overhanding the trapping to the tweezer. We present the end design in this chapter.

We start with an overview of the fundamental building blocks: the optical dipole trap (tweezer) and the optomechanical cavity. We proceed with the detection schemes of the nanosphere motion: homodyne detection of the locking cavity mode, detection from the Pound-Drever-Hall (PDH) error signal and detection in the tweezer transmission. We obtain the mass of the trapped nanosphere from the ratio of the linear and quadratic coupling rates to the locking cavity mode. In addition, we extract the optomechanical coupling rate to the control cavity mode from the optomechanically induced transparency (OMIT) signal. We conclude the chapter by analyzing and distinguishing different trapped objects including silica nanospheres and suspension droplets.

Contents

3.1 BUILDING BLOCKS

3.1.1 *Optical dipole trap*

The optical dipole trap for the nanospheres is created by focusing a Gaussian laser beam with a microscope objective[1]. The optical force of the focused laser on the nanosphere is typically split into the gradient force F_{grad}, which creates a strong harmonic potential in all three directions, and the scattering force F_{scatt}, which is a radiation pressure force pushing the nanosphere away from the focus [Ashkin et al., 1986, Jonáš and Zemánek, 2009]. For a nanosphere with polarizability $\alpha = 3\varepsilon_0 V \frac{n_s^2-1}{n_s^2+2}$ trapped by a laser polarized along the x-axis with electric field $E_x(x,y,z) = E_0 \frac{z_R}{z_R+iz} \exp(ikz) \exp(ik(x^2+y^2)/2(z-iz_R))$, the force components along the axial z-axis and a single transverse x-axis are:

$$\begin{aligned} F^x_{grad}(x,y,z) &= \frac{\alpha}{4}\frac{\partial |E_x|^2}{\partial x} = -\frac{2\alpha I_0}{\varepsilon_0 c}\frac{xW_0^2}{W^4(z)} e^{-\frac{2(x^2+y^2)}{W^2(z)}} \\ F^z_{grad}(x,y,z) &= \frac{\alpha}{4}\frac{\partial |E_x|^2}{\partial z} = -\frac{4\alpha I_0}{\varepsilon_0 c}\frac{z}{k^2 W^4(z)} e^{-\frac{2(x^2+y^2)}{W^2(z)}} \\ F^z_{scatt}(x,y,z) &= \frac{\alpha^2 k^3}{12\pi\varepsilon_0}|E_x|^2\frac{\partial \phi}{\partial z} = \frac{\alpha^2 k^4 I_0}{6\pi\varepsilon_0^2 c}\frac{W_0^2}{W^2(z)} e^{-\frac{2(x^2+y^2)}{W^2(z)}}, \end{aligned} \quad (3.1)$$

where $I_0 = \varepsilon_0 c|E_0|^2/2$ is the laser focal intensity, W_0 is the beam waist at the focus, $z_R = W_0^2\pi/\lambda$ is the Rayleigh length and $W(z) = W_0\sqrt{1+(z/z_R)^2}$ is the Gaussian beam waist at a distance z.

The scattering force displaces the trap potential minimum along the optical axis by $z_0 \approx \alpha k^6 W_0^4/(24\pi\varepsilon_0)$ away from the focus (for $z \ll z_R$), where the displacement is independent of the laser intensity. As the forces have a different dependency on the nanosphere volume ($F_{grad} \propto V$, $F_{scatt} \propto V^2$), the scattering force will be always greater than the axial gradient force for nanospheres with radius larger than $r_{max} = \sqrt[3]{3/\left(2k^5 W_0^2 \frac{n_s^2-1}{n_s^2+2}\right)}$. The calculation so far includes the point-like dipole interaction only, while for nanospheres larger than r_{max} the Mie calculus has to be used [Jonáš and Zemánek, 2009].

As the scattering force along the z-axis is constant, the axial trapping frequency is unaffected. The transverse mechanical frequencies decrease, mostly due to lower laser intensity at the shifted trapping position. For a small waist ($W_0 \sim \lambda$) the trap is elliptical in the transverse direction due to weak focusing along the polarization axis (Appendix C), leading to non-degenerate transverse frequencies. Typical mechanical frequencies in our three-dimensional trap potential are $\Omega_x/2\pi = 160$ kHz, $\Omega_y/2\pi = 184$ kHz and $\Omega_z/2\pi = 40$ kHz.

[1] Olympus LMPL 100x IR, working distance WD = 3.4 mm, NA = 0.8, focal distance $f = 1.8$ mm

From the ratio of the transverse frequencies Ω_x and Ω_y to the axial frequency Ω_z we estimate our effective numerical aperture to be $\mathrm{NA} = \Omega_z\sqrt{2}/\Omega_y \approx 0.32$. However, a more invested calculation in Appendix C involves the difference of the transverse frequencies Ω_y and Ω_x and shows that the numerical aperture is closer to $\mathrm{NA} \approx 0.56$. The calculated waists of the elliptical dipole trap are $W_x \approx 0.77\ \mu$m and $W_y \approx 0.67\ \mu$m.

The displacement from the laser focus $z_0 \approx 0.17\ \mu$m is much smaller than the Rayleigh length. The maximal nanosphere radius for stable trapping conditions in the Rayleigh approximation is $r_{max} \approx 114$ nm. We typically use nanospheres with a radius of $r = 71.5$ nm, which can still be considered a dipole particle. However, we successfully trapped nanospheres with a radius of $r = 127$ nm, for which the Rayleigh approximation breaks down (in this case $r \gtrsim \lambda/10$). Therefore, the limit on the nanosphere size r_{max} from the dipole approximation does not hold [Ashkin et al., 1986]. The mechanical frequencies for these nanospheres are smaller by about 30%, which we explain partially by a significant displacement from the laser focus.

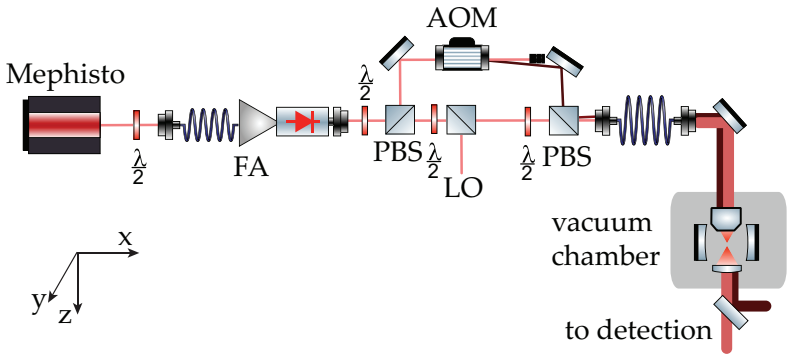

Figure 3.1: **Optical setup for trapping a nanosphere and feedback cooling of its center-of-mass motion.** A weak laser beam from a Mephisto laser is amplified with a fiber amplifier (FA) and split on a polarizing beamsplitter (PBS) with a 90 : 10 splitting ratio. A small part of the stronger, trapping laser is sampled to be used as a local oscillator (LO) for the detection. The weaker component (feedback laser) passes an acousto-optical modulator (AOM), which is used to apply a feedback to cool the nanosphere motion. The two components are subsequently overlapped in the single mode fiber, expanded and focused by the microscope objective. A collimation lens collects the trapping and feedback laser in the trap transmission. The feedback laser is subsequently filtered on a polarization beamsplitter and the trapping laser is used in detection.

The optical setup to create a stable trap for nanospheres is shown in Figure 3.13. A Mephisto laser[2] is amplified with a fiber amplifier[3] and split on a polarizing beamsplitter (PBS) with a ratio of 90 : 10 into

[2] Mephisto, wavelength 1064 nm, output power 2 W
[3] Nufern, 1064 nm, 5 W

the trapping and feedback laser, respectively. A small part of the trapping laser bypasses the vacuum chamber and is used as a local oscillator (LO) for detection of the nanosphere motion. The feedback laser passes through an acousto-optical modulator (AOM, RF frequency 80 MHz), which is used for parametric feedback cooling by modulating the total trap intensity. We use the first order of the AOM shifted by 80 MHz from the trapping laser, which allows for a separation in frequency space. The two lasers are recombined on another polarizing beamsplitter and subsequently coupled into a single mode fiber to overlap the modes. The laser is magnified at the fiber output and focused by the microscope objective to form an optical trap. The two beams are separated in the trap transmission on a Glan-Thompson polarizer. The trapping laser is used for detection of the nanosphere motion (see Section 3.2 for more details on the detection).

Parametric feedback cooling

Cooling of the three-dimensional motion of the nanosphere is needed to stabilize the nanosphere at low pressures. The trap created by the microscope objective is deep enough to keep the nanosphere even at 10^{-5} mbar, albeit the nanosphere's energy increases significantly at such low pressures. To prevent a loss of the nanosphere, we typically start cooling the nanosphere motion at pressures reached after prepumping ($p = 4 \times 10^{-2}$ mbar).

We employ parametric feedback cooling as a method to cool the nanosphere motion in all directions [Gieseler et al., 2012, Mestres et al., 2015, Jain et al., 2016]. It is implemented with a phase-locked loop (PLL, Zurich Instruments HF2LI) which creates a feedback signal that is applied to the nanosphere. The PLL detects the mechanical frequency by locking an internal oscillator to the nanosphere motion. The oscillator is then doubled in frequency, shifted in phase and applied to an AOM as an intensity modulation to the trapping laser. The feedback modulates the trap potential such that it stiffens anytime the nanosphere moves away from the equilibrium trap position. For more details see the PhD thesis by David Grass [Grass, 2018].

3.1.2 *Optomechanical cavity*

The central part of our experiment is a near-confocal cavity constructed of two identical cavity mirrors with a high reflection coating (Layertec) with a transmission per mirror of 20 ppm ($T_1 = T_2 = 20 \times 10^{-6}$) and estimated losses per mirror $L_1 = L_2 = 30 \times 10^{-6}$. The mirrors have radius of curvature (RoC) $RoC_1 = RoC_2 = 10$ mm and a separation of $L = \frac{c}{2\Delta\nu_{FSR}} \approx 10.7$ mm, which we obtain from the measurement of the cavity free spectral range $\Delta\nu_{FSR}$. The cavity length L allows us to calculate the cavity waist of the TEM_{00} mode $w_0 \approx 41.1\ \mu$m from Equation (A.6).

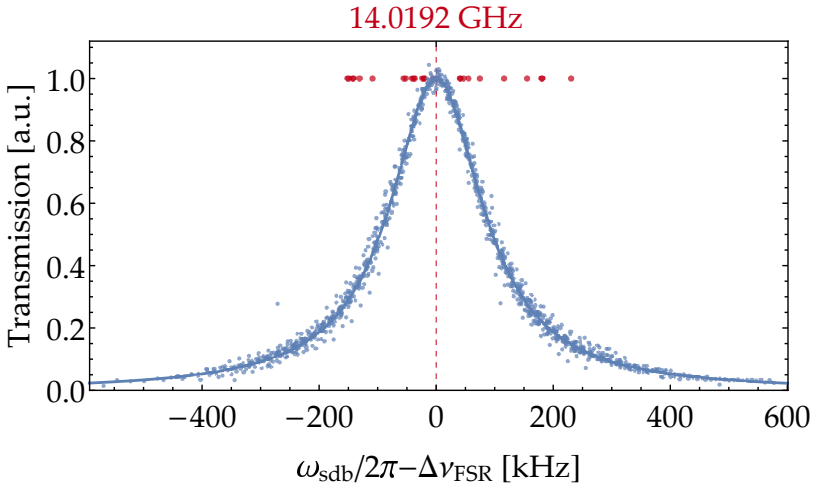

Figure 3.2: **Measurement of the cavity energy decay rate κ.** We took 26 scans of the same cavity resonance over the course of a month at pressures around 1 mbar (blue points). As the cavity length drifts over time, the individual scans are shifted in frequency to overlap them. The joint fit over all data points gives an average cavity decay rate $\kappa = 2\pi \times (193 \pm 1)$ kHz, while the average value of the free spectral range is $\Delta\nu_{FSR} \approx 14.0192$ GHz. Individual measurements of $\Delta\nu_{FSR}$ (red points) demonstrate an average cavity length stability better than $\lambda/2$.

We stabilize the laser to cavity resonance at ω_c (explained in detail in Section 3.1.3) and create a sideband[3] with an electro-optical modulator (EOM) at frequency $\omega_c + \omega_{\mathrm{sdb}}$. We use the sideband to scan over an adjacent cavity resonance $\omega_c + 2\pi \times \Delta\nu_{FSR}$ and measure an average free spectral range $\Delta\nu_{FSR} \approx 14.0192$ GHz and cavity full-width-at-half-maximum (FWHM) linewidth $\kappa = 2\pi \times (193 \pm 1)$ kHz (Figure 3.2). From the spread of measured values of $\Delta\nu_{FSR}$ we conclude that the cavity length changes less than ± 0.2 μm from the average value, demonstrating a length stability over the course of a month of better than $\lambda/2$.

[3] *In fact, we create both upper and lower sideband at $\omega_c \pm \omega_{sdb}$, while the carrier is suppressed but not eradicated. See Section 3.1.5.*

Naturally, $\Delta\nu_{FSR}$ changes as the pressure is decreased from 1 mbar to high vacuum, which is explained by the relative change of the refractive index of air. As it approaches a vacuum value of $n_{air} = 1$ the effective cavity length decreases, thus increasing the free spectral range $\Delta\nu_{FSR} = \frac{c}{2n_{air}L}$. We first lock the cavity at high pressure, where the refractive index of air is $n_{air}(1\ \mathrm{mbar}) \approx 1 + 2 \times 10^{-6}$ [Owens, 1967]. Once in vacuum, the free spectral range will differ by ~ 28 kHz, which agrees with an observed shift of around $20 - 30$ kHz. Based on this, we estimate that the resonance frequency experiences a substantial shift by more than 500 MHz, which can lead to a mode hop of the laser and a subsequent loss of the cavity lock during the pumping process. Therefore, we lock the cavity only when the pressure in the vacuum chamber is around 10^{-5} mbar, from where the cavity lock is stable.

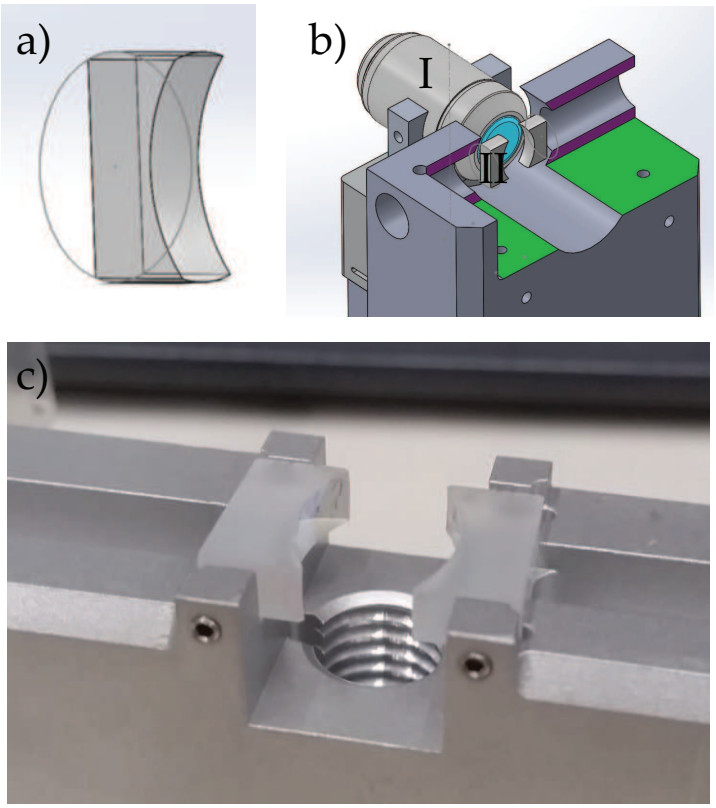

Figure 3.3: (a) End mirror is obtained after a cutting process where a 4 mm wide strip is created from its original circular profile with 12.7 mm diameter. (b) Microscope objective (I) and cavity (II) mounted together. The cavity holder is not shown for clarity. The microscope objective is mounted on a triaxial nanopositioner, which is used to position the nanosphere in the cavity mode. (c) Aluminum cavity holder with mirrors glued in. The screws seen in foreground are used to hold the mirrors at a fixed position while the glue is being cured and are removed subsequently. The hole (in this picture below the mirrors) is designed to approach the cavity with a collimation lens to collect the trapping light for detection.

The large numerical aperture and short working distance (WD) require sufficiently narrow cavity mirrors, which is not the case with the standard off-the-shelf mirror substrates with the radius $d/2 = 6.35$ mm $>$ WD. We therefore cut the substrates into 4 mm wide strips (Figure 3.3 (a)), which is done in collaboration with the group of Martin Weitz (particularly Tobias Damm) at the University of Bonn. A layer of First Contact[4] polymer, typically used for protecting and cleaning of optics, is coated on the inner mirror surface with the high finesse coating before cutting. Rhe cavity finesse remains unaffected after cutting the mirrors.

Frequently, the cavity mirrors are isolated from external acoustic vibrations by designing a minimal number of contact points with the cavity holder. Now, with a rectangular cross-section, the mirrors are

[4]Manufactured by Photonic Cleaning Technologies

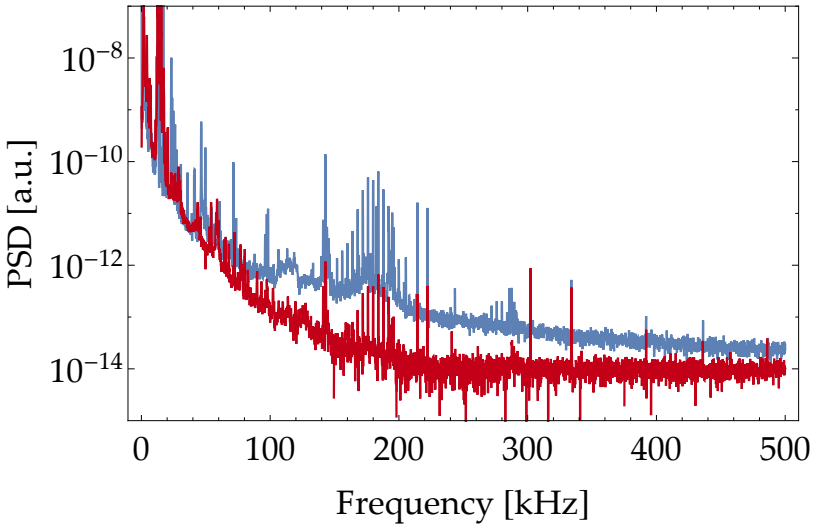

Figure 3.4: **Power spectral density of the locking error signal.** We see a distinctive drop in the power spectral density above 100 kHz before (blue) and after gluing (red) the cavity mirrors to the cavity holder. The flat noise response above 200 kHz in the red spectrum is due to electronic noise. We are subsequently able to reduce the lock bandwidth and optimize the lock parameters, further improving the response to external vibrations.

in contact with the aluminum holder on all sides (Figure 3.3 (c)) and susceptible to vibrations over a broad frequency range. The coupling of external vibrations to the cavity is reduced by gluing the cavity mirrors with a thin layer of soft UV glue[5]. This immediately dampens all the vibrations above 100 kHz (Figure 3.4). Together with further optimization of the lock parameters, the locked cavity is insensitive to noises such as closing the lab door or touching the optical table. Finally, we note that the vibration isolation is improved by mounting the cavity holder on top of a massive aluminum block (green surface on Figure 3.3 (b)), which is isolated from the chamber bottom by a 3 mm thick layer of viton. The vacuum chamber itself is set on a 3 mm thick layer of viton.

Loading of a nanosphere in the trap is a dirty process which can ruin the cavity finesse (see Section 3.5 for more details on trapping). Therefore, the cavity holder is designed to be small and easy to remove from the vacuum chamber until we trap a nanosphere in the tweezer. We then mount the holder by sliding it on top of a massive aluminum block. A possible clean alternative could be to deliver a single nanosphere into the trap with a hollowcore fiber [Grass et al., 2016].

[5] Norland Optic NOA65

3.1.3 *Cavity locking schemes*

The cavity resonance drifts over time and on different time scales. For example, significant length changes due to thermal expansion of cavity holders happen on slow time scales, from 0 to 100 Hz, while acoustic disturbances still have a large impact at frequencies well above 10 kHz. In order to stabilize the laser to the cavity, we employ diverse locking techniques such as side-of-fringe (used for the filter cavity) and Pound-Drever-Hall (PDH, used for the optomechanical cavity) [Drever et al., 1983]. In the following text we focus on the advantages and disadvantages of each technique.

Side-of-fringe locking

Let us assume perfect mode matching between a laser with frequency ω_l driving a cavity mode with resonance $\omega_{cav} = \omega_l + \Delta$, where the cavity has a FWHM linewidth of κ. Depending on the detuning Δ, the transmitted laser power is attenuated by the cavity transfer function $T(\Delta) = \frac{(\kappa/2)^2}{(\kappa/2)^2+\Delta^2}$. Therefore, we can detect relative frequency fluctuations between the cavity resonance and the laser by measuring the transmitted power (Figure 3.5). However, this method confines locking to frequencies away from the resonance, where the first derivative of the cavity transfer function is a linear function of the detuning:

$$\frac{dT(\Delta)}{d\Delta} = -\frac{2\left(\frac{\kappa}{2}\right)^2\Delta}{\left(\left(\frac{\kappa}{2}\right)^2+\Delta^2\right)^2}. \tag{3.2}$$

As the method locks the laser away from the cavity resonance, this locking scheme is called side-of-fringe.

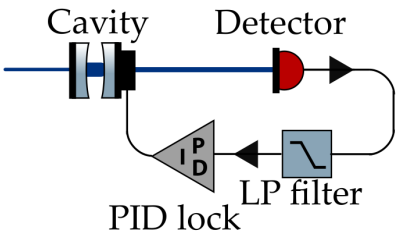

Figure 3.5: **Side-of-fringe locking setup.** The optical power transmitted through the cavity is detected with a photodiode. At the cavity resonance, change in relative frequency $\omega_l - \omega_{cav}$ will always result in a decrease of the transmitted power, hence we can only extract the information about the absolute frequency difference. However, the transmitted power is a monotonous function of the relative frequency fluctuations at a non-zero detuning. The PID lock uses the transmitted power as the error signal and modifies either the laser frequency or the cavity resonance, e.g. by changing the cavity length with a piezo element.

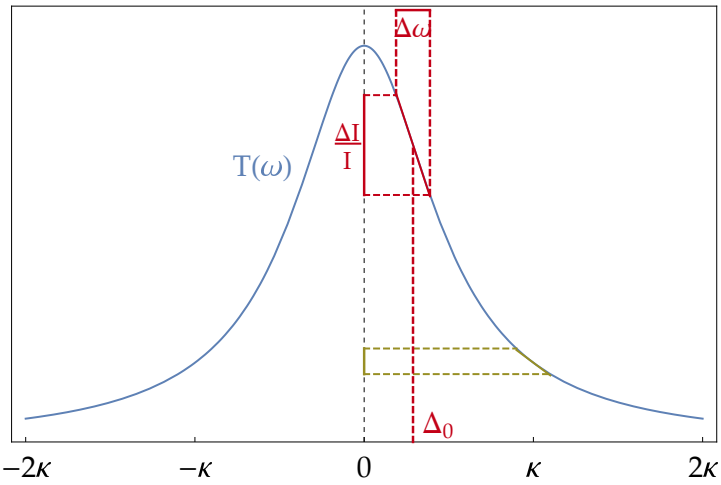

Figure 3.6: **Side-of-fringe locking in frequency space.** Side-of-fringe locking will turn frequency fluctuations $\Delta\omega$ into relative intensity fluctuations $\frac{\Delta I}{I}$. Shown in red, the detuning of Δ_0 gives us the highest sensitivity to these fluctuations, as well as the best error signal for locking. Equal frequency variation at the detuning of κ results in a smaller change of relative intensity, shown here in green.

Side-of-fringe locking should be avoided when the following two things are important:

1. **Desired set point changes regularly.** The error signal $dT(\Delta_0)/d\Delta$ strongly depends on the set point Δ_0. Therefore, any change of the set point will have to be followed by an optimization of the lock parameters.

2. **Cavity decay rate κ is small.** Fluctuations of the laser frequency $\Delta\omega_l(t)$ around the set point Δ_0[4] will be converted into fluctuations of the relative intracavity intensity (Figure 3.6):

[4] *Maximum effect will be around* $\Delta_0 = \frac{\kappa}{2\sqrt{3}}$

$$\epsilon(t) = \frac{\Delta I(t)}{\bar{I}} = -T'(\Delta_0)\Delta\omega_l(t). \tag{3.3}$$

Assuming a nanosphere is trapped by the cavity standing wave, we can estimate the heating rate imposed on the nanosphere motion by this noise [Gehm et al., 1998]:

$$\gamma_\omega = \left(\frac{\omega_0}{2}\right)^2 \left(T'(\Delta_0)\right)^2 S_{\dot\phi\dot\phi}\left(2\frac{\Omega_0}{2\pi}\right), \tag{3.4}$$

where $S_{\dot\phi\dot\phi}\left(2\frac{\Omega_0}{2\pi}\right)$ is the laser frequency noise at twice the mechanical frequency (*parametric heating*). The evolution of the motional energy is exponential, i.e. $\dot{E} = \gamma_\omega E$. Therefore, the heating rate γ_ω is better understood as *negative damping*. For a cavity linewidth $\kappa/2\pi = 193$ kHz, a mechanical frequency $\Omega_0/2\pi = 160$ kHz and laser frequency noise[6] $S_{\dot\phi\dot\phi}\left(2\Omega_0/2\pi\right) \approx$

[6] Mephisto Laser Specification Sheet

10^{-2} Hz^2/Hz, we expect a heating rate $\gamma_\omega \sim 0.04$ Hz, equal to the gas damping at pressures below $p \sim 10^{-5}$ mbar. Without an additional feedback cooling mechanism, the energy of the nanosphere motion would increase until the nanosphere is lost. For a nanosphere placed at the largest intensity gradient[5], laser frequency fluctuations will lead to a heating mechanism as described in Section 2.3.1.

[5] *There is no parametric heating at this position as the intensity is a linear function of the nanosphere position.*

The side-of-fringe lock can still be used on a cavity with large linewidth κ, such as the cavity mentioned in Section 3.1.5. For such a cavity with $\kappa_{FC}/2\pi = 80$ MHz, any additional intensity noise created by the frequency fluctuations will be negligible.

Pound-Drever-Hall locking

Instead of the side-of-fringe locking, we use the more elaborate Pound-Drever-Hall (PDH) locking scheme for the optomechanical cavity (Figure 3.7) [Drever et al., 1983, Black, 2001]. The principle behind this scheme is: The principal laser (carrier) at frequency ω_l and two weak sidebands at $\pm\omega_s \gg \kappa$ are driving the cavity mode at frequency ω_{cav}, to which we wish to stabilize the laser. As the sidebands are far detuned from the resonance (in our case: $\omega_s = 2\pi \times 20$ MHz, $\kappa = 2\pi \times 193$ kHz), they are rejected by the cavity with a $\pm\pi/2$ phase shift. On the other hand, the reflected part of the principal laser picks up a phase φ_d proportional to the frequency difference $\Delta = \omega_l - \omega_{cav}$. Mixing the carrier with the completely reflected sidebands results in a beatnote at ω_s, which we detect with a photodiode. A change of the cavity resonance is thus detected as a fluctuation of the relative phase between the carrier and its sidebands $\pi/2 - \varphi_d$. This produces an error signal around the cavity resonance. In essence, the PDH lock is a detection of the cavity phase quadrature, i.e. it can be used to read out the nanosphere motion.

We assume that we have a symmetric Fabry-Perot cavity, i.e. a cavity with equal mirror reflectivities $r_1^2 = r_2^2 = R$ and transmittivities $t_1^2 = t_2^2 = T$ with $R + T \neq 1$ in the most general case of non-zero losses. The laser outputs light at a frequency ω_l with a narrow linewidth, commonly described as a monochromatic source $E_d = E_0 e^{i\omega_l t}$. The electric field reflected from the cavity is $E_{\text{ref}} = E_d F(\Delta) e^{i\omega_l t}$, where function $F(\Delta)$ is the cavity response in reflection:

$$F(\Delta) = \frac{\sqrt{R} \cdot \left(e^{i\frac{\Delta}{\Delta\nu_{FSR}}} - 1 \right)}{1 - R e^{i\frac{\Delta}{\Delta\nu_{FSR}}}}. \tag{3.5}$$

Sidebands are created from a phase modulation on the carrier done by an electric-optic modulator (EOM):

$$\begin{aligned} E_d &= E_0 e^{i(\omega_l t + \beta \sin \omega_s t)} \\ &\approx E_0 \left[J_0(\beta) e^{i\omega_l t} + J_1(\beta) e^{i(\omega_l + \omega_s)t} - J_1(\beta) e^{i(\omega_l - \omega_s)t} \right], \end{aligned} \tag{3.6}$$

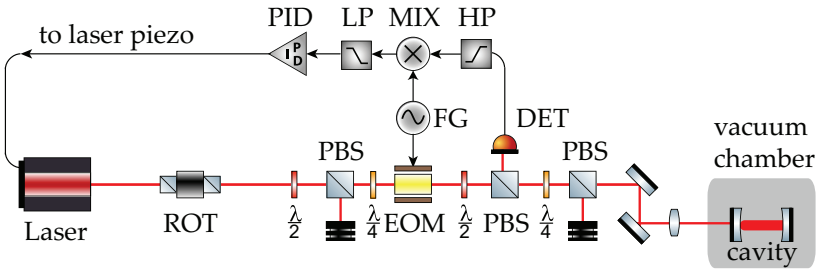

Figure 3.7: **Setup for Pound-Drever-Hall locking technique.** A dual output function generator (FG, Keysight 33522A) generates two synchronized 20 MHz drive tones, with one tone used to create sidebands on the laser carrier by driving a resonant electro-optical modulator (EOM, New Focus 4001). The carrier and sidebands pass through a quarter waveplate nested in between two polarization beamsplitters (PBS), such that half of the optical power is lost in both directions. This allows for some of the light reflected by the cavity to end up on the detector photodiode (DET). The signal is filtered with a high-pass filter (HP) with a cut-off frequency around 200 kHz and mixed with the other FG drive tone in order to create an error signal. The FG allows for a relative phase φ_s between the drive tones, which is necessary to optimize the error signal (see the main text for details). The laser frequency is locked to the cavity resonance with a PID lock (Toptica PID 110) actuating on the laser piezo.

where β is the modulation depth, ω_s is the sideband frequency and J_0, J_1 are the Bessel functions. The total power reflected off the cavity and detected on the PDH detector is:

$$\begin{aligned} P_{\text{ref}} &= P_c \left|F(\Delta)\right|^2 + P_s \left(\left|F(\Delta+\omega_s)\right|^2 + \left|F(\Delta-\omega_s)\right|^2\right) \\ &+ 2\sqrt{P_c P_s}\,\text{Re}\left[F(\Delta)F^*(\Delta+\omega_s) - F^*(\Delta)F(\Delta-\omega_s)\right]\cos\omega_s t \\ &- 2\sqrt{P_c P_s}\,\text{Im}\left[F(\Delta)F^*(\Delta+\omega_s) - F^*(\Delta)F(\Delta-\omega_s)\right]\sin\omega_s t, \end{aligned} \tag{3.7}$$

where $P_c = |E_0|^2 J_0^2(\beta)$ and $P_s = |E_0|^2 J_1^2(\beta)$. The real and imaginary part of the modulated signal $\chi(\Delta,\omega_s) = F(\Delta)F^*(\Delta+\omega_s) - F^*(\Delta)F(\Delta-\omega_s)$ represent the in- and out-of-phase components of the error signal, respectively. Oscillations at the second harmonic $2\omega_s$ and higher frequencies were neglected as the modulation depth is assumed small.

The first line of Equation (3.7) is the optical power of the reflected carrier and its sidebands, which is minimal when the laser frequency is resonant to the cavity. If we drive the cavity weakly and scan the laser frequency over the resonance slowly, we can use this signal to determine the cavity linewidth. The second and the third line contain the mixed signal at the PDH frequency, which is used to lock the

laser to the cavity. We demodulate this signal with a local oscillator $\propto \cos(\omega_s t + \theta)$, which gives us a cavity response at low frequencies:

$$\frac{\mathrm{Err}(\Delta)}{\sqrt{P_c P_s}} = -\mathrm{Re}\left[\chi(\Delta, \omega_s)\right] \cos\varphi_s - \mathrm{Im}\left[\chi(\Delta, \omega_s)\right] \sin\varphi_s,$$

while we filter out the contribution at the higher frequency $2\omega_s$.

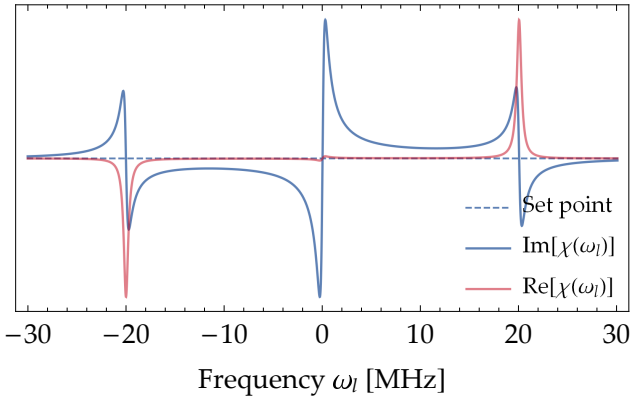

Figure 3.8: **In-phase (red) and out-of-phase (blue) components of the error signal.** The error signal depends on the relative phase φ_s between the detected beatnote at ω_s and the demodulation signal from the function generator, also at ω_s. The in-phase (out-of-phase) response is obtained for $\varphi_s = 0$ ($\pi/2$). The out-of-phase response shows a stronger dependence on the laser frequency ω_l, which is why the optimal phase for creating the error signal is $\varphi_s = \pi/2$.

An obvious choice for an error signal would be the imaginary part of $\chi(\Delta, \omega_s)$ as it crosses 0 at $\Delta = 0$ (Figure 3.8). We will observe it for $\varphi_s = \frac{\pi}{2}$. This error signal is what can be used to lock the laser frequency ω_l to the cavity resonant frequency ω_{cav}, which is an integer multiple of $\Delta\nu_{FSR}$. By choosing the lock set point, we can choose the detuning between drive and cavity frequency. We lock at $\omega_l = \omega_{cav}$, where $\mathrm{Err}(\Delta) = 0$ and Err is linear in the frequency difference Δ:

$$\mathrm{Err}(\Delta) = -4\sqrt{P_c P_s}\frac{\Delta}{\Delta\nu_{FSR}(1-r^2)}. \quad \Delta \ll \kappa \tag{3.8}$$

3.1.4 *Initial alignment of the tweezer trap to the cavity mode*

After a nanosphere is trapped in the tweezer and the laser is locked to the optomechanical cavity, we place the nanosphere in the cavity mode. The microscope objective is set on a three-dimensional nanopositioner[7], which is used to move the nanosphere. In the following we present two distinct methods which were used to reach a successful alignment.

[7] Mechonics MX35

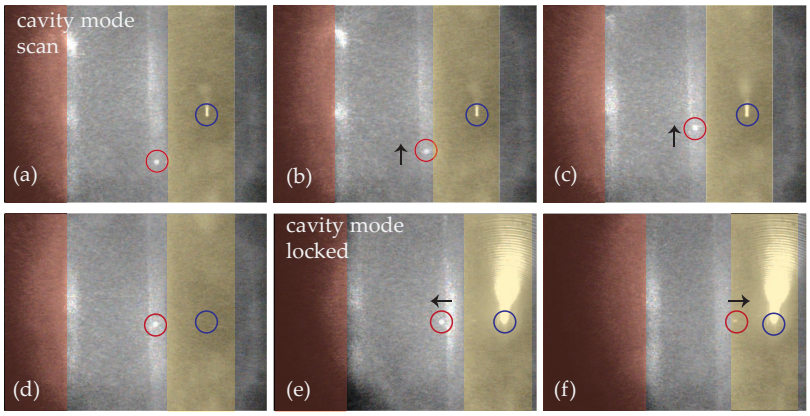

Figure 3.9: **Rough alignment of the trapped nanosphere (circled in red) to the cavity mode (circled in blue) using a camera in the cavity transmission.** The camera is placed behind the cavity mirror, with the field of view including both the microscope objective (marked in red) and the cavity mirror (marked in yellow). The arrows show the direction in which the nanosphere was moved compared to a previous image. (a) The laser frequency is scanned around the cavity resonance in order to see the cavity mode in transmission. The nanosphere is seen at the edge of the cavity mirror, scattering light in the camera direction. (b) We move the nanosphere up by moving the microscope objective with a nanopositioner. (c) We stop moving at level with the cavity mode. (d) Laser frequency is not close to the cavity resonance anymore, so the light is lost in the transmission. (e) We lock the laser to the cavity resonance, hence the cavity transmission blinds the camera. However, scattered light off the trapping laser is still clearly observed. (f) We move the nanosphere toward the cavity mode. As soon as it is behind cavity mirror, the scattered light is dimmer. However, the nanosphere is still seen and can now be moved into the cavity mode. As soon as the nanosphere disappears behind the bright cavity mode, the final alignment is done by optimizing the detection of the nanosphere motion the homodyne detection of the locking mode. The final alignment is reached

We set the trapping laser polarization orthogonal to the cavity axis, thus maximizing the light scattering in the direction of the cavity mirrors. Furthermore, the trapping laser frequency is always kept far detuned with respect to the cavity resonance in order to avoid coupling of the scattered light to the cavity mode. We set up a camera in the cavity transmission, which helps us to see a large area between the microscope objective and the cavity mirror, as well as the whole cavity mirror. The nanosphere is initially in the space between the objective and the mirror (Figure 3.9(a)), seen as a bright spot on the camera (red circle in Figure 3.9 points to the nanosphere position). We scan the laser frequency over the cavity resonance in order to provide a guideline on where the nanosphere should be placed (blue circle in Figure 3.9 points to the transmitted light of the driven cavity mode). We subsequently lock the laser to the cavity (Figure 3.9(e)) and move the particle into the area between the cavity mirrors until it disappears on the camera in the cavity light. From this point on

we resort to the homodyne detection in the cavity transmission to optimize the coupling of the nanosphere motion to the cavity mode, which we describe in detail in Section 3.3.2.

The previous method has a limited precision as the transmitted cavity light blinds the camera once the laser is locked (Figure 3.9(e)). An alternative method improves the precision with which we are able to place the nanosphere into the cavity mode. Instead of driving the cavity mode with an external laser, we now scan the frequency of the trapping laser close to a cavity resonance. Although a thorough explanation involves the theory from Chapter 5, we briefly comment on the method here: We place the nanosphere somewhere in between the cavity mirrors and start scanning the trapping laser frequency. Light scattered in the direction of the cavity mirrors bounces off the mirrors many times due to their high reflectivity. If a resonance condition is met, i.e. the trapping laser frequency is resonant to an arbitrary transverse cavity mode, a constructive interference of the scattered light in the cavity leads to an observable mode shape on the camera in the cavity transmission. The closer we are to the cavity center, the more the mode size converges toward the fundamental TEM_{00} mode, providing us with a way to align the nanosphere to the cavity axis within a couple of cavity waists. In practice, once we stop distinguishing mode features due to the image resolution, we lock the laser to the cavity. We are able to immediately observe the nanosphere motion in the homodyne detection. We have used both alignment methods intermittently.

3.1.5 *Generation of the control cavity mode*

The laser frequency is locked to a cavity resonance at frequency ω_{cav} via the PDH method. In order to achieve cavity cooling of the nanosphere motion, a laser (control laser) has to drive the cavity detuned with respect to the cavity resonance. We choose a detuning with respect to either of the adjacent longitudinal cavity resonances at frequencies $\omega_{cav} \pm 2\pi \times \Delta\nu_{FSR}$ in order to separate it from the locking mode. The control laser is created by shifting the laser frequency with an electro-optical modulator (EOM) since its broad frequency range allows large frequency shift by $\Delta\nu_{FSR}$. An alternative would be to directly lock a detuned laser directly to the cavity resonance [Yam et al., 2015], which would simplify the setup to a single cavity mode.

A part of the laser that is already locked to a cavity resonance at ω_{cav} passes through an EOM, which generates sidebands at $\omega_{cav} \pm 2\pi \times \Delta\nu_{FSR}$. We find approximately 38% of optical power in each of those sidebands, with the remaining optical power being distributed between the carrier (around 20%) and the higher-order sidebands at $\omega_c \pm 2\pi \times k \times \Delta\nu_{FSR}$, $k \geq 2$. We construct a filtering cavity (sFC) with a designed cavity FWHM linewidth $\kappa_{FC} = 2\pi \times 80$ MHz, intended

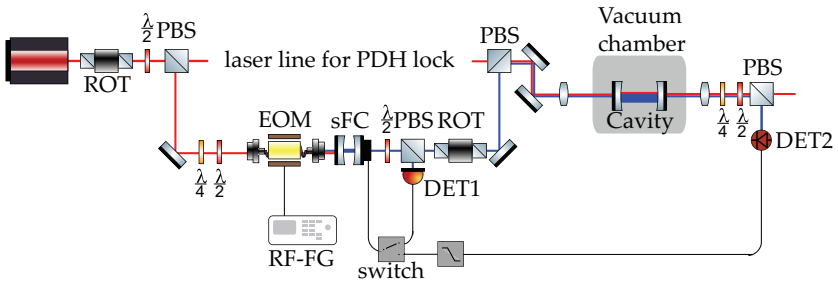

Figure 3.10: **Setup to create the control cavity mode.** We assume the principal laser at ω_l is already locked to a cavity resonance and a part of the light is split off into a fiber EOM. We apply a phase modulation at a free spectral range frequency $\Delta\nu_{FSR} \sim 14$ GHz, which to first order creates sidebands at $\pm\Delta\nu_{FSR}$. We lock a filtering cavity (sFC) with a side-of-fringe lock to transmit only one of the created sidebands. The error signal is either taken directly in the transmission (detected by DET1) or in the transmission of the optomechanical cavity (monitored by DET2), with the latter effectively stabilizing the intracavity power of the control mode.

to transmit only one of the first-order sidebands, while reducing the carrier power in transmission by a factor of $\sim 10^5$. The cavity mirrors (diameter $d = 12.7$ mm, radius of curvature RoC $= 25$ mm and cavity length $L_{FC} \sim 8$ mm) are mounted in two separate lens tubes[8], which are then glued to a cylindrical piezo placed in between. This way of mounting cavity mirrors allows for an easy exchange or cleaning of the mirrors, although they are already enclosed in such a way that no new dust can fall in between. We focus the laser with a 200 mm lens to mode match it to the cavity TEM_{00} mode. We confirm that the cavity linewidth is as expected and measure a transmission of roughly 80% at the filtering cavity resonance. Due to a small imperfection in the laser alignment, we still drive higher-order spatial modes $\mathrm{TEM}_{10}/\mathrm{TEM}_{01}$, which are suppressed well below 1% of the power in TEM_{00} mode.

We use two different detectors intermittently to lock the filtering cavity to the laser with a side-of-fringe lock. Less than 1% of the transmitted power is picked off immediately after the filtering cavity, which stabilizes the optical power of the control laser before the optomechanical cavity (cavity drive E_d). This lock is used before we set the desired detuning. The second detector is in the transmission of the optomechanical cavity, which stabilizes the intracavity power of the control laser independent of the chosen detuning (intracavity photon number $n_{phot} = \frac{E_d^2}{|\kappa/2+i\Delta|^2}$).

[8] Thorlabs SM05M05

3.1.6 *Vacuum system*

We use a scroll pump (Edwards nXDS6i) and a turbomolecular pump (Edwards nEXT300D) to reach high vacuum ($\sim 10^{-6}$ mbar) in the vacuum chamber. Using only the scroll pump with the gate valve to the turbomolecular pump (Gate valve 2) closed (Figure 3.11) we are able to reach a prepump pressure of 4×10^{-2} mbar. In the next stage we close the gate valve to the scroll pump (Gate valve 1) and open Gate valve 2 to start pumping with a turbomolecular pump. Although we suppress the turbo pump vibrations with a CF63 bellow, the cavity lock is disturbed while the pump is speeding up, probably due to hitting a particular mechanical resonance of the experimental setup. In order to stay clear of such resonances, we keep the turbo pump continuously running once the cavity is locked.

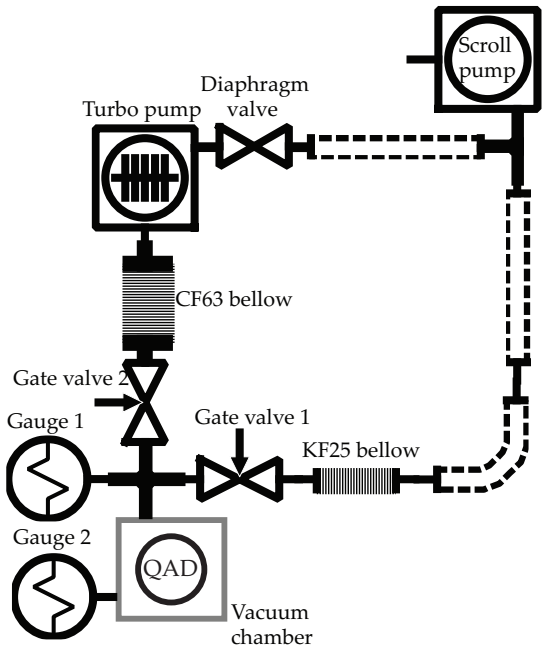

Figure 3.11: **Vacuum system.** We use a scroll pump and turbomolecular pump to pump down to the base pressure of the chamber at $\sim 10^{-6}$ mbar. The vacuum chamber has a cross CF63 piece connecting it to a pressure gauge (Gauge 1), directly to the scroll pump through Gate valve 1 and the turbo pump through Gate valve 2. We use a CF63 bellow to isolate the chamber from the vibrations of the turbo pump. A second pressure gauge is mounted directly onto the vacuum chamber (Gauge 2). Vacuum chamber features a Quick Access Door (QAD) which we use to retrieve and return the cavity.

A commonly used pressure gauge[9] is a two-part gauge with Pirani (operates above 10^{-4} mbar) and cold cathode gauges (operates below 10^{-2} mbar) with an overlapping operating region. We expect around 30% imprecision in measuring the pressure in either operational re-

[9] Pfeiffer Vacuum MPT 200

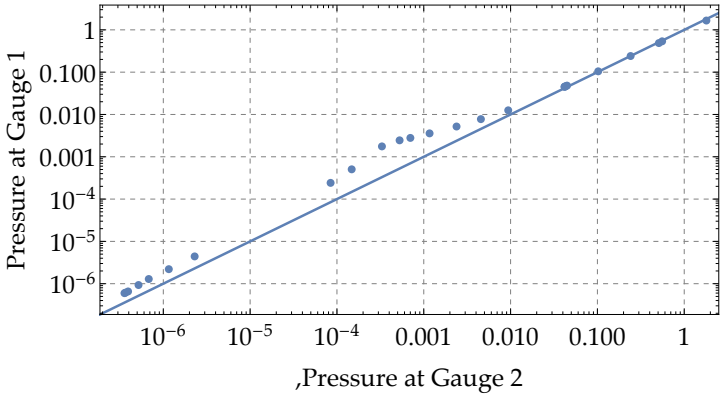

Figure 3.12: **Pressure measurements of two pressure gauges.** The points are defined by the pressures measured by two pressure gauges. The line represents a case of two pressure gauges measuring exactly the same values. The gauges are well calibrated at high pressures ($p > 10^{-2}$ mbar). However, starting at the overlapping operating regime, the gauges show a huge pressure difference. The sudden strong deviation between the measured values can be explained by opening Gate valve 2 to start pumping with the turbomolecular pump. In this case, the pressure probably didn't reach an equilibrium value in the whole vacuum system. The pressures at low pressures ($p < 10^{-5}$) have stabilized after hours of pumping and show a moderate disagreement of around 30%.

gime[10]. We mount one pressure gauge directly to the vacuum chamber and a second one in front of the gate valves leading to the pumps. The gauges show a difference of $\sim$ 30% in the pressure readout in high vacuum (Figure 3.12), which confirms that we will have a significant unknown in the estimate of the gas damping.

No leaks were observed with a helium leak tester. Still, pressure increases fast when we heat the vacuum chamber with a reflector lamp (shone through a large window on Quick Access Door: QAD). However, the rate of the pressure increase is slower after several days of pumping, which confirms that contamination (as a result of the trapping process) is the main reason for the slow pumping down to vacuum. Base pressure of the vacuum chamber is around 4×10^{-7} mbar after a night of pumping. Reasons for not being able to reach lower pressures might be the following:

- improperly cleaned viton (used for vibration isolation),
- frequent spraying of liquid and nanospheres for trapping and venting of the vacuum chamber to put the cavity inside,
- rubber O-rings at the quick access door (QAD), which is regularly used to move the cavity in and out of the vacuum chamber

[10] Operating manual

3.2 DETECTION OF THE NANOSPHERE MOTION WITH THE TRAPPING LASER

The nanosphere scatters a part of the trapping laser electric field $E_0 \exp(i\omega_t t)$ following the dipole radiation pattern. The light transmitted through the optical trap and collimated by a collection lens (NA= 0.2) can be described as a superposition of the forward scattered field $E_n \exp(i\omega_t t + i\varphi_n)$ and the electric field $E_t \exp(i\omega_t t + i\varphi_t)$, $E_t \approx E_0$. A single photodiode will detect an interference of the two fields with a constant phase relation of $\varphi_t - \varphi_n = \pi/2$ due to the Gouy phase of the transmitted trapping laser [Gieseler et al., 2012]. Therefore, the detection with a single photodiode is sensitive to the phase of the scattered field, i.e. to the nanosphere motion, with the highest sensitivity to the motion along the z-axis. In order to enhance the detection of the transverse motion (x- and y-motion) we use a split detection scheme (Figure 3.13).

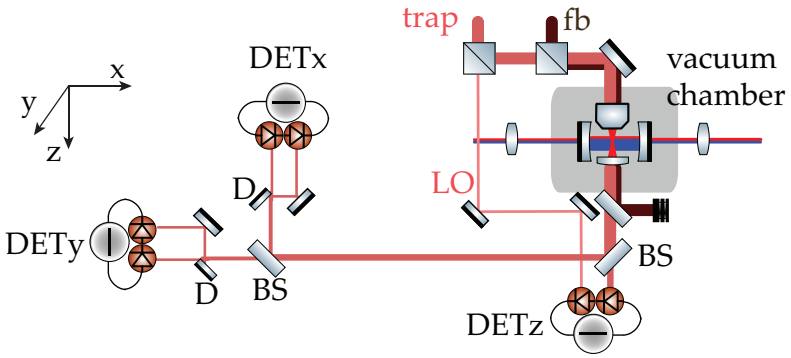

Figure 3.13: **Detection of the nanosphere motion with the trapping laser.** The feedback laser (fb) is separated in the trap transmission on a polarizing beamsplitter. The trapping laser is split into three paths with each path leading to a different detector to monitor a single axis of the nanosphere motion. A part of the trapping laser is split off before the vacuum chamber and used as a local oscillator (LO) for the detection of the z-motion (detZ). D-shaped mirrors are used to split the trapping laser along the x- and y-axis, which send the halves to the balanced photodetectors DETy and DETx in order to detect the y- and x-motion, respectively.

Let us analyze the split detection of the x-motion (DETx) as a specific example. We use a D-shaped mirror to split the laser mode along the vertical axis into left and right semicircles. Their respective powers are then subtracted from each other on a balanced detector (Thorlabs PDB-425C-AC). As both y- and z-motion show up with equal amplitudes in each detector photodiode, the sensitivity to these motions is suppressed. In practice, we show a total elimination of the y-motion and some suppression of the z-motion (Figure 3.14). We explain this by imperfectly aligning the collection lens along the optical axis of the transmitted light.

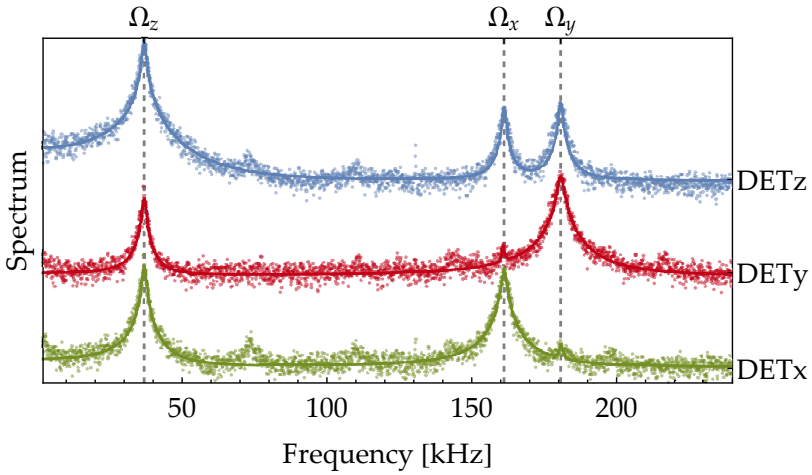

Figure 3.14: **Noise power spectrum of signals obtained in DETz (blue), DETx (green) and DETy (red).** All three directions of motion are observed as spectral peaks at frequencies Ω_z, Ω_x and Ω_y in DETz, however the detection is most sensitive to the z-motion. DETx (DETy) is used to detect the x-motion (y-motion) while the y-motion (x-motion) is suppressed to the noise level. The z-motion, although still observed in DETx and DETy, is sufficiently far away in frequency space to be efficiently filtered out by electronic bandpass filters.

The signal is further amplified by 10 dB with a voltage amplifier (Femto DHPVA). Half of the signal passes through a buffer (to account for the difference between the voltage amplifier input impedance of 50 Ω and the acquisition card input impedance of 1MΩ) and processed with an acquisition card (pico Technology PicoScope 5442B). The second half is used for parametric feedback cooling with a phase-locked loop (PLL, Zurich Instruments HF2LI). The PLL locks an internal oscillator to the dominant harmonic oscillation in the signal within a certain bandwidth. Still, a larger oscillation out of the given range limits the PLL input voltage range. This would result in an effectively smaller desired oscillation and is the main reason behind suppressing other oscillations in our detection scheme. The internal oscillator is squared in amplitude and applied as an amplitude modulation to the AOM, which increases the trap stiffness to stabilize the nanosphere motion. For more details about the trapping part of the setup, see the PhD thesis by David Grass [Grass, 2018].

3.3 HOMODYNE DETECTION OF THE LOCKING MODE

The phase quadrature of the cavity output holds information about the nanosphere motion (see Equation (2.71)). We are usually interested in detection of the motion along the cavity axis $\hat{x}$. Provided we levitate a nanosphere with the tweezer laser, we can move it with respect to the cavity standing wave, which is useful to optimize the linear coupling $g_0 \sin(2kx_0)$ and to scan the cavity mode profile. At

an arbitrary position, the homodyne spectrum is a complex combination of peaks at motional frequencies and their combinations. In the following we develop a full theory of the homodyne detection in this scenario.

3.3.1 *Modeling of the homodyne detection spectrum*

The homodyne measurement of the locking mode realizes an amplified detection of its phase quadrature. In a classical picture, the cavity output of the locking cavity mode $E_{p,out}e^{-i\omega_p t}$ is combined with an orthogonally polarized strong local oscillator (LO) mode $E_{LO}e^{-i(\omega_p t+\varphi)}$ on a polarizing beamsplitter PBS1 (Figure 3.15). The two modes are brought to interference on a second beamsplitter PBS2 and detected by a balanced photodetector[11], yielding an output voltage proportional to an intensity difference:

$$v(t) = \eta_{det}\frac{\varepsilon_0 c G_d}{2} \times \int_A \left(\left| E_{p,out}\vec{n}_x + E_{LO}\vec{n}_y e^{-i\varphi} \right|^2 - \left| E_{p,out}\vec{n}_x - E_{LO}\vec{n}_y \mathrm{e}^{-i\varphi} \right|^2 \right) dA. \tag{3.9}$$

The gain G_d of converting the laser intensity into electrical voltage is given by the detector specification, while η_{det} is the detection efficiency of the photodiodes. It is important to include an integration over the photodiode area A in order to account for the mode overlap of the two fields. In general, this integral can be exchanged by a single value of detection visibility $\mathcal{V}$, which we maximize in order to achieve the most efficient detection of the phase quadrature[6]. Precise balancing of the two detectors is necessary to suppress terms proportional to $|E_{LO}|^2$ and $|E_{p,out}|^2$, such that Equation (3.9) contains only the cross-terms:

$$v(t) = 2\eta_{det}\mathcal{V}G_d A\frac{\varepsilon_0 c}{2}\left(E_{LO}E^*_{p,out}\mathrm{e}^{-i\varphi} + E^*_{LO}E_{p,out}\mathrm{e}^{i\varphi} \right). \tag{3.10}$$

Taking $E_{LO} = E^*_{LO}$ (in essence, considering $E_{LO} \gg E_{p,out}$) and $E_{p,out} = \sqrt{\frac{2\hbar\omega_p}{A\varepsilon_0 c}}\left(\sqrt{\kappa_{IN}}\left(\alpha_0^p + \hat{a}_p\right) + \hat{a}^{p,2}_{\mathrm{IN}} \right)$ from cavity input-output theory (see Chapter 2), the optimal phase difference for detection of the phase quadrature is clearly $\varphi = \pi/2$. The strong coherent part of the signal is typically used to lock the detection quadrature as $v_{DC} \propto \sqrt{P_{LO}}|\alpha_0^p|\cos\varphi$, from which we see that the locking set point must be at $v_{DC} = 0$. The rest of the signal $v(t)$ contains the phase quadrature of the fluctuations of the locking mode:

$$v(t) = 2\eta_{det}\mathcal{V}G_d\sqrt{P_{LO}}\sqrt{\hbar\omega_p\kappa_{IN}}\left(\hat{a}_p - \hat{a}_p^\dagger\right). \tag{3.11}$$

[6] $\mathcal{V}$ *can be measured when* $P_{LO} \approx P_{p,out}$ *[Bachor and Ralph, 2004].*

[11] Thorlabs PDB420C-AC

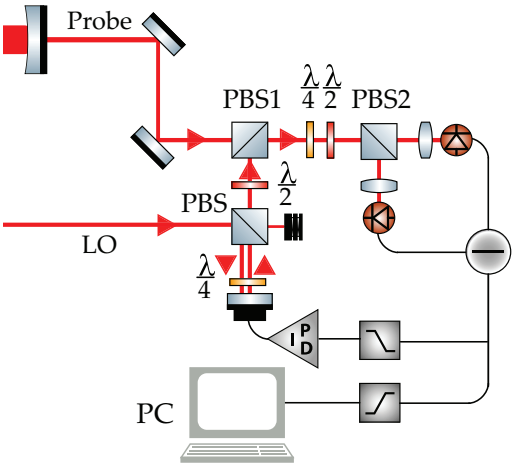

Figure 3.15: **Setup for the homodyne measurement.** The transmitted locking cavity field ($P_{out,p} \approx 7\mu$W) is mixed with an orthogonally polarized local oscillator (LO) laser ($P_{LO} \approx 1$ mW) on a polarizing beamsplitter (PBS1). The two lasers are split 50:50 between the reflection and transmission of the following polarizing beamsplitter (PBS2), after which we focus the mixed lasers on the two photodiodes of a balanced photodetector. The low-pass filtered signal is used for locking of the relative phase between the LO and the locking beam via applying the PID generated feedback signal to the piezo driven mirror. This mirror is placed orthogonal to the LO propagation in order to minimize beam pointing errors due to the piezo length change. The high-pass filtered signal can be either digitized and stored for further evaluation or immediately turned into a power spectrum with a spectrum analyzer.

The power spectrum of $v(t)$ is proportional to the spectrum of the locking mode phase quadrature:

$$S_{VV}(\omega) = 4\eta_{det}^2 \mathcal{V}^2 \frac{G_d^2}{R_{\mathrm{LOAD}}} P_{LO} \hbar\omega_p \kappa_{IN} S_{YY}^p(\omega). \tag{3.12}$$

Note that $S_{YY}^p(\omega)$ is proportional to $S_{xx}(\omega)$, which we showed in Equation (2.71) in Chapter 2.

So far we assumed a noiseless local oscillator, i.e. a laser without any classical phase and intensity noise. Let us now consider the most general case of local oscillator $E_{LO}(t) = E_{LO}(1 + \alpha_{LO}(t))e^{-i\varphi_{LO}(t)}$ with phase noise $\varphi_{LO}(t)$ and amplitude noise $\alpha_{LO}(t)$, but still a clean cavity mode. Assuming that any the locking mode fluctuation $\hat{a}_p$ is small compared to its coherent amplitude α_p, the main modification to $v(t)$ is:

$$v^{lo}(t) = 4i\eta_{det} \mathcal{V} G_d \sqrt{P_{LO} \hbar\omega_p \kappa_{IN}} \alpha_0^p \varphi(t). \tag{3.13}$$

In the case of no correlation between the phase noise $\varphi(t)$ and fluctuations $\hat{a}_p$, the total spectrum will be modified by:

$$S_{VV}^{LO}(\omega) = 16\eta_{det}^2 \mathcal{V}^2 \frac{G_d^2}{R_{\mathrm{LOAD}}} P_{LO} \hbar\omega_p \kappa_{IN} |\alpha_0^p|^2 S_{\varphi\varphi}(\omega) \tag{3.14}$$

Since the same laser is used both for driving the cavity and as a local oscillator, the same phase noise will be present in both fields. Accounting for a cavity response we obtain a spectrum for the cross-contribution:

$$S_{VV}^{LO-p}(\omega) = 8\eta_{det}^2 \mathcal{V}^2 \frac{G_d^2}{R_{\mathrm{LOAD}}} P_{LO} \hbar\omega_p \frac{2\kappa_{IN}}{\left(\frac{\kappa}{2}\right)^2 + \omega^2} |E_d^p|^2 S_{\varphi\varphi}(\omega). \quad (3.15)$$

$S_{VV}^{LO}(\omega)$ and $S_{VV}^{LO-p}(\omega)$ will ultimately limit the signal to noise performance of the homodyne detection.

Experimental spectrum with a nanosphere

Figure 3.16 shows a measured homodyne spectrum $S_{VV}(\omega)$ of the nanosphere motion (red) and the noise background (blue). In order to eliminate the noise from the homodyne spectrum, we subtract a homodyne spectrum obtained without a trapped nanosphere $S_{VV}^{bg}(\omega)$ (blue) from spectra obtained with the nanosphere signal $S_{VV}(\omega)$ (red). In the next step, we divide the difference by $\left(\frac{\kappa}{2}\right)^2 |\chi_p(\omega) + \chi_p^*(\omega)|^2 = \frac{\left(\frac{\kappa}{2}\right)^2}{\left(\frac{\kappa}{2}\right)^2+\omega^2}$ to account for the cavity response to the mechanical spectrum $S_{xx}(\omega)$. Thus obtained "processed" spectrum (green) is compared to a theoretical spectrum $c_{cal} \times S_{xx}(\omega)$ (green line) assuming only the thermal noise contribution to S_{YY}^{l} from Equation (2.71) and without any fit parameters.

The calibration constant c_{cal} was obtained from independent measurements ($\mathcal{V} = 0.92$, $P_{LO} \approx 0.2$ mW, $\kappa = 2\pi \times 193$ kHz) and, where no measurements could be performed, from detector specifications ($G_{V/W} = 250 \times 10^3$ V/W, $\eta_{det} \approx 0.7$). We detect the peak at $\Omega_x = 2\pi \times 169.5$ kHz and calculate the damping rate $\gamma_m = 2\pi \times 2.85$ kHz from the measured pressure $p = 2.39$ mbar. We assume a nanosphere of nominal radius, yielding a single photon coupling rate $g_0 \approx 2\pi \times 0.3$ Hz. The total coupling from the extracted intracavity photon number $|\alpha_0^p|^2 \propto P_{out,p} = 6.9\ \mu$W is $g = 2\pi \times 3.46$ kHz. The theoretical line matches the measured spectrum around $S_{xx}(\Omega_x)$ well. We conclude that we can convert spectra from V^2/Hz into $\mathrm{nm}^2/\mathrm{Hz}$ with great confidence.

Once we place a nanosphere in the cavity locking mode, we detect several peaks besides the expected harmonics of $\Omega_x/2\pi$. By comparison with the tweezer readout, we know that some peaks correspond to the nanosphere motion along z-axis (harmonics of $\Omega_z/2\pi \sim 40$ kHz), while some peaks are mixed terms of the x and the z-motion. Coupling to the motion along the y axis is suppressed by optimizing the tweezer laser polarization such that this motion is completely orthogonal to the cavity axis. However, the fact that we see the z-motion shows that the propagation of the tweezer laser is not fully orthogonal to the cavity axis. Instead, we assume that the oscillation plane

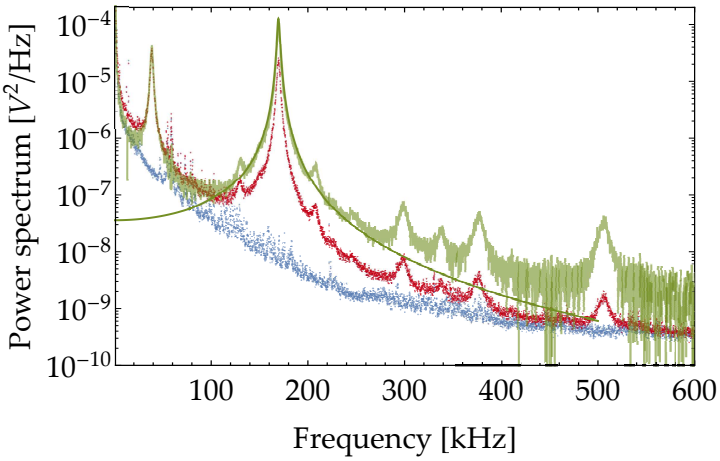

Figure 3.16: **Extraction of the mechanical spectrum $S_{xx}(\omega)$ from the measured homodyne spectrum.** The background homodyne spectrum without a nanosphere coupled to the cavity locking mode (blue) is subtracted from the measured homodyne spectrum (with the nanosphere maximally linearly coupled to the cavity mode, red) and corrected for the cavity response, thus obtaining a spectrum representing the mechanical spectrum $S_{xx}(\omega)$ (green). Thermal contribution to the spectrum with a separately calibrated detection sensitivity included (green line) is compared to it. We see an almost perfect match, such that we can with certainty convert this homodyne spectrum from V^2/Hz into nm^2/Hz.

given by the x and z axes is rotated by a small angle ϕ around the y-axis (Figure 3.17). Both the x and z-motion are projected onto the cavity axis such that:

$$\begin{aligned} g_0\hat{x} &\rightarrow g_0(\hat{x}\cos\phi + \hat{z}\sin\phi) \\ g_q\hat{x}^2 &\rightarrow g_q(\hat{x}\cos\phi + \hat{z}\sin\phi)^2 \\ &= g_q(\hat{x}^2\cos^2\phi + \hat{z}^2\sin^2\phi + \frac{1}{2}\sin 2\phi(\hat{x}\hat{z} + \hat{z}\hat{x})) \\ g_c\hat{x}^3 &\rightarrow g_c(\hat{x}\cos\phi + \hat{z}\sin\phi)^3. \end{aligned} \tag{3.16}$$

The coupling rate g_0^x to the x-motion is decreased by a factor of $\cos\phi$, which for a small angle ϕ is approximately unity. However, a non-zero angle allows for a coupling to the z-motion with linear and quadratic rates g_0^z and g_q^z, respectively. Other cross-terms that appear in an actual measurement (Figure 3.18) are:

- $\hat{x}\hat{z}$: Sidebands of S_{xx} generated by the first harmonic of z;
- $\hat{x}\hat{z}^2$: Sidebands of S_{xx} generated by the second harmonic of z;
- $\hat{x}^2\hat{z}$: Sidebands of $S_{x^2x^2}$ generated by the first harmonic of z.

We fit all of the peaks in the measured homodyne spectrum jointly:

$$S_{(x^iz^j)(x^iz^j)}(\omega) = a_{x^i\pm z^j}\frac{(i+j)\gamma_m(i\Omega_x \pm j\Omega_z)^2}{((i\Omega_x \pm j\Omega_z)^2 - \omega^2)^2 + (i+j)^2\gamma_m^2\omega^2}, \tag{3.17}$$

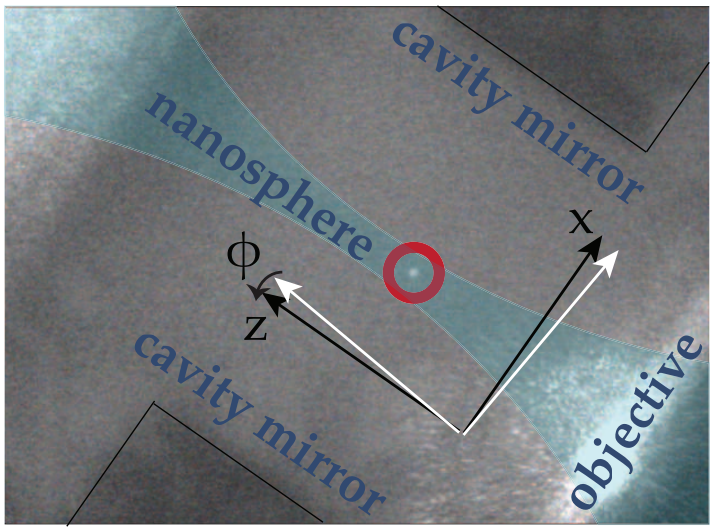

Figure 3.17: **The camera image of a nanosphere levitated in optical tweezers (objective)**. Blue overlay is a eye-guide which schematically represents the trapping laser propagation. The white arrows show the x and z motional axes as defined by the tweezer trap. The Cavity is placed roughly orthogonal to the tweezer laser, with the cavity x- and z-axes along black arrows. As the tweezer polarization is oriented along the x-axis, most of the scattered light from nanosphere is scattered along the z and y axes (into the direction of the camera), thus we see it bright in this image. Small rotation by the angle ϕ between these two coordinate systems is a source of coupling of the nanosphere's z-motion to the cavity mode.

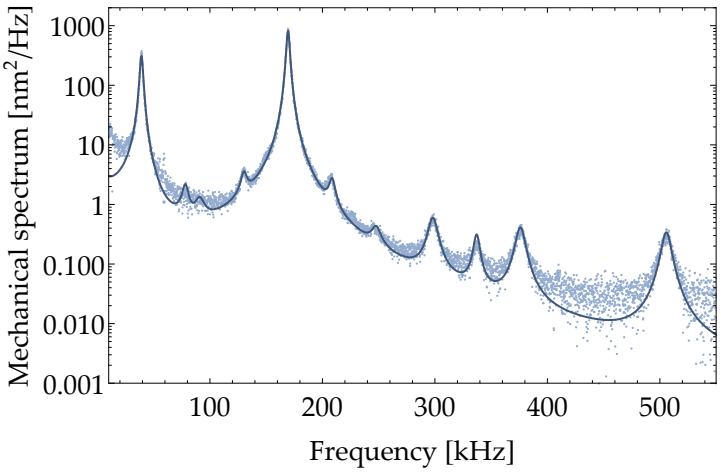

Figure 3.18: **Joint fit of the mechanical spectrum read out from the cavity phase quadrature.** Fit of the homodyne spectrum is obtained by jointly fitting the spectra of the x- and z-motion with all mixed contributions arising from coupling to the z-motion. This particular spectrum was taken with a nanosphere placed along the cavity axis in a way suited to observe the largest number of peaks contributing. The measured spectrum in the interval $(400 - 480)$ kHz, below 20 kHz and above 520 kHz is not used for the fit as the signal-to-noise ratio is basically 0, as also shown in Figure 3.16.

with each peak's linewidth and central frequency defined by $(i+j)\gamma$ and $\Omega_{peak} = i\Omega_x \pm j\Omega_z$, respectively. The sign change in Ω_{peak} is related to the existence of upper and lower sidebands for each peak at $i\Omega_x$. The peak amplitudes $a_{x^i \pm z^j}$ are taken to be independent of each other, although some relation is expected:

- The ratio of the peak amplitudes $a_x = S_{xx}(\Omega_x)$ and $a_z = S_{zz}(\Omega_z)$ depends on the angle ϕ, which we can use to extract ϕ:

$$\phi = \arctan\left(\sqrt{\frac{a_z}{a_x}}\frac{\Omega_z}{\Omega_x}\right) \approx 8.4^\circ. \tag{3.18}$$

  We estimate that the single photon coupling rate to the z-motion is $g_0^z/2\pi \approx 0.091$ Hz, which is smaller than g_0 by a factor of ~ 3.

- The peak amplitudes $a_{x^i+z^j}$ and $a_{x^i-z^j}$ are expected to be of equal size as they origin from the same cross-contribution $x^i z^j$. The ratios $a_{x^i}/a_{x^i+z^j}$ and $a_{x^i}/a_{x^i-z^j}$ depend on the angle ϕ as well and can be used to extract the particular value (Figure 3.19).

- The peak amplitudes $a_{x^i+z^j}$ and $a_{x^i-z^j}$ also depends on the nanosphere position and exhibit a phase shift $\pi/2 - i\phi$ and $\pi/2 + i\phi$ with respect to a_{x^i} (Figure 3.19).

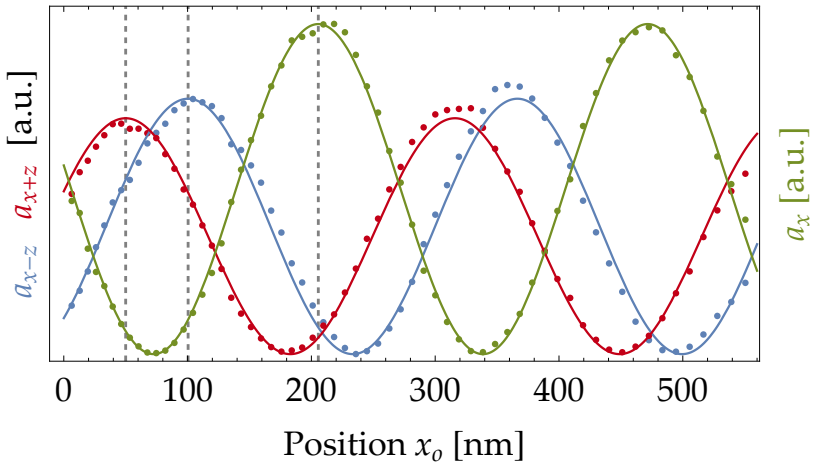

Figure 3.19: **Spectral amplitude of sidebands at Ω_{x-z} and Ω_{x+z} as a function of the nanosphere position in comparison to the amplitude of S_{xx}.** The mixing sidebands $S_{(xz)(xz)}$ show up out-of-phase with respect to the main spectral contribution S_{xx}. The two sidebands have a relative phase difference of 2ϕ due to the tilting of the tweezer axis by an angle ϕ. The dashed lines show the position of the largest intensity gradient ($x_0 \approx 200$ nm), which features the best detection of S_{xx}, and the positions of best detection of $S_{(xz)(xz)}$, which occur close to the cavity node or antinode at $x_0 \approx 75$ nm.

3.3.2 *Moving a nanosphere along the cavity standing wave*

Our experimental setup allows for positioning the nanosphere with respect to the cavity at sub-wavelength precision. In the following

we analyze the position-dependent coupling between nanosphere motion and the cavity mode in detail. We move the nanosphere along the cavity standing wave in single steps (given by the nanopositioner step size ~ 8 nm) and record a homodyne spectrum at each position. Each spectrum is fit as described earlier. The total moving distance is less than 1 μm, which would insignificantly displace the nanosphere ~ 10 nm away from the cavity axis, assuming the angle $\phi = 8.4°$ measured above.

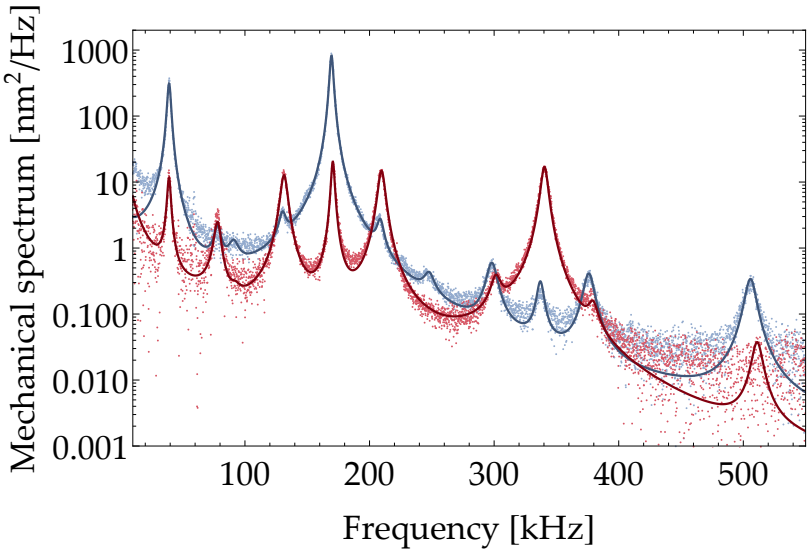

Figure 3.20: **Two homodyne spectra taken at the positions of maximum linear and quadratic couplings.** Homodyne measurement detects the phase quadrature of cavity field operators. Depending on the nanosphere position along the cavity standing wave, we can have the optimal linear (blue) or quadratic coupling (red). The linear coupling corresponds to the optimal detection of S_{xx} and the quadratic coupling enables the detection of $S_{x^2x^2}$. Shown as well are the fits of the full homodyne spectrum, which we use to extract information about the nanosphere motion.

The possibility to scan the nanosphere position along the standing wave means that we can set the interaction from an optimized readout of $\hat{x}$ (at the intensity slope, Equation 2.17) to a readout which is most sensitive to $\hat{x}^2$ (at the intensity minimum and maximum, Equation 2.19):

$$g_0(x_0) = g_0 \sin 2kx_0, \qquad g_q(x_0) = g_q \cos 2kx_0. \tag{3.19}$$

We notice that g_q and g_0 are exactly out of phase with respect to each other. The detected spectrum of the cavity phase quadrature S_{YY} from Equation (2.71), which now allows for the nanosphere to be at an arbitrary trap position x_0, is:

$$S_{YY}(\omega) \propto \left(\frac{g_0 \sin(2kx_0)}{x_{zpf}}\right)^2 S_{xx}(\omega) + \left(\frac{g_q \cos(2kx_0)}{x_{zpf}^2}\right)^2 S_{x^2x^2}(\omega) + \cdots, \tag{3.20}$$

where the high-Q limit ($\gamma \ll \Omega_x$) is assumed for the spectrum of $S_{x^2x^2}$ [Hauer et al., 2015]:

$$S_{x^2x^2}(\omega) = \frac{64\gamma_m\Omega_x^2}{(\omega^2+\gamma_m^2)((\omega^2-(2\Omega_x)^2)^2+4\omega^2\gamma_m^2)}\left(\frac{k_BT}{m\Omega_x^2}\right)^2. \quad (3.21)$$

The power spectral density $S_{x^2x^2}$ has three roots at frequencies $\omega = 0, \pm\Omega_x$ with FWHM linewidth of $2\gamma_m$.

We encounter a slight experimental problem while we move the nanosphere along the standing wave: the nanopositioner uses slip stick motion. It is known that slip stick motion creates a position-dependent friction, which leads to an unequal microstep size with an average of around 8 nm[12]. In fact, the microstep size increases with increasing translation along one direction. The cavity standing wave has a set periodicity of $\lambda/2$, so any deviations in coupling dependence from Equation (3.19) can be attributed to this inaccurate positioning. To correct for it we fit the x-scale with $2kx_0 \to 2kx_0(1+\mathrm{sf}\times x_0)$, where the scaling factor sf allows for a linear change in step size in the course of about 560 nm. We obtain a good fit to experimental data with step sizes from 6 nm (initial microstep) to 11 nm (final microstep), therefore showing that the calibration of the nanopositioner x-axis by the cavity standing wave works. From this point on, we plot the x-axis rescaled to the cavity standing wave.

Relation between the linear and quadratic coupling

Detection at positions of the maximum linear ($\sin 2kx_0 = 1$) and quadratic coupling ($\cos 2kx_0 = 1$) in S_{YY} gives us the ratio of the two contributions from the respective peak amplitudes a_x and a_{x^2}:

$$\frac{a_{x^2}|_{\sin 2kx_0=1}}{a_x|_{\cos 2kx_0=1}} = \frac{g_q^2 S_{x^2x^2}(2\Omega_x)}{g_0^2 x_{zpf}^2 S_{xx}(\Omega_x)} = k^2 x_{zpf}^2 \frac{n_{th}}{2}. \quad (3.22)$$

Thus, if we assume that the bath temperature is $T \sim 293$ K (which is reasonable at pressures $p > 1$ mbar) all parameters are known, hence we can extract the nanosphere mass as:

$$m = \frac{k^2 k_B T}{4\Omega_x^2}\frac{a_x|_{\cos 2kx_0=1}}{a_{x^2}|_{\sin 2kx_0=1}}. \quad (3.23)$$

Note that this is a relative measurement of two spectral peaks, i.e. it is not necessary to have a fully calibrated spectrum.

In the actual measurement, we move the nanosphere along the cavity standing wave (x-axis) and record the homodyne spectrum of the locking mode (Figure 3.20) at each position x_0. We fit all peaks jointly in $S_{YY}(\omega)$ and obtain the peak amplitudes $a_x(x_0)$ and $a_{x^2}(x_0)$. We plot them against the position x_0 and fit them with $\sin^2(2kx_0)$ and

[12] Mechonics, private communication

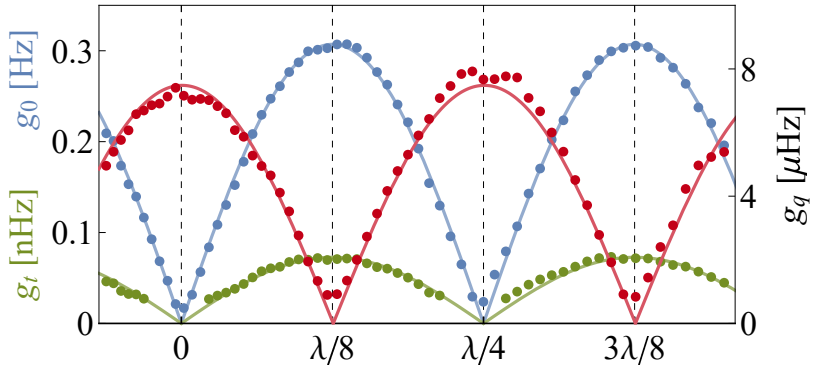

Figure 3.21: **Absolute magnitudes of the linear coupling (blue), quadratic coupling (red) and cubic coupling (green) as a function of the trap position along the cavity standing wave**. The quadratic coupling is seen out-of-phase with the linear and cubic coupling, as expected from Equation (3.19). The ratio between the maximum values of the linear and quadratic coupling is used to extract the nanosphere mass (and the radius). The vertical dashed lines mark the positions of the cavity node ($\lambda/4$) and the cavity antinode (0), as well as the positions of optimal linear coupling ($\lambda/8$ and $3\lambda/8$, halfway between the cavity node and antinode). As we actually measure the squared coupling rates ($S_{YY} \propto (g_0^x)^2, (g_q^x)^2$), we are not able to distinguish between a node and an antinode, hence we plot the absolute coupling rates. However, it will be possible to make a distinction from the sign of the frequency change.

$\cos^2(2kx_0)$ in order to extract the maximum values of a_x and a_{x^2}, respectively. From the ratio of these values we obtain a nanosphere mass of $m = 2.86(4)$ fg using Equation (3.23), extremely close to the calculated expected mass of $m = 2.83$ fg (density: $\rho = 1850\ \mathrm{kg/m^3}$ and radius: $r = 71.5$ nm, both specified by producer). For comparison, there are two other reports on measuring the mass of a charged nano- [Ricci et al., 2018] and microsphere [Blakemore et al., 2019] by applying an electric force. In the former case, the precise measurement of mass differs by $\sim 16\%$ from the expected value, while in the latter case both mass and radius are measured with great precision. However, the calculated density ($\rho \approx 1550\ \mathrm{kg/m^3}$) is significantly smaller from both the producer specified value ($\rho = 2000\ \mathrm{kg/m^3}$) and the density of amorphous silica ($\rho = 2200\ \mathrm{kg/m^3}$), probably because pores make up a big part of the microsphere volume.

For the producer-specified density $\rho = 1850\ \mathrm{kg/m^3}$ we estimate the nanosphere radius of $r = (71.8 \pm 0.9)$ nm, which fits extremely well to the nominal radius $r = (71.5 \pm 2)$ nm. We use the ratio between the quadratic and cubic coupling:

$$m = \left(\frac{2}{3}\right)^2 \frac{k^2 k_B T}{4\Omega_x^2} \frac{a_x^2|_{\sin 2kx_0=1}}{a_{x^3}|_{\cos 2kx_0=1}}. \tag{3.24}$$

to calculate the nanosphere radius as well, albeit with a larger error: $r = (71.5 \pm 1.5)$ nm. The calculated single photon coupling at the optimal cavity position is $g_0 = 2\pi \times 0.3$ Hz.

Change in the spring constant

The same series of homodyne measurements can be used to extract the mechanical frequencies Ω_x and Ω_z. Due to the presence of a cavity trapping potential, all trap frequencies should be modulated according to Equation (2.21) or Equation (2.22), depending on the intracavity photon number. Note that the tweezer trap along the y and z axis is orders of magnitude stronger compared to the trap induced by the cavity mode, as the cavity waist is ~ 40 times larger than the tweezer focus. Hence, we don't expect to see a significant change in Ω_z (see the estimate in Equation (2.27)). This is confirmed by our measurements. The confinement of the standing wave along the cavity axis however can become comparable in strength to the tweezer trap, thus even for modest intracavity powers we expect to see a modulation in Ω_x. In the case of a strong cavity mode, the nanosphere can be pulled away from the tweezer trap as far as $\lambda/4 = 256$ nm (when the trap position is at the cavity intensity minimum). In that case, the cavity standing wave is the stronger trap along the x-axis, but the tweezer trap is still dominant along the y- and z-axis.

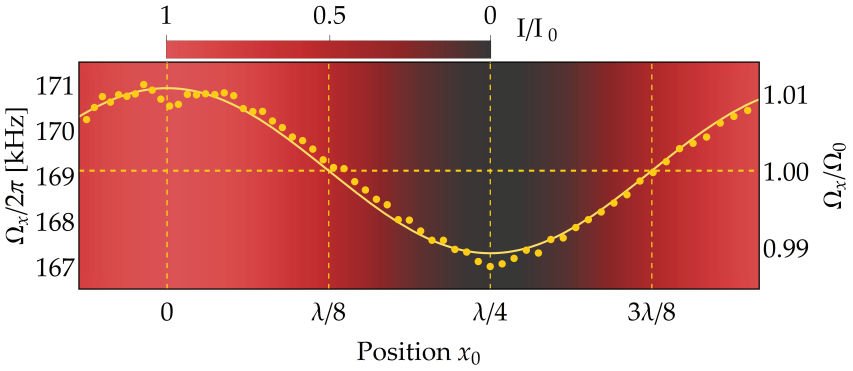

Figure 3.22: **Modulation of the mechanical frequency in the combined trap of the cavity and the tweezer**. Cavity provides an additional confinement with the nanosphere at the position of maximum cavity intensity (at $x_0 = 0$), while it lowers the overall trap stiffness at the minimum cavity intensity (at $x_0 = \lambda/4$). Magnitude of the frequency change is used to determine the intracavity photon number.

The position-dependence of Ω_x extracted from the homodyne spectra of the locking mode, shown in Figure 3.22, exhibits a clear periodicity along the cavity standing wave. Based on the magnitude of trap frequency modulation and the earlier determined nanosphere radius, we calculate the intracavity photon number of the locking mode to be

$|\alpha_0^p|^2 = 1.23 \times 10^8$ photons. We extract the photon number from the measured cavity output power $P_{out}^p = 6.9\ \mu$W as well:

$$|\alpha_0^p|^2 = \frac{P_{out}^p}{\hbar\omega_l}\kappa_2 \approx 1.32 \times 10^8, \tag{3.25}$$

where $\kappa_2 = \Delta\nu_{FSR}T_2$ is the cavity loss rate due to the transmission of the output mirror $T_2 = 20$ ppm. The two obtained values match well.

3.3.3 *Measurement of the cavity waist*

Following the scan along the cavity standing wave, we now move the nanosphere orthogonally to the cavity axis to probe the cavity Gaussian envelope. We move our nanosphere along the y-axis (z-axis) in steps of $\Delta y \approx 2.4\ \mu$m ($\Delta z \approx 4.2\ \mu$m) and optimize the position x_0 along the cavity to always reach the maximal linear coupling of the x-motion. Δy and Δz were chosen to be a multiple of 64 microsteps as we have found that this gives a constant step size. At each position we extract the peak amplitude a_x from the homodyne spectrum, which is proportional to the coupling rate $(g_0^x(z_0, y_0))^2$ (Equation (3.20)).

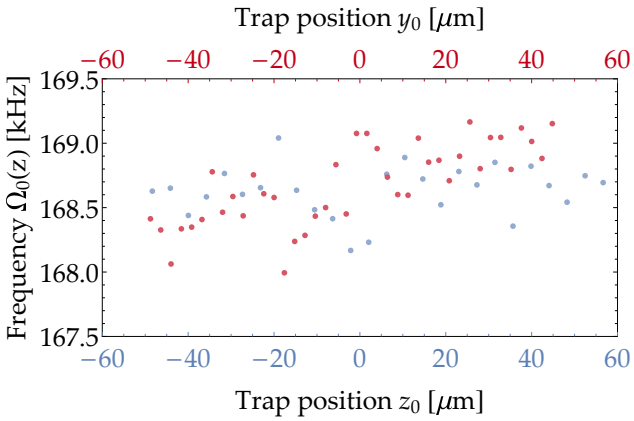

Figure 3.23: **Stability of the mechanical frequency $\Omega_0 = \Omega_x$ as we move the nanosphere along the z- (blue) and y-axis (red)**. Although a small scatter in the measured values is noticeable, it is still well below the frequency change induced by the cavity co-trapping. This confirms that we take the homodyne spectra in the vicinity of the maximum intensity gradient as we move the nanosphere as explained in the main text.

Due to the angle $\phi \approx 8.4°$ between tweezer propagation and cavity optical axis, the nanosphere moves diagonally across the cavity axis. For example, we estimate that with each step $\Delta y = 2.4\ \mu$m, the nanosphere moves $\Delta y \sin\phi \approx 300$ nm further along the cavity axis, which results in a modified coupling to the x-motion. Therefore, after each step we correct the nanosphere position along the cavity axis to achieve the highest linear coupling. At this position the interaction is purely linear and we don't expect to see an influence on the mechanical frequency, which is confirmed in Figure 3.23.

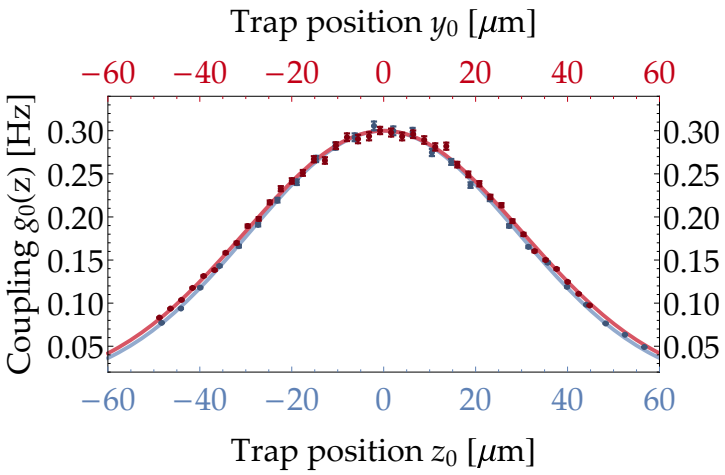

Figure 3.24: **Linear coupling g_0^x as we move the nanosphere along the z- and y-axis.** The single photon coupling rates are calibrated to $g_0^x = 2\pi \times 0.3$ Hz, as expected based on the calculated nanosphere radius. We fit a Gaussian envelope from Equation (3.26) to determine the cavity waist in each direction. The obtained Gaussian profiles overlap extremely well.

As we scan the nanosphere position across the cavity axis (Figure 3.24), the linear coupling g_0^x follows:

$$g_0^x(z_0, y_0) = g_0^x(0,0) e^{-\frac{z_0^2}{(w_0^z)^2}} e^{-\frac{y_0^2}{(w_0^y)^2}} \tag{3.26}$$

We calibrate the coupling rates to the expected maximum single photon coupling $g_0^x \approx 2\pi \times 0.3$ Hz, calculated from our previous measurement of the nanosphere radius in Section 3.3.2. The fit from Equation (3.26) provides the cavity mode waist in both radial directions:

$$w_0^z \approx (42.7 \pm 0.2)\ \mu\text{m}, \qquad w_0^y \approx (41.3 \pm 0.3)\ \mu\text{m} \tag{3.27}$$

which are close to the theoretical value of $w_0 = 41.1\ \mu$m.

3.4 DETECTION OF THE CAVITY CONTROL LASER: OPTOMECHANICALLY INDUCED TRANSPARENCY

In analogy to electromagnetically induced transparency (EIT) in atomic physics, the presence of an object with a (mechanical) resonance in an optical cavity can induce a "transparency" window. This optomechanically induced transparency (OMIT) has been demonstrated first with toroids and photonic crystal nanocavities [Weis et al., 2010, Safavi-Naeini et al., 2011]. Two driving fields with different frequencies are needed to demonstrate OMIT. The control laser, as defined in previous chapters, is used with a constant detuning during the measurement. For the second mode we add a weak probe laser with variable frequency ω_p which is scanned over the cavity resonance. When the frequency difference between the two lasers $\omega_c - \omega_p$ is close to

the nanosphere motional frequency Ω_x, a destructive interference between the control and probe mode modifies the cavity reflection and transmission response. The response can be used to extract the coupling between the control laser and the nanosphere motion, as well as the cavity decay rate κ and the control laser detuning Δ.

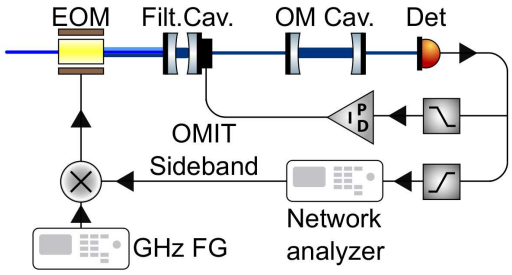

Figure 3.25: **Detection of the optomechanically induced transparency (OMIT).** The control laser is created in the same way as before, using an EOM which is driven with a function generator at a frequency of $\Delta\nu_{FSR}$ (GHz FG). We further modulate the phase of the drive at a frequency of ω_p (generated by the Network analyzer), which generates the necessary probe laser to be used for OMIT. Only the desired control laser with sidebands at $\pm\omega_p$ is transmitted through the filtering cavity (Filt. Cav.). The three modes experience a different cavity response by the optomechanical cavity (OM Cav.) and the beating between the components is recorded on a detector (Det). The detected signal with the dominant frequency component at a frequency ω_p is sent to the Network analyzer for a lock-in type measurement to extract the OMIT signal.

We set up a simple OMIT setup which creates additional sidebands of the control laser at a frequency $\pm\omega_p$, generated by a network analyzer (Figure 3.25). The sideband at a higher frequency is scanned over the cavity resonance and destructively interferes with the Anti-Stokes scattered photons from the nanosphere, which we observe on a single photodiode. We cannot neglect the sideband at the lower frequency in our analysis due to the mechanical frequency being on the order of the cavity decay rate $\Omega_x \sim \kappa$. Therefore, both sidebands will contribute to the OMIT and the detection. In comparison to other work on OMIT, we don't use a local oscillator to increase the signal-to-noise as we have limited power in the control laser, which we use only to drive the cavity. We discuss the theory of OMIT in the following.

3.4.1 *Theory of OMIT*

Transmission of the probe mode

We assume the control beam has already been created with a frequency ω_c, detuned by Δ with respect to the cavity resonant frequency $\omega_l - 2\pi \times \Delta\nu_{FSR}$. We generate sidebands of this mode at the frequencies $\omega_c \pm \omega_p$ by applying a small phase modulation $\varphi(t) = \beta \sin(\omega_p t)$ at a variable frequency ω_p. We use the fact that the mod-

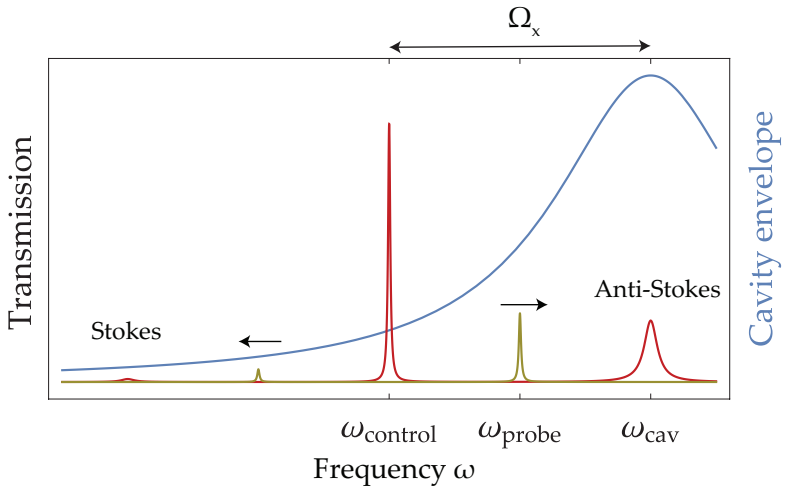

Figure 3.26: **Light and mechanical modes in the OMIT measurement**. We set the control laser (red) detuning $\omega_{cav} - \omega_c = \Delta = \Omega_x$, such that the Anti-Stokes sideband is resonant with the cavity (blue). We scan the cavity resonance with the probe laser (green), which destructively interferes with the Stokes and Anti-Stokes sidebands when $\omega_{probe} \sim \Omega_x$. We observe the optomechanical interaction in the cavity transmission and use it to obtain the coupling rate to the control laser.

ulation is small and keep the terms only up to the first order in β:

$$E_d^{in}(t) = E_d e^{-i\omega_c t - i\beta\sin(\omega_p t)} \approx E_d\left(1 + i\beta e^{-i\omega_p t} + i\beta e^{i\omega_p t}\right). \quad (3.28)$$

The carrier and its sidebands will experience a different cavity response as they are transmitted through the optomechanical cavity:

$$\begin{aligned} E_d^{out}(t) &= E_d t_c \\ &+ E_d i\frac{\beta}{2} t_{us}(\omega_p)\exp^{-i\omega_p t - i\varphi(\omega_p)} \\ &+ E_d i\frac{\beta}{2} t_{ls}(\omega_p)\exp^{i\omega_p t + i\varphi(\omega_p)}. \end{aligned} \quad (3.29)$$

The functions t_c, t_{us} and t_{ls} are the transmissions of the carrier, the upper and the lower sideband, respectively. These three modes together generate a signal on a photodiode proportional to $\left|E_d^{out}\right|^2$, which will have components at frequencies 0, ω_p and $2\omega_p$. We are interested only in the components oscillating at the probe frequency ω_p:

$$t_{\omega_p} = -\beta\,\mathrm{Re}\left(it_c t_{us}^* e^{i\omega_p t + i\varphi(\omega_p)}\right) - \beta\,\mathrm{Re}\left(it_c t_{ls}^* e^{-i\omega_p t - i\varphi(\omega_p)}\right). \quad (3.30)$$

In the experiment, a signal $\sin(\omega_p t)$ is created with a network analyzer and applied as a phase modulation to the function generator. The signal obtained in cavity transmission is fed to the network analyzer, which works as a lock-in amplifier and extracts components

oscillating with $\sin(\omega_p t)$ and $\cos(\omega_p t)$. For example, the extracted in-phase and out-of-phase components for the upper sideband are:

$$\begin{aligned} t^{in}_{\omega_p} &= -\beta\left[\mathrm{Re}(it_c t^*_{us})\sin(\varphi(\omega_p)) + \mathrm{Im}(it_c t^*_{us})\cos(\varphi(\omega_p))\right] \\ t^{out}_{\omega_p} &= -\beta\left[\mathrm{Re}(it_c t^*_{us})\cos(\varphi(\omega_p)) - \mathrm{Im}(it_c t^*_{us})\sin(\varphi(\omega_p))\right] \\ &\quad . \end{aligned} \tag{3.31}$$

The phase $\varphi(\omega_p) = \frac{d\varphi}{d\omega}\omega_p + \varphi_0$ is a frequency-dependent phase difference accumulated during multiple passes through the optical cavity. It thus also depends on the cavity decay rate through $\frac{d\varphi}{d\omega} = -\frac{(2\pi)^2}{2\kappa}$. It is easy to see that the magnitude of the response is independent of the phase $\varphi(\omega_p)$ as:

$$t^{amp}_{\omega_p} = \sqrt{(t^{in}_{\omega_p})^2 + (t^{out}_{\omega_p})^2} = 2\beta|it_c t^*_{us}|. \tag{3.32}$$

Optomechanics with the probe mode

We focus here on the transmission amplitudes t_{us} and t_{ls}, which we obtain by applying the small modulation from Equation (3.28) to the cavity drive in Langevin equations (2.47) such that the intracavity field amplitude is:

$$\alpha_0 \to \alpha_0 + \alpha_- e^{-i\omega_p t} + \alpha_+ e^{+i\omega_p t}. \tag{3.33}$$

Similarly, the nanosphere motion $\hat{x}$ will be modified as:

$$\hat{x} \to \hat{x} + Xe^{-i\omega_p t} + X^* e^{i\omega_p t}. \tag{3.34}$$

Implementing the modulations in Equations (2.47), we obtain a system of equations for α_-, α_+ and X:

$$\begin{aligned} \left(\frac{\kappa}{2} - i(\Delta+\omega)\right)\alpha_- &= -i\frac{g}{x_{zpf}}X + \beta E_d \\ \left(\frac{\kappa}{2} + i(\Delta-\omega)\right)\alpha^*_+ &= i\frac{g}{x_{zpf}}X + \beta E_d \\ m(\Omega_x^2 - \omega^2 - i\gamma_m\omega)X &= -\frac{\hbar g}{x_{zpf}}(\alpha_- + \alpha^*_+). \end{aligned} \tag{3.35}$$

The solution for the upper sideband $t_{us}(\omega_p) \equiv \alpha_+/\beta E_d$ and the lower sideband $t_{ls}(\omega_p) \equiv \alpha_-/\beta E_d$ is:

$$\alpha_\pm = \beta E_d \frac{1 + if(\mp\omega_p)}{-i(\Delta \mp \omega_p) + \frac{\kappa}{2} + 2\Delta f(\mp\omega_p)}, \tag{3.36}$$

where $f(\omega) = g^2\chi_m(\omega)/(i(\Delta-\omega)+\kappa/2)$. These can then be used in Equation (3.31) to write the detected signal in terms of the transmitted probe modes.

Typically, the optomechanical cavity is either driven with only one sideband or the system is sideband resolved, thus including only the

upper sideband response. We operate the system in the weak sideband resolved regime ($\Delta \sim \kappa$), hence we have to take both probes into consideration. The discrepancy to the single probe approach is clearly seen in Figure 3.27, where a simple cavity response is overlaid with the OMIT response.

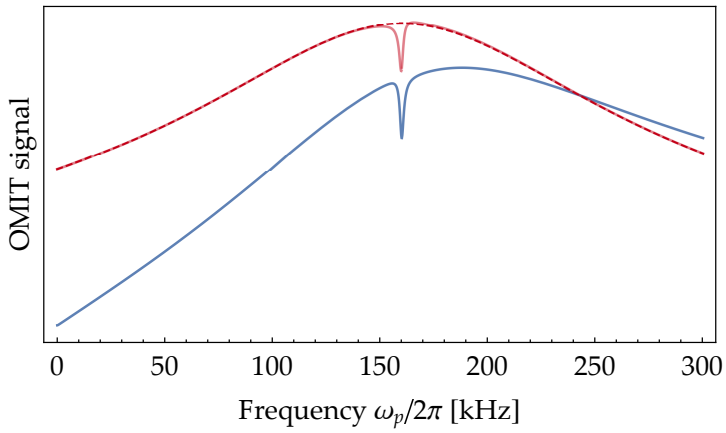

Figure 3.27: **Absolute signal of OMIT response with both lower and upper sideband accounted for (blue), compared to the case of taking only the upper sideband (red)**. We take the real experimental parameters ($\kappa/2\pi =$ 193 kHz, $\Omega_x/2\pi = 160$ kHz) and see that the lower sideband significantly impacts the OMIT amplitude response. Red dashed line shows the cavity transfer function $\propto \sqrt{\frac{(\kappa/2)^2}{(\kappa/2)^2+(\omega+\Delta)^2}}$.

3.4.2 *OMIT in experiment*

In order to improve the signal-to-noise ratio, we average the OMIT response for over 10 scans. This approach can lead to a broadening of the OMIT peak if the mechanical frequency is unstable during the averaging. However, the broadening doesn't influence the measured coupling, which we primarily extract from the total dip area. If we focus only on the upper sideband α_+ and assume a flat cavity response in the proximity of the dip $\omega_p \approx \Delta \approx \Omega_x$, the amplitude of the OMIT signal is (Equation (3.32)):

$$t^{amp}_{\omega_p} \propto |\alpha_+| \approx \left| 1 + i\frac{2G^2}{\kappa}\frac{\Omega_x}{\Omega_x^2 - \omega_p^2 - i\omega_p\gamma_m} \right|. \tag{3.37}$$

The integrated dip area over a sufficiently large frequency range around the dip $(\Omega_x - \delta\omega, \Omega_x + \delta\omega)$, $\delta\omega \gg \gamma_m$, yields:

$$\begin{aligned} \int_{\Omega_x-\delta\omega}^{\Omega_x+\delta\omega} t^{amp}_{\omega_p} d\omega_p &\propto \int_{\Omega_x-\delta\omega}^{\Omega_x+\delta\omega} \left(-\frac{2G^2}{\kappa}\frac{\Omega_x^2\gamma_m}{(\Omega_x^2-\omega_p^2)^2+\omega_p^2\gamma_m^2} \right) d\omega_p \\ &\approx -\frac{2G^2}{\kappa}. \end{aligned} \tag{3.38}$$

This confirms that the mechanical response to the probe mode is independent of the mechanical damping γ_m. However, the dip depth $t^{amp}_{\omega_{OMIT}}(\Omega_x) \propto 1 - \frac{2G^2}{\kappa\gamma_m}$ is a function of γ_m. Therefore, for different coupling rates the dip shape is changed but the total area remains the same. We demonstrate this in Figure 3.28 for three distinct cases of the coupling g and damping γ_m: $g = 2\pi \times 8$ kHz, $\gamma_m = 2\pi \times 10$ kHz (blue); $g = 2\pi \times 16$ kHz, $\gamma_m = 2\pi \times 10$ kHz (red) and $g = 2\pi \times 8$ kHz, $\gamma_m = 2\pi \times 5$ kHz (green).

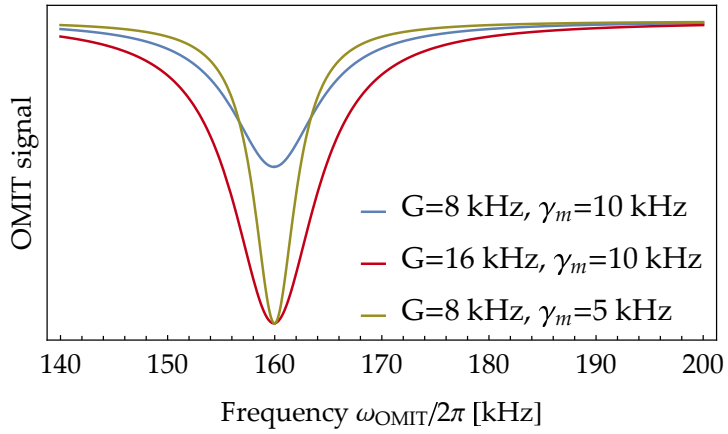

Figure 3.28: **OMIT dip feature for different total coupling rates g and mechanical dampings γ_m.** Note that a change of the mechanical damping without a modified coupling doesn't influence the total dip area (blue to green). On the other side, increasing the coupling rate extends the dip further down and increases the overall area (blue to red).

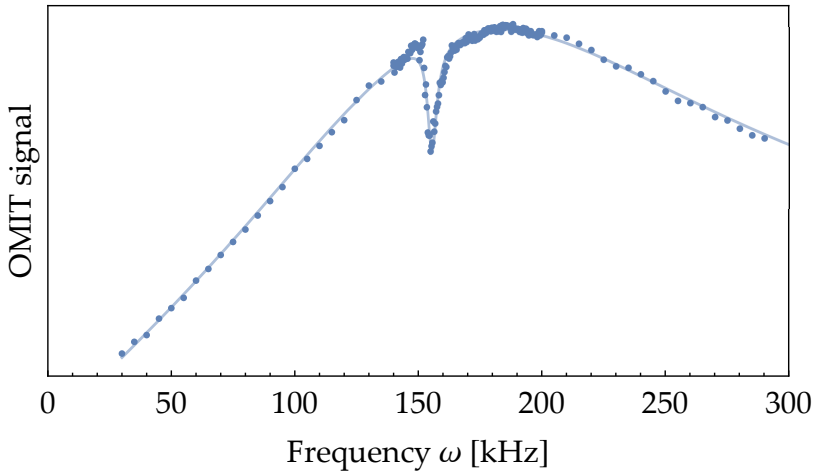

Figure 3.29: **An example of observed amplitude of OMIT response**. Due to an interaction of the nanosphere with the probe mode, dip is present at the mechanical frequency $\Omega_x = 2\pi \times 155.5$ kHz. We fit the dip feature jointly with the cavity response in order to extract the detuning Δ, the total optomechanical coupling g, the mechanical frequency Ω_x and the damping γ_m^{eff}. This measurement is taken at the pressure $p = 0.56$ mbar and used to extract the coupling rate $g = 2\pi \times 12.6$ kHz.

The network analyzer measures separately the in-phase and out-of-phase contributions, which we combine into the amplitude response $t_{\omega_p}^{amp}$, thus eliminating the dependence on the accumulated phase $\varphi(\omega_p)$. We remove the cavity decay rate κ from the fit as we know it exactly from independent measurements. From the fit of the amplitude response we obtain other optomechanical parameters: the control laser detuning Δ, the total coupling g, the mechanical frequency Ω_x and damping γ_m^{eff}. Although the effective damping γ_m^{eff} is a function of coupling g as well, we discard this dependence in the fit in favor of allowing for some linewidth broadening. An example of the detected OMIT response with the fitted theoretical function is shown in Figure 3.29. We will discuss more about OMIT in Chapter 4, where we regularly use it to obtain the coupling rate and calculate the optomechanical cooperativity.

3.5 TRAPPING OF NANOSPHERES

The silica nanospheres used for the experiments described in this thesis are all part of the same batch (Microparticles GmbH) with a nominal radius $r = (71.5 \pm 2)$ nm, density $\rho = 1850$ kg/m^3 and a refractive index $n_s = \sqrt{\varepsilon_s} = 1.449$ (value based on amorphous silica). They arrive suspended in a $p = 5$ wt.% (percentage of weight) aqueous solution. We mix a 5 μl sample of this solution with 5 ml of isopropanol ($\rho_{\text{IPA}} = 786$ kg/m^3, Sigma-Aldrich). Out of the 5 μl sample, the total volume occupied by the silica nanospheres is:

$$V_{sam} = \frac{\rho_{water} \times 5 \times 10^{-9}\text{m}^3}{\frac{1-0.01\times p}{0.01p}\rho + \rho_{water}} \approx 1.383 \times 10^{-10}\ \text{m}^3, \tag{3.39}$$

while the remaining volume $V_{rest} \approx 4.86 \times 10^{-9}$ m^3 contains only water. In order to get the nanospheres airborne, we spray this solution for a short time using a nebulizer[13], which sprays droplets with radius $r_{drop} = 2.1$ μm and volume $V_{drop} = \frac{4}{3}\pi r_{drop}^3$[7]. Each droplet contains $n_{per-drop}$ nanospheres of volume $V = \frac{4}{3}\pi r^3$ and mass $m = \rho V$ on average:

$$n_{per-drop} = \frac{V_{sam}}{V}\frac{V_{drop}}{5 \times 10^{-6}\ \text{m}^3} \approx 0.7, \tag{3.40}$$

thus we suppose that only single nanospheres will be trapped, with possible events of trapping only droplets of isopropanol or water, which have similar refractive indices. We don't observe an agglomerate of two or more nanospheres.

The nebulizer is placed within a self-constructed container which is connected to the vacuum chamber by a long ($\sim$ 0.5 m) tube with an inner diameter of 6 mm. Flow through the tube is controlled by a manual valve at its end, which we open for about half a second

[7] *In fact, r_{drop} is the median value of the droplets mass distribution, given as a droplet radius ("Mass Median Aerodynamic Diameter"). Note that this just provides a rough estimate of the nanosphere concentration.*

[13] Omron MicroAIR U22

a couple of times in succession to let the nanospheres through. The vacuum chamber is previously pumped down to about 1 mbar, after which pumping is stopped. After opening the valve leading to the nebulizer container several times, the pressure increases to well above 100 mbar. The correct value is unknown as the pressure gauge is not accurate in the high pressure regime and with liquid contamination in the chamber. We expect that the majority of the droplets evaporates over the path from the nebulizer container to the vacuum chamber. The remaining objects are free to diffuse in the vacuum chamber until one gets trapped with the help of the friction of the surrounding gas.

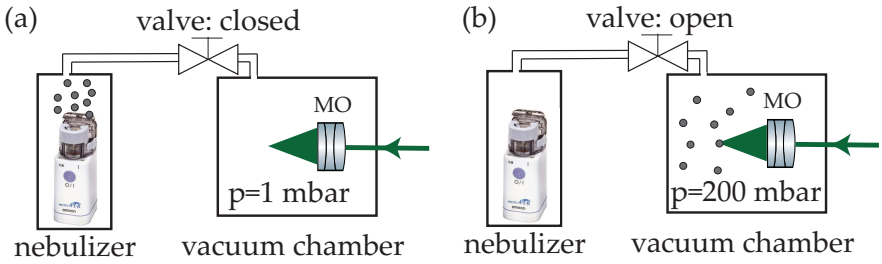

Figure 3.30: **Trapping of a nanosphere.** (a) We use a nebulizer to spray the nanospheres in a separate container at room pressure, while the vacuum chamber is kept at $\sim$ 1 mbar. (b) We open the manual valve for half a second to allow the nanospheres to be sucked into the vacuum chamber. We repeat the procedure for up to 5 times, after which the pressure gauge shows about 200 mbar. At this pressure the gas friction is strong enough to slow down the nanospheres until eventually a single nanosphere is trapped in the focused laser beam.

The droplets and nanospheres moving in the chamber pose a danger to the cavity finesse as they could contaminate the cavity mirrors. Small objects such as nanospheres are hard to clean off the mirror surface with the typical methods (acetone, FirstContact etc.). Therefore, we do not want the cavity in the vacuum chamber during the loading process. Hence we have constructed a cavity holder which is easy to remove and to put back by sliding it in and out of a massive aluminum holder. The cavity holder design has been described in Section 3.1.2.

The nanosphere solutions are stable for a couple of days, during which we see repeatable loading into the trap within a minute from the initial spraying. After a couple of days, we mostly see events of trapping an "empty" isopropanol droplet. We assume this is caused by agglomeration of nanospheres in the solution, which might result in an unstable trap due to a stronger scattering force for larger particles (see Section 3.1.1).

Material	ρ $\left[\frac{\text{kg}}{\text{m}^3}\right]$	n/ε
Silica	1850[14]	1.449[15]/2.1
Water	1000	1.326[16]/1.758
Isopropanol	786[17]	1.37[18]/1.877

Table 1: Table of most important properties of the three materials present in solution used in spraying.

All three components in the solution (silica nanospheres, water, isopropanol: properties listed in Table 1) might be present in the initially caught object. We assume that the trapped object will be either a spherical particle or a droplet, which assumes a spherical shape due to surface tension. We aim to compare all trapped objects to a case when we levitate a single nanosphere, which we confirm from the mass measurement using the optomechanical cavity in Section 3.3.2. Using this method, we have observed that only pure silica nanospheres remain trapped at typical minimum prepump pressure of $p = 4 \times 10^{-2}$ mbar. Any remaining liquid (trapped with the nanosphere) has evaporated under these vacuum conditions, hence it is beneficial to decrease pressure in the vacuum chamber immediately after trapping an object. In the region from 10^{-1} to 0.5 mbar we sometimes see a sudden decrease in the mechanical frequency and power of the scattered light, which we attribute to a loss of liquid components from the object. This effect occurs only once and is irreversible when cycling the pressure. After this "calibration" of our measurements, we are able to analyze all further objects by observing some or all of the following quantities:

1. **Absolute measurement of mass.** The mass of the trapped object will be a sum of the masses of the individual constituents:

$$m_t = m + \rho_{\text{IPA}} V_{\text{IPA}} + \rho_{H_2O} V_{H_2O}. \tag{3.41}$$

Through a measurement of the linear and quadratic coupling to the cavity locking mode (Section 3.3.2) we are able to determine the mass of the trapped object. By repeating the same measurement at different pressures, we might follow the evolution of the object's mass by decreasing the pressure in steps, until we are left with a silica nanosphere or nothing. The calculated mass of a single nanosphere was shown to be as expected, so from this point on we use the specified mass:

$$m = 2.83 \times 10^{-18} \text{ kg}.$$

[14] Density of amorphous silica as specified by the producer
[15] Optical constants of silica
[16] Optical constants of water
[17] Chemical properties of isopropanol
[18] Optical constants of isopropanol

2. **Mechanical frequency.** The mechanical frequency of the levitated object originates from the harmonic approximation to the dipole interaction potential energy:

$$\frac{m\Omega_t^2 x^2}{2} = -\frac{1}{2}\alpha \left.\frac{\partial^2 |E(x)|^2}{\partial x^2}\right|_{x_0} x^2,$$

which shows its dependence on the object's mass m and polarizability α, i.e. its index of refraction. So far we have only discussed a case of a polarizable object of a uniform index of refraction ($\alpha = \varepsilon_0 V \chi$). However, a case of a core-shell nanosphere system can be solved analytically to give the polarizability of a composite object [van de Hulst, 1957]:

$$\alpha_t(q, \varepsilon_{sh}) = 3\varepsilon_0 V \frac{\varepsilon_{sh} - 1}{\varepsilon_{sh} + 2} \frac{1 + q^3 \frac{2\varepsilon_{sh}+1}{\varepsilon_{sh}-1}\frac{\varepsilon_s - \varepsilon_{sh}}{\varepsilon_s + 2\varepsilon_{sh}}}{1 + q^3 \frac{2\varepsilon_{sh}-2}{\varepsilon_{sh}+2}\frac{\varepsilon_s - \varepsilon_{sh}}{\varepsilon_s + 2\varepsilon_{sh}}}, \tag{3.42}$$

where $q = \frac{r}{r_t}$ and ε_{sh} are the ratio of the object's radius to the silica nanosphere radius and the relative permittivity of the shell material, respectively (Figure 3.31). Therefore, the mechanical frequency of the trapped object compared to the fundamental mechanical frequency of a silica nanosphere is:

$$\frac{\Omega^t_{x,y,z}}{\Omega_{x,y,z}} = \sqrt{\frac{\alpha_t}{\alpha}\frac{m}{m_t}}. \tag{3.43}$$

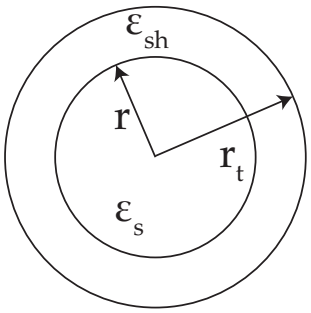

Figure 3.31: **Silica nanosphere with a liquid shell.** The nanosphere of radius r and dielectric permitivitty ε_s is enveloped in a liquid shell with dielectric permitivitty ε_{sh}, resulting in a object with a radius r_t.

We distinguish between two special cases:

- $q = 1$: object is a silica nanosphere with typical mechanical frequencies[8] $\left(\Omega_z, \Omega_x, \Omega_y\right)/2\pi \approx (60, 262, 290)$ kHz.
- $q = 0$: object is a droplet of IPA or water with polarizability $\alpha_{drop} = 3\varepsilon_0 V \chi_{\mathrm{IPA}/H_2O}$. Trap frequencies of an IPA and water droplet are expected to be $\left(\Omega_z^{IPA}, \Omega_x^{IPA}, \Omega_y^{IPA}\right)/2\pi \approx (85, 372, 411)$ kHz and $\left(\Omega_z^{w}, \Omega_x^{w}, \Omega_y^{w}\right)/2\pi \approx (71, 309, 342)$

[8] *The optical power used for trapping was larger for these measurements*

kHz, respectively. The mechanical frequency is significantly increased due to the droplet's density being larger than the density of silica.

Any object with $0 < q < 1$ will have frequencies in between these two extreme cases.

3. **Scattered light intensity.** We detect the nanosphere motion from the transmitted trapping laser (see Section 3.2), where the detector current is proportional to the electric field of the forward scattered light:

$$i(t) \propto E_{scatt} E_{tw} \cdot z(t) \propto \alpha_t z(t). \tag{3.44}$$

Therefore, the power spectrum of the detector signal is a function of both the object's polarizability α_t and the mass m_t:

$$S_{ii}(\omega) \propto \alpha_t^2 \frac{k_B T}{m_t \Omega_z^2}. \tag{3.45}$$

From the Breit-Winger fit (Equation (3.17)) to the spectrum of the direct detection we obtain a single proportionality constant:

$$a_t \propto \frac{\alpha_t^2}{m_t}. \tag{3.46}$$

Note that this is essentially a different dependence from Equation (3.43), so by combining the two we are able to extract the object's mass and the polarizability. For an object made of only one material, the relation in Equation (3.46) simplifies to $a_t \propto \chi^2 V/\rho$.

4. **Mechanical damping.** Gas damping is simplified to $\gamma_m \propto r^2/m$ for pressures below 10 mbar, as seen from Equation (2.33). As the pressure gauge might give inaccurate values by up to 30%, the measurement of the gas damping is not as accurate as other measurements.

We now discuss how we determine the composition of the trapped object. There are three possible cases of what we trap initially: a silica nanosphere, a droplet of isopropanol or water, or a nanosphere with a liquid shell around it. Droplets evaporate in moderate vacuum conditions, while liquid shells remain almost until we reach the pre-pump pressure. Regardless of initially trapping a nanosphere with or without a shell, only a silica nanosphere can remain in high vacuum.

3.5.1 *Single silica nanosphere*

We have described a measurement of the mass and radius of a single silica nanosphere extensively in Section 3.3.2. Note that we have actually characterized several nanospheres so far and have calculated

radii in the range of $71 - 72$ nm. Hence, we decide to compare all trapped objects to a nanosphere with a nominal radius of $r = 71.5$ nm.

3.5.2 *Liquid trapped object*

For simplicity, let's assume we have trapped an object which contains only isopropanol and forms a nanosphere of radius r_{IPA}. As in the case of silica nanospheres, the mechanical frequencies will depend on density, but not on radius. Hence we can compare the two frequencies easily:

$$\frac{\Omega_{x,y,z}^{\mathrm{IPA}}}{\Omega_{x,y,z}} = \sqrt{\frac{\rho}{\rho_{\mathrm{IPA}}}\frac{\chi_{\mathrm{IPA}}}{\chi}}, \tag{3.47}$$

where $\chi_{\mathrm{IPA}} = 3\frac{\varepsilon_{\mathrm{IPA}}-1}{\varepsilon_{\mathrm{IPA}}+2}$. In case of isopropanol (water) we get that the mechanical frequencies will be higher by a factor of 1.42 (1.18). Droplets evaporate as we decrease the pressure, therefore we can already distinguish between silica nanospheres and liquid objects. Large frequency difference for the two liquids allows us to additionally distinguish between an isopropanol an a water droplet.

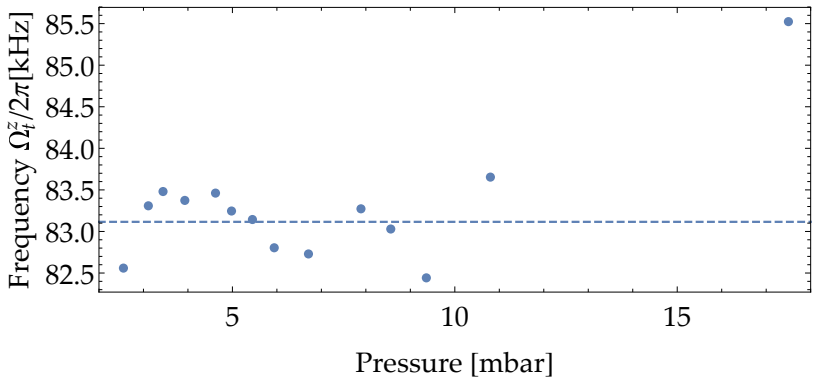

Figure 3.32: **Mechanical frequency Ω_z^t of a trapped object as a function of pressure.** We extract the mechanical frequency of the z-motion from the spectrum of the nanosphere motion as we decrease the pressure from 17 mbar to around 2.5 mbar, at which point the object is lost. With an exception of the outlier at the highest pressure, all other points are around the average frequency (dashed line). As the frequency directly depends on the object's density, we conclude that the trapped object was made of a single liquid constituent.

The measurements of the trapped objects were conducted over the course of a couple of days, during which the trapping intensity does not significantly change and we can therefore compare the object's frequency to the frequency of a silica nanosphere.

Figure 3.32 shows a frequency measurement on a trapped IPA droplet. The average axial mechanical frequency $\Omega_z^t/2\pi = 83.2$ kHz from our measurement in Figure 3.32 fits well to the expected trap frequency of an isopropanol droplet of $\Omega_z^{\mathrm{IPA}}/2\pi = 85$ kHz. Assuming

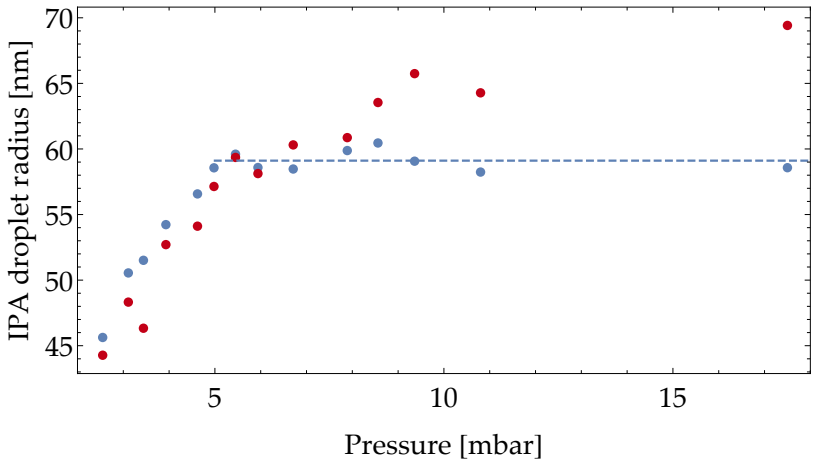

Figure 3.33: **IPA Droplet radius evaluated from the intensity of the scattered light (blue) and the mechanical damping (red).** Data obtained in former manner is overlaid with data measured in latter approach in such a way that values are overlapping in the lower pressure regime, where pressure measurements and spectral fits are more trustworthy. Dashed line is an average of 8 data points at pressures $p > 5$ mbar, before the IPA droplet starts to decrease in size.

a material density equal to isopropanol, we can extract the droplet's radius in two ways (Figure 3.33). First we use the gas damping to calculate the nanosphere radius (red dots), which shows a constant drop in radius as we decrease the pressure. A second measurement is using the scattered light intensity (blue dots), i.e. the variance of the object z-motion deduced from the trapping laser, which shows that the radius is stable at all pressures $p > 5$ mbar. Below this pressure both measurements exhibit the same behavior, hence we calibrate r_t using the former measurement in such a way to obtain a perfect overlap. This procedure is repeated for all observed droplets and results in approximately the same calibration constant. A discrepancy between the two methods appears above ~ 8 mbar, which we attribute to an imperfect fitting of a Lorentzian function to a spectral peak with large mechanical damping. The droplet's initial radius $r_t = 59$ nm is obtained as an average radius at the higher pressures, based on the estimate from the light scattering. The droplet's radius just before the complete evaporation was ~ 45 nm.

3.5.3 *Silica nanosphere with a liquid shell*

Occasionally we trap an object with mechanical frequency less than 10 % higher than the frequency of a sole silica nanosphere, which cannot be explained by trapping a droplet. We observe that the object's frequency drops instantaneously during the pumping process around 10^{-1} mbar. After this singular event the object's frequency stays constant and is equal to the typical nanosphere frequency. Therefore, we

argue that the initial object was a silica nanosphere with an additional liquid shell. To demonstrate a loss of material, we record a spectrum of the object's z-motion before and after the pumping process, both roughly at $p \approx 10$ mbar (Figure 3.34).

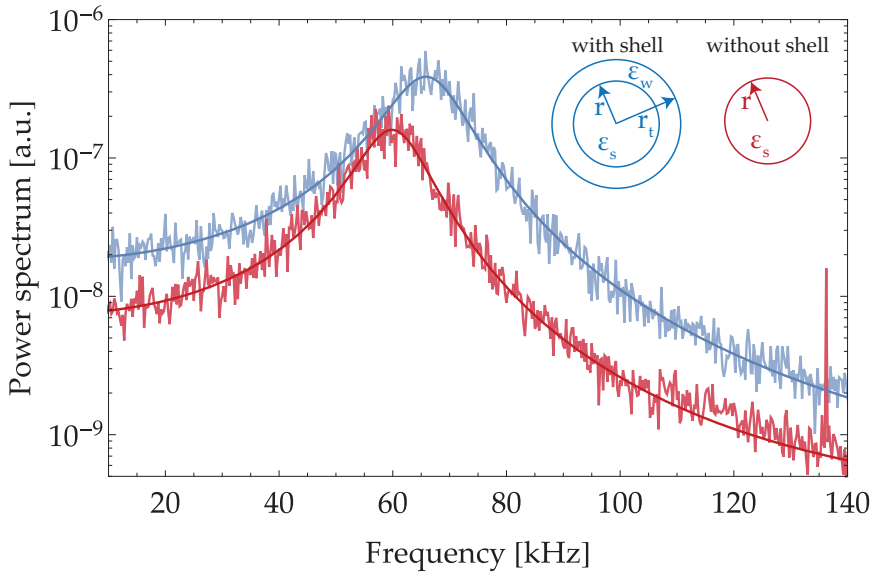

Figure 3.34: **Power spectra of the nanosphere motion before (blue) and after the evaporation of the water shell (red) at $p \approx 10^{-1}$ mbar.** The spectra were taken at equal pressures $p \sim 10$ mbar. The mechanical frequency clearly demonstrates that the object's average density increased after the evaporation. As the resulting object is confirmed to be a silica nanosphere, the shell material then must have a density smaller than the density of silica. The spectral peak decreases due to a large drop in the scattered power (coming from the smaller polarizability of a silica nanosphere). Inset: Here we show the object of radius r_t before the evaporation of the water shell (blue) and the remaining silica nanosphere with radius r (red).

In order to check whether we indeed trap a composite nanosphere-liquid object, we combine the relations from Equation (3.43) and Equation (3.46) to obtain the mass m_t of the initially trapped object:

$$\frac{m_t}{m} = \frac{a_t}{a}\left(\frac{\Omega_z}{\Omega_z^t}\right)^4 \approx 2.25, \tag{3.48}$$

where m is the mass of a silica nanosphere. Following this result we calculate the object's radius, assuming either an isopropanol or a water shell:

$$r_t^{\mathrm{IPA}} = \sqrt[3]{r^3 + \frac{3}{4\pi}\frac{m_t - m}{\rho_{\mathrm{IPA}}}} \approx 112.9\ \mathrm{nm}, \quad r_t^{H_2O} \approx 106.5\mathrm{nm}. \tag{3.49}$$

It is hard to conclude what the material is based just on this calculation. A more extensive method includes calculating the radius from

Equation (3.43) and Equation (3.46) separately and obtaining two different values of r_t. As shown in Table 2, the radii obtained in the three different ways are clearly more consistent with the case of a water shell. Therefore, we conclude that the initial object was a nanosphere with a water shell with a thickness of around 30 nm. This also makes sense as nanospheres arrive suspended in an aqueous solution, such that water sticks to the nanosphere surface layer even before we mix them with isopropanol [Costa et al., 2003].

Material	r_t from (i) [nm]	r_t from (ii) [nm]	r_t from (iii) [nm]
Water	104.2(3)	106.0	106.5(3)
IPA	83.8(2)	97.9	112.9(3)

Table 2: Radii of the trapped object assuming either a water or an isopropanol shell, as determined from (i) frequency change, (ii) variance change and (iii) change in mass calculated by combining (i) and (ii). More consistent values are obtained in the case of a water shell.

In conclusion, we observed several cases in which we trapped isopropanol droplets and none where we trap water. We explain this by the fact that water is chemically bonded with silica through silanol groups, which are stable at high pressures and room temperature [Costa et al., 2003]. All droplets start to evaporate at $p \approx 5$ mbar and are fully gone before reaching $p \approx 2$ mbar, although the vapor pressure of isopropanol at room temperature is $p_{\mathrm{IPA}} \approx 50$ mbar[19]. The question of isopropanol evaporation at such low pressures might be resolved by continuously following the droplet's dynamics and including the cavity for a periodic measurement of the droplet's mass. On the other hand, we occasionally trap silica nanospheres with a shell, which evaporates at a slightly lower pressure $\sim 10^{-1}$ mbar. From two separate measurements we deduce that the material composition matches water, which again fits to the hydrophilic property of the silica nanospheres.

Due to the weak trapping potentials and detection methods which require strong light scattering by the object, the condensation and evaporation of single aerosol droplets was investigated so far only for microparticles with radii $r > 0.5$ μm [Knox, 2011, Rothfuss et al., 2018], while studies on nucleation were conducted on a cloud of nanoparticles with radii ~ 10 nm [Pichelstorfer et al., 2018]. Here we presented methods to follow the aerosol dynamics in the intermediate region of radii 30-110 nm, which might be useful in aerosol physics, particularly to determine the accommodation coefficients of the liquids under examination.

[19] CRC Handbook of Chemistry and Physics 44th ed.

4

CAVITY OPTOMECHANICS IN HIGH VACUUM

In Chapter 2 we defined quantum optomechanical cooperativity as $C = \frac{4g^2}{\kappa\Gamma}$, where g is the coupling of the nanosphere motion to a cavity mode, κ is the cavity decay rate and Γ is the heating of the nanosphere motion. Cooperativity is a single parameter describing the system's capacity to enter the quantum regime of light-matter interaction, e.g. Equation (2.69) shows that the minimum phonon occupation is $\bar{n} = (\kappa/4\Omega_x)^2 + C^{-1}$. In our previous work on the cavity cooling of particles we were trapping particles with the locking cavity mode [Kiesel et al., 2013]. There, the cooperativity $C \approx 10^{-7}$ was mostly limited by the particle loss at modest vacuum pressures $p \approx 1$ mbar. Still, the coupling rates were sufficiently strong to expect strong cooperativity $C > 1$ at pressures below 10^{-7} mbar.

In the current setup a stable trap is realized in an optical tweezer, which limits the cooperativity by recoil heating of the trapping laser. We characterize the setup fully by measuring the total coupling to the control mode from OMIT and the heating rate through relaxation measurements. Furthermore, we discuss the setup limitations and possible improvements by the level of complexity. The work presented in this chapter is also part of our recent paper "Levitated cavity optomechanics in high vacuum" [Delić et al., 2019a].

Contents

4.1 OPTOMECHANICAL COUPLING RATE g

We extract the total coupling g of the axial nanosphere motion to the control cavity mode from the OMIT signal. The response of the optomechanical system depends on the effective mechanical frequency Ω_x^{eff} and damping γ_m^{eff}, as well as the cavity decay rate κ and the control laser detuning Δ. As shown in Section 3.4.1, the size of the transparency window depends only on the coupling $\propto g^2$, while the width of the transparency window is the effective damping $\gamma_m^{\text{eff}} = \gamma_m + \Gamma_{opt}$, where $\Gamma_{opt} \approx 4g^2/\kappa$ in the case of a sideband resolved regime. In reality, fitting of the full response in the OMIT measurement is demanding as there is a multitude of fit parameters. Therefore, we fix the value of the cavity decay rate $\kappa = 2\pi \times 193$ kHz (determined in Section 3.1.2) and we fit the frequency $\Omega_x = \Omega_x^{\text{eff}}$ and damping $\gamma_m = \gamma_m^{\text{eff}}$ as constants, i.e. independent of other parameters. We examine the mechanical damping in Section 4.1.1.

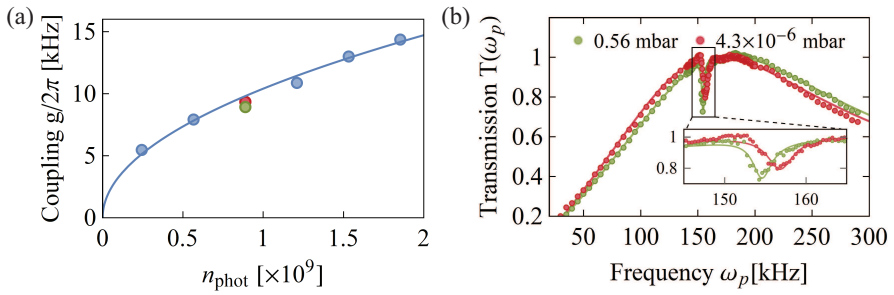

Figure 4.1: **Optomechanical coupling extracted from OMIT measurements.** (a) Total linear coupling $g = g_0\sqrt{n_{\text{phot}}}$ as a function of the intracavity photon number n_{phot} of the control laser at the pressure $p = 0.56$ mbar (blue and green points). The coupling at $p = 4.3 \times 10^{-6}$ mbar (red point) is comparable to achieved coupling at higher pressures, demonstrating reproducible alignment over several orders of magnitude in pressure. (b) We calculate coupling from the measurements of the optomechanically induced transparency (OMIT). Shown here are two measurements at the pressures of $p = 0.56$ mbar (green) and $p = 4.3 \times 10^{-6}$ mbar (red) executed for equal intracavity photon number $n_{\text{phot}} = 0.9 \times 10^9$. We drive the cavity with the control laser with a fixed detuning Δ and two sidebands with relative detuning $\pm\omega_p$ with respect to the control laser. Response at broad frequencies is given by the cavity transmission shape as a function of the cavity decay rate κ and Δ, where both drive sidebands have to be taken into account. A dip is present at $\omega_p = \Omega_x \approx 2\pi \times 155$ kHz due to a destructive interference between the nanosphere motion and the drive sidebands. Inset: The mechanical dip is shown in greater detail. We extract the total coupling g from the dip area.

We characterize the total coupling by taking OMIT signals for different intracavity photon numbers at high pressure $p = 0.56$ mbar (Figure 4.1). The intracavity photon number n_{phot} was calculated from the optical power leaking from the cavity, accounting for all transmission coefficients. The solid line is a function $g = g_0\sqrt{n_{\text{phot}}}$,

where we assume a single photon coupling $g_0/2\pi = 0.3$ Hz. The nanosphere motion is stable at this pressure and feedback cooling was not employed. Three-dimensional feedback cooling is turned on at the prepump pressure $p = 4 \times 10^{-2}$ mbar, before pumping the vacuum chamber into high vacuum.

In high vacuum we repeat the OMIT measurement for a photon number $n_{\text{phot}} = 0.9 \times 10^9$. The nanosphere position along the cavity standing wave changes during the pumping process. We optimize the linear coupling to the cavity control mode once the pressure has stabilized in high vacuum. We subsequently turn off the feedback cooling along the x-axis as the motion is stabilized by the cavity cooling. However, the feedback cooling is still needed to stabilize the nanosphere motion along the y- and z-axis. The measured coupling rate $g = 2\pi \times 9.6$ kHz is equal to the value obtained at higher pressure, demonstrating a repeatable coupling over many orders of magnitude in pressure. We compare the OMIT signals for the same photon number n_{phot} at two different pressures in Figure 4.1(b). The inset focuses on the transparency window. The linewidth of the feature is larger at the lower pressure, probably due to a fluctuation of the mechanical frequency. However, the total area remains approximately the same, as the area is a function of the coupling rate and not the damping (Section 3.4.1).

4.1.1 *Mechanical damping*

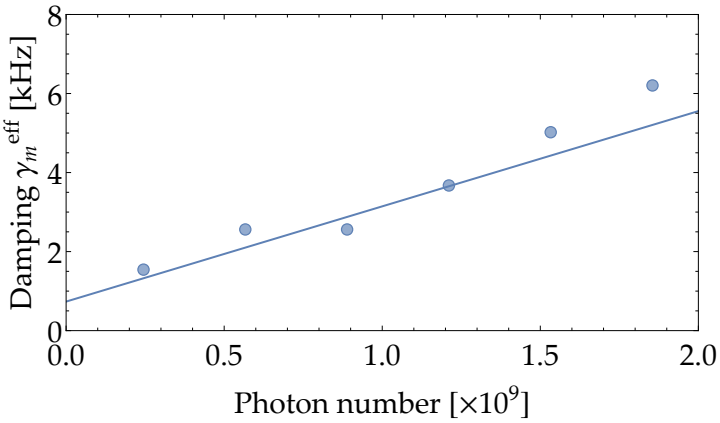

Figure 4.2: **Effective damping γ_m^{eff} obtained from the OMIT measurements at a pressure $p = 0.56$ mbar as a function of the intracavity photon number n_{phot}.** The line is a theoretical estimate based on the gas damping γ_m at this pressure, the cavity decay rate κ and the single photon coupling g_0.

Although we fit the mechanical damping γ_m^{eff} in the OMIT as a constant, we expect it to depend on the coupling g as $\gamma_m^{\text{eff}} \approx \gamma_m + 4g^2/\kappa$. Assuming a gas damping rate of $\gamma_m = 2\pi \times 0.73$ kHz at $p = 0.56$ mbar and the single photon coupling $g_0 = 2\pi \times 0.3$ Hz, the measured damping matches the theory well (Figure 4.2).

4.2 HEATING RATE Γ

In a deep sideband resolution limit $\kappa \ll \Omega_x$, the occupation of the mechanical oscillator is given by the balance of the cooling rate Γ_{opt} and the heating by the environment Γ. The heating rate Γ consists of two distinct heating mechanisms: the heating by gas collisions $\Gamma_m = \gamma_m n_{th}$ and recoil heating Γ_{rec}, which is further split into the different sources of recoil heating, e.g. the tweezer laser and the control cavity mode:

$$\Gamma = \gamma_m n_{th} + \Gamma_{rec}^{tw} + \Gamma_{rec}^{cav}. \tag{4.1}$$

The gas induced heating is the dominant heating rate at pressures $p > 10^{-7}$ mbar. Below this pressure recoil heating from the tweezer laser will become the leading contribution. Recoil heating due to the cavity mode can always be neglected, as mentioned in Section 2.3.1.

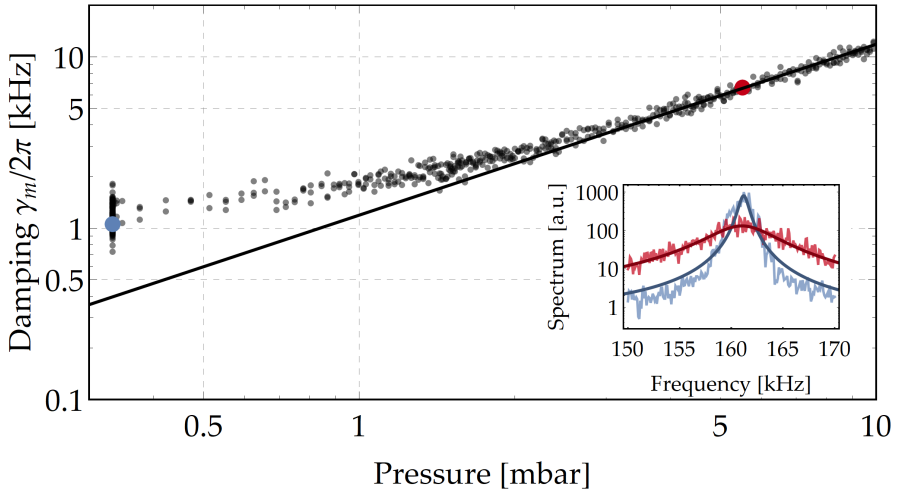

Figure 4.3: **Incorrect mechanical damping due to the broadening of the spectral peak.** We continuously acquire spectra of the nanosphere motion as we increase the pressure from 0.3 mbar to 10 mbar. We fit a Breit-Wigner function to the spectrum and extract the mechanical damping. At pressures $p < 2$ mbar we observe a broadening of the spectral line, which gives a higher value than expected. The solid line is a theoretical curve for a nanosphere with nominal radius and density. Inset: We compare the spectrum of the x-motion at $p \approx 5$ mbar (red) to the spectrum at $p \approx 0.3$ mbar (blue), where the extracted mechanical dampings are marked in the main part of the figure with their respective colors. The fit at the lower pressure is clearly not following the data as well as the fit at the higher pressure.

At pressures $p \geq 2$ mbar we estimate the heating rate from a Breit-Wigner fit to the spectrum of the nanosphere motion, from which we extract the damping γ_m. We assume that the nanosphere motion is in equilibrium with the environment, such that the thermal occupation $n_{th} = k_B T_0/(\hbar\Omega_x) \approx 3.8 \times 10^7$ is given by the room temperature $T_0 \approx 293$ K. The mechanical frequency changes significantly during a single measurement, which is manifested by an inhomo-

geneous broadening of the spectral peak at pressures $p \leq 2$ mbar. Therefore, the fit gives a higher value for mechanical damping than expected (Figure 4.3), which leads to an overestimate of the heating rate. One possible solution would be to obtain time traces instead of spectra, which can be used to eliminate the impact of the mechanical frequency in post-processing. The solution we pursue here is to measure the heating rate by relaxation measurements.

The energy of the nanosphere motion is initially decreased with feedback cooling. We switch the feedback off and monitor the variance of its motion over time [Jain et al., 2016]. A single evolution is not enough to detect an overall, monotonous increase of the variance as this is a stochastic process. Therefore, repeat the measurement and conduct an ensemble average of the calculated variances. During the relaxation process, the averaged energy increases exponentially in time:

$$\langle E \rangle = E_{eq} + (E_{cool} - E_{eq})\mathrm{e}^{-\gamma t}, \tag{4.2}$$

where E_{eq} and E_{cool} are the energy in an equilibrium with the environment and the energy of the cooled nanosphere, respectively, and $\langle \cdot \rangle$ denotes the ensemble average. The rate γ is the total coupling to the environment, dominated by gas damping γ_m and radiation damping γ_{rad} [Novotny, 2017]. During the ring-down time (feedback cooling is switched on), the energy evolves as:

$$\langle E \rangle = E_{cool} + (E_{eq} - E_{cool})\mathrm{e}^{-(\gamma+\gamma_{fb})t}, \tag{4.3}$$

where γ_{fb} is the damping added by the feedback cooling.

At pressures between 4×10^{-2} mbar and 2 mbar it takes $t \sim 1/\gamma_m <$ 10 ms for the nanosphere motion to fully relax. From the fit of Equation (4.2) to the calculated ensemble average we obtain the mechanical damping γ_m (Figure 4.4(b)). At lower pressures we need to cool the nanosphere motion to keep it trapped, therefore we cannot allow for a full relaxation. However, on short time scales the energy increases linearly (Figure 4.4(c)):

$$\langle E \rangle = E_{cool} + (E_{eq} - E_{cool})\gamma t \approx E_{cool} + E_{eq}\gamma t, \tag{4.4}$$

where we assumed that the motion is initially strongly cooled $E_{eq} \gg E_{cool}$. The steady state energy of the uncooled nanosphere motion is given as the ratio of the heating and the cooling rate $\frac{E_\infty}{\hbar\Omega_x} = \frac{\Gamma}{\gamma}$, such that the linear evolution provides us directly with the heating rate:

$$\langle E \rangle = E_{cool} + \hbar\Omega_x \Gamma t. \tag{4.5}$$

The heating rate along all three motional axes as a function of pressure is shown in Figure 4.4(a). The circles and diamonds show the heating rate obtained in the absence of the cavity from relaxation and spectral measurements, respectively. The minimum heating rate is $\Gamma = 2\pi \times 28$ kHz, which was measured at a pressure

$p = 4 \times 10^{-7}$ mbar. The two crosses denote measurements in the presence of the control cavity mode at $p = 4.3 \times 10^{-6}$ mbar, right after the OMIT measurement. The control mode detuning was set to zero in order to eliminate the phase noise heating, while the intracavity photon number was set to $n_{\mathrm{phot}} = 0.9 \times 10^9$ again. The heating rate in this case is $\Gamma = 2\pi \times 175$ kHz, which we will use to calculate the optomechanical cooperativity. All heating rates can be explained just by the collisions with the gas (red shaded area).

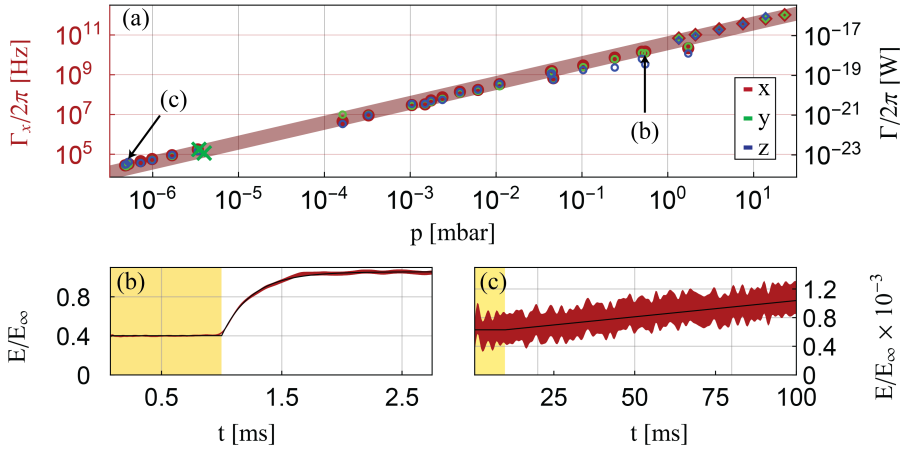

Figure 4.4: **Heating rate Γ at different pressures.** a): Mechanical losses $\Gamma_x/2\pi$ of a levitated particle motion along the cavity axis (x) as a function of pressure (red symbols). We measure the mechanical losses either via energy relaxation (circles and dots) at low pressures or via a spectral method (diamonds) at higher pressures. Note that the axis $\Gamma/2\pi$ in units of $[W]$ applies for all spatial directions compared to the $\Gamma_x/2\pi$ axis. The red shaded area is a theory curve accounting for the uncertainties during the measurement for the x-direction. The two crosses mark relaxation measurements while the particle motion was coupled to the cavity. b) and c): Energy relaxation measurement: The particle is prepared in a low energy state with feedback cooling (yellow shaded area). After switching feedback cooling off, the particle relaxes towards thermal equilibrium. At a pressure of $p \approx 0.5$ mbar (b), the full relaxation to thermal equilibrium is observed, while for lower pressures, i.e. $p = 4 \times 10^{-7}$ mbar (c) only the linear part of the relaxation can be observed.

4.3 OPTOMECHANICAL COOPERATIVITY

We measured the total coupling $g = 2\pi \times 9.6$ kHz and the heating rate $\Gamma = 2\pi \times 175$ kHz at a pressure of $p = 4.3 \times 10^{-6}$ mbar. This leads to optomechanical cooperativity of $C \approx 0.01$. In the following we will discuss the current limitations to the cooperativity and provide ideas on how to increase it to the strong cooperativity regime $C > 1$.

4.3.1 *Co-trapping with the tweezer and the cavity standing wave*

The cavity mode provides a restoring force for the nanosphere, which for large n_{phot} is comparable to the trapping force of the tweezer. As a consequence, the nanosphere position along the cavity axis was optimized after every change of the control laser power in the OMIT measurements in Section 4.1. The principle behind the optimization is presented in Figure 4.5. The nanosphere is trapped in a combination of the potentials created by the control and the trapping laser. We consider here only the influence of the cavity potential along the cavity axis, as the restoring force along the cavity transverse axes is significantly smaller due to the large cavity waist ($w_0 = 41.1\ \mu$m). The cavity standing wave potential moves the nanosphere away from the largest intensity gradient (optimal position for linear interaction with the cavity mode) towards the intensity maximum of the standing wave (Figure 4.5, left panel). The optimization works only until the tweezer restoring force is comparable to the restoring force of the cavity standing wave. In the following text we estimate the maximum attainable total coupling based on the given trapping potential. We first model the full trap potential and calculate the equilibrium trap position.

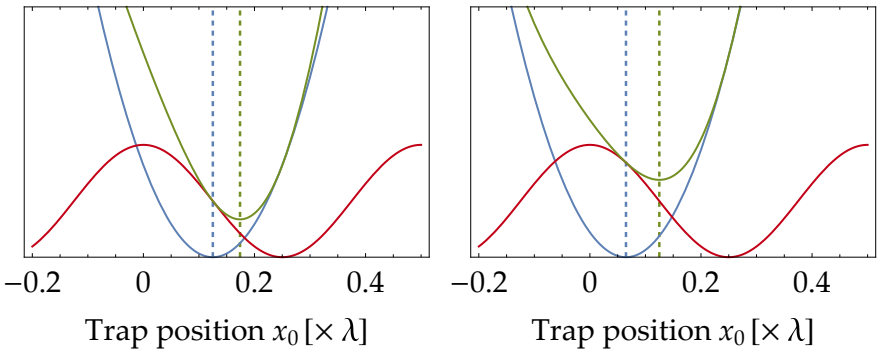

Figure 4.5: **Positioning the nanosphere to optimize the linear coupling to the cavity mode.** Shown are optical trapping potentials of the tweezer (blue, solid) and the cavity control mode (red, solid) together with the joint potential (green, solid). Adding a strong cavity control mode influences the intended nanosphere trap position (blue, dashed) given by the tweezer potential. The combined potential (green, solid) presents a joint trap position (green, dashed). Left panel: Original trap position is at the intensity slope of the cavity control mode, ideal for cavity optomechanics. Joint trap position is unfortunately moved toward the potential minimum of the control mode (to the right in this case). Right panel: We reposition the tweezer focus away from the potential minimum of the control mode (in the left direction), such that the joint potential has a minimum at the cavity intensity slope.

Optimizing the trap position

The nanosphere is initially trapped in the tweezer potential at a position x_0 with a mechanical frequency $\Omega_x = 2\pi \times 160$ kHz. We add the cavity standing wave potential to it, generating a joint trap potential:

$$U(x) = \frac{m\Omega_x^2(x-x_0)^2}{2} + \frac{\alpha}{\varepsilon_0 c}\frac{2P_{cav}}{w_0^2\pi}\cos^2(kx), \tag{4.6}$$

where P_{cav} is the intracavity power, w_0 is the cavity waist and α is the nanosphere polarizability. The cavity standing wave trap depth is $U_{cav} = \frac{\alpha}{\varepsilon_0 c}\frac{2P_{cav}}{w_0^2\pi}$. The nanosphere attains a new trap position x_j defined by $\frac{\partial U(x)}{\partial x}\Big|_{x_j} = 0$:

$$m\Omega_x^2(x_j - x_0) = U_{cav}k\sin(2kx_j), \tag{4.7}$$

which we numerically solve for an arbitrary initial trap position x_0. The joint trap position x_j for an intracavity photon number $n_{\text{phot}} = \frac{P_{cav}}{\hbar\omega_l}\frac{2L}{c} = 7.6 \times 10^9$ is shown in Figure 4.6 as a function of the initial trap position x_0.

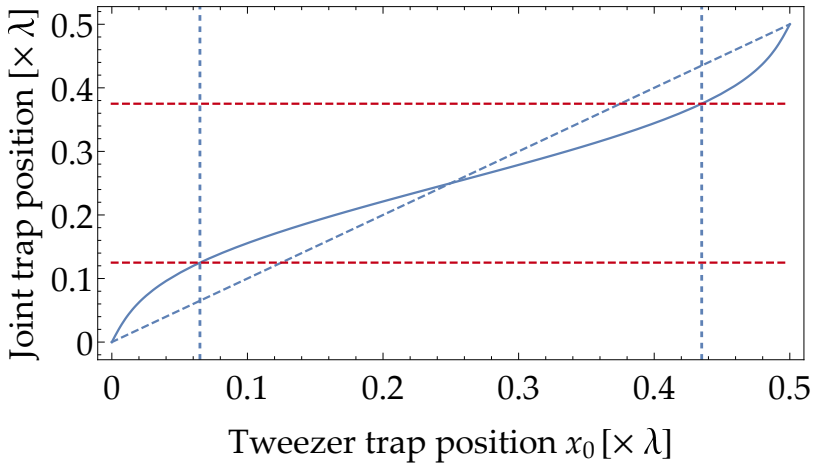

Figure 4.6: **Joint trap position x_j as a function of the tweezer trap position x_0.** For a strong control mode with $n_{phot} = 7.6 \times 10^9$ photons, the nanosphere is trapped in the combined minimum of the tweezer and the cavity potential. The horizontal red dashed line represent the position of maximum linear coupling, i.e. the desired position for the nanosphere. The vertical blue dashed lines show the required position of the tweezer focus in order to reach an optimal coupling to the cavity mode. For comparison, the diagonal blue dashed line $x_j = x_0$ is in the case of $n_{phot} = 0$.

The positions of maximum linear coupling are defined by $\sin(2kx_j) = \pm 1$ (see Equation (2.17)), hence the final trap position has to be at $x_j = \lambda/8 + l\lambda/4$, $l \in \mathcal{Z}$. In the case of $x_j = \lambda/8$, the trapping laser should initially be focused at:

$$x_0 = \frac{\lambda}{8} - \frac{U_{cav}k}{m\Omega_x^2}, \tag{4.8}$$

with a limit $x_0 \geq 0$. The maximal number of photons in the control mode is $n_{\text{phot}}^{max} \approx 1.5 \times 10^{10}$ (Figure 4.7) with the total coupling $g \approx 2\pi \times 38$ kHz. For photon numbers close to n_{phot}^{max} we create a double-well potential. To avoid jumping of the nanosphere from one well to the other, the trap depth of a single well has to be larger than the energy of the nanosphere motion :

$$\Delta U = U(0) - U(x_j) \approx \frac{U_{cav}}{2}\left(1 - \frac{U_{cav}k^2}{m\Omega_x^2}\right) \approx 2k_B T_0. \qquad (4.9)$$

Once the nanosphere motion is cooled with the cavity mode, the trap is certainly deep enough to localize the nanosphere in the desired well.

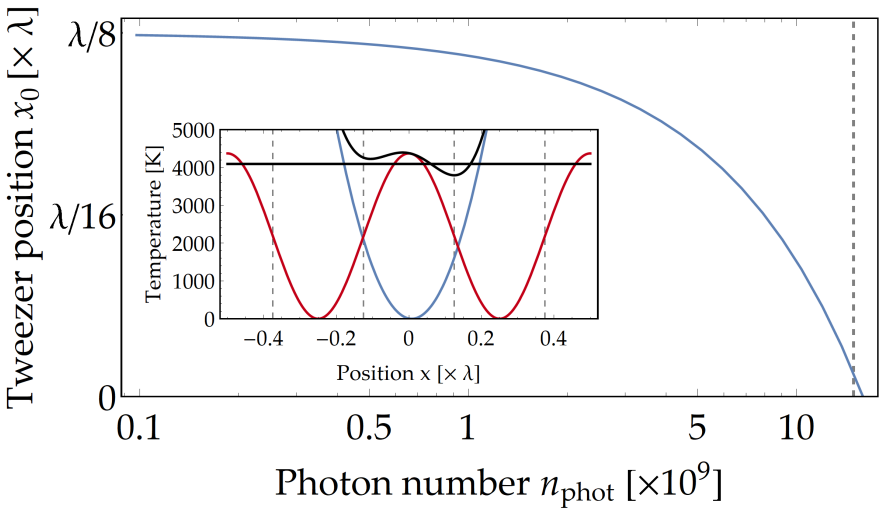

Figure 4.7: **The optimal tweezer position to reach the maximum linear coupling to the cavity mode as a function of the intracavity photon number.** As we increase the intracavity photon number, the initial tweezer position has to be moved away from the optimal position for linear optomechanics $x_j = \lambda/8$. The optimization for an uncooled nanosphere motion can definitely be done for up to $n_{\text{phot}}^{max} \approx 1.5 \times 10^{10}$ photons in the cavity mode. Inset: In the case of a strongly driven cavity (dashed vertical line in the main graph) the cavity (red) and the tweezer potential (blue) create a double-well potential (black). The horizontal black line shows the energy of the nanosphere motion at room temperature in such a trap, which is about two times smaller than the trap depth of the right trap.

Phase noise heating

Note that the heating due to phase noise is proportional to the intracavity photon number, which for n_{phot}^{max} already results in an added phonon number $\bar{n}_{phase} \approx 250$. Laser phase noise is readily decreased with a filtering cavity with small linewidth $\kappa_{FC} \ll \Omega_x$. In principle, reducing laser phase noise with a filtering cavity of $\kappa_{FC}/2\pi = 75$ kHz

in a double pass configuration would be enough to reach the ground state of the x-motion [Hoelscher-Obermaier, 2017]:

$$\bar{n}_{phase,filt} = \left(\frac{\left(\frac{\kappa_{FC}}{2}\right)^2}{\left(\frac{\kappa_{FC}}{2}\right)^2 + \Omega_x^2} \right)^2 \bar{n}_{phase} \approx 0.7. \tag{4.10}$$

4.3.2 *Limitations to the cooperativity*

We determined the optomechanical cooperativity $C \approx 0.01$ at a pressure $p = 4.3 \times 10^{-6}$ mbar.

We list here the improvements towards $C > 1$ in increasing order of complexity:

1. **Immediate effect**
   (a) **Base pressure of the vacuum chamber.** We measured a heating rate $\Gamma = 2\pi \times 28$ kHz at a pressure of $p = 4 \times 10^{-7}$ mbar and a total coupling of up to $g \approx 2\pi \times 14$ kHz at a pressure $p = 0.56$ mbar. Combining these two values would result in a cooperativity of $C \approx 0.14$.
   (b) **Increased coupling by better nanosphere positioning.** By moving the tweezer position to compensate for the additional restoring force of the cavity standing wave, we would be able to realize a coupling rate of $g = 2\pi \times 38$ kHz and a cooperativity of $C = 1$ at the base pressure of the vacuum chamber.
2. **Improving the current setup**
   (a) **Going to the recoil heating limit.** We could reach lower pressures by baking out the vacuum chamber, where the recoil heating of the trapping laser becomes the dominant heating source with a rate $\Gamma \approx 2\pi \times 6.5$ kHz. The cooperativity would be $C \approx 4.6$.
   (b) **Larger power of the trapping laser.** In reality, we are limited by the drive power of the optical cavity, which at this moment is not enough to reach the required $g = 2\pi \times 38$ kHz. The current bottleneck are the large losses in the EOM used to generate the sidebands at $\sim \Delta\nu_{FSR}$. A possible solution is to reverse the role of the locking and the control laser, as there are no optical elements restricting the optical power in the locking laser path.
3. **Exchanging the system hardware**
   (a) **Higher cavity finesse $\mathcal{F}$.** The optomechanical cooperativity is directly proportional to the cavity finesse as $C \propto \kappa^{-1} \propto \mathcal{F}$. We expect to achieve a finesse of $C = 200.000$

with better mirror coatings, which is an increase by a factor of ~ 3.

(b) **Smaller cavity waist w_0.** The smaller the cavity waist, the larger the coupling rate as $g_0 \propto V_{cav}^{-1} \propto w_0^{-2}$. However, this requires a completely different cavity design.

4.4 CONCLUSION AND OUTLOOK

We have presented here and in previous chapters the state-of-the-art setup for levitated optomechanics in the dispersive regime with the full supporting theory. Using an external trapping laser, we are able to position the nanosphere along the cavity standing wave with subwavelength precision. We use this to fully characterize the cavity mode and the nanosphere, which results in an accurate mass measurement of a silica nanosphere. We successfully levitate a nanosphere in high vacuum (down to pressures of $p \approx 4 \times 10^{-7}$ mbar) using three-dimensional feedback cooling and measure a stable and reproducible coupling rate of up to $g/2\pi \approx 15$ kHz using optomechanically induced transparency. We identify the most important heating sources of the nanosphere motion and measure the total heating rate Γ as a function of pressure, which is still dominated only by gas collisions. We use this to obtain an optomechanical cooperativity $C \approx 0.01$. At the end we identify co-trapping by the cavity standing wave and phase noise heating as current limitations of this setup. We present some possible experimental improvements, which would allow us to achieve the strong cooperativity regime. In the following chapters we will present a different route, which immediately improves the cooling performance without any changes to the basic experimental setup.

Part II

CAVITY COOLING OF A LEVITATED NANOSPHERE BY COHERENT SCATTERING

5

CAVITY COOLING BY COHERENT SCATTERING: THEORY

In the previous chapters we considered the tweezer and the cavity modes to be mutually non-interacting due to a difference in both polarization and optical frequency. In particular, the tweezer polarization was oriented along the cavity axis, thus minimizing the dipole scattering off the nanosphere into the cavity mode. By rotating the polarization and tuning the tweezer frequency close to a cavity resonance, we can drive the cavity mode with only the dipole scattering. This is the mechanism behind Purcell enhancement [Purcell et al., 1946, Motsch et al., 2010], as well as cavity cooling by coherent scattering [Vuletić et al., 2001, Hosseini et al., 2017].

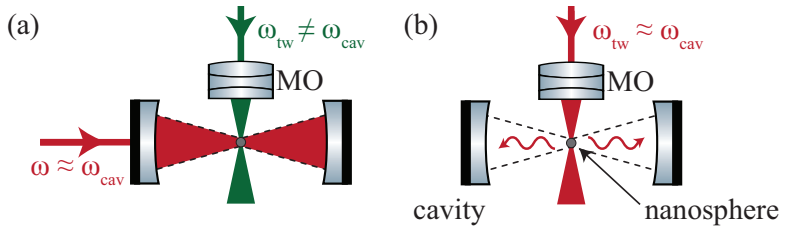

Figure 5.1: **Different paradigms for cavity cooling of a levitated nanosphere.** (a) Cavity cooling by coherent scattering is based on dipole radiation being emitted into an empty cavity mode. The cavity is not driven by an external laser, but through the scattering of the tweezer laser, which is tuned close to the cavity resonance. (b) In standard dispersive optomechanics an external laser drives the cavity through one of the cavity mirrors. The tweezer is used only for trapping of the nanosphere, where the frequency is far detuned from the resonance and the scattering into the cavity is minimized by aligning the polarization along the cavity axis.

In this Chapter, we show that we can drive the optical cavity by coherent scattering off the nanosphere, which can be perceived as an input mirror. The astonishing consequence is that we reach a new regime in optomechanics by linearly coupling the center-of-mass motion along the cavity axis to the cavity electric field (and not cavity intensity) with larger coupling rates than in the standard optomechanics. A major prerequisite for this is to have the stability in positioning a nanosphere along the cavity standing wave, something we demonstrated in Chapter 3.

The Chapter is organized as follows: We start with the classical picture of dipole radiation into a cavity mode, where the cavity enhances the scattered light (Purcell effect). The quantum picture is shown in Section 5.2, where we arrive at three-dimensional cavity cooling starting from the dipole interaction Hamiltonian. If the reader is interested in the comparison of the resulting optomechanical effects with the dispersive regime, it is recommended to jump to the conclusion in Section 5.3.

The theoretical work in this chapter was mostly done during a secondment in the group of Prof. Vladan Vuletić at the Massachusetts Institute of Technology. The research stay has been co-sponsored by the Doctoral program "Complex Quantum Systems" (CoQuS) and the Austrian Marshall Plan Foundation. Some of the results presented here and in the following chapter are in our work "Cavity cooling of a levitated nanosphere by coherent scattering" [Delić et al., 2019b].

Contents

5.1 CLASSICAL DESCRIPTION OF SCATTERING INTO A CAVITY MODE

When we couple a laser to a cavity through an input cavity mirror, we usually assume perfect mode matching, i.e. the driving laser has the same spatial properties as the driven cavity mode. Owing to being smaller than the laser wavelength, the nanosphere scatters light according to a dipole radiation pattern. As it doesn't conform to a single Hermite-Gaussian mode, only some photons scattered by the nanosphere will couple to a particular TEM cavity mode with an overall mode matching $\beta \ll 1$. The overlap of the scattered light and the cavity mode in frequency space gives rise to a Purcell enhancement of the dipole radiation, which will be the topic of this section. The formalism has already been described for atoms in [Tanji-Suzuki et al., 2011], which we will use in order to obtain a classical picture of the coherent scattering off a nanosphere.

5.1.1 *Mode overlap of the dipole radiation pattern and a single cavity TEM_{00} mode*

Let us assume that the incident electric field E_{in} is polarized along the y-axis, such that the dipole scattering is maximized towards the cavity mirrors. As a first step, we calculate the ratio of the incident laser that is scattered off the nanosphere into a free space TEM_{00} defined by the cavity mode. We obtain the mode overlap as ratio from the TEM_{00} mode profile with the dipole radiation pattern.

The electric field of the dipole scattering at a distance R from the nanosphere is given by:

$$E_{rad}(R,\theta) = \frac{k^2 \sin\theta}{4\pi\epsilon_0}\frac{e^{ikR}}{R}\alpha E_{in}, \tag{5.1}$$

where θ is the angle between the polarization vector of the incident field E_{in} and the direction along which the radiated field E_{rad} propagates. The radiation field is effectively zero along the polarization axes of the incident field E_{in}. The incident field is polarized orthogonal to the cavity axis ($\theta = \pi/2$) in order to maximize dipole scattering toward the cavity mirrors. The electric field of the TEM_{oo} spatial cavity mode at a position x along the cavity axis and a distance ρ away from the cavity axis is:

$$E_{00} = E_0 \frac{w_0}{w[x]} \mathrm{e}^{-\frac{\rho^2}{w^2[x]}} \mathrm{e}^{-ikx-\frac{ik\rho^2}{2x}}, \tag{5.2}$$

where $w(x) = w_0\sqrt{1+(x/x_R)^2}$ is the waist along the cavity axis and x_R is the Rayleigh range.

The fraction of the scattered photons into a cavity mode is quantified by the mode overlap between a single TEM_{oo} cavity mode and

the dipole radiation pattern. We assume that the fundamental cavity mode has a waist w_0 at the cavity center and the waist $w_1 = w(L/2)$ at the cavity mirror, where L is the cavity length. The nanosphere is ideally placed at the cavity center, where the strongest interaction with the cavity mode is expected. The mode overlap is calculated at the cavity mirrors where $R \gg \lambda$. Therefore, we can use the far-field approximation of the dipole radiation pattern $e^{ikR}/R = e^{ikx+ik\rho^2/(2x)}/x$, where x is the distance from the nanosphere to the cavity mirror along the cavity axis. The amount of photons scattered under a small angle $\delta\theta = \pi/2 - \theta$ with respect to the cavity axis is $\propto \sin\theta = \cos\delta\theta \approx 1 - (2w_1/L)^2 \approx 1$, hence we assume $\sin\theta \equiv 1$.

The overlap of the two modes is:

$$\begin{aligned}
\frac{1}{E_{in}E_0}\int_0^{2\pi}\int_0^{\infty} E_{00}E_{rad}\rho d\rho d\varphi &= \frac{k^2\alpha}{2\epsilon_0}\frac{w_0}{w[x]x}\int_0^{\infty} e^{-\frac{\rho^2}{w^2[x]}}\rho d\rho = \\
\frac{k^2\alpha}{2\epsilon_0}\frac{w_0}{x}\frac{-w[x]}{2}\int_0^{\infty} e^{-\frac{\rho^2}{w^2[x]}} d\left(-\frac{\rho^2}{w[x]^2}\right) &= \frac{k^2\alpha}{2\epsilon_0}\frac{-w_0 w[x]}{2x} e^{-\frac{\rho^2}{w^2[x]}}\Big|_0^{\infty} = \\
\frac{k^2\alpha}{2\epsilon_0}\frac{-w_0 w[x]}{2x}\left(\lim_{\rho\to\infty} e^{-\frac{\rho^2}{w^2[x]}} - e^{-\frac{0}{w^2[x]}}\right) &= \frac{k^2\alpha w_0}{4\epsilon_0}\frac{w[x]}{x}. \qquad (5.3)
\end{aligned}$$

At distances x greater than the Rayleigh range x_R, the mode overlap normalized over an effective mode area of the cavity mode $A = \pi w_0^2/2$ is:

$$\beta = \frac{1}{A}\frac{1}{E_{in}E_0}\int_0^{2\pi}\int_0^{\infty} E_{00}E_{rad}\rho d\rho d\varphi = \frac{k\alpha}{\epsilon_0 w_0^2\pi}. \qquad (5.4)$$

It is compelling to see if there is a significant mode overlap when the incident field E_{in} is polarized along the cavity axis, i.e. $\theta \approx 0$. For small angle θ we approximate $\sin\theta \approx \tan\theta = \frac{\rho}{L/2}$ and obtain a non-zero mode overlap:

$$\beta_{min} = \frac{\alpha}{\epsilon_0 w_0^3\sqrt{\pi}}. \qquad (5.5)$$

In the case of a near-confocal cavity of waist $w_0 \approx 41\mu$m, the mode overlap is smaller by a factor of $\frac{\beta}{\beta_{min}} \sim 100$ when compared to the maximum overlap. Therefore, the power scattered into a single cavity mode $P_{\text{scatt}} \propto |\beta|^2$ is decreased by a factor of 10^4 by fine-tuning the polarization of the incident electric field. In reality, a small angular deviation $\phi = 8.4^\circ$ from a perfectly straight angle between the tweezer and cavity axes leads to a constant offset $\theta \approx \phi + \frac{\rho}{L/2}$, which modifies the mode overlap $\beta \approx \beta_{min} + \beta\sin\phi$. This results in a higher scattered power $\propto |\beta|^2\sin^2(\phi) \approx 2\times 10^{-2}|\beta|^2$ than expected only from β_{min}.

The electric field of the scattered light into one half of the cavity mode, e.g. toward the right:

$$E_M = i\beta E_{in}, \qquad (5.6)$$

where $|E_{in}|^2 = \frac{2I_{in}}{\varepsilon_0 c}$ is the electric field of the incident laser with intensity I_{in}. The imaginary unit i is added due to the Gouy phase $\pi/2$ of the cavity mode at large distances $x \gg x_R$. It is important to note that Equation (5.6) holds for any incident electric field irrespective of its mode cross-section. Even for a tightly focused incident laser we assume the mode waist of E_{in} is still larger than the nanosphere radius $W_0 \gg r$ such that the incident field is resembling a plane wave.

The laser power scattered into the mode E_M is $P_M = |\beta|^2 I_{in} w_0^2 \pi/2 \approx 1$ nW for our typical system parameters ($r = 71.5$ nm, $I_{in} \approx 2 \times 10^{11} \frac{\mathrm{W}}{\mathrm{m}^2}$). The total power emitted by the dipole into free space $P_{4\pi}$ is obtained by an integration of the radiated intensity $I_{rad} = \varepsilon_0 c |E_{rad}|^2/2$ over the surface of a sphere with an arbitrary radius R:

$$P_{4\pi} = \frac{ck^4}{12\pi\varepsilon_0}|\alpha E_{in}|^2 = \frac{k^2 w_0^4 \pi}{6}|\beta|^2 I_{in}. \tag{5.7}$$

The ratio of the power scattered into both modes E_M and the power scattered into free space is called *free space cooperativity*:

$$\eta_{\mathrm{fs}} = \frac{2P_M}{P_{4\pi}} = \frac{6}{k^2 w_0^2}. \tag{5.8}$$

We doubled the power P_M in order to account for the scattering into both directions of the cavity. The cavity collects the light scattered into the solid angle η_{fs}.

5.1.2 *Enhanced scattering by the cavity*

The light scattered into the mode E_M is reflected many times by the cavity mirrors, which leads to an interference of the scattered photons. For example, the scattered electric field E_M toward the mirror M1 will reflect once and interfere with the electric field E_M scattered in the opposite direction (toward mirror M2) (Figure 5.2). A weak built-up *right-traveling* cavity electric field $E_{c,r}$ ($E_{c,r} \ll E_{in}$) reaches a steady-state amplitude depending on the relative phase shift between the scattered fields:

$$E_{c,r} = E_M + r_1 e^{ik(L+2\Delta x)} E_M + r_1 r_2 e^{2ikL} E_{c,r}, \tag{5.9}$$

where r_1^2 and r_2^2 is the reflectivity of the mirrors M1 and M2, respectively. Δx is the nanosphere position along the cavity axis, relative to the cavity center. E_M is the electric field scattered toward mirror M2, while $r_1 e^{ik(L+2\Delta x)} E_M$ is the field scattered in the opposite direction and subsequently reflected from mirror M1. Note that we have assumed a positive sign next to the accumulated phase shift ikL for the right-traveling wave. As we will see later, the choice of the sign coincides with the phase and direction of a quantized cavity mode.

Our cavity is designed to be double-sided, hence we assume equivalent transmittivities $|t_1|^2 = |t_2|^2$. Still, we continue using an arbitrary

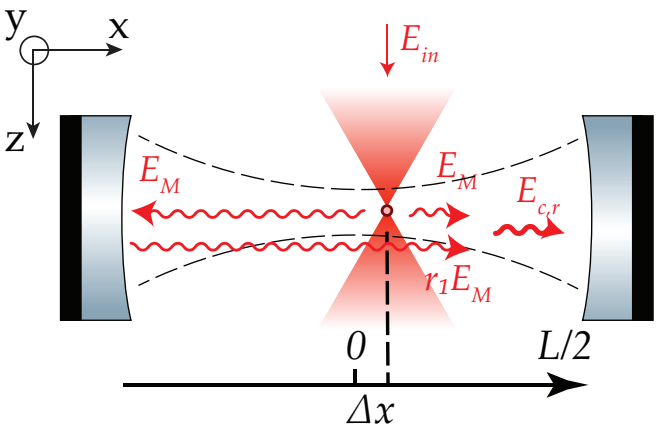

Figure 5.2: **Coherent enhancement of the dipole radiation by the cavity.** The nanosphere scatters the incident field E_{in} into the cavity mode (outlined by the dashed lines). The scattered electric field E_M is reflected from the mirror M1 and interferes with the component E_M scattered toward the mirror M2, creating the right-traveling electric field $E_{c,r}$. The interference can be destructive or constructive, depending on the nanosphere position Δx.

$|r_1|^2$ and $|r_2|^2$ as we might have some additional losses. The steady-state amplitude of the right-traveling cavity electric field $E_{c,r}$ is:

$$E_{c,r} = i\beta E_{in} \frac{1 + r_1 e^{ikL} e^{2ik\Delta x}}{1 - r_1 r_2 e^{2ikL}}. \tag{5.10}$$

Let us consider a simple case of a resonant incident laser $\omega_{tw} = \omega_{cav}$, such that the accumulated phase shift during one cavity circulation is $e^{2ikL} = 1$. Without a loss in generality we assume $e^{ikL} = 1$, i.e. the cavity standing wave has an intensity maximum at the cavity center. The cavity electric field is:

$$E_{c,r} = i\beta E_{in}(1 + r_1 e^{2ik\Delta x}) \frac{\mathcal{F}}{\pi}, \tag{5.11}$$

where we used the definition of the cavity finesse $(1 - r_1 r_2)^{-1} \equiv \mathcal{F}/\pi$. The power of the right-traveling cavity electric field is:

$$P_{c,r} = \frac{|E_{c,r}|^2}{2\varepsilon_0 c} \frac{w_0^2 \pi}{2} = I_{in} \frac{w_0^2 \pi}{2} |\beta|^2 \left(\frac{\mathcal{F}}{\pi}\right)^2 \left(1 + r_1^2 + 2r_1 \cos(2k\Delta x)\right), \tag{5.12}$$

where Δx is the nanosphere position with respect to the cavity center. In general, Δx is a combination of the steady-state trap position x_0 and the nanosphere motion along the cavity axis $x(t)$, which we neglect at the moment. For a nanosphere trapped at the position of the intensity maximum ($\cos 2kx_0 = 1$) and assuming $|r_1|^2 \approx 1$, the power of the right-traveling field is:

$$P_{c,r} = 2 I_{in} w_0^2 \pi |\beta|^2 \left(\frac{\mathcal{F}}{\pi}\right)^2. \tag{5.13}$$

In conclusion, although a small fraction of the incident laser $\propto |\beta|^2 P_{in}$ is scattered into the cavity mode, the intracavity power is enhanced by the cavity finesse $\left(\frac{\mathcal{F}}{\pi}\right)^2$.

DETUNED TWEEZER LASER. In the case of a detuned incident laser $\omega_{tw} = \omega_{cav} - \Delta$, the accumulated phase shift of the traveling field is approximately $e^{2ikL} = e^{-i\Delta/\Delta\nu_{FSR}}$:

$$\frac{1}{|1 - r_1 r_2 e^{2ikL}|^2} \approx \frac{1}{\left|1 - r_1 r_2 \cos\frac{\Delta}{\Delta\nu_{FSR}} + i r_1 r_2 \sin\frac{\Delta}{\Delta\nu_{FSR}}\right|^2} \approx \frac{(\mathcal{F}/\pi)^2 \left(\frac{\kappa}{2}\right)^2}{\left(\frac{\kappa}{2}\right)^2 + \Delta^2}.$$

Hence, the cavity enhancement is modified by the cavity response at the detuned frequency.

PURCELL FACTOR. A fraction of the right-traveling laser leaks out of the cavity through the mirror M2 with power $P_2 = |t_2|^2 P_{c,r}$. In case of no additional losses, the transmission through mirror M2 attributes for one half of the cavity photon losses:

$$P_2 = 2 I_{in} w_0^2 |\beta|^2 \left(\frac{\mathcal{F}}{\pi}\right)^2 |t_2|^2. \tag{5.14}$$

A double-sided cavity without absorption and scattering losses has a cavity finesse $\mathcal{F}_{max} = \pi/|t_2|^2$. The finesse of a cavity with additional losses is $\mathcal{F} < \mathcal{F}_{max}$, hence $P_2 = 2 I_{in} w_0^2 |\beta|^2 \frac{\mathcal{F}}{\pi} \frac{\mathcal{F}}{\mathcal{F}_{max}}$. For the optimal case $\mathcal{F} = \mathcal{F}_{max}$, the ratio of the total power leaked through the cavity mirrors $P_1 + P_2$ to the power emitted into the whole space $P_{4\pi}$ in absence of a cavity is commonly referred to the Purcell factor of enhancement η [Purcell et al., 1946]:

$$\eta = \frac{P_1 + P_2}{P_{4\pi}} = 4\frac{\mathcal{F}}{\pi}\eta_{\text{fs}} = \frac{24\mathcal{F}/\pi}{k^2 w_0^2}. \tag{5.15}$$

Therefore, although the cavity collects only a small solid angle of the whole dipole radiation, it stimulates radiation into the cavity. This results in an overall enhancement of the scattered power. As shown in [Tanji-Suzuki et al., 2011], the Purcell factor of the dipole interaction is equivalent to the atomic cooperativity obtained from the quantum treatment.

5.1.3 *Modified enhanced scattering into the cavity*

The scattered electric field E_M is strongly amplified in a high finesse cavity. In this case the coherent scattering of the built-up intracavity fields $E_{c,r}$ and $E_{c,l}$ has to be taken into account, such that the total scattered electric field is:

$$E_M = i\beta(E_{in} + E_{c,r} + E_{c,l}). \tag{5.16}$$

The left- and right-traveling electric fields $E_{c,l}$ and $E_{c,r}$ are related by a phase $E_{c,l}e^{-ik(L-2\Delta x)} \approx E_{c,r} \equiv E_c$. We use this to eliminate the left-traveling electric field:

$$E_c = r_1 r_2 e^{2ikL} E_c + i\beta \left(E_{in} + E_c \left(1 + r_2 e^{ik(L-2\Delta x)} \right) \right) \left(1 + r_1 e^{ik(L+2\Delta x)} \right). \tag{5.17}$$

We assume an arbitrary detuning of the incident laser, an intensity maximum of the cavity field at the cavity center ($e^{ikL} \approx 1$) and near to unity reflectivities $|r_1|^2, |r_2|^2 \approx 1$:

$$\begin{aligned} E_c &= \frac{i\beta E_{in} \left(1 + e^{2ik\Delta x} \right)}{1 - r_1 r_2 + i\frac{\Delta}{\Delta\nu_{FSR}} - i4\beta \cos^2 k\Delta x} \\ &= \frac{i\beta \Delta\nu_{FSR} E_{in} \left(1 + e^{2ik\Delta x} \right)}{\frac{\kappa'}{2} + i\Delta'}. \end{aligned} \tag{5.18}$$

We introduced the modified cavity energy decay rate κ' and the modified detuning Δ' as:

$$\begin{aligned} \kappa' &= \kappa + 8\,\mathrm{Im}(\beta)\Delta\nu_{FSR} \cos^2 k\Delta x, \\ \Delta' &= \Delta - 4\,\mathrm{Re}(\beta)\Delta\nu_{FSR} \cos^2 k\Delta x. \end{aligned}$$

The modification to the detuning Δ' is a recurring factor $4\,\mathrm{Re}(\beta)\Delta\nu_{FSR} = U_0$, where U_0 is the nanosphere-induced frequency shift defined in Equation (2.15). Note the following effects from Equation (5.18):

1. **Modified cavity energy decay rate.** The nanosphere scatters light out of the cavity, hence the total cavity decay rate is modified by a position-dependent $\kappa_{scatt} = 8\,\mathrm{Im}(\beta)\Delta\nu_{FSR} \cos^2 kx_0$. The scattering rate is a function of the imaginary part of the mode overlap $\mathrm{Im}(\beta) \propto \mathrm{Im}(\alpha)$. The nanosphere polarizability obeys the Kramers-Kroenig relation $\mathrm{Im}(\alpha) = \frac{6\pi\varepsilon_0}{k^3}|\alpha|^2$:

$$\mathrm{Im}(\beta) = |\beta|^2 \frac{1}{\eta_{fs}} = \left(\frac{k|\alpha|}{\varepsilon_0 w_0^2 \pi} \right)^2 \frac{k^2 w_0^2}{6} \propto r^6. \tag{5.19}$$

   Furthermore, this is a confirmation that the scattering into the cavity $|\beta|^2$ is a fraction η_{fs} of the scattering into the whole space $\mathrm{Im}(\beta)$.

2. **Modified detuning by the nanosphere.** The nanosphere has a different refractive index compared to the environment, thus it changes the cavity resonance frequency by $U(x) = U_0 \cos^2 kx_0$.

3. **Linear optomechanical coupling to the cavity mode.** The nanosphere motion induces a position-dependent frequency shift to the cavity resonance with a rate U_0:

$$\frac{\partial\omega_{cav}}{\partial x} = -U_0 k \sin 2kx_0 = \frac{g_0}{x_{zpf}} \sin 2kx_0. \tag{5.20}$$

4. **Position-dependent drive of the cavity mode.** The amplitude of the created cavity electric field E_c depends on the nanosphere position $\Delta x = x_0 + x(t)$, which is an observable effect only with atoms and dipole scatterers. This leads to a different coupling mechanism of the cavity mode to the nanosphere motion when compared to standard optomechanics. We will explore this in detail in the following chapter.

The first three points mentioned above exist also in standard optomechanics theory, as shown in Chapter 2. Before we examine the fourth point in detail, we apply the formalism of coherent scattering to a case when the cavity is driven through an input mirror. We compare the results to the theory from Chapter 2 to demonstrate that the coherent scattering picture is applicable.

Cavity driven through the cavity mirror

Let us consider a case of an external laser driving the cavity mode through the input mirror M1 [Horak et al., 1997, Vuletić and Chu, 2000]. We apply the formalism of coherent scattering in order to calculate the right-traveling cavity field. Only a fraction of the input field $t_1\beta_1 E_{in}^{M1}$ is transmitted through the input mirror. We assume a perfect mode matching of the input field E_{in}^{M1} and the driven cavity mode $E_{c,r}$, i.e. $\beta_1 = 1$. Including the coherently scattered light fields, the steady-state cavity electric field satisfies the following relation at the nanosphere position Δx:

$$\begin{aligned} E_{c,r} &= r_1 r_2 e^{2ikL} E_{c,r} + t_1 E_{in}^{M1} e^{ik\left(\frac{L}{2}+\Delta x\right)} \\ &+ i\beta E_{c,r}\left(1 + r_2 e^{ik(L-2\Delta x)}\right)\left(1 + r_1 e^{ik(L+2\Delta x)}\right). \end{aligned} \tag{5.21}$$

We include a phase $e^{ik\left(\frac{L}{2}+\Delta x\right)}$ to account for the phase that the right-traveling field accumulates between the input mirror and the nanosphere position. This is important in order to later implement a proper quantization of the cavity field $E_{c,r}$. Comparing Equations (5.21) and (5.17), we conclude that the nanosphere acts as an input mirror for the trapping laser with a transmission $|\beta|$. Although $\beta \ll t_1$, the incident intensity I_{in} is typically orders of magnitude higher than the typical I_{in}^{M1}, both due to a tighter focus and the larger powers needed to levitate a nanosphere.

Without any loss in generality we set $e^{ikL} \approx 1$ and $|r_1|^2$, $|r_2|^2 \approx 1$. Instead of quantizing the cavity standing wave, we use the notation of quantized traveling fields. However, we still keep the boundary conditions that the cavity mirrors set on the created cavity standing

wave. The right- and left-traveling fields are quantized as [Clerk et al., 2010]:

$$\begin{aligned} E_r &\propto i\sqrt{\frac{\hbar\omega_l}{2\varepsilon_0 V_{cav}}}\left(\hat{a}e^{ikx}e^{-i\omega_l t} - \hat{a}^\dagger e^{-ikx}e^{i\omega_l t}\right) \\ E_l &\propto -i\sqrt{\frac{\hbar\omega_l}{2\varepsilon_0 V_{cav}}}\left(\hat{a}e^{-ikx}e^{-i\omega_l t} - \hat{a}^\dagger e^{ikx}e^{i\omega_l t}\right). \end{aligned}$$

The earlier notation of the accumulated phase with a positive sign leads to the component $E_r \propto \hat{a}$. By keeping a convention of negative phase shifts e^{-ikx}, we arrive at the equation governing the dynamics of the creation operator $\hat{a}^\dagger$. Note that the total electric field is $E_t = E_r + E_l \propto 2\left(\hat{a}e^{-i\omega_l t} + \hat{a}^\dagger e^{i\omega_l t}\right)\sin kx$, in agreement with the usual cavity mode quantization.

It is important to choose a correct coordinate system for the propagation of the traveling fields, which is commonly chosen to be at the input cavity mirror. Therefore, we displace the calculated electric field $E_{c,r}$ by $e^{il\left(\frac{L}{2}+\Delta x\right)}$ in order to obtain the classical analogue of E_r. Although it seems like an unnecessary trick, this is an important step in dealing with the quantization of the electric field generated by coherent scattering. The quantum Langevin equation for the annihilation operator $\hat{a}$ is:

$$\dot{\hat{a}} = -\left(\frac{\kappa'}{2} + i\Delta\right)\hat{a} + E_d - iU_0 k\hat{a}\hat{x}\sin 2kx_0, \tag{5.22}$$

[9] $\kappa_1 = |t_1|^2\Delta\nu_{FSR}$

where $E_d = t_1 E_{in}\Delta\nu_{FSR}\sqrt{\frac{2\varepsilon_0 V_{cav}}{\hbar\omega_l}} = \sqrt{\frac{P_{in}\kappa_1}{\hbar\omega_l}}$ is the cavity driving field[9]. This equation is in agreement with the Langevin equation (2.47) from Chapter 2. Therefore, using the classical picture of coherent scattering we are able to reach a quantum description, with the quantization of the scattered light done as the final step. We now return to the case of coherent scattering of the trapping laser.

5.1.4 *Quantum Langevin equations of motion for coherent scattering*

The cavity electric field E_c in Equation (5.18) is the right-traveling field at the nanosphere position $\Delta x = x_0 + \hat{x}$. In order to implement the quantization correctly, we need to calculate the electric field at the cavity center[10] which serves as a coordinate system origin:

[10] *We conduct this by shifting* $1 + e^{2ik\Delta x} \to e^{-ik\Delta x} + e^{-ik\Delta x} = 2\cos k\Delta x$

$$\dot{\hat{a}} = -\left(\frac{\kappa'}{2} + i\Delta'\right)\hat{a} + iE_d\cos(kx_0) - iE_d k\sin(kx_0)\hat{x} - i\frac{g}{x_{zpf}}\sin(2kx_0)\hat{x}. \tag{5.23}$$

Figure 5.3 demonstrates the position dependence of the different coupling rates, in comparison to the dispersive coupling for an externally driven cavity. The dispersive coupling with the cavity driven by coherent scattering $g\sin 2kx_0$ is the optomechanical coupling to the

intensity of the cavity mode, which is created by the coherently scattered light. The additional coupling rate $g' \sin kx_0 = E_d k x_{zpf} \sin kx_0$ describes a coupling of the nanosphere motion to the cavity electric field and is intrinsically linearized. This is a yet unexplored interaction for macroscopic mechanical objects, although it was already demonstrated in atomic systems. Cooling of the atomic motion by coherent scattering was both shown in the sideband-resolved regime [Leibrandt et al., 2009] and in the sideband-unresolved regime [Hosseini et al., 2017].

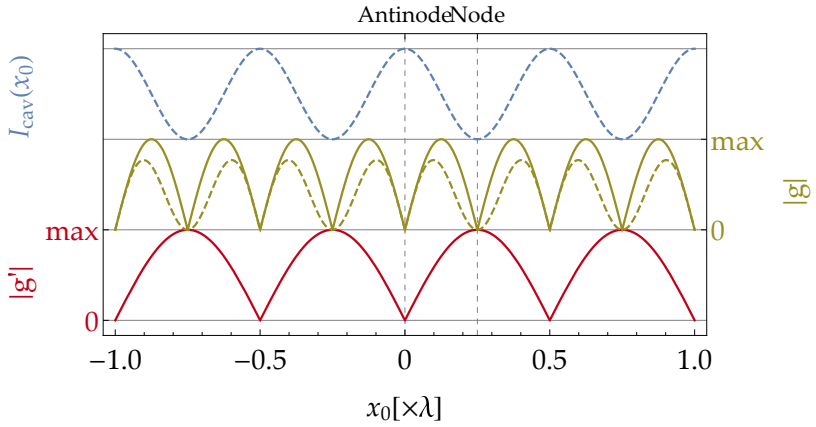

Figure 5.3: **Optomechanical coupling rates from different coupling mechanisms.** The nanosphere motion is coupled to the intensity profile of an externally driven cavity in the dispersive regime (green solid) and to the electric field in the case of coherent scattering (red). For a cavity driven by coherent scattering, the residual dispersive coupling exhibits a tilt toward the intensity maximum (green dashed). The cavity standing wave intensity profile I_{cav} is plotted for reference (blue dashed line). Maximum of the coupling through coherent scattering $|g'|$ is observed at the cavity nodes, in contrast to the dispersive coupling $|g|$, which is the strongest halfway between the node and the antinode.

In analogy to the cavity drive with an external laser in Section 2.1.1, coherently scattered photons drive the cavity with a photon rate $E_d = \sqrt{\frac{P'_{in}\kappa_{nano}}{\hbar\omega_l}}$. The nanosphere acts as an input mirror with the position-dependent input rate κ_{nano}:

$$\kappa_{nano}(x_0) = 4|\beta|^2 \Delta\nu_{FSR} \cos^2(kx_0). \tag{5.24}$$

$P'_{in} = I_{in} w_0^2 \pi/2$ is the power of the trapping laser rescaled to the cavity mode area and I_{in} is the intensity of the trapping laser. The relation between the input rate κ_{nano} and the loss rate into free space $\kappa_{scatt}^{max} = 8\,\mathrm{Im}(\beta)\Delta\nu_{FSR}$ is:

$$\kappa_{nano} = \frac{\kappa_{scatt}}{2}\eta_{\mathrm{fs}}. \tag{5.25}$$

The scattering rate of the trapping laser into the cavity mode is $\eta_{fs}\kappa_{scatt}$, consistent with the definition of η_{fs} from above. After a linearization of the cavity mode operators ($\hat{a} \to \alpha_0 + \hat{a}$) we obtain:

$$\begin{aligned}\dot{\hat{a}} &= -\hat{a}\left(\frac{\kappa'}{2} + i\Delta\right) - i\frac{g(x_0) + g'(x_0)}{x_{zpf}}\hat{x} \\ &+ \sqrt{\kappa_{IN}}(\hat{a}^1_{\mathrm{IN}} + \hat{a}^2_{\mathrm{IN}}) + \sqrt{\kappa_{scatt}\cos^2(kx_0)}\hat{a}_{nano},\end{aligned} \tag{5.26}$$

where we added the loss channels of the mirrors $\hat{a}^{1,2}_{\mathrm{IN}}$ and the nanosphere $\hat{a}_{nano}$.

We assume that there is no additional cavity drive through the cavity mirrors. The intracavity photon number then depends only on the nanosphere position x_0 and the laser detuning Δ:

$$n_{\mathrm{phot}} = |\alpha_0|^2 = \frac{E_d^2\cos^2(kx_0)}{\left(\frac{\kappa'}{2}\right)^2 + \Delta^2}. \tag{5.27}$$

As the coupling rate to the cavity standing wave contains a position-dependent photon number

$$g(x_0) = g_0\sqrt{n_{\mathrm{phot}}}\sin 2kx_0 = g_0\frac{E_d}{\sqrt{\left(\frac{\kappa'}{2}\right)^2 + \Delta^2}}\cos kx_0 \sin 2kx_0, \tag{5.28}$$

the optimal position for this coupling is at $x_0 = \frac{1}{k}\arctan(1/\sqrt{2})$ with an amplitude $\max(g) = \frac{U_0 k x_{zpf} E_d}{\sqrt{\left(\frac{\kappa'}{2}\right)^2+\Delta^2}}\frac{4}{3\sqrt{3}}$. The ratio of the coupling rates $\max(g')$ and $\max(g)$ is:

$$\frac{\max(g')}{\max(g)} = \frac{E_d k x_{zpf}}{\frac{U_0 k x_{zpf} E_d}{\sqrt{\left(\frac{\kappa'}{2}\right)^2+\Delta^2}}\frac{4}{3\sqrt{3}}} \approx 1.3\frac{\sqrt{\left(\frac{\kappa'}{2}\right)^2 + \Delta^2}}{U_0}, \tag{5.29}$$

which depends only on the cavity linewidth κ, the trapping laser detuning Δ and the nanosphere-induced frequency shift U_0. For an optimally detuned trapping laser in the resolved-sideband regime ($\kappa/2 \ll \Omega_x$), the ratio is $\sim \Omega_x/U_0 \gg 1$, which shows that we can neglect the standard optomechanical interaction with the cavity mode driven by coherent scattering. This will change for an increased U_0, e.g. in the case of a smaller cavity mode volume or a larger nanosphere.

We now compare the coupling rates in the case of driving the cavity through the input mirror with E_d^{M1} and with the coherent scattering off the nanosphere with E_d^{coh}:

$$\frac{g'}{g} = \frac{E_d^{coh} k x_{zpf}}{\frac{U_0 k x_{zpf} E_d^{M1}}{\sqrt{\left(\frac{\kappa'}{2}\right)^2+\Delta^2}}} \overset{\Delta=0}{=} \frac{\kappa}{2U_0}\frac{E_d^{coh}}{E_d^{M1}} \sim \sqrt{\frac{I_{in}}{I_{cav}}}, \tag{5.30}$$

which is a ratio of the trapping laser intensity I_{in} and the created intracavity intensity I_{cav} for an externally driven cavity. In principle, the former is higher due to a smaller waist of the trapping laser compared to the cavity waist $W_0 \ll w_0$, i.e. a smaller interaction cross-section. Note that a significantly smaller cavity drive E_d^{coh} can be used to reach the same coupling rates $g' = g$ as $\kappa \gg U_0$.

Previous calculations show an increased strength of the optomechanical interaction. We focus on the system Hamiltonian in the further text, which will provide us with the full dynamics of the nanosphere motion and the cavity mode operators.

5.2 QUANTUM DESCRIPTION OF COHERENT SCATTERING

Note that in Chapter 2 we dismissed the Hamiltonian containing the interference between the trapping laser E_{tw} and the cavity mode E_{cav} as they are orthogonally polarized and driven at different frequencies. We relax these constraints in order to allow for coherent scattering of the trapping laser into the cavity. Hence, we now expect to have an interference term $\propto E_{tw}E_{cav}$, which we investigate here in detail. The aim is to reproduce the effects seen in the classical formalism presented earlier in this chapter, as well as to gather a full understanding of the different optomechanical interactions.

5.2.1 *Interference between the tweezer and the cavity mode*

The full dipole interaction between the nanosphere and available light fields is given by the Hamiltonian:

$$\hat{H}^i_{light-nano} = -\frac{1}{2}\alpha \left|\vec{E}\right|^2 = -\frac{1}{2}\alpha \left|\vec{E}_{cav} + \vec{E}_{tw}\right|^2,$$

where we neglected the free modes. Keep in mind that $-\frac{1}{2}\alpha \left|\vec{E}_{tw}\right|^2$ and $-\frac{1}{2}\alpha \left|\vec{E}_{cav}\right|^2$ lead to the harmonic potential and the linearized optomechanical interaction, respectively. We now allow for interference between the tweezer and the cavity field:

$$\hat{H}^i_{cav-tw} = -\frac{1}{2}\alpha \left(E_{tw}E^*_{cav} + E^*_{tw}E_{cav}\right).$$

Although we assume a quantized cavity mode, we still presume a strong, coherent trapping laser:

$$\hat{H}^i_{cav-tw} = -\frac{1}{2}\alpha\epsilon E_{tw}\left(\hat{a}^\dagger f^*(\vec{r})f_t(\vec{r})e^{-i(\omega_{tw}-\omega_{cav})t} + \hat{a}f(\vec{r})f_t^*(\vec{r})e^{i(\omega_{tw}-\omega_{cav})t}\right), \tag{5.31}$$

where $\epsilon = \sqrt{\frac{\hbar\omega_c}{2\varepsilon_0 V_{cav}}}$ is the cavity electric field-per-photon, while $f(\vec{r})$ and $f_t(\vec{r})$ are the electric field profiles of the cavity mode and the trap-

ping laser, respectively. Equation (5.31) resembles the Hamiltonian of the cavity drive in Equation (2.4) with the drive photon rate:

$$E_d = \alpha\epsilon E_{tw}/2\hbar. \tag{5.32}$$

In contrast to (2.4), the cavity drive depends on the position of the input mirror, i.e. the nanosphere. To keep things simple, we assume that the nanosphere is positioned on the cavity axis ($y_0 = z_0 = 0$) at an arbitrary position $\Delta x = x_0 + x(t)$, such that the cavity mode function is to first order $f(\vec{r}) = \cos k(x_0 + x(t))$. The interaction Hamiltonian in the rotating frame picture is:

$$\frac{\hat{H}^i_{l-n}}{\hbar} = -\underbrace{U_0 \cos^2 k\Delta x \hat{a}^\dagger \hat{a}}_{\text{from } |E_{cav}|^2} - \underbrace{E_d \cos k\Delta x \left(\hat{a}^\dagger + \hat{a}\right)}_{\text{from } E_{cav}E^*_{tw}} - \underbrace{\sum_{j=x,y,z} \frac{m\Omega_j^2 \hat{j}^2}{2\hbar}}_{\text{from } |E_{tw}|^2}, \tag{5.33}$$

with the total system Hamiltonian $\hat{H} = \hbar\Delta\hat{a}^\dagger\hat{a} + \hat{H}^i_{l-n}$. Due to the coherent scattering driving the cavity mode, we assume that the cavity operators $\hat{a}$ contain a coherent and a fluctuating component $\hat{a} \to \alpha_0 + \hat{a}$. Neglecting the fundamental trapping potential in Equation (5.33), we obtain the other two terms:

- After linearization of the cavity operators, $U_0 \cos^2 k\Delta x \hat{a}^\dagger\hat{a}$ leads to the standard optomechanical interaction

$$\hat{H}^1_{OM} = \hbar U_0 k|\alpha_0| \sin(2kx_0)\hat{x}\left(\hat{a}^\dagger + \hat{a}\right) \tag{5.34}$$

  and the shift of the cavity frequency $\Delta' = \Delta - U_0 \cos^2 kx_0$.

- The cavity drive $E_d \cos k\Delta x \left(\hat{a}^\dagger + \hat{a}\right)$ is also the source of the previously suppressed optomechanical interaction

$$\hat{H}^2_{OM} = \hbar E_d k \sin(kx_0)\hat{x}\left(\hat{a}^\dagger + \hat{a}\right). \tag{5.35}$$

  This interaction is intrinsically linear as it is proportional to the cavity electric field E_{cav}.

The two interaction Hamiltonians $\hat{H}^1_{OM}$ and $\hat{H}^2_{OM}$ have a fundamentally different dependence on the nanosphere position x_0. Due to the coupling of the nanosphere motion to the cavity intensity, the Hamiltonian $\hat{H}^1_{OM}$ has the periodicity of the cavity standing wave, while the Hamiltonian $\hat{H}^2_{OM}$ expresses the coupling to the cavity electric field at half of the standing wave periodicity.

As shown in the previous section, the cavity is weakly populated by the coherently scattered light due to a large ratio between cavity waist and tweezer waist, w_0/W_0. Therefore, the interaction $\hat{H}^2_{OM}$ is significantly stronger than the interaction $\hat{H}^1_{OM}$. Although the cavity amplitude $|\alpha_0|$ can be significantly increased by driving the cavity

through the cavity mirrors, we focus solely on driving through the nanosphere as it's encouraging to explore the effects in this simple case. Therefore, from this point on we neglect $\hat{H}^1_{OM}$.

With the purpose of motivating the study of coherent scattering, we have investigated only the interaction with the cavity mode profile. In the following we assume the following trapping laser and cavity mode profiles:

$$\begin{aligned} f_t(x,y,z) &= \frac{1}{\sqrt{1+\left(\frac{z}{z_R}\right)^2}} e^{ik(z+x\sin\phi)} e^{-i\varphi_G(z)} e^{-\frac{y^2+x^2}{W_0^2}} \\ f(x,y,z) &= \cos k(x_0+x+z\sin\phi) e^{-\frac{y^2+z^2}{w_0^2}}, \end{aligned} \tag{5.36}$$

which we will use to extract all contributions to the optomechanical interaction. Note that we included the interaction with the x- and z-motion due to a small tilting angle ϕ of the trapping laser, while assuming $\cos\phi \approx 1$.

5.2.2 *Interaction with the x-motion*

The dominant linear and quadratic interaction is from the cavity mode profile:

$$\hbar(\hat{a}^\dagger + \hat{a}) \left(g_x \sin kx_0 \frac{\hat{x}}{x_{zpf}} + g_{x,q} \cos kx_0 \left(\frac{\hat{x}}{x_{zpf}}\right)^2 \right), \tag{5.37}$$

where $g_x = E_d k x_{zpf}$ (for our parameters: $g_x/2\pi \approx 66$ kHz) and $g_{x,q} = E_d k^2 x_{zpf}^2/2$ are the linear and quadratic coupling rate. Note that the maximum linear (quadratic) coupling is at the cavity node (antinode). Additional smaller contributions are:

- Linear coupling due to the tilt ϕ of the trapping laser:

$$i\hbar(\hat{a}^\dagger - \hat{a}) \underbrace{E_d k x_{zpf} \sin\phi}_{g_x^{(1)}} \cos kx_0 \frac{\hat{x}}{x_{zpf}} \tag{5.38}$$

  The coupling rate $g_x^{(1)}$ is a factor of $1/\sin\phi \sim 9$ smaller compared to g_x. The interaction is of a different type compared to the dominant linear interaction, with the maximum coupling at the cavity antinode. Therefore, we will not include it in the linear interaction, but we will compare it to the quadratic interaction at this position in Section 5.2.6.

- Quadratic coupling due to the Gaussian envelope of the trapping laser:

$$-\hbar(\hat{a}^\dagger + \hat{a}) \underbrace{\frac{E_d x_{zpf}^2}{W_0^2}}_{g_{x,q}^{(1)}} \cos kx_0 \left(\frac{\hat{x}}{x_{zpf}}\right)^2. \tag{5.39}$$

The coupling rate $g^{(1)}_{x,q}$ is a factor of $q = k^2 W_0^2/2 \sim 8.54$ smaller compared to $g_{x,q}$, but is still a sizable contribution due to the small focus of the trapping laser. The total quadratic coupling is $\bar{g}_{x,q} = E_d x_{zpf}^2 (k^2 - 1/W_0^2)$.

We focus only on the linear interaction with the x-motion in the Langevin equations:

$$\begin{aligned}
\dot{\hat{p}} &= -m\Omega_x^2 \hat{x} - \gamma_m \hat{p} - \hbar \frac{g_x}{x_{zpf}} \sin kx_0 \left(\hat{a}^\dagger + \hat{a}\right) + F_{th}(t) \\
\dot{\hat{x}} &= \frac{\hat{p}}{m} \\
\dot{\hat{a}} &= -\left(\frac{\kappa}{2} + i\Delta'\right)\hat{a} + iE_d \cos kx_0 - i\frac{g_x}{x_{zpf}} \sin kx_0 \, \hat{x} + \\
&+ \sqrt{\kappa_{nano}(x_0)}\hat{a}_{tw} + \sqrt{\kappa_{in}}\left(\hat{a}^1_{\mathrm{IN}} + \hat{a}^2_{\mathrm{IN}}\right). \qquad (5.40)
\end{aligned}$$

The cavity is driven by the coherently scattered light with a rate $E_d \cos kx_0$. As a result, the cavity operators include a coherent amplitude α_0 as $\hat{a} \to \alpha_0 + \hat{a}$, where:

$$\alpha_0(x_0) = \frac{iE_d \cos kx_0}{\frac{\kappa}{2} + i\Delta'}, \qquad n_{\mathrm{phot}} = |\alpha_0|^2. \qquad (5.41)$$

Here we see how the cavity field is created from the scattering of the trapping laser into the cavity mode. Interestingly, the maximum coupling is reached for $\sin kx_0 = \pm 1$, which implies that the cavity mode remains empty $n_{\mathrm{phot}} \propto \cos kx_0 = 0$. We will investigate later how this impacts the heating by the phase noise.

After the operator displacement and only up to first order in the operators, the Langevin equations become:

$$\begin{aligned}
\dot{\hat{a}} &= -\left(\frac{\kappa}{2} + i\Delta'\right)\hat{a} - i\frac{g(x_0)}{x_{zpf}}\hat{x} + \sqrt{\kappa_{nano}}\hat{a}_{tw} + \sqrt{\kappa_{in}}\left(\hat{a}^1_{\mathrm{IN}} + \hat{a}^2_{\mathrm{IN}}\right) \\
\ddot{\hat{x}} &= -\gamma_m \dot{\hat{x}} - \Omega_0^2 \hat{x} + \frac{\hbar g(x_0)}{x_{zpf}}\left(\hat{a}^\dagger + \hat{a}\right) + f_{th}(t). \qquad (5.42)
\end{aligned}$$

The procedure to solve the system of equations shown above was explained in detail in Chapter 2. In conclusion, the coherently scattered light into the cavity mode leads to cavity cooling of the nanosphere x-motion for a trapping laser red-detuned with respect to the cavity resonance.

5.2.3 *Interaction with the z-motion*

The dominant interaction with the z-motion arises from the trapping laser phase $kz + \varphi_G(z)$, where $\varphi_G(z) = -\arctan(z/z_R)$ is the Gouy phase shift. For a tightly focused laser both the plane-wave phase shift kz and the Gouy phase have to be taken into account as they are

[11] The ratio of the two contributions is $kz_R = q$

of comparable magnitudes[11]. In the Lamb-Dicke regime (for small nanosphere motion $k\sqrt{\langle z^2\rangle} \ll 1$), the trapping laser electric field is approximately:

$$E_{tw}(x,y,z) = E_{tw}\left[1 + i\left(k - \frac{1}{z_R}\right)\hat{z} - \frac{(k-1/z_R)^2}{2}\hat{z}^2 + \mathcal{O}(\hat{z}^3)\right]. \tag{5.43}$$

The linear and quadratic rates are then $g_z = E_d(k - 1/z_R)z_{zpf}$ (for our parameters: $g_x/2\pi \approx 130$ kHz) and $g_{z,q} = E_d(k-1/z_R)^2 z_{zpf}^2/2$, respectively. The optomechanical interaction to both $\hat{z}$ and $\hat{z}^2$ is maximum at the cavity antinode:

$$\hbar\left[\left(E_d + \frac{g_{z,q}}{z_{zpf}^2}\hat{z}^2\right)\left(\hat{a}^\dagger + \hat{a}\right) + i\frac{g_z}{z_{zpf}}\hat{z}\left(\hat{a}^\dagger - \hat{a}\right)\right]\cos kx_0. \tag{5.44}$$

Additional coupling rates are:

- Linear coupling from the tilt ϕ of the trapping laser:

$$\hbar(\hat{a}^\dagger + \hat{a})\underbrace{E_d k z_{zpf}\sin\phi}_{g_z^{(1)}}\sin kx_0\frac{\hat{z}}{z_{zpf}} \tag{5.45}$$

- Quadratic coupling due to the waist function of the trapping laser:

$$-\hbar(\hat{a}^\dagger + \hat{a})\underbrace{E_d\frac{z_{zpf}^2}{2z_R^2}}_{g_{z,q}^{(1)}}\cos kx_0\frac{\hat{z}^2}{z_{zpf}^2} \tag{5.46}$$

- Quadratic coupling from the Gaussian envelope of the cavity mode is neglected as the cavity waist $w_0^{-1} \ll W_0^{-1}, k$.

The system dynamics including the z-motion is well described by the following equations:

$$\begin{aligned}
\dot{\hat{a}} &= -\left(\frac{\kappa}{2} + i\Delta'\right)\hat{a} - iE_d k\sin kx_0\,\hat{x} - E_d k\cos kx_0\,\hat{z} \\
&+ \sqrt{\kappa_{nano}}\hat{a}_{tw} + \sqrt{\kappa_{in}}\left(\hat{a}_{\mathrm{IN}}^1 + \hat{a}_{\mathrm{IN}}^2\right) \\
\ddot{\hat{z}} &= -\gamma_m\dot{\hat{z}} - \Omega_z^2\hat{z} + i\frac{\hbar E_d k}{m}\cos kx_0\left(\hat{a}^\dagger - \hat{a}\right) + f_{th}^z(t).
\end{aligned} \tag{5.47}$$

The cavity cooling of the z-motion is maximal for the nanosphere positioned at $\cos kx_0 = \pm 1$ (intensity maximum), in the contrast to the optimal position for the cavity cooling of the x motion (intensity minimum) [Leibrandt et al., 2009]. At the intensity maximum, the coupling to the x motion is intrinsically quadratic, which we will demonstrate in the following.

The nanosphere z-motion is:

$$\tilde{z}\left((\Omega_0^z)^2 - \omega^2 + i\gamma_m\omega - i\frac{\hbar(E_d k)^2}{m}\left(\chi_c^*(-\omega) - \chi_c(\omega)\right)\right) = \tilde{f}_{th}^z, \tag{5.48}$$

which leads to cavity cooling for the red-detuned trapping laser. For a nanosphere positioned somewhere between the intensity maximum and minimum, it is expected to have cavity cooling of both x- and z-motion.

5.2.4 *Coupling to the motion along the y-axis*

A rotation of the linear polarization of the trapping laser by an angle $\alpha/2$ leads to a rotation of the trapping potential by α, while the fundamental mechanical frequencies are unchanged (Appendix C). We define the motion along the potential semi-major and semi-minor axes as $u(t)$ and $v(t)$ with the mechanical frequencies Ω_x and Ω_y, respectively. The projections of the motion onto the x- and y-axis (defined by the cavity axis in case $\alpha = 0$):

$$x = u\cos\alpha + v\sin\alpha, \qquad y = u\sin\alpha - v\cos\alpha. \tag{5.49}$$

Rotation by an angle $\alpha = 45^\circ$ allows for an equal coupling of both u- and v-motion to the cavity mode. Due to the optomechanical interaction being originally along the cavity axis, only the projections of these motions to the cavity axis will be cooled.

Let us assume the optimal position of $\sin kx_0 = 1$ for cavity cooling of the motion along the x-axis. The Hamiltonian $\hat{H}^2_{OM}$ of the interaction with the u- and v-motion projected onto the cavity axis is:

$$\hat{H}^2_{OM} = \frac{\hbar E_d k}{\sqrt{2}}\left(\hat{u}+\hat{v}\right)\left(\hat{a}^\dagger + \hat{a}\right), \tag{5.50}$$

with the system dynamics described by the following Langevin equations:

$$\begin{aligned}
\ddot{\hat{u}} + \gamma_m\dot{\hat{u}} + \Omega_x^2\hat{u} - \frac{\hbar E_d k}{\sqrt{2}m}\left(\hat{a}^\dagger + \hat{a}\right) &= f^u_{th}\\
\ddot{\hat{v}} + \gamma_m\dot{\hat{v}} + \Omega_y^2\hat{v} - \frac{\hbar E_d k}{\sqrt{2}m}\left(\hat{a}^\dagger + \hat{a}\right) &= f^v_{th}\\
\dot{\hat{a}} + \left(\frac{\kappa}{2} + i\Delta\right)\hat{a} - i\frac{E_d k}{\sqrt{2}}(\hat{u}+\hat{v}) &\approx 0.
\end{aligned} \tag{5.51}$$

The sum and the difference of the first two equations yields:

$$\begin{aligned}
\overbrace{(\ddot{\hat{u}}+\ddot{\hat{v}})}^{\ddot{x}} + \gamma_m\overbrace{(\dot{\hat{u}}+\dot{\hat{v}})}^{\dot{x}} + (\Omega_x^2\hat{u}+\Omega_y^2\hat{v}) - 2\frac{\hbar E_d k}{\sqrt{2}m}\left(\hat{a}^\dagger+\hat{a}\right) &= f^u_{th}+f^v_{th}\\
\overbrace{(\ddot{\hat{u}}-\ddot{\hat{v}})}^{\ddot{y}} + \gamma_m\overbrace{(\dot{\hat{u}}-\dot{\hat{v}})}^{\dot{y}} + (\Omega_x^2\hat{u}-\Omega_y^2\hat{v}) &= f^u_{th}-f^v_{th}.
\end{aligned}$$

This shows that two-dimensional cooling is possible only in the case of non-degenerate frequencies $\Omega_x \neq \Omega_y$. Otherwise, the projected dynamics along the y-axis remains unaffected by the cavity mode.

5.2.5 *Phase noise heating*

The phase noise contributes to the heating of the nanosphere motion, as shown in Section 2.3.1. It is commonly included as a small phase modulation $\varphi(t)$ of the cavity drive, which in this case leads to the most general electric field of the trapping laser $E_{tw} \rightarrow E_{tw}e^{i\varphi(t)}e^{ik\hat{z}}$. From Equation (2.67) the minimum phonon occupation due to phase noise heating is:

$$\bar{n}^{phase} = \frac{n_{\text{phot}}}{\kappa} S_{\dot{\varphi}\dot{\varphi}}(\Omega_0), \tag{5.52}$$

where Ω_0 is the relevant mechanical frequency and $n_{\text{phot}} = \frac{E_d^2 \cos^2(kx_0)}{(\kappa/2)^2+\Delta^2}$ is the intracavity photon number from the coherently scattered light, which depends on the nanosphere position x_0.

We calculate the expected cavity drive $E_d/2\pi \approx 2.9 \times 10^9$ Hz from our current parameters ($P_{in} = 0.17$ W, $W_0 \approx 0.7$ μm, $r = 71.5$ nm). For a drive resonant to the cavity and the nanosphere positioned at the cavity antinode ($\cos kx_0 = 1$), the coherently scattered light will be enhanced to $n_{\text{phot}} \approx 8.8 \times 10^8$ photons in the cavity mode. This is smaller than the maximum intracavity photon number with the conventional cavity drive ($n_{\text{phot}} \approx 1.9 \times 10^9$) that we reached in Chapter 4.

The phase noise heating of the x-motion depends on how well the nanosphere is positioned in the vicinity of the cavity node. In principle, for a nanosphere placed precisely at the cavity node ($\cos(kx_0) \equiv 0$) no phase noise heating will occur. In practice, we can position the nanosphere with the nanopositioner (average step size of $\sim$ 8 nm) within 4 nm from the cavity node, resulting in a contribution to the phonon occupation from the phase noise heating of:

$$\bar{n}_x^{phase} = \frac{E_d^2 \cos^2\left(k\left(\frac{\lambda}{4} + 4\text{ nm}\right)\right)}{\kappa\left(\left(\frac{\kappa}{2}\right)^2 + \Omega_x^2\right)} \underbrace{S_{\dot{\varphi}\dot{\varphi}}(\Omega_x)}_{0.0023\text{ Hz}^2/\text{Hz}} \approx 2 \times 10^{-3}. \tag{5.53}$$

This shows that for a sufficiently stable setup we don't expect the phase noise heating to have a strong effect on the nanosphere x-motion. On the other side, the cavity mode is coupled to the nanosphere z-motion at the cavity antinode. There, the phase noise heating of an unfiltered solid state laser will provide a hard limit on the phonon occupation of the z-motion:

$$\bar{n}_z^{phase} = \frac{E_d^2}{\kappa\left(\left(\frac{\kappa}{2}\right)^2 + \Omega_z^2\right)} \underbrace{S_{\dot{\varphi}\dot{\varphi}}(\Omega_z)}_{0.05\text{ Hz}^2/\text{Hz}} \sim 10^2. \tag{5.54}$$

5.2.6 *Quadratic cavity cooling of the x-motion*

The quadratic coupling of the x-motion has already been discussed in the case of standard optomechanics in Chapter 2 and the single

photon quadratic coupling rate $g_q/2\pi \approx 8$ μHz was measured in Chapter 3. With a total coupling of around $g_t^q = g_q\sqrt{n_{phot}}/2\pi \approx 0.25$ Hz, cavity cooling via the quadratic optomechanical coupling will be considerably weak.

Cavity cooling by coherent scattering provides a 10 times stronger quadratic coupling rate of the x-motion with $g_t^q/2\pi \approx 2.4$ Hz. It is still too small to achieve an appreciable cooling rate:

$$\Gamma_-^q = (g_t^q)^2\kappa \left| \frac{1}{\frac{\kappa}{2} - i(-2\Omega_m + \Delta)} \right|^2 \overset{\Delta=2\Omega_m}{\approx} 2\pi \times 10^{-4} \text{ Hz}. \tag{5.55}$$

For comparison, the recoil heating rate is on the order of 10^4 Hz. However, in a special case of $\gamma_m \ll \Gamma_-^q n_{th}$ a change of phonon distribution results in an effective cooling of the nanosphere motion [Nunnenkamp et al., 2010]. In this case, the mean phonon number of the cooled state is:

$$\bar{n} = \sqrt{\frac{\gamma_m n_{th}\kappa}{\pi(g_t^q)^2}}. \tag{5.56}$$

The effect is valid already for $\gamma_m/2\pi < 4$ kHz, which is satisfied at pressures below $p = 4$ mbar. In high vacuum ($p = 10^{-6}$ mbar) we expect a mean phonon occupation of $\bar{n} \approx 2 \times 10^4$, which is cooling by around a factor of 10^3 from the thermal occupation n_{th} with only quadratic coupling.

5.2.7 *Impact of the cavity birefringence on the cavity cooling*

Induced by stress or by manufacturing imprecisions, Fabry-Pérot cavities frequently exhibit birefringence. Birefringence is usually recognized by two different resonance frequencies ω_{cav} depending on the laser polarization. Furthermore, depending on the direction of the applied stress and the mirror symmetry, the polarization axes of the non-degenerate cavity modes are in general a combination of the vertical and the horizontal polarization defined in the laboratory frame:

$$V \to \sin\Phi\ \mathrm{H} + \cos\Phi\ \mathrm{V} \qquad H \to \cos\Phi\ \mathrm{H} - \sin\Phi\ \mathrm{V}, \tag{5.57}$$

where Φ is the angle of the polarization plane rotation.

In order to maximize the dipole scattering into the cavity in our current geometry, the trapping laser has to be polarized vertically, i.e. along the y-axis. In principle, the scattered light could drive both birefringent cavity modes. Therefore, the birefringence angle and the splitting of the cavity resonances $\omega_{cav}^1 - \omega_{cav}^2$ are crucial for a successful and strong cavity cooling. For example, in the case of a non-zero birefringence angle $\Phi \neq 0$, the trapping laser has to be red-detuned from both cavity modes, as the cavity drive with frequency in between the resonances at ω_{cav}^1 and ω_{cav}^2 could lead to a net heating of the nanosphere motion. Therefore, we characterize the cavity birefringence in Section 6.1.1.

5.2.8 *Optomechanical cooperativity*

At sufficiently low pressures ($p < 10^{-7}$ mbar), heating of the nanosphere motion is given by the recoil heating of the trapping laser:

$$\Gamma_{rec}^{tw} = \frac{4}{5}\frac{\omega_l}{\Omega_x}\frac{I_{in}}{mc^2}\frac{k^4|\alpha|^2}{6\pi\varepsilon_0^2} = \frac{2}{15}\frac{k^2 w_0^2}{\Delta\nu_{FSR}}\underbrace{E_d^2 k^2 x_{zpf}^2}_{g_x^2}, \tag{5.58}$$

where I_{in} is the trapping laser intensity. As it turns out, the optomechanical cooperativity $C = \frac{4g_x^2}{\kappa\Gamma_{rec}^{tw}}$ depends only on the cavity finesse and the waist:

$$C = \frac{30\mathcal{F}/\pi}{k^2 w_0^2} = \frac{5}{4}\eta, \tag{5.59}$$

where η is the Purcell factor. The limit to the cavity cooling is then given only by the Purcell factor as well as $\bar{n} = (\kappa/4\Omega_x)^2 + C^{-1} = (\kappa/4\Omega_x)^2 + 5/(4\eta)$. Already for the current cavity with the finesse $\mathcal{F} = 73,000$ and waist $w_0 = 41.1\mu$m we calculate $C \approx 11$, a significant improvement over the cooperativity reached in the dispersive regime.

5.3 CONCLUSION

5.3.1 *Benefits of the coherent scattering in comparison to the standard optomechanics*

Here we compile a list of the benefits of cavity cooling by coherent scattering compared to the dispersive regime from Chapter 2. We focus only on the nanosphere x-motion if not explicitly mentioned otherwise.

1. **Each photon that scatters into the cavity mode has to interact with the nanosphere.** The direct consequence of this is that we expect a clean detection of the cavity photons. For example, in the heterodyne detection of the scattered photons we will observe only the Stokes and anti-Stokes photons, without a contribution at the trapping laser frequency. In the dispersive regime we are limited in detection by the non-interacting cavity photons, which add classical- and shot noise into the detection.

2. **Increased coupling rate.** In the dispersive regime, the optomechanical interaction is given by the cavity mode area at the nanosphere position, i.e. $g \propto w_0^{-2}$. For coherent scattering the trapping laser is focused onto a much smaller waist $W_0 < w_0$, such that the interaction is effectively increased to $g \propto (w_0 W_0)^{-1}$. For example, the cavity drive required to reach equal coupling rates in the dispersive regime is $E_d^{disp}/2\pi \approx 4 \times 10^{10}$ Hz, an order of magnitude higher compared to the drive by coherent scattering.

3. **Coupling to the electric field of the cavity mode.** Due to this, the optimal position for cavity cooling of the motion along the cavity axis is at the cavity node. This has several beneficial consequences for the system dynamics:
   - The Cavity is not populated by the coherently scattered light, i.e. it remains empty.
   - As the cavity is empty, there is no co-trapping of the nanosphere with the cavity. Therefore, the nanosphere position doesn't have to be optimized if we change the cavity drive E_d.
   - The laser phase noise doesn't couple to the cavity as the cavity is empty. In principle, it is possible to completely suppress the heating of the nanosphere x-motion by the phase noise, while it provides an ultimate limit of the phonon occupation in standard optomechanics as the cavity is strongly driven.
4. **Multi-dimensional cavity cooling.** The scattering process happens in a plane defined by the x- and z-axis, therefore the cavity cools the nanosphere motion along both axes. In principle, we can extend the scheme to a genuine three-dimensional cavity cooling by rotating the trap.

5.3.2 *Summary of the position-dependent optomechanical effects*

In this section we aim to provide an overview of the optomechanical effects depending on the nanosphere position.

1. **Cavity node or intensity minimum.**
   - Strong cavity cooling of the x-motion (and y-motion).
   - Weak cavity cooling of the z-motion.
   - Intracavity photon number n_{phot} is zero.
   - No heating of the x-motion due to phase noise.
2. **Cavity antinode or intensity maximum.**
   - Weak cavity cooling of the x-motion (and y-motion).
   - Strong cavity cooling of the z-motion.
   - Intracavity photon number n_{phot} is maximum.
   - Strong heating of the z-motion due to phase noise.

In contrast, in the dispersive regime the highest coupling rate to the x-motion is for a nanosphere positioned at the maximum intensity gradient, i.e. halfway between a cavity node and an antinode. The z-motion can be coupled to the cavity mode as well by tilting the trapping axis, albeit with a significantly smaller coupling rate.

6

CAVITY COOLING BY COHERENT SCATTERING: EXPERIMENT

Cavity cooling by coherent scattering promises many advantages over optomechanics in the dispersive regime. To name a few: higher coupling rates, three-dimensional cavity cooling and the suppression of phase noise heating are all extremely encouraging. Here we demonstrate all the predicted behavior from the previous Chapter. We first focus on the applied modifications to the experimental setup and the four different detection schemes employed to follow the nanosphere dynamics. We investigate in particular the position-dependent and polarization-dependent cavity cooling by coherent scattering, confirming all theoretical predictions. We estimate the phase noise suppression based on the determined cavity drive and nanosphere position. We end the chapter with a brief outlook on interesting future experiments.

Contents

6.1 EXPERIMENTAL SETUP

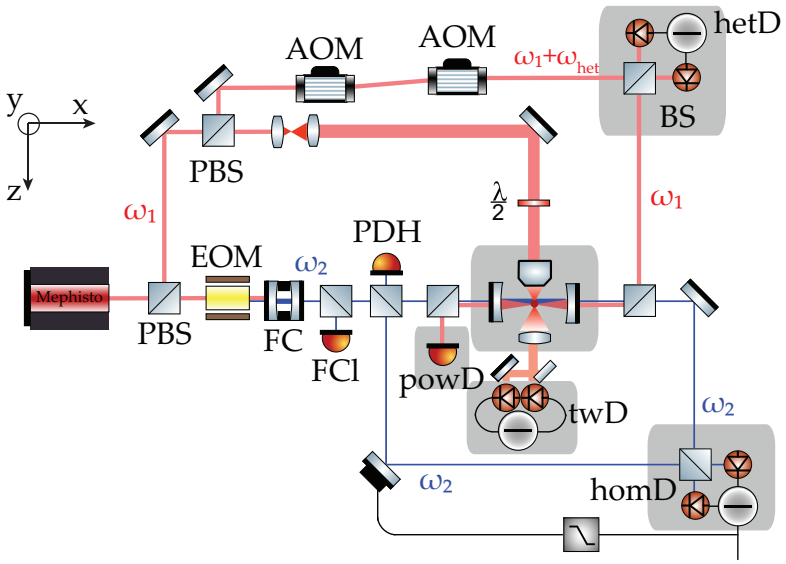

Figure 6.1: **The experimental setup for cavity cooling by coherent scattering.** A laser (Mephisto, frequency ω_1) is focused with a microscope objective and used for trapping of a nanosphere. We set the direction of the dipole scattering by changing the linear polarization of the trapping laser with a half waveplate ($\lambda/2$). The trapping laser is sampled in the trap transmission to detect the three-dimensional nanosphere motion (twD). A part of the principal laser is polarized horizontally and shifted in frequency with an electro-optical modulator (EOM) to $\omega_2 = \omega_1 + 2\pi \times \Delta\nu_{FSR} + \Delta$ and locked to a cavity resonance by directly changing the laser frequency ω_1. The phase quadrature of the locking cavity mode, which is coupled to the nanosphere axial motion through conventional optomechanics, is detected in the cavity transmission with a homodyne detection (homD). The intracavity power of the enhanced coherent scattering is monitored on a single photodiode in the transmission of one of the cavity mirrors (powD). The coherently scattered light leaked through the other cavity mirror is modulated with a far detuned laser at ω_{het}. The resulting signal is detected with a balanced photodetector and forms a heterodyne measurement of the nanosphere motion (hetD).

6.1.1 *Optical driving scheme*

In Section 3.1.5 we described the preparation of the control laser. It is detuned by a free spectral range $\Delta\nu_{FSR}$ from the principal laser frequency ω_1, which is already locked to a cavity resonance at $\omega_{cav}^{(1)}$. The control laser at ω_2 passes a filter cavity, which is locked to transmit only the desired laser mode. Instead of driving the cavity, we could amplify it and use as the trapping laser. However, a sudden loss of the filter cavity lock can result in a shutdown of the fiber amplifier and the subsequent loss of the trapped nanosphere. Therefore, we decided on using the detuned mode to lock the laser to the cavity

(Figure 6.1). The principle laser doesn't pass any frequency modifying elements, which makes it ideal to be used as the trapping laser. We describe the setup in the following.

Let us assume that the laser frequency ω_1 is in the vicinity of a cavity resonance at frequency $\omega_{cav}^{(1)}$. As before, we detune the laser frequency from the principal laser by $\omega_2 - \omega_1 = 2\pi \times \Delta\nu_{FSR} + \Delta$ with an EOM, close to the adjacent longitudinal cavity resonance at frequency of $\omega_{cav}^{(2)}$. The EOM also creates the PDH sidebands at ± 6 MHz, well within the linewidth of the filter cavity κ_{FC}. The selected modes (the carrier mode at ω_2 with the PDH sidebands) drive the optomechanical cavity. In the cavity reflection we set up a PDH detector, which provides an error signal used to stabilize the laser directly to the cavity.

The locking works as follows: The lock reacts to a variation in the cavity resonance frequency by following with the principal laser frequency ω_1. Let's assume we manually change the detuning Δ by $\delta\omega$, upon which the lock changes the laser frequency to $\omega_1 - \delta\omega$ to compensate. Consequently, the detuning of the principal laser mode with respect to its cavity resonance (at $\omega_{cav}^{(1)}$) is effectively changed by the amount $-\delta\omega$. The frequency deviation $\delta\omega$ must not be large or the lock won't be able to follow the change due to the slower response of the filtering cavity. In practice, jumps in detuning below 10 MHz are fine.

We split off a part of the principal laser and amplify it in order to use it as the trapping laser. Although, the trapping and the control laser are the same in this setup, we still separate the optical paths by referring to the trapping laser as the "driving mode" and to the cavity mode populated by the scattered photons as the "scattering mode".

Cavity birefringence

In Section 5.2.7 we mentioned that a birefringent cavity might have polarization axes that don't conform to the horizontally and vertically polarized light in the laboratory frame. This would lead to suboptimal coherent scattering as the scattered light would drive two cavity modes with different polarizations. We devise a setup to characterize the linearly polarized light leaking out of the cavity (Figure 6.2). We first place a half-wave plate ($\frac{\lambda}{2}$) in front of the cavity input mirror to set a particular linear polarization of the driving laser. We use the PDH detector in the cavity reflection to optimize the polarization such that we drive and lock to the horizontally polarized cavity resonance.

In cavity transmission we have a polarizing beamsplitter (PBS) with detectors DET1 and DET2 monitoring the beamsplitter transmission and reflection outputs, respectively. The distribution of laser power between the two arms is proportional to the ratio of the horizontal

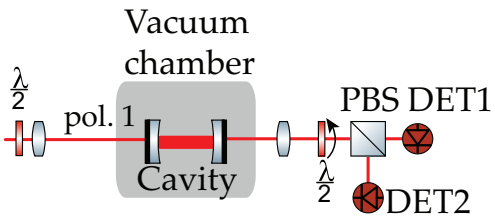

Figure 6.2: **The experimental setup to characterize the cavity polarization axes.** The optical cavity can experience birefringence, which is typically observed as the presence of two distinct cavity resonances with orthogonal polarizations. We use a half-wave plate ($\frac{\lambda}{2}$) in front of the cavity input mirror to drive only one of the birefringent cavity modes with polarization "pol.1". In the cavity transmission we set up a polarizing beamsplitter (PBS) and detectors DET1 and DET2, which we use to measure the ratio of the horizontal and vertical polarization in the locked cavity mode. A rotatable half-wave plate in cavity transmission is used to scan the full range of linear polarizations in detection.

and vertical polarization in the cavity resonance. In addition, we set up a rotatable half-wave plate such that we can detect all linear polarizations and calibrate the detection for fully horizontal and vertical polarizations. In Figure 6.3 we present the measurement of the cavity mode polarization from the optical powers detected by DET1 and DET2. A "scan" measurement is done by rotating the half-wave plate in cavity transmission, while a "pure" measurement shows that the examined cavity mode is horizontally polarized, i.e. that the symmetry axes of the cavity birefringence are aligned with horizontal and vertical in the laboratory frame. We might have expected this, as the mirror circular symmetry is broken by cutting the mirrors into strips. Additionally, we set the mirrors into place with a single screw applying pressure (and stress) along the vertical axis from the top. This is the optimal configuration for the cavity polarization axes, as the light scattered off the vertically polarized driving mode will be collected in a single, vertically polarized cavity mode.

We then check the frequency difference between the birefringent modes. As done in Chapter 3 we lock the laser with frequency ω_1 at an arbitrary polarization (horizontal or vertical) to a cavity resonance at $\omega_{cav}^{(1)}$. An orthogonally polarized laser at ω_2 is detuned by roughly the free spectral range $\Delta\nu_{FSR}$ and is driving the adjacent longitudinal cavity resonance at $\omega_{cav}^{(2)}$. By scanning the detuning over the cavity resonance $\omega_{cav}^{(2)}$ we are able to deduce the detuning $\sim \Delta\nu_{FSR}$ between the two longitudinal cavity modes. For example, if the lock mode is vertically polarized, the measured frequency will be $\Delta\nu_{FSR} + \nu_{bf}$, where ν_{bf} is the cavity birefringence frequency, i.e. the separation of a split longitudinal mode (Figure 6.4). In the other case of initial polarizations, reached by rotating the half-wave plate in front of the cavity, we will measure $\Delta\nu_{FSR} - \nu_{bf}$. We calculate the birefringence

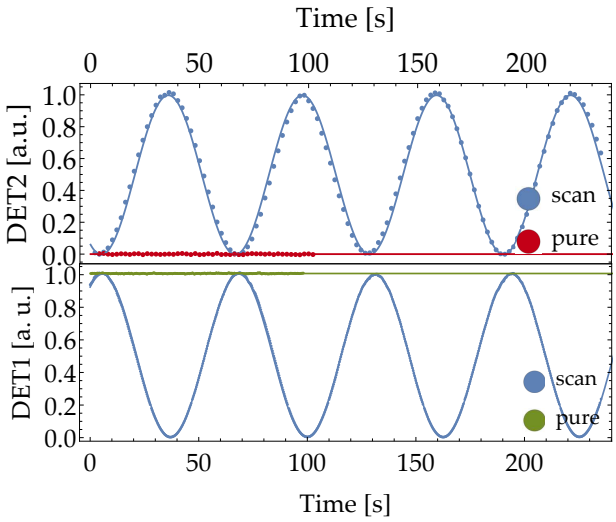

Figure 6.3: **Measurement of the cavity polarization axes.** We rotate the half-wave plate in the cavity transmission to scan the whole range of linear polarizations in the detection (blue data in the lower and upper panels), with minimum and maximum detector voltage recalibrated to 0 and 1, respectively. Upon removing the tunable half-wave plate in the cavity transmission, we are able to characterize the pure polarization of the locked cavity mode. We detect all the optical power in the PBS transmission (green, lower panel) and no power in the PBS reflection (red, upper panel), proving that the examined cavity mode is horizontally polarized. The cavity birefringence thus splits a longitudinal mode into the horizontally and vertically polarized cavity modes.

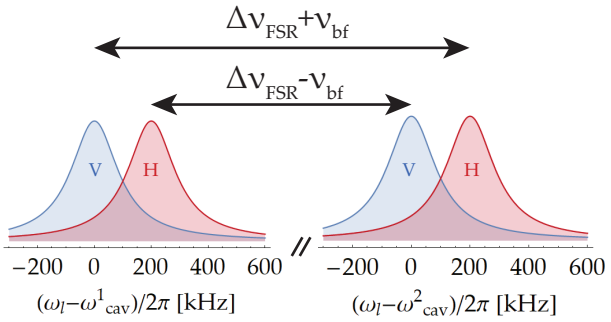

Figure 6.4: **Measurement of the cavity birefringence frequency.** The free spectral range frequency is always measured as a spacing of orthogonally polarized successive cavity resonances. Cavity resonances are split by the birefringence frequency ν_{bf}, which modifies the real free spectral range by $\pm\nu_{bf}$. By rotation of the half-wave plate in front of the cavity input, we are able to choose the locking mode polarization and extract the birefringence frequency from the difference of two orthogonally polarized drive modes.

frequency $\nu_{bf} \approx 200$ kHz from the free spectral range measurements. Additionally, we determine that the vertically polarized mode has the lower resonance frequency, as shown in Figure 6.4. Hence, a

laser resonant to the vertically polarized mode (required for coherent scattering) will be red detuned from the horizontally polarized mode. The reverse configuration might lead to heating of the nanosphere motion if the scattered mode is not purely vertically polarized.

6.1.2 *Overview of the detection schemes*

We operate four distinct detection schemes in order to follow the full system dynamics:

1. **Detection of the trapping laser (twD).** This detection is ideal to measure the relative change of the motional temperature as the detection sensitivity is independent of the nanosphere position along the cavity axis x_0. The detection of the nanosphere z-motion from the trapping laser is unmodified compared to the setup described in Section 3.2. The detection schemes used to detect the x- and y-motion are slightly modified to attain a separate detection of the two-dimensional motion even in a rotated trap potential. This is achieved by placing the D-shaped mirror, used to split the laser mode, on a rotation stage.

2. **Homodyne detection of the locking mode (homD).** We use homodyne detection to monitor the phase quadrature of the locking mode, as described in Section 3.3. For that purpose, we split off a part of the control laser immediately after the filter cavity and use it as a local oscillator (Figure 6.1). The best detection of the nanosphere motion is at the largest intensity gradient as $S_{hom} \propto g_{lock}^2 \propto \sin^2(2kx_0)$.

3. **Heterodyne detection of the scattered mode (hetD).** A spectrally resolved detection of the scattered photons (heterodyne detection) is used to distinguish between the Stokes (heating) and Anti-Stokes (cooling) photons, which are attenuated and amplified by the cavity response, respectively. The detected spectrum is of the following form:

$$S_{het}(\omega) \propto g_z^2 \cos^2 kx_0 S_{zz}(\omega) + g_x^2 \sin^2 kx_0 S_{xx}(\omega). \tag{6.1}$$

4. **Direct detection of the scattered photons (powD).** The optical power of the photons leaking through one of the cavity mirrors is detected with a photodiode. From it we can extract the built-up intracavity power P_{cav} and deduce the nanosphere position along the cavity axis as:

$$P_{cav} \propto \cos^2 kx_0. \tag{6.2}$$

In the following sections we focus on the last two detection schemes.

6.1.3 *Heterodyne detection*

Theoretical description

A frequency shifted local oscillator at a frequency $\omega_{het} + \omega_1$ is used to amplify the cavity signal in the heterodyne detection scheme. It is important that $\omega_{het} \gg \Omega_{x,y,z}$ in order to observe both motional sidebands generated by the optomechanical interaction. Note that, compared to the homodyne detection, the phase in the heterodyne detection is constantly oscillating with the same frequency ω_{het}. Therefore, this detection is sensitive to both phase and amplitude quadratures of the cavity mode, albeit with a twice lower sensitivity due to averaging the quadratures over time. As a result, the heterodyne detection is able to detect both x- and z-motion as they are coupled to the cavity phase and amplitude quadrature, respectively (Chapter 5). The spectrum of the heterodyne detection involving only the linear interaction is:

$$S_{het}(\omega) \propto |\chi_c(\omega)|^2 \left[\left(\frac{g_x}{x_{zpf}} \right)^2 S_{xx}(\omega) + \left(\frac{g_z}{z_{zpf}} \right)^2 S_{zz}(\omega) \right], \quad (6.3)$$

where $\chi_c(\omega) = 1/(\kappa/2 + i(\omega - \Delta))$ is the detuning-dependent susceptibility of the cavity mode.

Experimental realization

We split off some of the principal laser mode directly after the laser to create a local oscillator for the heterodyne detection. Two AOMs change the laser frequency by their difference in RF drive frequency: The first AOM initially changes the frequency by ~ -190 MHz, while the second one applies a positive frequency shift by ~ 210 MHz. As a result, the local oscillator ($P_{LO}^{het} \approx 200$ μW) will be detuned by the heterodyne frequency $\omega_{het}/2\pi \approx 20$ MHz from the frequency of the scattered light. The cutoff of the balanced heterodyne detector (Thorlabs PDB425-AC) is at 75 MHz, well above the heterodyne frequency. The local oscillator and the scattered mode leaking through one of the cavity mirrors are mixed in a fiber beamsplitter with the splitting ratio of roughly 50:50. The heterodyne signal is the difference of the power in both output arms.

In an ideal case, the noise floor of the heterodyne detection should be defined entirely by the local oscillator shot noise (shot noise limited in detection) [Bachor and Ralph, 2004]. However, we expect the AOM drivers to add a substantial amount of intensity noise. We check the total noise of the local oscillator by completely blocking the scattered mode and the optical path to one of the detector photodiodes, allowing us to obtain the intensity noise of just the local oscillator. We notice that the driver-induced intensity noise is the dominant noise component in the band 0-10 MHz (Figure 6.5). We repeat the measurement after unblocking the optical path to the second photodiode

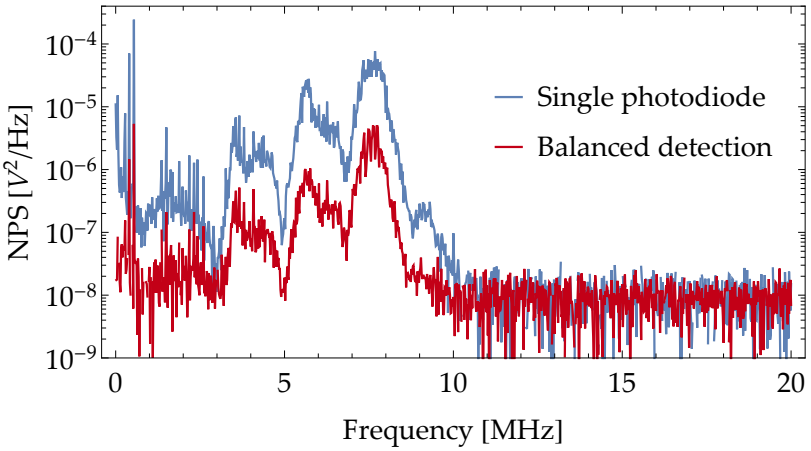

Figure 6.5: **Laser intensity noise induced by AOMs.** The AOM drivers introduce a large noise contribution to the laser intensity noise in the bandwidth $0-10$ MHz (blue). The intensity noise is decreased in the balanced detection by ~ 10 dB (red), limited by the beamsplitter ratio.

and measure a suppression of ~ 10 dB of the intensity noise due to common-mode rejection of the balanced detector. The low suppression is due to the actual measured beamsplitter ratio of 47.6:52.4, far from the ideal 50:50.

We then check that the detection is shot noise limited in the range around the designated heterodyne frequency $\omega_{het}/2\pi \approx 20$ MHz. For this purpose, we measure the spectrum of the balanced detection in the range 15-25 MHz with only the local oscillator (Figure 6.6(a)). The integrated spectral power is changing linearly with the local oscillator power (Figure 6.6(b)), such that the shot noise limit in detection is confirmed.

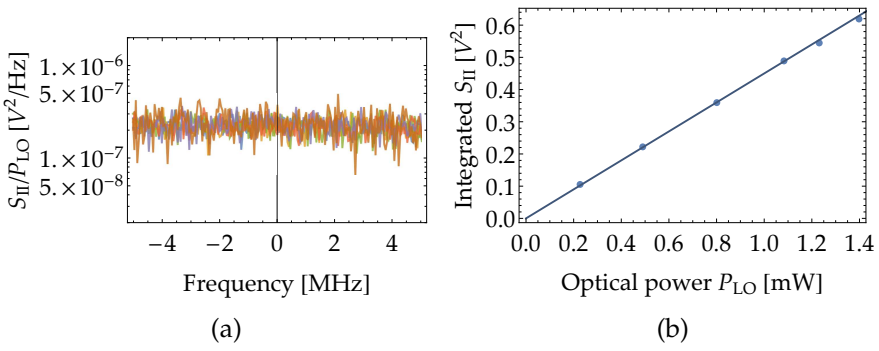

Figure 6.6: **Characterization of the shot noise around the heterodyne center frequency in the heterodyne detection.** (a) Spectra of the heterodyne detection normalized to the power of the local oscillator P_{LO}. Calibrated spectra for different P_{LO} overlap, demonstrating that the noise background is the shot noise. (b) The integrated unnormalized measured power spectrum shows a linear dependence on the power of the local oscillator, as we would expect from the shot noise.

6.1.4 *Direct detection of the coherently scattered light*

The coherently scattered light that is transmitted through the left mirror in Figure 6.1 is collected on a single photodiode (Thorlabs, SM05PD4A) with the signal current amplified by a transimpedance amplifier (Femto DHPCA). We detect the power of the cavity-enhanced scattered light on this detector, which is useful to optimize the nanosphere position along the cavity axis. For example, we know from Chapter 5 that the destructive (constructive) interference of the coherent scattering occurs for a nanosphere placed at the cavity node (antinode). Note that we neglect the Stokes and Anti-Stokes photons as we use a low pass filter to isolate only the cavity-enhanced light at the driving laser frequency. However, this optical path can be combined with the existing heterodyne detection in order to use all available information about the motion, effectively doubling our detection efficiency.

6.2 EXPERIMENTAL RESULTS

6.2.1 *Polarization dependent cavity cooling*

Due to the directionality of the dipole radiation, both the cavity drive and the cavity cooling can be modified by changing the tweezer polarization θ. For example, for a tweezer polarized along the cavity axis ($\theta = 0$), we expect a suppression of coherently scattered light by a factor of $|\beta_{min}|^2 \approx 10^4$. As discussed in Section 5.1.1, due to the tilted tweezer axis by an angle ϕ the signal will be suppressed by a factor $\sin^{-2}\phi \approx 10^2$ (compared to the case of optimal coherent scattering for $\theta = \pi/2$).

We directly observe the polarization-dependent suppression of coherent scattering in the heterodyne detection (Figure 6.7). We detune the trapping laser by $\Delta = 2\pi \times 4$ MHz to avoid affecting the nanosphere motion. We compare the heterodyne spectra for maximum ($\theta = \pi/2$) and minimum scattering ($\theta = 0$) into the cavity mode (Fig. 6.7) while keeping the nanosphere at the same trapping position. We observe that the overall spectrum is attenuated by a factor of ~ 100, from which we calculate a tweezer tilting angle $\phi \approx 5.7^\circ$. From the ratio of the overall transduction factors in the homodyne detection (see Section 3.3 for the details about the method) we obtain a similar value $\phi \approx 6.3^\circ$, confirming that the seen suppression is consistent with the non-orthogonal tweezer and cavity axes[12].

[12] *In Section 3.3 we determined a slightly larger angle $\phi \approx 8.4^\circ$. The setup has been realigned since, resulting in a smaller tilting angle.*

Cavity cooling

In Section 5.2 we discussed a possibility to conduct three-dimensional cavity cooling of the nanosphere motion by positioning of the nanosphere to the largest intensity gradient ($x_0 = \lambda/8$) and rotating

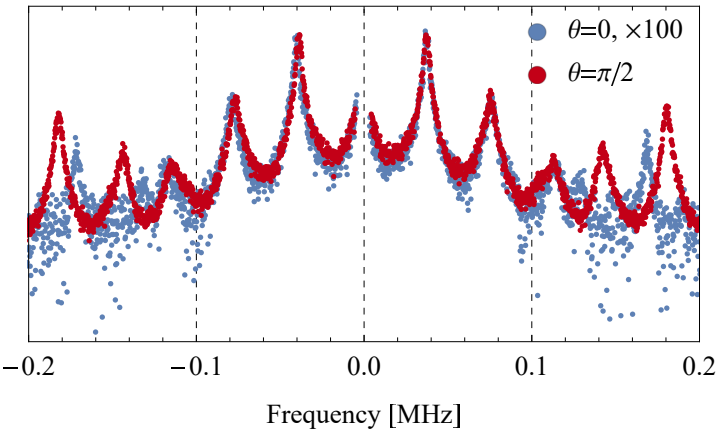

Figure 6.7: **Suppression of coherent scattering by polarization control** Overlapped heterodyne measurements for trap laser polarization $\theta = 0$ and $\theta = \pi/2$. Heterodyne measurements are acquired for trap laser far detuned by $\Delta = 2\pi \times 4$ MHz to avoid affecting the nanosphere motion. The nanosphere is positioned halfway between a cavity node and an antinode ($x_0 = \lambda/8$). The heterodyne spectrum in the case of $\theta = 0$ has been multiplied by a factor of 100 to overlap it with the spectrum from $\theta = \pi/2$. Note that, due to the rotation of the trap axes by $\theta = \pi/2$, we couple the $x(y)$-motion for $\theta = \pi/2$ ($\theta = 0$).

the tweezer polarization (and the elliptical trap) to $\theta = \pi/4$. The driving mode is initially far detuned by $\Delta/2\pi = 4$ MHz to obtain a measurement of the nanosphere motion at room temperature. For cooling we detune the driving mode closer to the resonance with $\Delta = 2\pi \times 300$ kHz. At the beginning the tweezer polarization is set to $\theta = 0$ and the scattering into the cavity mode is suppressed. No significant cavity cooling is observed (Figure 6.8 (a)).

We turn the polarization to $\theta = \pi/4$ in order to couple both x- and y-motion to the cavity, while at the same time scattering some light into the cavity mode. Both transverse motions are detected as spectral peaks at frequencies Ω_x and Ω_y in the heterodyne detection of the scattered mode, as well as in the homodyne detection of the locking mode[13]. The quadrant-type direct detection is rotated by the same angle θ to follow the trap rotation. By doing this, we again optimize the detection of the rotated motional axes in the detectors previously used for detecting the x- and y-motion. The motion along the rotated trap axes is again well separated in the noise power spectrum in Figure 6.8 (b). The signature of strong, genuine three-dimensional cavity cooling is a reduced area and increased linewidth of all peaks compared to the case of far detuned tweezer laser, which we use to extract the coupling rates $(g_x, g_y, g_z)/2\pi = (20, 30, 71)$ kHz. The realization of three-dimensional cavity cooling is also providing a fully passive stabilization scheme of the nanosphere motion. As a note, we were able to keep the nanosphere trapped at a pressure of $p = 4 \times 10^{-6}$ mbar without additional active feedback.

[13] *Remember that we have the best linear coupling of the x-motion to the locking mode at the intensity slope.*

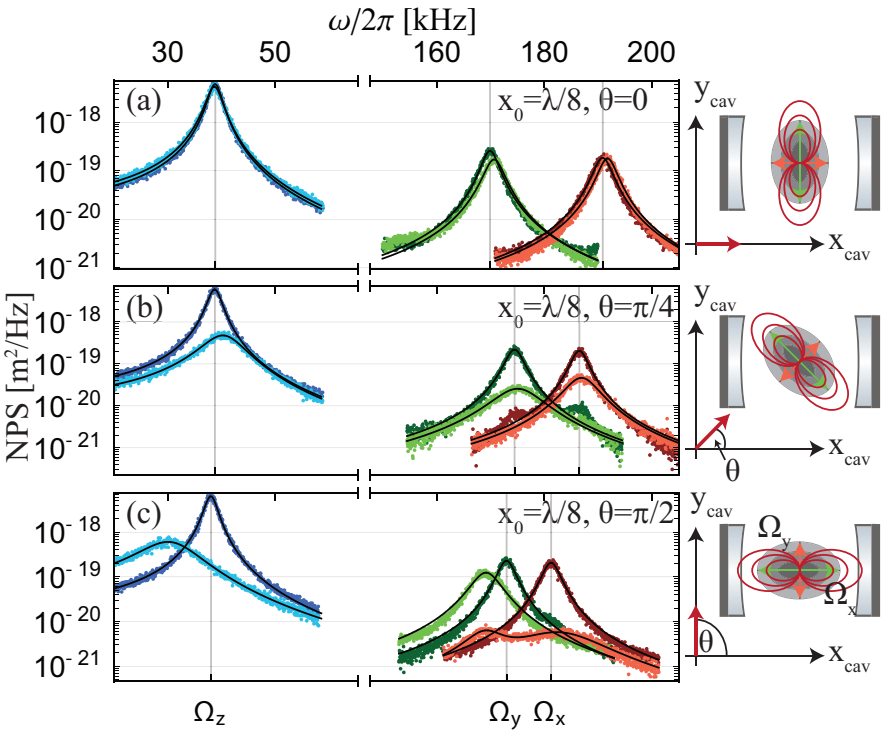

Figure 6.8: **Polarization dependent cavity cooling.** Polarization dependent cavity cooling. Shown are noise power spectra (NPS) measured for a particle located at $x_0 = \lambda/8$ away from a cavity antinode and for three different polarizations of the optical tweezer as illustrated on the right panel. The red arrow indicates the polarization. The sketch also indicates the transverse optical tweezer potential (grey ellipse) and the dipole emission (red ellipses), both of which are locked to the tweezer polarization. Noise power spectra in each panel have been obtained along the tweezer axis (z, blue) and in its transverse directions (x, red; y, green). Cooling measurements are performed with a tweezer detuning close to the mechanical frequency ($\Delta = 2\pi \times 300$ kHz, bright color). Measurements at large detuning ($\Delta = 2\pi \times 4$ MHz, dark color), where scattering into the cavity mode is negligible, serve as reference for no cooling. The nanoparticle was always positioned halfway between the cavity node and antinode to couple all three directions of motion. (a) At $\theta = 0$ no cooling is observed, because polarization along the cavity axis suppresses scattering into the cavity. Imperfect alignment between tweezer and cavity axes results in residual cooling along y-z direction. (b) At $\theta = \lambda/4$ full 3D cavity cooling by coherent scattering is observed, since the cavity axis does not coincide with a principal axis of the optical tweezer. Cooling both broadens the spectra and reduces the overall area. The shift in center frequency is due to the additional optical spring generated by the cavity field. (c) For $\theta = \pi/2$ scattering into the cavity is maximal, as is the cooling along the cavity axis (x) and the tweezer axis (z). Almost no photons are scattered in the third direction (y), resulting in negligible cooling.

Finally, we set the tweezer polarization to $\theta = \pi/2$, which couples predominantly the x- and z-motion to the cavity mode with rates $(g_x, g_y, g_z)/2\pi = (42, 16, 94)$ kHz. Therefore, we observe even

stronger cooling of these two motions (Figure 6.8 (c)). The y-motion is cooled much weaker, but still exhibits residual coupling to the cavity mode. We explain this by a presence of a circularly polarized component of the laser beam (See Appendix C for the mechanical frequencies in the circularly polarized trap laser). This is confirmed by a smaller frequency difference $\Omega_x - \Omega_y$ when compared to the case of $\theta = 0$. In detail, the largest frequency difference is expected for a case of perfect linear polarization. Perfectly circular polarization will result in a round trap potential and degenerate mechanical frequencies (See Appendix C for the calculations).

6.2.2 *Position-dependent cavity cooling*

Cavity cooling by coherent scattering is inherently dependent on the nanosphere position along the cavity axis. We expect maximum cooling of the x-motion (z-motion) to be at the cavity node (antinode). We can set the respective position using the nanopositioner with step size of ~ 8 nm. We move the nanosphere along the cavity axis and monitor the nanosphere dynamics in all three dimensions.

Positioning of the nanosphere along the cavity axis

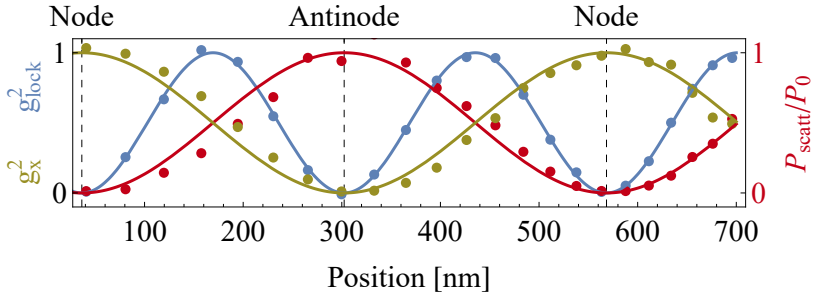

Figure 6.9: Positioning of the particle based on different detection schemes. We extract the coupling of the x-motion to the locking cavity mode g^2_{lock} from the homodyne measurement (blue), demonstrating the standard optomechanical periodicity $g_{lock} \propto \sin(2kx_0)$. Coupling to the cavity mode populated by coherent scattering $g_x \propto \sin kx_0$ is derived from the heterodyne detection (green), where we keep the trap laser far detuned from the cavity resonance by $\Delta = 2\pi \times 4$ MHz in order not to disturb the particle motion. Furthermore, the power scattered out of the cavity (red) is seen out-of-phase with g_x. We are able to reconstruct the nodes and antinodes of the cavity mode used for cavity cooling by coherent scattering.

In order to determine the nanosphere position along the cavity axis, we monitor the power of the scattered light, as well as the coupling to the x- and z-motion through the heterodyne and homodyne detec-

tions. As mentioned earlier, the three detections show the following position dependence:

$$\begin{aligned} \text{scattered light}: &\quad P_{\text{scatt}} \propto \cos^2 kx_0 \\ \text{heterodyne}: &\quad (g_x^{het})^2 \propto \sin^2 kx_0, \quad (g_z^{het})^2 \propto \cos^2 kx_0 \\ \text{homodyne}: &\quad (g_{x,lock}^{hom})^2 \propto \sin^2 2kx_0, \quad (g_{z,lock}^{hom})^2 \propto \sin^2 2kx_0, \end{aligned} \tag{6.4}$$

allowing us to accurately determine the nanosphere position. An example of the measurements is shown in Figure 6.9, where we plot the different detector signals as a function of the position. For example, to achieve the cooling of both x/y- and z-motion, we maximize the g_{lock}^2, i.e. we optimize the peak height of the x-motion in the homodyne detection of the locking cavity mode. In this measurement we intentionally keep the detuning far away from the resonance ($\Delta = 2\pi \times 4$ MHz) in order to avoid cooling of any motion.

Position-dependent cavity cooling

We now set the polarization angle $\theta = \pi/2$ to maximize the scattering into the cavity mode. The cooling performance is measured at a detuning of $\Delta/2\pi = 400$ kHz. We move the particle in steps of ~ 20 nm along the cavity axis at pressures of $p = 4$ mbar (Fig. 6.10(a-c)) and $p = 0.06$ mbar (Fig. 6.10(d-f)). The particle position is deduced from the scattered power (Fig. 6.10(a),(d)) and independently confirmed by homodyne and heterodyne detection, as described in Section 6.2.2.

The maximal effective damping γ_{eff}^x (γ_{eff}^z) of the nanosphere motion is observed at the cavity node (antinode), in agreement with the theory predictions (Fig. 6.10(b),(e)). We fit the mechanical damping by a simple model $\gamma_{\text{eff}}^{x[z]} = \gamma_{\text{min}} + (\gamma_{\text{max}} - \gamma_{\text{min}}) \sin^2 kx_0[\cos^2 kx_0]$, yielding the optical linear damping rate $(\gamma_{\text{max}}^{x[z]} - \gamma_{gas})/2\pi = 10[6.2]$ kHz. From this we extract the maximal coupling rates $g_x = 2\pi \times 60$ kHz and $g_z = 2\pi \times 120$ kHz for the respective optimal nanosphere positions, yielding a cavity drive $E_d/2\pi = 2.5 \times 10^9$ Hz. The expected cavity drive (calculated from the tweezer power $P_{in} = 0.17$ W and the calculated trap waists) $E_d/2\pi \approx 2.8 \times 10^9$ Hz matches the determined value well. For comparison, the cavity drive required to reach the same coupling rate g_x in the dispersive regime is $E_d^{disp}/2\pi = 4.2 \times 10^{10}$ Hz, which corresponds to an intracavity photon number that is larger by a factor of $(E_d^{disp}/E_d)^2 \approx 280$.

We obtain the effective mode temperatures of the x- and z-motion T_{eff}^x and T_{eff}^z from the area underneath the noise power spectra from direct detection and normalized to the bath temperature T_0 (Fig. 6.10(c),(f)). At $p = 0.06$ mbar we observe temperatures below T_0 even where no cooling is expected through purely linear interaction. For the x-motion, including a quadratic interaction with an average temperature $T_{\text{eff}}^x/T_0^x|_{\text{quad}} = 0.11$ [Nunnenkamp et al., 2010] yields good agree-

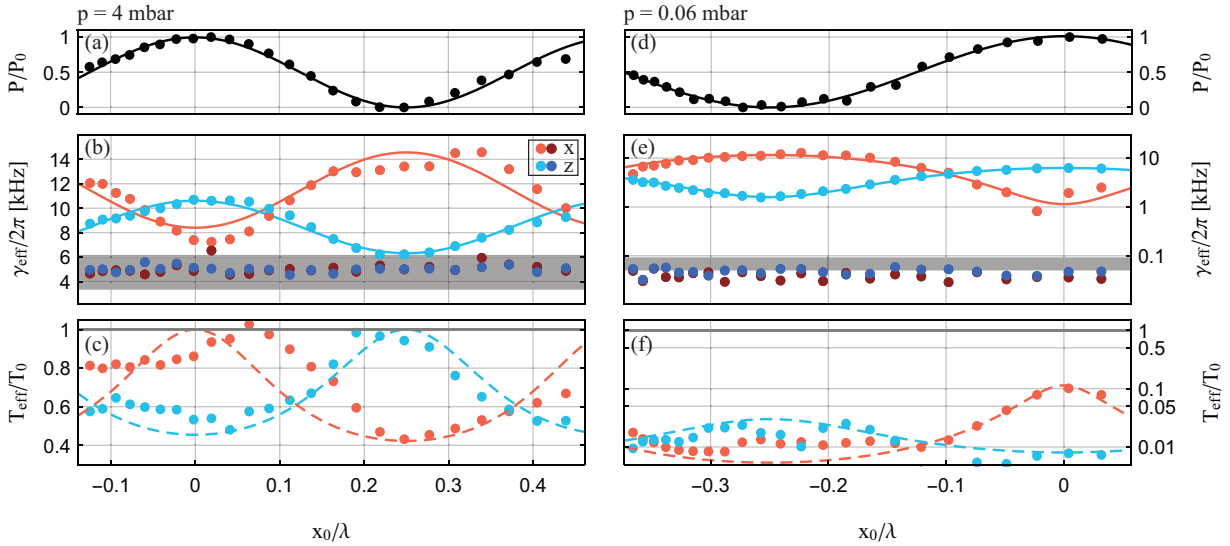

Figure 6.10: **Position dependent cavity cooling.** Shown are relative coherent scattering powers P/P_0 (top), mechanical damping rates γ_m^{eff} (middle) and inverse cooling factors T_{eff}/T_0 (bottom) for different particle positions x_0 along the cavity axis and at background pressures of $p = 4$ mbar (left) and 6×10^{-2} mbar (right). (top panel; (a),(d)) Coherent scattering into the cavity mode. The black line is a fit to the data following the expected sinusoidal behavior with periodicity $\lambda/2$. The scattering is minimal (maximal) for a particle placed at the node $x_0 = \lambda/4$ (antinode $x_0 = 0$) of the cavity field. (middle panel; (b),(e)) The damping γ_m^{eff} of the nanoparticle motion is obtained via the width (FWHM) of the mechanical noise power spectra for the x-axis (red) and z-axis (blue). Bright colors indicate measurements with cavity cooling ($\Delta = 2\pi \times 400$ kHz), dark colors without cooling ($\Delta = 2\pi \times 4$ MHz). The grey line shows the theoretically predicted gas damping γ_{gas} by the environment, which agrees with the observed damping in the absence of cooling. As expected, maximal damping along the x (z)-direction is obtained for minimal (maximal) coherent scattering powers at $x_0 = \frac{\lambda}{4}$ ($x_0 = 0$), as predicted by our theoretical model (solid line). Bottom panel ((c),(f)): The effective mode temperatures T_{eff} are obtained by NPS integration. As expected for both directions, maximum damping implies maximal cooling. Purely linear coupling would result in a maximum temperature of $T_{\text{eff}}/T_0 = 1$ (grey line). A theoretical model that also includes quadratic coupling matches the data very well without free parameters (dashed lines).

ment with the experimental data. The strong cooling of the z-motion is mostly due to a small angle between the tweezer axis and the z_{cav}-axis, resulting in a projection of the z-motion onto the cavity axis. For comparison, the dashed line in Fig. 6.10(c),(f) is based on a theoretical model that includes the linear and, in case of the x-motion, quadratic interaction:

$$\begin{aligned} \frac{T_{\text{eff}}^x}{T_0} &= \frac{1}{T_0} \frac{1}{\frac{\sin^2 kx_0}{T_{\text{lin}}^x} + \frac{\cos^2 kx_0}{T_{\text{quad}}^x}} \\ \frac{T_{\text{eff}}^z}{T_0} &= \frac{\gamma_{gas}}{\gamma_{\text{min}}^z \sin^2 kx_0 + \gamma_{\text{max}}^z \cos^2 kx_0}. \end{aligned} \tag{6.5}$$

It is entirely parametrized by the minimum and maximum temperatures $T^x_{\text{eff, lin}} = T_0\gamma_{gas}/\gamma_{\text{eff}}$ and $T^x_{\text{eff, quad}}$ and the observed mechanical dampings $\gamma^z_{\text{min/max}}$.

6.2.3 *Suppression of the phase noise*

Phase noise fed into the cavity can be characterized even in the absence of a nanosphere. We drive the cavity through the input mirror with a control laser with an arbitrary detuning Δ and photon rate E_d (as in Chapter 2) and monitor the heterodyne spectrum in the cavity transmission, which is:

$$S_{het} \propto \frac{E_d^2}{\left(\frac{\kappa}{2}\right)^2 + (\omega + \Delta)^2} S_{\dot\phi\dot\phi}(\omega). \tag{6.6}$$

The spectrum of the nanosphere motion will be added on top of the phase noise from Equation (6.6). Note that the expression on its right hand side is almost equal to the phonon occupation added by the phase noise heating from Equation (5.52). Therefore, to compare different optomechanical setups it is enough to compare the phase noise contribution in the heterodyne detection. Furthermore, to get a reasonable measure of the phase noise heating suppression, we assume cavity drives that yield equal coupling rates for the two cooling schemes.

The phonon occupations and the respective coupling rates in the two regimes are:

$$\begin{aligned}
\bar n_x^{phase,disp} &= \frac{(E_d^{disp})^2}{\kappa\left(\left(\frac{\kappa}{2}\right)^2 + \Omega_x^2\right)} S_{\dot\phi\dot\phi}(\Omega_x), \qquad & g_x^{disp} &= g_0 \frac{E_d^{disp}}{\sqrt{\left(\frac{\kappa}{2}\right)^2 + \Omega_x^2}} \\
\bar n_x^{phase,coh} &= \frac{E_d^2 \cos^2 kx_0}{\kappa\left(\left(\frac{\kappa}{2}\right)^2 + \Omega_x^2\right)} S_{\dot\phi\dot\phi}(\Omega_x), \qquad & g_x^{coh} &= E_d k x_{zpf},
\end{aligned} \tag{6.7}$$

where $g_0 = 2\pi \times 0.3$ Hz is the dispersive single photon coupling of the x-motion to the cavity mode. Assuming $g_x^{disp} = g_x^{coh}$ in the two coupling scenarios, the required cavity drive in the dispersive regime is $E_d^{disp}/2\pi \approx 4.2 \times 10^{10}$ Hz. The ratio of added phonon occupations due to phase noise heating is:

$$\frac{\bar n_x^{phase,coh}\Big|_{\text{node}}}{\bar n_x^{phase,disp}} = \frac{E_d^2 \cos^2 kx_0}{\left(E_d^{disp}\right)^2} = \frac{g_0^2 \cos^2 k(\lambda/4 + \delta x)}{k^2 x_{zpf}^2 \left(\left(\frac{\kappa}{2}\right)^2 + \Omega_x^2\right)}, \tag{6.8}$$

where δx is the distance from the particle position to the cavity node. In the experiment we positioned the particle within $\delta x \approx 20$ nm and observed 50 times less intracavity photons n_{phot} compared to the cavity antinode position (Figure 6.10(a),(d)), resulting in a decrease of

the phase noise heating by a factor of $\sim 1.5 \times 10^4$. More precise positioning will allow even further improvement in the phase noise suppression.

In the case of three-dimensional cavity cooling, the particle is located at the largest intensity gradient ($\cos^2 kx_0 = 1/2$) with the measured coupling rate $g_x = 2\pi \times 20$ kHz, which is the optimal position for the dispersive coupling. There, the required cavity drive in the dispersive regime would be $E_d^{disp}/2\pi = 1.3 \times 10^{10}$ Hz. Even in this case, the phase noise heating would be suppressed by:

$$\frac{\bar{n}_x^{phase,coh}\Big|_{\text{gradient}}}{\bar{n}_x^{phase,disp}} \approx \frac{1}{60}. \tag{6.9}$$

In conclusion, the proximity to the intensity minimum (optimal position for the cavity cooling of the x-motion) results in minimal coupling of the phase noise into the cavity. Furthermore, compared to the dispersive regime we achieve the same coupling rate with a lower cavity drive in the case of coherent scattering, which additionally decreases the constraint on phase noise.

6.3 CONCLUSION AND OUTLOOK

Let us assume a case of one-dimensional cavity cooling by coherent scattering of the x-motion with the nanosphere positioned at the cavity node. The observed high coupling rate $g_x = 2\pi \times 60$ kHz will allow to reach a lower phonon occupation then in the dispersive regime (Chapter 2). Assuming a weak locking mode, the minimum phonon number is limited by the sideband resolution and the tweezer recoil heating to:

$$\bar{n}_x = \left(\frac{\kappa}{4\Omega_x}\right)^2 + \frac{\kappa\Gamma_{rec}}{4g_x^2} \approx 0.16.$$

As discussed above, and in stark contrast to the dispersive scheme, phase noise heating will add only $\bar{n}_x^{phase} \approx 0.01$ to the total occupation, rendering it negligible. In conclusion, given sufficiently low pressures there are no major obstacles for ground state cooling of the x-motion. For a nanosphere at the largest intensity gradient, we expect to significantly cool all three directions to $(\bar{n}_x, \bar{n}_y, \bar{n}_z) = (1, 0.29, 2.2)$ phonons with additional occupation due to phase noise heating $(\bar{n}_x^{phase}, \bar{n}_y^{phase}, \bar{n}_z^{phase}) = (0.22, 0.27, 18.5)$. In the case of optimal cooling of the z-motion at the cavity antinode, the total phonon occupation will be $\bar{n}_z \approx 150$, with the largest contribution coming from the phase noise with $\bar{n}_z^{phase} \approx 148$ phonons.

The optomechanical cooperativity in the case of coherent scattering is given only by the cavity waist w_0 and the finesse $\mathcal{F}$. The cavity waist is small in many cavity configurations (see Appendix A), but the cavity can be unstable (near-concentric cavity) or too short to

allow an external laser to pass through the cavity (near-planar, microcavity). The best of both (long and stable) is reached with a geometrically asymmetric cavity ("quasi-confocal" cavity), with waists as low as 8 μm [Kawasaki et al., 2018]. On the other side, mirrors with highly reflective coatings at 1064 nm have been used to create cavities with high finesses $\mathcal{F} > 200,000$. Therefore, we may expect that by a careful design one can reach the cooperativity as high as $C = \frac{30\mathcal{F}/\pi}{k^2 w_0^2} > 1000$.

On the other hand, without any significant changes to the cavity the coupling rates can still be boosted by increasing the nanosphere radius or the trap laser power. Note that the co-trapping by the cavity mode is evaded as the cavity remains empty for a nanosphere placed at the node. For example, trapping a nanosphere with a radius of $r = 100$ nm would lead to a significantly increased coupling rate $g_x/2\pi \approx 115$ kHz. Assuming equal mechanical frequencies for a larger nanosphere (yet to be demonstrated), the system will enter the ultra-strong coupling regime ($g/\Omega_x \approx 0.64$) [Frisk Kockum et al., 2019]. This opens up a domain of unexplored optomechanics, such as the entanglement with a red detuned driving laser due to breaking of the rotating wave approximation [Genes et al., 2008a, Hofer, 2015].

7

LIST OF PUBLICATIONS

Cavity cooling of an optically levitated submicron particle

Kiesel, N., Blaser, F., Delić, U., Grass, D., Kaltenbaek, R. and Aspelmeyer, M., *Cavity cooling of an optically levitated submicron particle*, **PNAS** 110, 35, p.14180-14185 (2013)

This is proof-of-principle paper on cavity cooling of a levitated particle. We used a strong locking cavity mode to levitate a particle in the cavity standing wave and an additional, detuned control mode to cool the particle motion along the cavity axis. All of the measurements were done at a relatively high pressure of 8 mbar.

Cavity cooling of a levitated nanosphere by coherent scattering

Delić, U., Reisenbauer, M., Grass, D.,Kiesel, N., Vuletić, V. and Aspelmeyer, M., *Cavity cooling of a levitated nanosphere by coherent scattering*, **Phys.Rev.Lett.** 122, 123602 (2019), Editors' Suggestion

This paper contains a first demonstration of the cavity cooling by coherent scattering, as expected from the theory of Chapter 5. The experimental measurements are presented in Chapter 6.

Levitated cavity optomechanics in high vacuum

Delić, U., Grass, D., Reisenbauer, M., Damm, T., Weitz, M. ,Kiesel, N. and Aspelmeyer, M., *Levitated cavity optomechanics in high vacuum*, arXiv:1902.06605 (2019)

Here we present the results of Chapter 4 together with the results of the cavity scan from Section 3.3.2.

Other publications

Magrini, L., Norte, R., Riedinger, R., Marinković, I., Grass, D., Delić, U., Gröblacher, S., Hong, S. and Aspelmeyer, M., *Near-field coupling of a levitated nanoparticle to a photonic crystal cavity*, **Optica** Vol. 5, Issue 12, pp. 1597-1602 (2018)

Appendices

A

GAUSSIAN BEAM OPTICS

In the course of my PhD studies I spent a lot of time learning a great deal about optical cavities and Gaussian beams. In a hope that future PhD students (at least of this group) won't have to spend as much time as I had, I compile a list of interesting relations in the following.

A.1 GAUSSIAN BEAM

A freely propagating focused Gaussian beam is defined by a single parameter: the (minimum) waist w_0, which is sometimes referred to as the beam radius. Properties of the Gaussian beam are:

- Rayleigh range x_R: The distance from the cavity waist at which the mode radius is $\sqrt{2}w_0$:

$$x_R = \frac{w_0^2 \pi}{\lambda}. \tag{A.1}$$

  The beam radius at a distance x is:

$$w(x) = w_0 \sqrt{1 + \left(\frac{x}{x_R}\right)^2}, \tag{A.2}$$

  which is simplified to $w(x) \approx \frac{w_0 x}{x_R}$ for $x \gg x_R$.

- Radius of curvature is a function of position x as well:

$$RoC(x) = x \left[1 + \left(\frac{x_R}{x}\right)^2\right]. \tag{A.3}$$

  It has a minimum value $RoC = 2x_R$ at $x = x_R$. At $x = 0$ the Gaussian beam behaves as a plane wave.

- In the limit of $x \gg x_R$, the beam divergence for slowly spreading beams is:

$$\theta \approx \frac{\lambda}{w_0 \pi} \tag{A.4}$$

- Complex beam parameter $q(x) = x + i x_R$ is used in the ray transfer matrix analysis to calculate the beam propagation through a system of lenses and other optical elements. The alternative definition is:

$$\frac{1}{q(x)} = \frac{1}{RoC(x)} - i \frac{\lambda}{\pi w^2(x)} \tag{A.5}$$

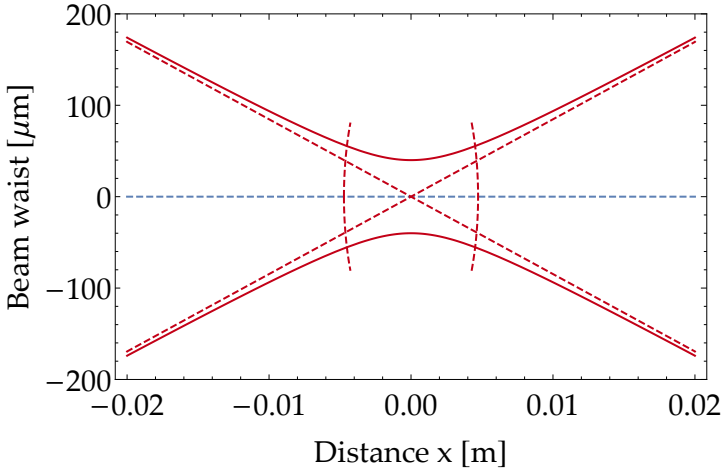

Figure A.1: **Focused Gaussian beam around its waist.** The waist of a Gaussian beam is defined as the smallest beam radius, which we position here at $x = 0$. The beam waist function follows a Gaussian beam envelope, which for large distances x asymptotically approaches a line (dashed).

A.2 CAVITY WAIST

Imagine a Gaussian beam confined between two cavity mirrors positioned at coordinates L_1 and L_2 and with radii of curvature RoC_1 and RoC_2, respectively. The boundary condition for a stable cavity mode is given by the mode radius of curvature at the cavity mirrors: $RoC(L_1) = RoC_1$ and $RoC(L_2) = RoC_2$. The resulting waist of the cavity mode is:

$$w_0^2 = \frac{\lambda}{\pi}\sqrt{\frac{L(RoC_1 - L)(RoC_2 - L)(RoC_1 + RoC_2 - L)}{(RoC_1 + RoC_2 - 2L)^2}}. \tag{A.6}$$

Mode waists at the cavity mirrors are:

$$w_1 = \sqrt{\frac{\lambda RoC_1}{\pi}\sqrt{\frac{L(RoC_2 - L)}{RoC_1 + RoC_2 - L}(RoC_1 - L)}} \tag{A.7}$$

$$w_2 = \sqrt{\frac{\lambda RoC_2}{\pi}\sqrt{\frac{L(RoC_1 - L)}{RoC_1 + RoC_2 - L}(RoC_2 - L)}} \tag{A.8}$$

Simplifications are possible for a specific cavity configuration.

A.3 CAVITY MODE VOLUME

In some books on resonator optics [Hodgson and Weber, 2005], the cavity mode volume is defined as space occupied by the waist func-

tion $w(x) = w_0\sqrt{1+\left(\frac{x}{x_R}\right)^2}$, where w_0 is the cavity waist and $x_R = \frac{w_0^2\pi}{\lambda}$ is the Rayleigh length:

$$V_c^{waist} = \int_{L_1}^{L_2} w^2(x)\pi dx. \tag{A.9}$$

Apparently, this expression assumes that all of the electric field at certain position x is uniform along the radial axes and equal to 0 at distances greater than $w(x)$. Thusly determined cavity mode volume of a confocal cavity is $V_c^{waist} = \frac{4w_0^2\pi L}{3}$.

However, the light field is not located only within the waist function. The easiest way to see that is in the quantization of the electric field, which gives $E^-, E^+ \propto \sqrt{\frac{\hbar\omega_L}{2\epsilon_0 V_c}}$. The cavity mode volume is defined here as the space the electric field occupies. Integrated intensity of the cavity mode $I(r,z) = \frac{I_0}{1+(x/x_R)^2}\exp(-\frac{2r^2}{w^2(x)})\cos^2(kx) \propto E^+E^-$ divided by the intensity at the cavity waist I_0 yields the mode volume V_c:

$$V_c = \int_0^{2\pi} d\phi \int_{-L/2}^{L/2} dz \int_0^{\infty} \frac{I(r,z)}{I_0} r dr. \tag{A.10}$$

The resulting cavity mode volume $V_c = w_0^2\pi L/4$ is independent of the cavity configuration.

A.4 CAVITY CONFIGURATIONS

Through the course of this thesis we have mentioned (near-)confocal cavities, where the cavity length is close to the mirror's radius of curvature $L \sim RoC_2 = RoC_1$. This is the most stable cavity configuration as it is insensitive to a small translational and rotational motion of the mirrors. However, it comes at a price that the cavity waist is big:

$$w_0 = \sqrt{\frac{L\lambda}{2\pi}}, \tag{A.11}$$

which is simplified from Equation (A.6). For a $\sim$ 1cm long cavity the cavity waist is $w_0 \approx 41.1$ μm. The nanospheres are significantly smaller than the cavity waist, resulting in a weak interaction between the nanosphere motion and the cavity mode. We cover cavity configurations with smaller cavity waists in the following.

A stable laser amplification between the two mirrors occurs only if the stability criterion is satisfied:

$$0 \leq g_1 g_2 \leq 1, \qquad \text{stability parameter: } g_i = 1 - \frac{L}{R_i}. \tag{A.12}$$

This is often represented graphically as a region between two hyperbolas and the horizontal and vertical axes (Figure A.2). We overlay

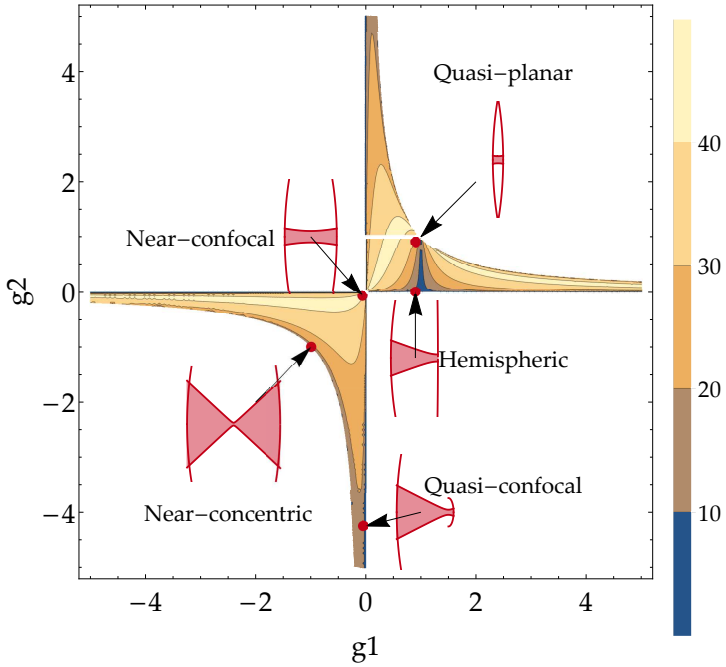

Figure A.2: **Contour plot of the cavity waist as a function of the stability parameters g_1 and g_2.** The relevant stable cavity configurations are given by the condition $0 \leq g_1 g_2 \leq 1$. Cavity configurations mentioned in the main text are shown here as points in the plot.

the stability region with the contour plot of the cavity waist, calculated in the case of $RoC_1 = 10$ mm and arbitrary L and RoC_2. Another stability criterion is given by the overlap of the mirrors' foci, where the cavity is resistant to length changes on the order of $\delta L = RoC_1 + RoC_2 - L$.

1. In symmetric cavities the cavity mirrors have equivalent radii of curvature $RoC_1 = RoC_2 = RoC$, with a stable cavity operating in the range $0 < L < 2RoC$. Around $L \approx RoC$ (near-confocal cavity) the cavity waist changes little with a cavity length change.

    - **Confocal cavity** is the most stable configuration in terms of length drifts and tilts. Small cavity misalignments don't result in a change of the cavity waist, hence a precise tuning of the cavity length is unnecessary ($\delta L \approx L$). The cavity used in the course of this thesis is a near-confocal cavity, i.e. $L \approx RoC$.

    - **Near-concentric cavity** is constructed when the two centers of mirror curvatures overlap at the cavity center, i.e. $L = 2RoC - \Delta L$ with $\Delta L \to 0$. This is a highly unstable design, as even the smallest tilt of cavity change could result in a loss of the cavity mode ($\delta L = \Delta L$).

- **Quasi-planar** is given by $L \to 0$, i.e. when the two cavity mirrors are extremely close to each other. This configuration is unsuitable for our experiment as the trapping laser will be cut by the cavity mirrors.

2. Asymmetric cavities relax the condition on the radii of curvature: $RoC_1 \neq RoC_2$. There are two common cavity designs:
   - **Hemispheric cavity** is created from the mirrors with $RoC_1 = L$, $RoC_2 = \infty$.
   - **Quasi-confocal cavity** is created from the mirrors with $RoC_1 \gg RoC_2$, $L \approx \frac{RoC_2}{2} + RoC_1$. Cavity mirrors with small radius of curvature $RoC_2 \ll 1$ mm (mirrors) typically have a depth of several microns, therefore the cavity waist will be far away from the surface of the micromirror. As $\delta L \approx \frac{RoC_2}{2}$ and $RoC_2 \gg \Delta L$ (from the concentric cavity), this design is extremely resistant to length changes.

B

MIE SCATTERING THEORY

Here we give a brief overview of the origin of the light-nanosphere interaction for an arbitrary nanosphere size. There are several books [Bohren and Huffman, 1983], which gives extensive introduction into the generalized Mie scattering theory.

B.1 ELECTRIC FIELD OF THE DIPOLE SCATTERING

Assuming a spherical particle, it is appropriate to expand the intrinsic plane-wave light field into spherical harmonics. Without loss of generality, the incident light is assumed linearly polarized along the y-axis. The incident electric field as a sum of spherical harmonics is:

$$\begin{aligned} E_{i\theta} &= \frac{\cos\varphi}{\rho}\sum_{n=1}^{\infty} E_n(\psi_n\pi_n - i\psi_n'\tau_n) \\ E_{i\varphi} &= \frac{\sin\varphi}{\rho}\sum_{n=1}^{\infty} E_n(\psi_n'\pi_n - i\psi_n\tau_n), \end{aligned} \tag{B.1}$$

where $E_n = i^n E_0 \frac{2n+1}{n(n+1)}$ depends on the intrinsic electric field E_0. $\psi_n(\rho) = \rho j_n(\rho)$ is the Riccatti-Bessel function, while $\pi_n(\theta) = \frac{P_n^1(cos\theta)}{\sin\theta}$ and $\tau_n(\theta) = \frac{dP_n^1(cos\theta)}{d\theta}$ are helpful angle-dependent functions. The scattered electric field is obtained from a boundary condition on the nanosphere surface:

$$\begin{aligned} E_{s\theta} &= \frac{\cos\varphi}{\rho}\sum_{n=1}^{\infty} E_n(ia_n\xi_n'\tau_n - b_n\xi_n\pi_n) \\ E_{s\varphi} &= \frac{\sin\varphi}{\rho}\sum_{n=1}^{\infty} E_n(b_n\xi_n\tau_n - ia_n\xi_n'\pi_n), \end{aligned} \tag{B.2}$$

where $\xi_n(\rho) = \rho h_n^{(1)}(\rho)$ is also a Riccatti-Bessel function. The scattering amplitudes from the previous equation are:

$$\begin{aligned} a_n(x) &= \frac{n_s\psi_n(n_sx)\psi_n'(x) - \psi_n(x)\psi_n'(n_sx)}{n_s\psi_n(n_sx)\xi_n'(x) - \xi_n(x)\psi_n'(n_sx)} \\ b_n(x) &= \frac{\psi_n(n_sx)\psi_n'(x) - n_s\psi_n(x)\psi_n'(n_sx)}{\psi_n(n_sx)\xi_n'(x) - n_s\xi_n(x)\psi_n'(n_sx)}. \end{aligned} \tag{B.3}$$

We will first investigate the light scattering in the forward direction ($\theta = 0$) for which $\tau_n(0) = \pi_n(0) = 1$. For small nanospheres ($n_s kr \ll 1$) we have to the smallest order in ρ:

$$\begin{aligned} b_1 &\approx -\frac{i}{45}(n_s^2-1)x^5 + \mathcal{O}(x^7) \\ b_2 &\approx \mathcal{O}(x^7) \\ a_1 &\approx -\frac{2i}{3}\frac{n_s^2-1}{n_s^2+2}x^3 - \frac{2}{5}\frac{(n_s^2-1)(n_s^2-2)}{(n_s^2+2)^2}x^5 + \mathcal{O}(x^6) \\ a_2 &\approx -\frac{i}{15}\frac{n_s^2-1}{2n_s^2+3}x^5 + \mathcal{O}(x^7). \end{aligned} \tag{B.4}$$

We keep only the terms up to x^3 such that the largest contributions to the electric fields $E_{s\varphi}$ and $E_{s\theta}$ are:

$$E_{s\varphi} = E_0 \frac{i\sin\varphi}{\rho^2}\frac{n_s^2-1}{n_s^2+2}x^3 = \frac{E_{i\varphi}^{n=1}}{\rho^2}\frac{n_s^2-1}{n_s^2+2}x^3. \tag{B.5}$$

This expression is reminiscent of the dipole scattering:

$$E_{s\varphi} = \frac{k^3\alpha}{4\pi\epsilon_0}\frac{E_{i\varphi}^{n=1}}{r^2}, \tag{B.6}$$

which provides the definition of the particle polarizability $\alpha = 3\epsilon_0 V \frac{n_s^2-1}{n_s^2+2}$.

C

SINGLE-BEAM DIPOLE TRAP OF AN ARBITRARILY POLARIZED INCIDENT LASER BEAM

The path on how to calculate the trapping potential of a linearly polarized, tightly focused laser is shown in [Novotny and Hecht, 2012]. Here we assume an arbitrary laser polarization and determine the resulting potential. Let us assume the following electric field of the trapping laser:

$$\mathbf{E}_{inc} = E^x_{inc}\mathbf{n}_x + E^y_{inc}\mathbf{n}_y, \tag{C.1}$$

where $E^x_{inc} \propto E_x = \cos(\alpha)(\cos^2(\beta) + i\sin^2(\beta))$ and $E^y_{inc} \propto E_y = \sin(\alpha)(1-i)\sin(\beta)\cos(\beta)$ are the electric field components along the polarization axes $\vec{n}_x$ and $\vec{n}_y$, respectively. The laser is propagating along the z-axis. The angle $\alpha/2$ (β) is the linear (circular) polarization angle as applied with a half-wave plate (quarter-wave plate). For $\alpha = \beta = 0$ the laser is polarized along the x-axis.

The electric field just after passing through the microscope objective is:

$$\begin{aligned}\mathbf{E}_\infty(\theta,\phi) = &\left(\mathbf{E}_{inc}(\theta,\phi)\cdot\begin{bmatrix}-\sin\phi\\ \cos\phi\\ 0\end{bmatrix}\right)\cdot\begin{bmatrix}-\sin\phi\\ \cos\phi\\ 0\end{bmatrix}\sqrt{\cos\theta}\\ + &\left(\mathbf{E}_{inc}(\theta,\phi)\cdot\begin{bmatrix}\cos\phi\\ \sin\phi\\ 0\end{bmatrix}\right)\cdot\begin{bmatrix}-\cos\phi\cos\theta\\ \sin\phi\cos\theta\\ -\sin\theta\end{bmatrix}\sqrt{\cos\theta}\end{aligned}$$

The electric field at the focus is determined from the electric field at the objective E_∞:

$$\mathbf{E}(\rho,\varphi,z) \propto \int_0^{\theta_{max}}\int_0^{2\pi}\mathbf{E}_\infty(\theta,\phi)e^{ikz\cos\theta}e^{ik\rho\sin\theta\cos(\phi-\varphi)}\sin\theta d\phi d\theta, \tag{C.2}$$

where the following coordinate transformation was used: $x = \rho\cos\varphi$, $y = \rho\sin\varphi$, while $\theta_{max} = \arcsin(\mathrm{NA})$. The integral in Equation (C.2) is simplified by using the helping functions I_{00}, I_{01} and I_{02}:

$$\begin{aligned} I_{00} &= \int_0^{\theta_{max}} f_w(\theta)\sqrt{\cos\theta}\sin\theta(1+\cos\theta)J_0(k\rho\sin\theta)e^{ikz\cos\theta}d\theta \\ I_{01} &= \int_0^{\theta_{max}} f_w(\theta)\sqrt{\cos\theta}\sin^2\theta J_1(k\rho\sin\theta)e^{ikz\cos\theta}d\theta \\ I_{02} &= \int_0^{\theta_{max}} f_w(\theta)\sqrt{\cos\theta}\sin\theta(1-\cos\theta)J_2(k\rho\sin\theta)e^{ikz\cos\theta}d\theta. \end{aligned} \tag{C.3}$$

final expression for the electric field at the focus $\mathbf{E}(\rho,\varphi,z)$:

$$\mathbf{E}(\rho,\varphi,z) = \frac{ikf}{2}E_0 e^{-ikf} \times \begin{bmatrix} I_{00}E_x + I_{02}E_x\cos 2\varphi + I_{02}E_y\sin 2\varphi \\ I_{00}E_y - I_{02}E_y\cos 2\varphi + I_{02}E_x\sin 2\varphi \\ -2iI_{01}(E_x\cos\varphi + E_y\sin\varphi) \end{bmatrix}. \tag{C.4}$$

In principle, we have to numerically integrate functions I_{0n} for all ρ and z. However, the nanosphere experiences only a small central part of the focus. We use a Taylor expansion of the Bessel functions up to the second order[14] in ρ and z. Therefore, we can evaluate only a couple of important integrals once:

[14] *In principle, the Bessel functions can be expanded to an abritrary order in ρ and z, which might be useful in the full characterization of the combined tweezer and cavity potentials.*

$$\begin{aligned} i_{00} &= \int_0^{\theta_{max}} f_w(\theta)\sqrt{\cos\theta}\sin\theta(1+\cos\theta)d\theta \\ i_{00}^{\rho} &= -\int_0^{\theta_{max}} f_w(\theta)\sqrt{\cos\theta}\sin\theta(1+\cos\theta)\left(\frac{k\sin\theta}{2}\right)^2 d\theta \\ i_{00}^{z} &= \int_0^{\theta_{max}} f_w(\theta)\sqrt{\cos\theta}\sin\theta(1+\cos\theta)ik\cos\theta d\theta \\ i_{00}^{z2} &= -\int_0^{\theta_{max}} f_w(\theta)\sqrt{\cos\theta}\sin\theta(1+\cos\theta)(k\cos\theta)^2 d\theta \\ i_{01}^{\rho} &= \int_0^{\theta_{max}} f_w(\theta)\sqrt{\cos\theta}\sin^2\theta\frac{k\sin\theta}{2}d\theta \\ i_{02}^{\rho} &= \int_0^{\theta_{max}} f_w(\theta)\sqrt{\cos\theta}\sin\theta(1-\cos\theta)\frac{1}{2}\left(\frac{k\sin\theta}{2}\right)^2 d\theta. \end{aligned}$$

With the help of the integrals above, the electric field at the focus is expressed as:

$$\mathbf{E}(\rho,\varphi,z) = \frac{ikf}{2}E_0 e^{-ikf} \times \begin{bmatrix} i_{00}E_x + i_{00}^{\rho}E_x\rho^2 + i_{02}^{\rho}(E_x\cos 2\varphi + E_y \sin 2\varphi)\rho^2 + i_{00}^{z}E_x z + i_{00}^{z2}E_x z^2 \\ i_{00}E_y + i_{00}^{\rho}E_y\rho^2 - i_{02}^{\rho}(E_y\cos 2\varphi - E_x \sin 2\varphi)\rho^2 + i_{00}^{z}E_y z + i_{00}^{z2}E_y z^2 \\ -2i \times i_{01}^{\rho}(E_x\cos\varphi + E_y\sin\varphi)\rho \end{bmatrix}.$$

Note that for $\rho \neq 0$ the component of the electric field along the trapping laser is not zero.

The radial and axial mechanical frequencies are obtained from the dipole interaction in the focused electric field:

$$\frac{m\Omega_z^2 z^2}{2} + \frac{m\Omega_x^2 x^2}{2} + \frac{m\Omega_y^2 y^2}{2} = -\frac{\alpha}{2}\sum_{j=x,y,z}\left.\frac{\partial^2|\mathbf{E}|^2}{\partial j^2}\right|_{j=0} j^2, \tag{C.5}$$

while keeping only the terms up to the second order in x, y and z on the right-hand side of the equation. The incident laser electric field is given by the optical power $|E_0|^2 = \frac{4P_0}{\epsilon_0 c W_0^2 \pi}$. Note that the waist $W_0 = f_0 \times f \times \mathrm{NA}$ depends on the numerical aperture and the filling factor f_0 of the objective, therefore the electric field $\vec{E} \propto f/W_0 = 1/(f_0\mathrm{NA})$ doesn't depend on the focal length f and the waist W_0.

C.1 VALIDITY OF THE APPROXIMATION OF SMALL ρ, z

The harmonic potential is an approximation to the full potential landscape defined by the tightly focused laser (Figure C.1). Root-mean-square amplitude of the harmonic motion of the nanosphere with a radius of $r = 71.5$ nm along the x-axis is:

$$x_{rms} = \sqrt{\frac{k_B T}{m\Omega_x^2}} \approx 38\mathrm{nm}, \tag{C.6}$$

where we assume room temperature $T = 293$ K, the nanosphere mass $m = 2.8 \times 10^{-18}$ kg and the mechanical frequency $\Omega_x = 2\pi \times 160$ kHz. For a nanosphere displaced by x_{rms} from the potential minimum, the discrepancy between the harmonic and the full potential is only $\sim 0.1\%$ of the full potential. Therefore, we assume the potential is well estimated by the harmonic approximation.

C.2 LINEARLY POLARIZED LASER ALONG THE x-AXIS

Let us assume a laser polarized along the x-axis ($E_x = 1$, $E_y = 0$). In order to calculate the axial mechanical frequency, we set $\rho = 0$ and calculate $|\vec{E}|^2$:

$$|\mathbf{E}|^2 = \left(\frac{kf}{2}\right)^2 E_0^2\left(i_{00}^2 + (|i_{00}^z|^2 + 2i_{00}i_{00}^{z2})z^2 + \mathcal{O}(z^4)\right). \tag{C.7}$$

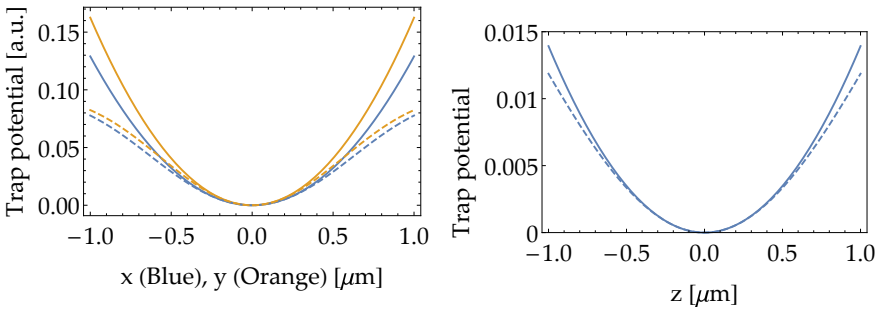

(a) Potential along the x- and the y-axis

(b) Potential along the z-axis

Figure C.1: **Validity of the approximation of small ρ and z.** Starting from the initially linearly polarized laser along the x-axis, we calculate the precise (dashed lines) and the approximate (solid lines) trap potentials up to the second order in ρ. (a) Potential along the x-axis (blue) and the y-axis (orange) (b) Potential along the z-axis. For motional amplitudes below 100 nm the approximation of the harmonic potential is within a 1% of the full potential.

The axial frequency is:

$$\Omega_z = \sqrt{\left(\frac{k}{2f_0 \times \mathrm{NA}}\right)^2 \frac{2\alpha P_0}{\epsilon_0 c} \frac{-(|i_{00}^z|^2 + 2i_{00}i_{00}^{z2})}{m}}, \tag{C.8}$$

We set $z = 0$ in order to calculate the transverse frequencies, which gives $|E|^2 \propto a\rho^2 + b\rho^2 \cos^2\varphi + c\rho^2 \sin^2\varphi$. The transverse frequencies are determined when we transform back into Cartesian coordinates with $x = \rho\cos\varphi$ and $y = \rho\sin\varphi$:

$$\begin{aligned} \Omega_x &= \sqrt{\left(\frac{k}{2f_0 \times \mathrm{NA}}\right)^2 \frac{2\alpha P_0}{\epsilon_0 c} \frac{-(2i_{00}(i_{00}^\rho + i_{02}^\rho) + 4(i_{01}^\rho)^2)}{m}} \\ \Omega_y &= \sqrt{\left(\frac{k}{2f_0 \times \mathrm{NA}}\right)^2 \frac{2\alpha P_0}{\epsilon_0 c} \frac{-(2i_{00}(i_{00}^\rho - i_{02}^\rho))}{m}}. \end{aligned} \tag{C.9}$$

We determine the filling factor $f_0 = 0.7$ and the optical power $P_0 = 0.17$ W from the well known mechanical frequencies $(\Omega_z, \Omega_x, \Omega_y)/2\pi \approx (39, 160, 184)$ kHz,

C.3 ARBITRARY LINEAR POLARIZATION OF THE TRAPPING LASER

We set the angle of the circular polarization $\beta = 0$. The mechanical frequencies Ω_x and Ω_y are independent of the angle of the linear polarization α. However, the axes of the respective motions are rotating with an angle α such that we always define them as $x = \rho\cos(\varphi - \alpha)$ and $y = \rho\sin(\varphi - \alpha)$.

C.4 ARBITRARY CIRCULAR POLARIZATION OF THE TRAPPING LASER

We set $\alpha = 0$ and allow for an arbitrary angle of the circular polarization β. Similarly to the case of linear polarization, the motional axes rotate by an angle β, i.e. the new axes are defined as $x = \rho\cos(\varphi - \beta)$ and $y = \rho\sin(\varphi - \beta)$. In addition, the mechanical frequencies are modified as well (Figure C.2):

$$\Omega_x = \sqrt{\left(\frac{k}{2f_0 \times \mathrm{NA}}\right)^2 \frac{2\alpha P_0}{\epsilon_0 c} \frac{-2i_{00}(i_{00}^{\rho} + i_{02}^{\rho}\cos(2\beta) + 4(i_{01}^{\rho}\cos(\beta))^2)}{\rho_d}}$$

$$\Omega_y = \sqrt{\left(\frac{k}{2f_0 \times \mathrm{NA}}\right)^2 \frac{2\alpha P_0}{\epsilon_0 c} \frac{-2i_{00}(i_{00}^{\rho} - i_{02}^{\rho}\cos(2\beta)) + 4(i_{01}^{\rho}\sin(\beta))^2}{\rho_d}}$$

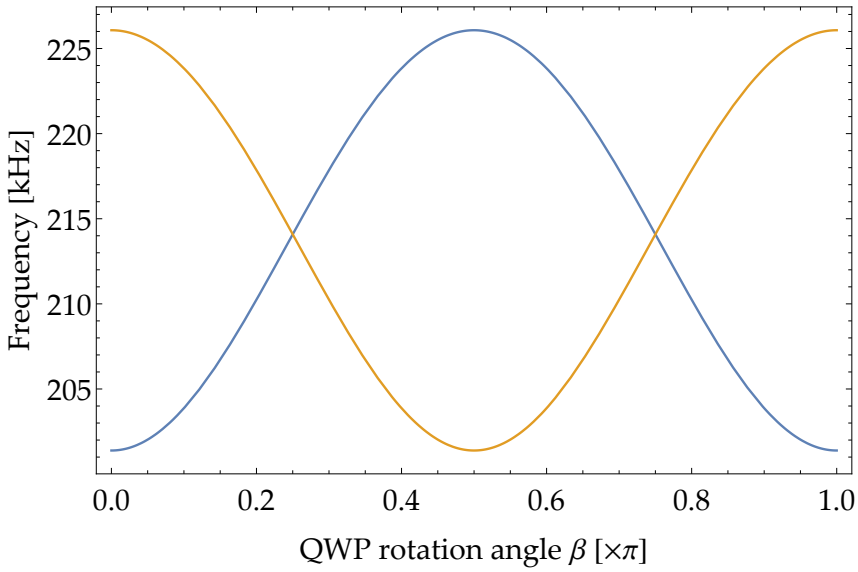

Figure C.2: **Impact of rotating a QWP on radial mechanical frequencies in a tweezer trap.** Motional frequencies Ω_x (blue) and Ω_y (orange) depending on QWP angle β. Realistic parameters have been chosen ($f_0 = 0.8$, $P_0 = 0.75$ W).

D

GENERATION OF HIGHER ORDER CAVITY MODES

The higher-order cavity modes TEM_{01} and TEM_{10} can be used for three-dimensional cavity cooling in the resolved sideband case [Yin et al., 2011] or for feedback cooling of the nanosphere motion transverse to the cavity axis [Kubanek et al., 2011]. In our previous work we used the cavity to levitate zhe particle with small transverse frequencies $\Omega_y, \Omega_z \ll \kappa/2$ [Kiesel et al., 2013]. Hence, feedback cooling was the only viable mechanism to be combined with axial cavity cooling in order to have three-dimensional cooling of the nanosphere motion.

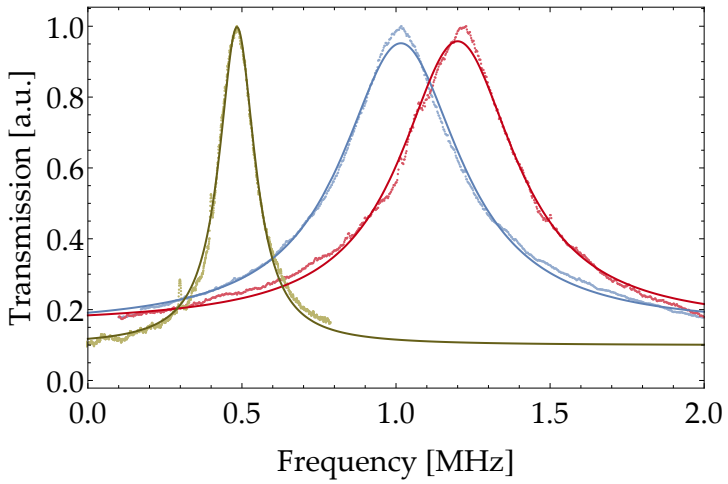

Figure D.1: The resonance scans of the TEM_{01} (blue) and TEM_{10} (red) cavity modes compared to the resonance scan of the TEM_{00} mode. Note that the TEM_{00} mode is shifted in frequency in order to present it jointly with the higher order modes. The separation between the higher order modes has been left as is. The cavity FWHM linewidth of the TEM_{01} and TEM_{10} modes is twice as large as the linewidth of TEM_{00} mode, which we explain by the larger mode waist at the cavity mirrors.

Driving a higher-order mode is achievable in many ways. Optimal methods would be to use a spatial light modulator (SLM), a digital mirror device (DMD) [Papageorge et al., 2016] or a phase plate to create a higher-order free space mode, thus achieving a good mode matching with higher-order cavity mode. In comparison, driving the

TEM_{01} or TEM_{10} cavity modes with the free space TEM_{00} mode results in a mode overlap:

$$\int_{-\infty}^{+\infty} dz \int_{-\infty}^{+\infty} dy f_{00}(x=0, y+y_0, z) f_{01}(x=0, y, z), \tag{D.1}$$

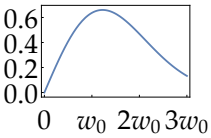

Figure D.2: Mode overlap of the TEM_{00} and TEM_{01} modes as a function of the displacement of the TEM_{00} mode from the center of the cavity mirror.

where we can achieve around $\sim 70\%$ mode matching at best (Figure D.2). This mode matching can be achieved by driving a single lobe of the higher-order mode with the laser TEM_{00} mode. Designing a non-confocal cavity results in transverse modes which are distinguishable by resonant frequencies. In general, the resonance of an arbitrary TEM_{mn} cavity mode with a longitudinal number q is expressed as:

$$\nu_{qmn} = \frac{c}{2L}\left[q + \frac{(m+n+1)\arccos(g_1 g_2)}{\pi}\right], \tag{D.2}$$

where $g_i = 1 - \frac{L}{RoC_i}$ is the stability parameter for the i-th mirror. The estimated frequency separation for the cavity in this thesis is $\nu_{q01} - \nu_{q00} \approx 7$ GHz. Although Equation (D.2) predicts degenerate frequencies for the same family of transverse modes with $m+n =$ const, cavity birefringence induces a splitting between the TEM_{01} and TEM_{10} modes, as also seen in Figure D.1. It is about twice as large as the splitting observed between the two orthogonally polarized TEM_{00} modes in Section 6.1.1.

We construct a setup which uses both an EOM and an AOM to create the higher-order modes (Figure D.3). The EOM is needed to generate a laser sideband in the ballpark of the TEM_{01} and TEM_{10} cavity resonances at $\nu_{01/10} - \omega_c/2\pi \approx 7$ GHz. Additionally, we apply a phase modulation at 10 MHz to create sidebands for PDH locking. We use a fiber Bragg grating (FBG) to transmit only one of the GHz sidebands. The additional frequency shift to match the cavity resonance is applied with the AOM (RF drive frequency 200 MHz, total shift $\sim \pm 400$MHz). The AOMs are set up in a double pass configuration to minimize beam pointing noise. PDH locking to the TEM_{01} and TEM_{10} cavity resonances is done by applying a frequency modulation to the AOM drivers. On the other hand, the amplitude modulation is used to change the cavity drive or apply feedback cooling to the transverse nanosphere motion. We drive the TEM_{01} and TEM_{10}. In the reflection, we set up a detector in each output arm of a $50:50$ beamsplitter. In order to suppress for example the TEM_{01} mode from the photodiode meant to measure TEM_{10}, we create paper masks to filter the modes spatially. The detected signal is used in PDH locking (bandwidth: $0-20$ Hz) and the detection of the transverse nanosphere motion.

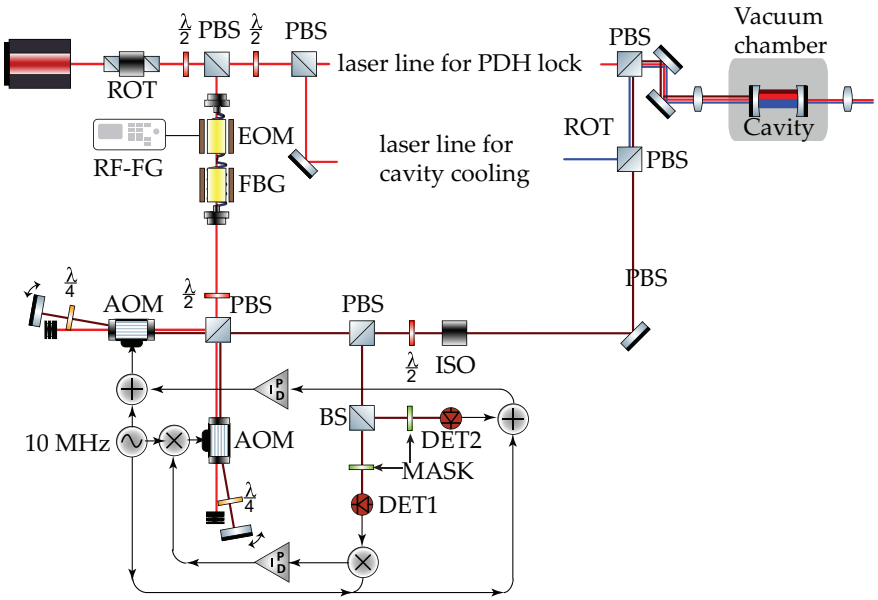

Figure D.3: A part of laser is coupled into an electro-optical modulator (EOM), which is used to generate sidebands at $\sim \nu_{q01} - \nu_{q00} = 7$ GHz. Additional sidebands are created at ± 10 MHz to be used in a PDH lock. We lock a fiber Bragg grating (FBG) to select only one of the GHz sidebands. We subsequently amplify the laser with a fiber amplifier (Keopsys, 2W). The laser is subsequently split in two paths, with either passing an acousto-optical modulator (AOM) in a double pass configuration. The AOM shifts the laser beams by ~ 400 MHz, in addition to changing the laser frequency to lock to the cavity resonance. The reflection from the input cavity mirror changes its polarization upon returning through the Faraday isolator (ISO) and a halfwave plate ($\lambda/2$) such that it goes to the detection arm. There, the reflected laser containing both TEM_{01} and TEM_{10} modes is split equally between two arms, each one containing a spatial mask to filter the light driving only one spatial mode. Each mode is locked with a separate PDH lock acting back on the AOMs.

E

SIMULATION OF THE NANOSPHERE MOTION

The discussion in Section 7 showed that the existence of an angle between the cavity and the tweezer optical axes can explain the complex shape of the homodyne spectrum. Furthermore, we generate homodyne spectra via a two-dimensional simulation of the system. Although we take the two-dimensional nanosphere motion into account, the equations of motion are still fully separable. The field of numerical simulation contains numerous methods to simulate the motion of a driven damped harmonic oscillator. Yet, it is hard to do it efficient and fast in Mathematica. Shown in Figure E.1 is our program which showed extraordinary speed-up compared to simpler versions:

```
(*x motion*)
dt = 1 * 10^-9; (*Time step [s]*)
radius = 71.5 * 10^-9; (*Radius [m]*) ρ = 1850; (*Density in kg/m^3*)
mass = ρ * 4/3 π * (radius)^3; (*Nanosphere mass*)

v0 = 2 Sqrt[kB * T0/mass]; (*Initial condition for velocity [m/s] at temperature T0=290 K*)

(*Damping [Hz] for typical nanosphere at pressure p=2.6 mbar:*)
γ0 = ΓB[radius, 2.6 * 100, ρ]/(2 π)
ω0x = 169 000; (*Oscillation frequency [Hz]*)

(*Matrix describing the system of differential equations of LHO:*)
mat = {{1, dt}, {-4 π^2 ω0x^2 × dt, 1 - 2 π * γ0 × dt}};
NT = 2 000 000 * 20; (*Number of steps to do, 20 averages of 2 million points*)
n = 2 kB * T0/mass * 2 π * γ0; (*Magnitude of a single kick:*)

(*Generating kicks from a normal distribution:*)
Timing[wn = Sqrt[dt] Sqrt[n] RandomVariate[NormalDistribution[0, 1], NT];]
simulate[x_, w_] := mat.x + {{0}, {1}} w; (*Function that simulates motion*)
x0 = {{0}, {v0}}; (*Initial condition for position and velocity*)
xn = FoldList[simulate, x0, wn]; (*Actual simulation happens with FoldList*)
time = Range[NT + 1] * dt * 10^3; (*List of time points*)

(*Data to export: time as x-axis, position as y-axis*)
datax = Transpose[{time, xn[[All, 1, 1]] * 10^9}];
```

Figure E.1: Code for simulation of a one-dimensional motion of the linear harmonic oscillator

Using this program, we are able to simulate the x- and z-motion independently and use the generated time traces to create a simulated

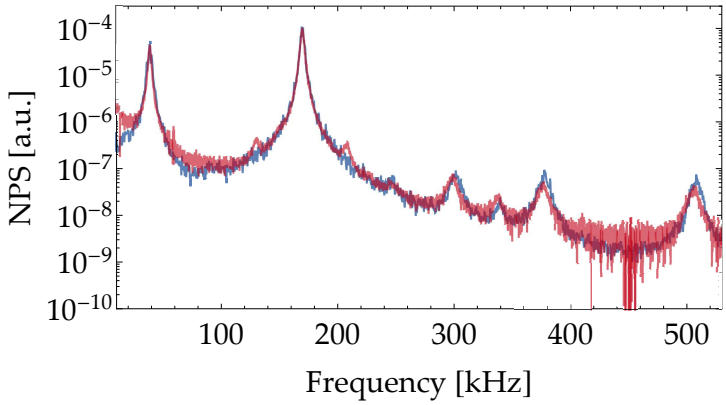

Figure E.2: **Comparison of the simulated (blue) and the measured spectrum (red) at a particular position** x_0. Correspondence is apparent everywhere except at $\Omega_x \pm \Omega_z$, as we don't expect the existence of additional peaks at this position. We used a rounded up mechanical frequency $\Omega_x/2\pi = 169.2$ kHz for the simulation instead of the exact fit value, hence we notice an obvious frequency difference between the simulated and the real peak at the spectral frequency $3\Omega_x/2\pi$.

homodyne spectrum for different angles ϕ. We show an experimentally obtained spectrum overlaid with the homodyne spectrum of the simulated motion in Figure E.2, calculated at the exact nanosphere position. The significant overlap confirms that the non-zero angle ϕ leads to mixing of the spectral contributions.

BIBLIOGRAPHY

[Aoki et al., 2006] Aoki, T., Dayan, B., Wilcut, E., Bowen, W. P., Parkins, A. S., Kippenberg, T. J., Vahala, K. J., and Kimble, H. J. (2006). Observation of strong coupling between one atom and a monolithic microresonator. *Nature*, 443:671–674.

[Arcizet et al., 2006] Arcizet, O., Cohadon, P.-F., Briant, T., Pinard, M., and Heidmann, A. (2006). Radiation-pressure cooling and optomechanical instability of a micromirror. *Nature*, 444:71–74.

[Asenbaum et al., 2013] Asenbaum, P., Kuhn, S., Nimmrichter, S., Sezer, U., and Arndt, M. (2013). Cavity cooling of free silicon nanoparticles in high vacuum. *Nature Communications*, 4:2743.

[Ashkin, 2006] Ashkin, A. (2006). *Optical trapping and manipulation of neutral particles using lasers*.

[Ashkin and Dziedzic, 1971] Ashkin, A. and Dziedzic, J. M. (1971). Optical Levitation by Radiation Pressure. *Applied Physics Letters*, 19:283–285.

[Ashkin and Dziedzic, 1976] Ashkin, A. and Dziedzic, J. M. (1976). Optical levitation in high vacuum. *Applied Physics Letters*, 28:333.

[Ashkin and Dziedzic, 1977] Ashkin, A. and Dziedzic, J. M. (1977). Feedback stabilization of optically levitated particles. *Applied Physics Letters*, 30:202.

[Ashkin et al., 1986] Ashkin, A., Dziedzic, J. M., Bjorkholm, J. E., and Chu, S. (1986). Observation of a single-beam gradient force optical trap for dielectric particles. *Optics Letters*, 11:288–290.

[Aspelmeyer et al., 2013] Aspelmeyer, M., Kippenberg, T. J., and Marquardt, F. (2013). Cavity Optomechanics. *ArXiv e-prints*.

[Bachor and Ralph, 2004] Bachor, H.-A. and Ralph, T. C. (2004). *A Guide to Experiments in Quantum Optics, 2nd, Revised and Enlarged Edition*.

[Barker and Shneider, 2010] Barker, P. F. and Shneider, M. N. (2010). Cavity cooling of an optically trapped nanoparticle. *Phys. Rev. A*, 81(2):023826.

[Beresnev et al., 1990] Beresnev, S. A., Chernyak, V. G., and Fomyagin, G. A. (1990). Motion of a spherical particle in a rarefied gas. Part 2. Drag and thermal polarization. *Journal of Fluid Mechanics*, 219:405–421.

[Black, 2001] Black, E. D. (2001). An introduction to Pound-Drever-Hall laser frequency stabilization. *American Journal of Physics*, 69:79–87.

[Blakemore et al., 2019] Blakemore, C. P., Rider, A. D., Roy, S., Fieguth, A., Kawasaki, A., Priel, N., and Gratta, G. (2019). Precision mass and density measurement of individual optically-levitated microspheres. *arXiv e-prints*, page arXiv:1902.05481.

[Bohren and Huffman, 1983] Bohren, C. F. and Huffman, D. R. (1983). *Absorption and scattering of light by small particles*.

[Chan et al., 2011] Chan, J., Alegre, T. P. M., Safavi-Naeini, A. H., Hill, J. T., Krause, A., Gröblacher, S., Aspelmeyer, M., and Painter, O. (2011). Laser cooling of a nanomechanical oscillator into its quantum ground state. *Nature*, 478:89–92.

[Chang et al., 2010] Chang, D. E., Regal, C. A., Papp, S. B., Wilson, D. J., Ye, J., Painter, O., Kimble, H. J., and Zoller, P. (2010). Cavity opto-mechanics using an optically levitated nanosphere. *Proceedings of the National Academy of Science*, 107:1005–1010.

[Clerk et al., 2010] Clerk, A. A., Devoret, M. H., Girvin, S. M., Marquardt, F., and Schoelkopf, R. J. (2010). Introduction to quantum noise, measurement, and amplification. *Rev. Mod. Phys.*, 82:1155–1208.

[Costa et al., 2003] Costa, C. A. R., Leite, C. A. P., and Galembeck, F. (2003). Size dependence of stÃűber silica nanoparticle microchemistry. *The Journal of Physical Chemistry B*, 107(20):4747–4755.

[Delić et al., 2019a] Delić, U., Grass, D., Reisenbauer, M., Damm, T., Weitz, M., Kiesel, N., and Aspelmeyer, M. (2019a). Levitated cavity optomechanics in high vacuum. *arXiv e-prints*.

[Delić et al., 2019b] Delić, U., Reisenbauer, M., Grass, D., Kiesel, N., Vuletić, V., and Aspelmeyer, M. (2019b). Cavity cooling of a levitated nanosphere by coherent scattering. *Phys. Rev. Lett.*, 122:123602.

[Drever et al., 1983] Drever, R. W. P., Hall, J. L., Kowalski, F. V., Hough, J., Ford, G. M., Munley, A. J., and Ward, H. (1983). Laser phase and frequency stabilization using an optical resonator. *Applied Physics B: Lasers and Optics*, 31:97–105.

[Fonseca et al., 2016] Fonseca, P. Z. G., Aranas, E. B., Millen, J., Monteiro, T. S., and Barker, P. F. (2016). Nonlinear Dynamics and Strong Cavity Cooling of Levitated Nanoparticles. *Physical Review Letters*, 117(17):173602.

[Frisk Kockum et al., 2019] Frisk Kockum, A., Miranowicz, A., De Liberato, S., Savasta, S., and Nori, F. (2019). Ultrastrong coupling between light and matter. *Nature Reviews Physics*, 1:19–40.

[Gardiner and Zoller, 2000] Gardiner, C. and Zoller, P. (2000). *Quantum noise*.

[Gehm et al., 1998] Gehm, M. E., O'hara, K. M., Savard, T. A., and Thomas, J. E. (1998). Dynamics of noise-induced heating in atom traps. *Phys. Rev. A*, 58:3914–3921.

[Genes et al., 2008a] Genes, C., Mari, A., Tombesi, P., and Vitali, D. (2008a). Robust entanglement of a micromechanical resonator with output optical fields. *Phys. Rev. A*, 78(3):032316.

[Genes et al., 2008b] Genes, C., Vitali, D., Tombesi, P., Gigan, S., and Aspelmeyer, M. (2008b). Ground-state cooling of a micromechanical oscillator: Comparing cold damping and cavity-assisted cooling schemes. *Phys. Rev. A*, 77(3):033804.

[Gieseler et al., 2012] Gieseler, J., Deutsch, B., Quidant, R., and Novotny, L. (2012). Subkelvin Parametric Feedback Cooling of a Laser-Trapped Nanoparticle. *Physical Review Letters*, 109(10):103603.

[Gieseler et al., 2013] Gieseler, J., Novotny, L., and Quidant, R. (2013). Thermal nonlinearities in a nanomechanical oscillator. *Nature Physics*, 9:806–810.

[Gigan et al., 2006] Gigan, S., Böhm, H. R., Paternostro, M., Blaser, F., Langer, G., Hertzberg, J. B., Schwab, K. C., Bäuerle, D., Aspelmeyer, M., and Zeilinger, A. (2006). Self-cooling of a micromirror by radiation pressure. *Nature*, 444:67–70.

[Giovannetti and Vitali, 2001] Giovannetti, V. and Vitali, D. (2001). Phase-noise measurement in a cavity with a movable mirror undergoing quantum Brownian motion. *Phys. Rev. A*, 63(2):023812.

[Grass, 2018] Grass, D. (2018). Levitated optomechanics in vacuum using hollow core photonic crystal fibers and optical cavities, PhD thesis. *Universität Wien*.

[Grass et al., 2016] Grass, D., Fesel, J., Hofer, S. G., Kiesel, N., and Aspelmeyer, M. (2016). Optical trapping and control of nanoparticles inside evacuated hollow core photonic crystal fibers. *Applied Physics Letters*, 108(22):221103.

[Gröblacher et al., 2009] Gröblacher, S., Hammerer, K., Vanner, M. R., and Aspelmeyer, M. (2009). Observation of strong coupling between a micromechanical resonator and an optical cavity field. *Nature*, 460:724–727.

[Hauer et al., 2015] Hauer, B. D., Maciejko, J., and Davis, J. P. (2015). Nonlinear power spectral densities for the harmonic oscillator. *Annals of Physics*, 361:148–183.

[Hodgson and Weber, 2005] Hodgson, N. and Weber, H. (2005). *Laser Resonators and Beam Propagation*.

[Hoelscher-Obermaier, 2017] Hoelscher-Obermaier, J. (2017). Generation and Detection of Quantum Entanglement in Optomechanical Systems, PhD thesis. *Universität Wien*.

[Hofer, 2015] Hofer, S. G. (2015). *Quantum Control of Optomechanical Systems, PhD Thesis*. University of Vienna.

[Hofer et al., 2013] Hofer, S. G., Vasilyev, D. V., Aspelmeyer, M., and Hammerer, K. (2013). Time-Continuous Bell Measurements. *Physical Review Letters*, 111(17):170404.

[Horak et al., 1997] Horak, P., Hechenblaikner, G., Gheri, K. M., Stecher, H., and Ritsch, H. (1997). Cavity-Induced Atom Cooling in the Strong Coupling Regime. *Physical Review Letters*, 79:4974–4977.

[Hosseini et al., 2017] Hosseini, M., Duan, Y., Beck, K. M., Chen, Y.-T., and Vuletić, V. (2017). Cavity Cooling of Many Atoms. *Physical Review Letters*, 118(18):183601.

[Jackson, 1998] Jackson, J. D. (1998). *Classical Electrodynamics, 3rd Edition*.

[Jacobs et al., 1999] Jacobs, K., Tittonen, I., Wiseman, H. M., and Schiller, S. (1999). Quantum noise in the position measurement of a cavity mirror undergoing Brownian motion. *Phys. Rev. A*, 60:538–548.

[Jain et al., 2016] Jain, V., Gieseler, J., Moritz, C., Dellago, C., Quidant, R., and Novotny, L. (2016). Direct Measurement of Photon Recoil from a Levitated Nanoparticle. *Physical Review Letters*, 116(24):243601.

[Jayich et al., 2012] Jayich, A. M., Sankey, J. C., Børkje, K., Lee, D., Yang, C., Underwood, M., Childress, L., Petrenko, A., Girvin, S. M., and Harris, J. G. E. (2012). Cryogenic optomechanics with a Si_3N_4 membrane and classical laser noise. *New Journal of Physics*, 14(11):115018.

[Jonáš and Zemánek, 2009] Jonáš, A. and Zemánek, P. (2009). Light at work: The use of optical forces for particle manipulation, sorting, and analysis. *Electrophoresis*, 29(24):4813.

[Kawasaki et al., 2018] Kawasaki, A., Braverman, B., Pedrozo, E., Shu, C., Colombo, S., Li, Z., Özel, Ö., Chen, W., Salvi, L., Heinz, A.,

Levonian, D., Akamatsu, D., Xiao, Y., and Vuletić, V. (2018). A geometrically asymmetric optical cavity for strong atom-photon coupling. *arXiv e-prints*.

[Kiesel et al., 2013] Kiesel, N., Blaser, F., Delić, U., Grass, D., Kaltenbaek, R., and Aspelmeyer, M. (2013). Cavity cooling of an optically levitated submicron particle. *Proceedings of the National Academy of Science*, 110:14180–14185.

[Knox, 2011] Knox, K. J. (2011). *Light-Induced Processes in Optically-Tweezed Aerosol Droplets*.

[Kubanek et al., 2011] Kubanek, A., Koch, M., Sames, C., Ourjoumtsev, A., Wilk, T., Pinkse, P. W. H., and Rempe, G. (2011). Feedback control of a single atom in an optical cavity. *Applied Physics B: Lasers and Optics*, 102:433–442.

[Kubo, 1966] Kubo, R. (1966). The fluctuation-dissipation theorem. *Reports on Progress in Physics*, 29:255–284.

[Leibrandt et al., 2009] Leibrandt, D. R., Labaziewicz, J., Vuletić, V., and Chuang, I. L. (2009). Cavity Sideband Cooling of a Single Trapped Ion. *Physical Review Letters*, 103(10):103001.

[Loudon, 1973] Loudon, R. (1973). *The quantum theory of light.*

[Mestres et al., 2015] Mestres, P., Berthelot, J., Spasenović, M., Gieseler, J., Novotny, L., and Quidant, R. (2015). Cooling and manipulation of a levitated nanoparticle with an optical fiber trap. *Applied Physics Letters*, 107(15):151102.

[Millen et al., 2015] Millen, J., Fonseca, P. Z. G., Mavrogordatos, T., Monteiro, T. S., and Barker, P. F. (2015). Cavity Cooling a Single Charged Levitated Nanosphere. *Physical Review Letters*, 114(12):123602.

[Monteiro et al., 2018] Monteiro, F., Ghosh, S., van Assendelft, E. C., and Moore, D. C. (2018). Optical rotation of levitated spheres in high vacuum. *Physical Review A*, 97:051802.

[Monteiro et al., 2013] Monteiro, T. S., Millen, J., Pender, G. A. T., Marquardt, F., Chang, D., and Barker, P. F. (2013). Dynamics of levitated nanospheres: towards the strong coupling regime. *New Journal of Physics*, 15(1):015001.

[Motsch et al., 2010] Motsch, M., Zeppenfeld, M., Pinkse, P. W. H., and Rempe, G. (2010). Cavity-enhanced Rayleigh scattering. *New Journal of Physics*, 12(6):063022.

[Murch et al., 2008] Murch, K. W., Moore, K., Gupta, S., and Stamper-Kurn, D.-M. (2008). Observation of quantum-measurement backaction with an ultracold atomic gas. *Nat.Phys.*, 4:561–564.

[Murr et al., 2006] Murr, K., Nußmann, S., Puppe, T., Hijlkema, M., Weber, B., Webster, S. C., Kuhn, A., and Rempe, G. (2006). Three-dimensional cavity cooling and trapping in an optical lattice. *Physical Review A*, 73:063415.

[Nimmrichter et al., 2010] Nimmrichter, S., Hammerer, K., Asenbaum, P., Ritsch, H., and Arndt, M. (2010). Master equation for the motion of a polarizable particle in a multimode cavity. *New Journal of Physics*, 12(8):083003.

[Novotny, 2017] Novotny, L. (2017). Radiation damping of a polarizable particle. *Phys. Rev. A*, 96(3):032108.

[Novotny and Hecht, 2012] Novotny, L. and Hecht, B. (2012). *Principles of Nano-Optics*.

[Nunnenkamp et al., 2010] Nunnenkamp, A., Børkje, K., Harris, J. G. E., and Girvin, S. M. (2010). Cooling and squeezing via quadratic optomechanical coupling. *Phys. Rev. A*, 82(2):021806.

[Owens, 1967] Owens, J. C. (1967). Optical refractive index of air: dependence on pressure, temperature, and composition. *Applied Optics IP*, 6:51.

[Palomaki et al., 2013] Palomaki, T. A., Harlow, J. W., Teufel, J. D., Simmonds, R. W., and Lehnert, K. W. (2013). Coherent state transfer between itinerant microwave fields and a mechanical oscillator. *Nature*, 495:210–214.

[Papageorge et al., 2016] Papageorge, A. T., Kollár, A. J., and Lev, B. L. (2016). Coupling to modes of a near-confocal optical resonator using a digital light modulator. *Optics Express*, 24:11447.

[Pflanzer et al., 2012] Pflanzer, A. C., Romero-Isart, O., and Cirac, J. I. (2012). Master-equation approach to optomechanics with arbitrary dielectrics. *Physical Review A*, 86(1):013802.

[Phelps and Meystre, 2011] Phelps, G. A. and Meystre, P. (2011). Laser phase noise effects on the dynamics of optomechanical resonators. *Phys. Rev. A*, 83(6):063838.

[Pichelstorfer et al., 2018] Pichelstorfer, L., Stolzenburg, D., Ortega, J., Karl, T., Kokkola, H., Laakso, A., Lehtinen, K. E. J., Smith, J. N., McMurry, P. H., and Winkler, P. M. (2018). Resolving nanoparticle growth mechanisms from size- and time-dependent growth rate analysis. *Atmospheric Chemistry & Physics*, 18:1307–1323.

[Purcell et al., 1946] Purcell, E. M., Torrey, H. C., and Pound, R. V. (1946). Resonance Absorption by Nuclear Magnetic Moments in a Solid. *Physical Review*, 69:37–38.

[Purdy et al., 2010] Purdy, T. P., Brooks, D. W. C., Botter, T., Brahms, N., Ma, Z. Y., and Stamper-Kurn, D. M. (2010). Tunable Cavity Optomechanics with Ultracold Atoms. *Phys. Rev. Lett.*, 105:133602.

[Purdy et al., 2013] Purdy, T. P., Yu, P. L., Peterson, R. W., Kampel, N. S., and Regal, C. A. (2013). Strong Optomechanical Squeezing of Light. *Physical Review X*, 3:031012.

[Rabl et al., 2009] Rabl, P., Genes, C., Hammerer, K., and Aspelmeyer, M. (2009). Phase-noise induced limitations on cooling and coherent evolution in optomechanical systems. *Phys. Rev. A*, 80(6):063819.

[Ricci et al., 2018] Ricci, F., Cuairan, M. T., Conangla, G. P., Schell, A. W., and Quidant, R. (2018). Accurate mass measurement of a levitated nanomechanical resonator for precision force sensing. *arXiv e-prints*.

[Riedinger et al., 2018] Riedinger, R., Wallucks, A., Marinković, I., Löschnauer, C., Aspelmeyer, M., Hong, S., and Gröblacher, S. (2018). Remote quantum entanglement between two micromechanical oscillators. *Nature*, 556:473–477.

[Romero-Isart et al., 2010] Romero-Isart, O., Juan, M. L., Quidant, R., and Cirac, J. I. (2010). Toward quantum superposition of living organisms. *New Journal of Physics*, 12(3):033015.

[Romero-Isart et al., 2011] Romero-Isart, O., Pflanzer, A. C., Blaser, F., Kaltenbaek, R., Kiesel, N., Aspelmeyer, M., and Cirac, J. I. (2011). Large quantum superpositions and interference of massive nanometer-sized objects. *Phys. Rev. Lett.*, 107:020405.

[Rothfuss et al., 2018] Rothfuss, N. E., Marsh, A., Rovelli, G., Petters, M. D., and Reid, J. P. (2018). Condensation kinetics of water on amorphous aerosol particles. *The Journal of Physical Chemistry Letters*, 9(13):3708–3713. PMID: 29924626.

[Safavi-Naeini et al., 2011] Safavi-Naeini, A. H., Alegre, T. P. M., Chan, J., Eichenfield, M., Winger, M., Lin, Q., Hill, J. T., Chang, D. E., and Painter, O. (2011). Electromagnetically induced transparency and slow light with optomechanics. *Nature*, 472:69–73.

[Safavi-Naeini et al., 2013a] Safavi-Naeini, A. H., Chan, J., Hill, J. T., Gröblacher, S., Miao, H., Chen, Y., Aspelmeyer, M., and Painter, O. (2013a). Laser noise in cavity-optomechanical cooling and thermometry. *New Journal of Physics*, 15(3):035007.

[Safavi-Naeini et al., 2013b] Safavi-Naeini, A. H., Gröblacher, S., Hill, J. T., Chan, J., Aspelmeyer, M., and Painter, O. (2013b). Squeezed light from a silicon micromechanical resonator. *Nature*, 500:185–189.

[Schleier-Smith et al., 2011] Schleier-Smith, M. H., Leroux, I. D., Zhang, H., van Camp, M. A., and Vuletić, V. (2011). Optomechanical Cavity Cooling of an Atomic Ensemble. *Physical Review Letters*, 107(14):143005.

[Schliesser et al., 2006] Schliesser, A., Del'Haye, P., Nooshi, N., Vahala, K. J., and Kippenberg, T. J. (2006). Radiation Pressure Cooling of a Micromechanical Oscillator Using Dynamical Backaction. *Physical Review Letters*, 97(24):243905.

[Schliesser et al., 2008] Schliesser, A., Rivière, R., Anetsberger, G., Arcizet, O., and Kippenberg, T. J. (2008). Resolved-sideband cooling of a micromechanical oscillator. *Nature Physics*, 4:415–419.

[Stratton, 1941] Stratton, J. A. (1941). *Electromagnetic theory*. International series in pure and applied physics. McGraw-Hill, New York, NY.

[Tanji-Suzuki et al., 2011] Tanji-Suzuki, H., Leroux, I. D., Schleier-Smith, M. H., Cetina, M., Grier, A. T., Simon, J., and Vuletić, V. (2011). Interaction between Atomic Ensembles and Optical Resonators. *Advances in Atomic Molecular and Optical Physics*, 60:201–237.

[Teufel et al., 2011a] Teufel, J. D., Donner, T., Li, D., Harlow, J. W., Allman, M. S., Cicak, K., Sirois, A. J., Whittaker, J. D., Lehnert, K. W., and Simmonds, R. W. (2011a). Sideband cooling of micromechanical motion to the quantum ground state. *Nature*, 475:359–363.

[Teufel et al., 2011b] Teufel, J. D., Li, D., Allman, M. S., Cicak, K., Sirois, A. J., Whittaker, J. D., and Simmonds, R. W. (2011b). Circuit cavity electromechanics in the strong-coupling regime. *Nature*, 471:204–208.

[Thompson et al., 2008] Thompson, J. D., Zwickl, B. M., Jayich, A. M., Marquardt, F., Girvin, S. M., and Harris, J. G. E. (2008). Strong dispersive coupling of a high-finesse cavity to a micromechanical membrane. *Nature*, 452:72–75.

[van de Hulst, 1957] van de Hulst, H. (1957). *Light scattering by small particles*. John Wiley and Sons.

[Vuletić et al., 2001] Vuletić, V., Chan, H. W., and Black, A. T. (2001). Three-dimensional cavity Doppler cooling and cavity sideband cooling by coherent scattering. *Phys. Rev. A*, 64(3):033405.

[Vuletić and Chu, 2000] Vuletić, V. and Chu, S. (2000). Laser Cooling of Atoms, Ions, or Molecules by Coherent Scattering. *Physical Review Letters*, 84:3787–3790.

[Walls and Milburn, 2008] Walls, D. F. and Milburn, G. J. (2008). *Quantum Optics*. Springer.

[Weis et al., 2010] Weis, S., Rivière, R., Deléglise, S., Gavartin, E., Arcizet, O., Schliesser, A., and Kippenberg, T. J. (2010). Optomechanically Induced Transparency. *Science*, 330:1520.

[Yam et al., 2015] Yam, W., Davis, E., Ackley, S., Evans, M., and Mavalvala, N. (2015). Continuously tunable modulation scheme for precision control of optical cavities with variable detuning. *Optics Letters*, 40:3675.

[Yin et al., 2011] Yin, Z.-Q., Li, T., and Feng, M. (2011). Three-dimensional cooling and detection of a nanosphere with a single cavity. *Phys. Rev. A*, 83(1):013816.

LIST OF FIGURES